In silico particle margination in blood flow

Inaugural–Dissertation

zur

Erlangung des Doktorgrades

der Mathematisch-Naturwissenschaftlichen Fakultät

der Universität zu Köln

vorgelegt von

Kathrin Müller
aus Ulm

Jülich
2015

Berichterstatter: (Gutachter)	**Prof. Dr. Gerhard Gompper** **Prof. Dr. Joachim Krug** **Prof. Dr. Udo Seifert**

Tag der mündlichen Prüfung: 02.12.2014

Kurzzusammenfassung

Ein tiefgreifendes Verständnis der Margination, der Migration von Teilchen im Blutfluss zur Gefäßwand, ist notwendig, um die Entstehung von Krankheiten, wie z. B. Blutungs- oder Herz-Kreislauf Krankheiten, besser zu verstehen. Margination von Teilchen ist eine Voraussetzung für eine eventuelle Bindung an die Gefäßwand. Die Bindung an die Gefäßwand ist wiederum für Blutplättchen, das Protein namens von Willebrand-Faktor (VWF), aber auch für Trägerteilchen von Kontrast- und Arzneimitteln, notwendig um ihre jeweilige Aufgabe zu erfüllen. Während der Hämostase, einem Prozess um Blutverlust im Fall einer Verletzung zu verhindern, binden Blutplättchen an die verletzte Gefäßwand, um die Wunde mit einem Blutpfropfen zu schließen. In Regionen, in denen hohe Scherraten vorherrschen, wird die Bindung von Blutplättchen an die Wand durch den langen multimeren VWF vermittelt, welcher im gestreckten Zustand Bindungsstellen bereitstellt. Jedoch ist der Auslöser für die Entfaltung des VWF durch Scherkräfte immer noch nicht vollständig verstanden. Fehlfunktionen dieses Vorgangs und Veränderungen der beteiligten Blutkomponenten können auf der einen Seite zur Bildung von unerwünschten Blutpfropfen und diese wiederum zu Schlaganfall und Herzinfarkt und auf der anderen Seiten zu einer Blutungsstörung führen. Des Weiteren ist die Ausschüttung von Kontrast- und Arzneimitteln durch Trägerteilchen in das Gewebe eine Erfolg versprechende Strategie zur Früherkennung und Behandlung von Krankheiten, wie z. B. Krebs. In dieser Arbeit wird die Abhängigkeit der Margination vom Volumenanteil der roten Blutkörperchen (red blood cells – RBCs), von der Scherrate, vom Gefäßdurchmesser und von der Teilchendeformierbarkeit, -größe und -form betrachtet, um Aufschluss über relevante physikalische Mechanismen zu geben.

Methodisch wird die Margination anhand von Computersimulationen untersucht. Dafür werden zwei mesoskopische hydrodynamische teilchenbasierte Simulationsmethoden verwendet, die dissipative particle dynamics (DPD) und die smoothed dissipative particle dynamics (SDPD) Methode. Außerdem werden zweidimensionale (2D) und dreidimensionale (3D) mesoskopische Modelle für die RBCs, Blutplättchen, Trägerteilchen und den VWF herangezogen, um Blutfluss in einer vereinfachten Geometrie eines Mikrogefäßes zu simulieren.

Durch eine abstoßende hydrodynamische Wechselwirkung zwischen Kanalwand und RBCs entsteht nahe der Wand ein RBC-freier Bereich (RBC-free-layer – RBC-FL). Für ausreichend hohe Scherraten und einen ausreichend hohen Volumenanteil von RBCs (Hämatokrit) werden die untersuchten Teilchen quasi im RBC-FL gefangen. Mit zunehmendem Hämatokrit steigt die Marginationswahrscheinlichkeit. Für deformierbare Teilchen hängt die Margination deutlich von der Scherrate ab. Mit zunehmender Scherrate und Deformierbarkeit sinkt dabei die Marginationswahrscheinlichkeit. Darüber hinaus zeigen die Simulationen, dass Teilchen mit einer Größe im Mikrometerbereich und einer ellipsoiden Form mit hohem Seitenverhältnis, ähnlich der Form von Blutplättchen, am ehesten als Trägerteilchen geeignet sind. Größere Teilchen würden sich durch Wechselwirkung mit den RBCs von der Wand entfernen und kleinere Teilchen, mit einer Größe im Nanometerbereich, weisen eine zu geringe Margination in den Bereich nahe der Wand auf. Außerdem deuten die Rotationsdynamik und weitere Studien über Teilchenadhäsion darauf hin, dass ellipsoide Formen besser geeignet sind als kugelförmige. Darüber hinaus ist die Margination in schmalen Kanälen am effizientesten. In breiten Kanälen ist der RBC-FL zu groß, um eine ausreichende Menge an Teilchen nahe der Wand zu gewährleisten. Jedoch nimmt die Teilchendichte mit zunehmender Kanalbreite und abnehmender Teilchengröße zu, was leichte Abnahmen der Margination ausgleichen kann. Den Prozess der Margination betreffend wurde gezeigt, dass hydrodynamische Wechselwirkungen die scherinduzierte Teilchenmigration weg vom RBC-FL verlangsamen und die Margination beschleunigen. Die Verteilung der Blutplättchen im RBC-FL wird jedoch hauptsächlich durch die Volumenausschluss-Wechselwirkung und Kollisionen mit RBCs bestimmt. Den VWF betreffend führen starke interne attraktive Wechselwirkungen zwischen Monomeren eines Polymermodels beim Erreichen einer kritischen Scherrate nicht nur zu einem Übergang von einem globulären zu einem entfalteten Zustand, wie für den VWF im Experiment beobachtet, sondern auch zu ausreichend guter Margination. Außerdem wurde die Adhäsion von VWF an die Gefäßwand als ein weiterer möglicher Auslöser für die Entfaltung identifiziert, denn die Bindung von einem Ende des Polymers an die Wand verringert die kritische Scherrate um eine Größenordnung und führt zu einer längeren Konfiguration. Die zusätzliche Bindung eines Blutplättchens führt zu einer noch stärkeren Entfaltung. Diese Schlussfolgerungen wurden durch die gemeinsame Interpretation von 2D und 3D Simulationen erreicht, denn es wurde gezeigt, dass die Margination in 2D und 3D qualitativ vergleichbar ist.

Abstract

A profound knowledge of margination, the migration of blood components to the vessel wall in blood flow, is required in order to understand the genesis of various diseases, as e.g., cardiovascular diseases or bleeding disorders. Margination of particles is a pre-condition for potential adhesion. Adhesion to the vessel wall is required for platelets, the protein von Willebrand factor (VWF), but also for drug and imaging agent carriers in order to perform their particular tasks. In the haemostasis, a process to prevent blood loss in case of an injury, platelets adhere to the injured vessel wall in order to close a lesion by a blood clot. In regions, where high shear rates prevail, platelet adhesion is mediated by the large multimeric VWF, which, if stretched, provides binding sites for platelets. However, the triggers for VWF stretching are still not fully understood. Moreover, malfunction of this process and alteration of involved blood components might lead on the one hand to undesirable blood clots and subsequently to stroke or heart attack and, on the other hand, to severe bleeding disorders. Furthermore, the delivery of imaging agents and drugs via targeted carriers provides a promising strategy for early detection and therapy of diseases, for instance cancer. In this work, the dependence of margination on system parameters such as the volume faction of red blood cells (RBCs), shear rate, channel size, and particle deformability, size, and shape is examined, in order to shed light on the relevant physical mechanisms.

Methodological, margination is investigated by means of computer simulations. Therefore, two mesoscopic hydrodynamic particle-based simulation approaches, the dissipative particle dynamics (DPD) method and the smoothed dissipative particle dynamics (SDPD) method, are employed. Furthermore, two-dimensional (2D) and three-dimensional (3D) mesoscopic models for RBCs, platelets, carriers, and the VWF are employed to study blood flow in microcirculation in a simplified geometry.

For high enough shear rates and volume faction of RBCs (hematocrit), the investigated particles become quasi-trapped in the RBC-free-layer (RBC-FL), a region depleted of RBCs, which originates from a repulsive hydrodynamic lift of RBCs from the wall. With increasing hematocrit, the margination probability increases. The margination of deformable particles is also markedly influenced by the shear rate. With increasing shear rate and deformability, the margination decreases. Furthermore, the study indicates that micron-particles with an ellipsoidal shape and high aspect ratio, such as platelets, are favourable for drug carriers, rather than nano-carriers or considerably larger particles. Large particles might be moved away from the wall by RBCs and also nano-carriers show less margination into regions close to the wall. Moreover, the rotational dynamics and different studies of particle adhesion lead to a preference of an ellipsoidal shape over a spherical one. In addition, margination has been found to be most efficient in narrow channels. For wide channels, the RBC-FL thickness is too large to promote a high enough fraction of particles to be close to the wall. Furthermore, with increasing channel size, increasing hematocrit, or decreasing carrier size, an increase of carrier concentration is observed. Concerning the margination process, hydrodynamic interactions have been shown to slow down the shear-induced migration away from the RBC-FL, and to speed up the migration from the center to the RBC-FL. However, the shape of the particle distribution is mainly determined by excluded-volume interactions and collisions with RBCs. Regarding the VWF, strong attractive interactions between monomers of a polymer model lead not only to a globule stretching transition at a critical shear rate, as observed for the VWF in experiments, but also to a sufficient margination. Furthermore, adhesion of the VWF to the wall is identified as an additional trigger for stretching, since adhesion of one end of the polymer to the wall decreases the critical shear rate by an order of magnitude and leads to more extended conformations. Additionally, the adhesion of a platelet leads to even further stretching. All these conclusions are drawn by a combined interpretation of 2D and 3D simulations, since the margination in 2D and 3D has been shown to be qualitatively comparable.

Contents

List of Abbreviations

RBC	red blood cell	1
WBC	white blood cell	1
VWF	von Willebrand factor	1
CVD	cardiovascular disease	1
EM	electron microscopy	
ULVWF	ultra-large VWF	5
VWD	von Willebrand disease	7
ADAMTS13	“a disintegrin and metalloprotease with thrombospondin type 1 motif, member 13”	7
RES	reticulo-endothelial system	8
NSE	Navier-Stokes equation	9
MC	Monte Carlo	10
MD	molecular dynamics	10
BD	Brownian dynamics	11
SD	Stokesian dynamics	11
LGA	lattice-gas automata	11
LB	lattice Boltzmann	11
MPC	multi-particle collision dynamics	12
SRD	stochastic rotation dynamics	12
DPD	dissipative particle dynamics	12
SDPD	smoothed dissipative particle dynamics	12
SPH	smoothed particle hydrodynamics	12
TT	tank-treading	13
TB	tumbling	13
COM	center-of-mass	13
SW	swinging	13
2D	two-dimensional	13
3D	three-dimensional	13
RBC-FL	RBC-free-layer	14

FPM	fluid particle model	23
SDPD+a	SDPD with angular momentum conservation	25
SDPD–a	SDPD without angular momentum conservation	25
WLC	wormlike chain	36
BC	boundary condition	39
KS	Keller and Skalak	41
LJ	Lennard-Jones	43
PAL	potential adhesion layer	52
MSD	mean squared displacement	62
ESL	endothelial surface layer	146

List of Symbols

O_2	Oxygen	2
CO_2	Carbon dioxide	2
D_{RBC}	Average diameter of RBC	3
h_{RBC}	Height of RBC	3
D_{WBC}	Diameter of white blood cell	4
D_{c}	Carrier diameter	8
T	Temperature	9
k_{B}	Boltzmann constant $k_{\mathrm{B}} \approx 1.38 \times 10^{-23}\,\mathrm{J\,K^{-1}}$	9
$\mathbf{v}$	Velocity vector	9
$\mathbf{r}$	Position vector	9
p	Pressure	9
ρ	Mass density	9
η	Dynamic viscosity	9
$\mathbf{F}, \mathbf{f}, f$	Forces	9
Re	Reynolds number	9
τ_{diff}	Typical diffusion time	9
τ_{convec}	Typical convection time	9
V_{t}	Typical system velocity	9
L_{t}	Typical system length scale	9
ν	Kinematic viscosity	9
$\mathcal{T}(\mathbf{r})$	Oseen tensor	10
$\mathbb{1}$	Unity matrix	10
F_{L}	Lift force	13
R_{v}	Vesicle radius	13
$\dot{\gamma}$	Linear shear rate	14
h_{v}	Vesicle distance from wall	14
v_{L}	Lift velocity	14
N_{p}	Number of point particles	19

$\mathbf{F}^{\mathrm{C}}$	Conservative force	19
$\mathbf{F}^{\mathrm{D}}$	Dissipative force	19
$\mathbf{F}^{\mathrm{R}}$	Random force	19
r_{c}	Cut-off radius	19
a	Conservative force coefficient	19
$\hat{\mathbf{e}}$	Position vector normalized to unity	19
c_s	Speed of sound	20
β	Compressibility	20
ω^{D}	Dissipative force weight function	20
γ	Dissipative force coefficient	20
ω^{R}	Random force weight function	20
σ	Random force coefficient	20
dt	Simulation timestep	20
ξ	Random number	20
k	Exponent of dissipative weight function tuning the viscosity	21
$\tilde{g}(\mathbf{r}), g(\mathbf{r})$	Field variables	21
$W(\mathbf{r}, r_h)$	Kernel function	21
r_h	Smoothing length	21
$\delta(\mathbf{r})$	Delta function	21
dV	Fluid volume element	22
m	mass	22
N	Quantity of fluid particles	22
V_h	Volume around fluid particle	22
$\mathbf{G}(\mathbf{r})$	Vector field	22
$F(\mathbf{r})$	Function related to kernel function as $\nabla W = -\mathbf{r}F$	22
$\boldsymbol{\omega}$	Particle spin	22
I	Moment of inertia	22
ξ_{b}	Bulk viscosity	23
η_{r}	Rotational viscosity	23
$\mathbf{N}$	Torque	23
$\mathbf{F}^{\mathrm{D_T}}$	Translational part of dissipative force	23
$\mathbf{F}^{\mathrm{D_R}}$	Rotational part of dissipative force	23
$\boldsymbol{\mathcal{T}}$	Tensor	23
$d\boldsymbol{\mathcal{W}}$	Matrix of independent Wiener increments	24
$d\boldsymbol{\mathcal{W}}^S$	Symmetric part of $\boldsymbol{\mathcal{W}}$	24

$d\boldsymbol{\mathcal{W}}^A$	Antisymmetric part of $\boldsymbol{\mathcal{W}}$	24
$d\overline{\boldsymbol{\mathcal{W}}}^S$	Traceless symmetric part of $\boldsymbol{\mathcal{W}}$	24
W_t	Wiener process	24
p_0, α, b	SDPD model parameters for pressure equation of state	26
t	Time	26
λ_v	Constant of modified velocity-Verlet integration	26
r_w	Thickness of near-wall layer for adaptive shear force calculation	27
Δh	Distance from wall	27
C_k	Adaptive force strength	27
α_r	Relaxation parameter	27
l	Length scale	28
E	Energy	28
L_c	Channel length	29
W	Diameter/Width of channel	29
$\bar{V}, \bar{v}$	Average velocity	29
$R_\mathrm{i}, R_\mathrm{o}$	Radius of inner and outer cylinder	31
$v_\varphi(r)$	Radial angular velocity	31
Ω	Rotational frequency	31
N_v	Number of vertices	35
N_s	Number of springs	35
N_t	Number of triangles	35
U	Potential energy	35
l_j, l_0, l_m	Spring lengths (instantaneous, equilibrium, maximum)	36
l_p	Persistence length	36
k_p	Spring constant	36
η_m	Membrane viscosity	37
k_b	Bending constant	37
ϑ	Bending angle	37
C_1, C_2, C_0	Curvatures	37
κ_r, κ_g	Bending rigidities	37
A, A_0^{tot}	Area of cell (instantaneous, desired)	37
A_j, A_0	Area of triangle (instantaneous, desired)	37
V, V_0^{tot}	Volume of cell (instantaneous, desired)	37
k_a, k_d, k_v	global and local area, and volume constraint coefficient	37
D_r	Effective RBC diameter	37

D_0	Cell diameter	38
L_0	Cell contour length	39
A_p	Area of flat plane	39
$\dot{\gamma}_w$	Wall shear rate	39
n	Number density	39
$g(r)$	Radial distribution function	39
θ_{i}	Inclination angle	40
λ	Viscosity contrast	41
R_0	Effective vesicle radius	41
L_x, L_y, L_z	Side lengths of simulation box	41
$\mathbf{u}$	Eigenvector $\mathbf{u} = (u_x, u_y, u_z)$	42
r_m	Potential minimum position	43
σ_{LJ}	Lennard-Jones (LJ) radius	43
ϵ	Strength of LJ potential	43
$\bar{\dot{\gamma}}$	Average shear rate	44
τ_{RBC}	RBC relaxation time	44
$\dot{\gamma}^*$	Normalized average shear rate	44
H_{t}	Tube hematocrit	45
Δr	Radial distance from the wall	46
$\Delta_{\mathrm{RBC-FL}}$	RBC-FL thickness	50
δ	Thickness of near wall region	52
p_δ	Margination probability in region δ	52
$P_{\mathrm{COM}}(r)$	Center-of-mass (COM) distribution	54
Δ_{MAX}	Distance of peak of COM distribution to wall	57
$p(\Delta_{\mathrm{MAX}})$	Height of the peak of COM distribution	57
$\Delta_{\langle r_{\mathrm{RBC-FL}} \rangle}$	Average COM position in RBC-FL	57
$\Delta_{\langle r \rangle}$	Average COM position in whole channel	57
D_{L}, D_{S}	Carrier long, short diameter	62
κ	Aspect ratio of D_{L} and D_{S}	62
θ	Angle between short axis and radial unit vector	67
ψ	Angular velocity	67
R_{L}, R_{S}	Carrier long, short radius	70
H_{d}	Discharge hematocrit	94
$H(r)$	RBC cross sectional density profile	94
R	Channel half width/ radius	94

Q	Flow rate	95
Φ_{t}	Tube volume fraction	96
Φ_{d}	Discharge volume fraction	97
$\Phi(r)$	Carrier cross sectional density profile	97
a_{m}	Monomer radius	113
κ_{s}	Spring constant	114
R_g	Radius of gyration	115
ν	Polymer scaling exponent	115
N_{m}	Number of monomers	115
L	Length of polymer	116
τ	Characteristic timescale	117
k_s	Spring strength	117
R_S	Extension in flow direction	117
ς	Stress	119
φ	Angle between neighbouring bonds	128
$\boldsymbol{\mathcal{I}}$	Moment of inertia tensor	158
τ_{v}	Vesicle relaxation time	159
Δb	Bond length	175

List of Figures

List of Tables

1. Introduction

1.1. Motivation and relevance

Blood is an essential and complex fluid. It consists of red blood cells (RBCs), white blood cells (WBCs), platelets, the protein von Willebrand factor (VWF), and substances that are solved in a watery solution – the blood plasma. Blood takes care of many important functions in the body, for instance the supply of oxygen and nutrients, removal of waste products, immunological functions, preventing blood loss in case of an injury, and wound heeling [1]. However, due to the complexity of the system malfunctions can lead to severe diseases.

One of the leading causes of human disability and death in the world are cardiovascular diseases (CVDs) [2]. In the year 2008 more than 17 million people died from CVDs [2]. By definition, CVDs are diseases related to the dysfunction of the blood circulation (vessels) and/or the heart. For instance, heart attack or stroke might be a consequence of reduction or disruption of the blood flow to the heart or brain, respectively. One possible reason are blood clots, which either form locally (thrombus) or have been formed elsewhere and were transported via the blood (embolus), leading to an obstruction of blood vessels. Embolism and thrombosis can have several reasons. For instance, an undesirable blood clot may form, due to an increased coagulability of the blood, caused by altered blood components, e.g., platelets and VWF, which are involved in the haemostasis, a process to prevent blood loss by platelet aggregation and coagulation. Furthermore, the dysfunction of the haemostasis may lead to severe bleeding disorders [3, 4]. For these reasons, it is of great importance to understand the process of the haemostasis and to identify the involved blood components including their particular function. Thus, triggers for an alteration of the haemostasis, for instance behavioural risk factors and inherent genetic defects can be determined and treatment can be developed. A first step towards understanding the haemostasis, requires the investigation of platelet and VWF distribution in blood flow, depending on blood flow properties.

Another major cause of human death in the world is cancer. In 2013 about 8 million people died from cancer [5]. Cancer develops due to the occurrence of abnormal cells that multiplicate uncontrolled and change their characteristics [1]. Although, plenty of progress has been achieved in understanding and developing treatment of cancer, the impact on patient survival is still small [6]. Thus, cancer genesis, but also the development of early detection and therapy strategies for cancer is still a recent research interest. For early detection and therapy a sufficient delivery of imaging agents and drugs at e.g., the tumor site is needed, which requires a controlled distribution of this substances in the blood circulation. Hence, a profound knowledge of the influence of blood flow properties and particle properties, as size, shape, and deformability on imaging agent and drug-carrier distribution in the blood vessels is required.

1.2. Biological/medical background

The circulatory or cardiovascular system is responsible for the circulation of blood in order to distribute oxygen (O_2), carbon dioxide (CO_2), nutrients, hormones etc. In arteries primarily oxygenated blood is transported from the heart to the tissue. The arteries branch into the smaller arterioles and even further into the smallest blood vessels, the capillaries. In capillaries the principal exchange of nutrients and oxygen with the tissue takes place. Afterwards, the primarily deoxygenated blood is transported from the capillaries to the venules, the veins, and finally to the heart. During this process about 5 litres of blood are transported per minute, what leads to over 7000 litres per day, for a healthy adult human. The diameter of veins and arteries is in the cm to mm range, arterioles and venules have diameters of some tens of µm, and capillaries are only of a few µm wide. Thus, blood circulation in arterioles, venules and capillaries is called microcirculation [1].

Mephisto in Goethes famous tragedy “Faust” has already stated correctly “Blut ist ein ganz besonderer Saft” (“Blood is quite a peculiar sort of juice”) [7]. The blood plasma amounts to about 55 % of the blood volume and contains mainly water (95 % by volume). Additional to the three types of so-called formed elements, RBCs, WBCs, and platelets, blood constituents are proteins and other solutes (e.g., nutrients, hormones) [1].

Red blood cells (RBCs) or erythrocytes constitute the majority of cells with a count of about 5×10^6 per µl. The volume fraction of RBCs, called the hematocrit, is 37 % to 54 %, varying for male and female [1]. RBCs have been discovered already around 1660–1670 by the Dutch scientist Jan Swammerdam and Anton van Leeuwenhoek [9].

RBCs are cells without a nucleus and their main components are water and haemo-

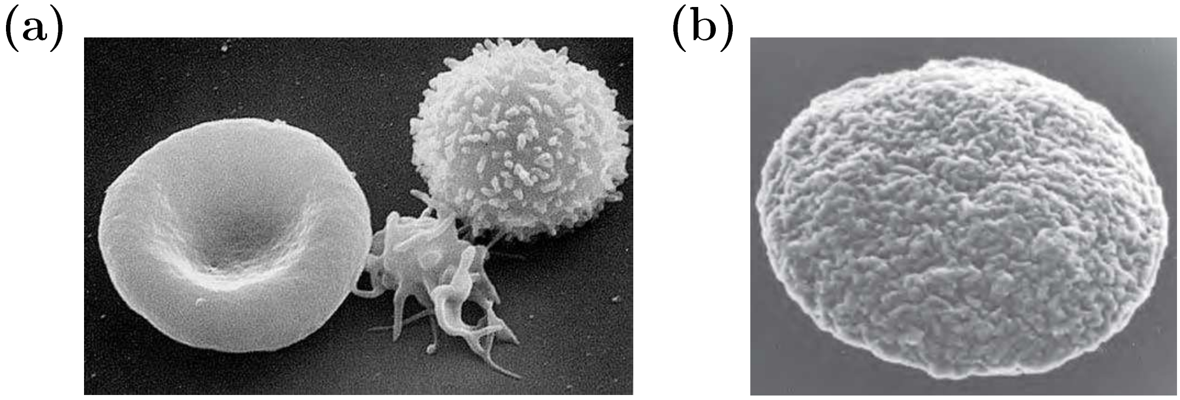

Figure 1.1.: Scanning electron microscopy (EM) images of formed blood elements: (a) red blood cell (RBC) (left), activated platelet (middle), and white blood cell (WBC) (right) and (b) non-activated platelet. Source of the image (a): The National Cancer Institute at Frederick (NCI-Frederick). The image (b) is reprinted from Ref. [8]. Copyright (2007), with permission from Elsevier.

globin, which is responsible for the red colour. RBCs are produced in the red bone marrow and remain in the blood for 100 to 200 days. RBCs are mainly responsible for the transport of O_2 from the lungs to the tissue and transports part of the CO_2, a waste product from the cell metabolism, back to the lung. Their discocyte (biconcave disc-like) shape, see the electron microscopy (EM) image in Fig. 1.1 (a), is favourable for fast exchange of O_2 which is performed by diffusion, since the large surface area to volume ratio increases the speed of the O_2 uptake and release [10,11]. With an average diameter of $D_{\mathrm{RBC}} = 7.5\,\mu\mathrm{m}$ and a height of $h_{\mathrm{RBC}} = 2\,\mu\mathrm{m}$, RBCs have to be very elastic in order to get through the small capillaries with a typical diameter of $5\,\mu\mathrm{m}$ to $8\,\mu\mathrm{m}$ [1]. Therefore, RBCs have a viscous membrane, which consists of a lipid bilayer, and a cytoskeleton, a network which consists mainly of spectrin proteins linked by short actin filaments to the inner monolayer, see Fig. 1.2. The lipid bilayer is area preserving, the non-compressible inner cytosol is volume preserving, and the RBC membrane is viscoelastic due to the attached spectrin network and the lipid membrane [12].

The smallest formed element is the **platelet** or thrombocyte. Platelets have been discovered almost 200 years later than the RBCs, in 1842 by the French scientist Alfred Donné [9]. Platelets are thin cellular fragments without a nucleus and with a disc-like shape as presented in Fig. 1.1 (b). Their diameter varies between $2\,\mu\mathrm{m}$ and $4\,\mu\mathrm{m}$ and they possess a thickness of about $0.5\,\mu\mathrm{m}$ [1]. After their budding off from the cells, called megakaryocytes, in the bone marrow, they remain in the blood for about 7 to 10 days. In addition to their outer membrane, they possess an internal cytoskeleton, composed of polymers of actin and tubulin. Compared to RBCs, platelets are stiffer [8,14]. On

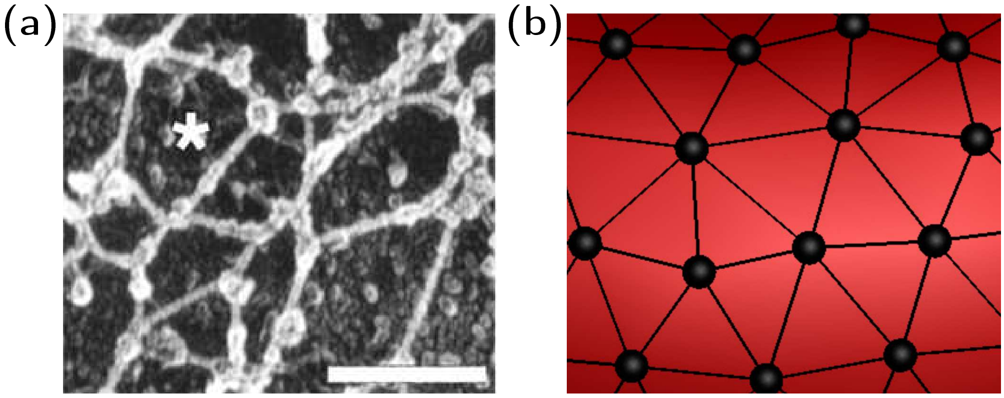

Figure 1.2.: Illustration of spectrin network. (a) Electron micrographs of RBC membrane skeleton from mice. The bar gives the reference length of $200\,\mathrm{nm}$. The picture is taken from Ref. [13]. (b) Illustration of a spectrin network structure.

average $150 - 400 \times 10^3$ per µl platelets can be found in human blood.

Cessation of bleeding is mediated by platelet accumulation next to a vascular injury. Platelets in circulation screen the vascular bed for irregularities. As soon as a defect is detected, the platelets react with adhesion. The process of initial platelet-plug formation is called primary haemostasis. Low platelet counts may retard the primary haemostasis and lead to a severe increase of bleeding times [15]. As the key player in the primary haemostasis, platelets have several receptors, which can interact with subendothelial components, such as collagen, to facilitate adhesion to the damaged vessel wall in case of an injury [16, 17]. Additionally, the adhesion can be mediated by several proteins, including the von Willebrand factor (VWF) [15]. The interactions of platelets with VWF is important especially at high shear rates, as discussed below in more detail. In response to the initial tethering of some platelets, other platelets in the surrounding can become activated, which is required for their firm adhesion to the extracellular matrix [17]. Activation leads to a more spherical shape and a formation of sticky tethers with activated receptors, see Fig. 1.1 (a). Accumulation of adhered platelets results in a plug, which is then further stabilized by e.g., fibrinogen fibres during the secondary haemostasis.

Another cell species are **white blood cells (WBCs)** or leucocytes with a count of about 7×10^3 per µl [1]. WBCs have been discovered in 1843 by the French scientist Gabriel Andral and the English scientist William Addison [9]. In contrast to RBCs, WBCs possess a nucleus. They have an almost spherical shape, see Fig. 1.1 (a), with a diameter of $D_{\mathrm{WBC}} = 6 - 20\,\mu\mathrm{m}$ depending on the category. As a part of the immune system, WBCs recognize foreign substances and infectious agents. WBCs migrate to the wall (marginate), bind to it and transmigrate into the tissue to reach the invading organism. Furthermore, WBCs eliminate the intruder by phagocytosis [1, 18].

As mentioned above, proteins are soluted in blood. These proteins are important for different functions e.g., the blood coagulation. One example is the glycoprotein called **von Willebrand factor (VWF)**, which mediates platelet aggregation at the vessel wall in case of an injury by platelet binding, see Figs. 1.3 (a,b). VWF has been (immunologically) discovered as recently as 1971 by Zimmermann and colleagues [4]. The VWF mediates the adhesion of platelets to the vessel wall at high shear rates where platelets cannot bind autonomously. The VWF is the largest protein found in blood, with a contour length of multimers which can be larger than 100 µm [19, 20]. This multimeric protein is composed of identical subunits, the dimers, which have a length of approximately 70 nm and a thickness of about 10 nm. These dimers are synthesized in the endoplasmatic reticulum [4]. The dimers consist of different domains which are responsible for interactions with different counterparts, for instance platelets, enzymes, or the subendothelium, see Figs. 1.3 (c,d). The multimer is assembled in the Golgi complex and can be released into the blood plasma, stored in the Weibel-Palade bodies, secreted basolaterally into the subendothelium, or stored in platelet α-granules. Stored VWF is often unusually long in comparison with plasmatic VWF [4, 15]. The ultra-large VWF (ULVWF) is typically released in response to signals which indicate vascular damage [4]. ULVWF has been experimentally detected in blood plasma not only after an induced release from endothelial storage sites, but also in case of certain blood diseases [15].

The adhesion of platelets to VWF is mediated by the glycoprotein Ibα (GPIbα) that is expressed on the surface of platelets. Platelet binding to VWF is able to withstand very high forces which would correspond to abnormally high shear rates and may occur in a stenosed (constricted) vessel [26]. However, GPIbα binding to immobilized VWF has high association as well as dissociation rates [27]. Therefore, platelets mainly slide along the VWF chains in the direction of the flow [28]. Their velocity typically corresponds to about 2% of the velocity of freely flowing platelets. The low velocity facilitates the formation of bonds between platelets and subendothelial ligands (e.g., collagen) which leads to eventual platelet arrest [15, 27]. Several experimental studies [29–32] indicate that adhesion of platelets to VWF mainly depends on the shear rate and the length of VWF. These studies also suggest that an increased shear rate leads to a conformational change of VWF from a globular to a stretched configuration, which is accompanied by increased platelet adhesion. Experiments with a single VWF in shear flow [19] have

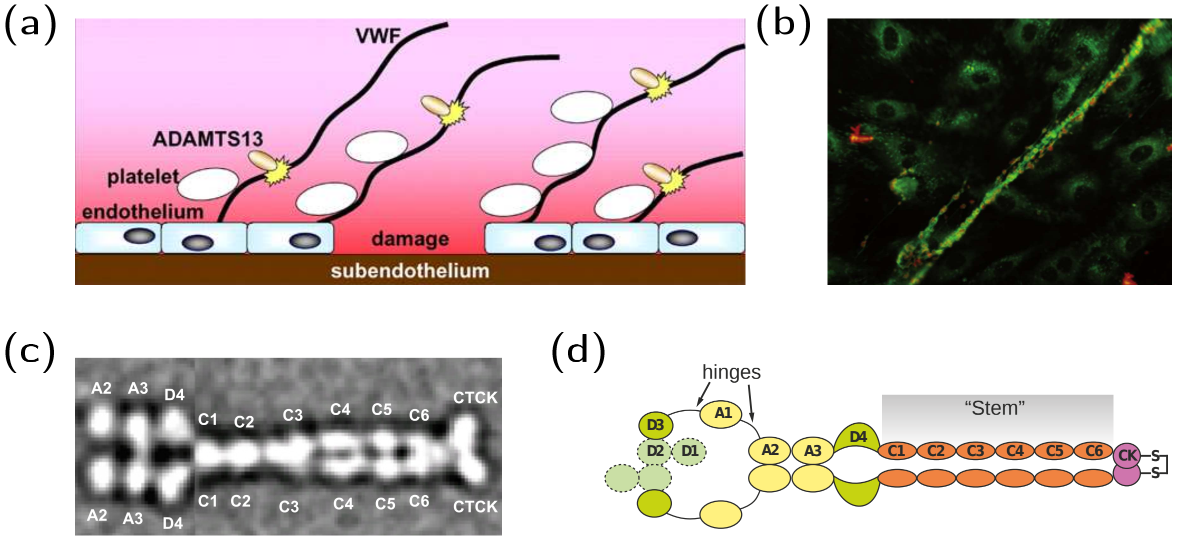

Figure 1.3.: Von Willebrand factor (VWF) mediated platelet adhesion and VWF dimer. (a) Illustration of VWF and platelet interaction in case of an injury. Picture taken from Ref. [21]. (b) Release of VWF string (green) after stimulation of endothelial cells (green in background) and platelets (red dots) adhere to VWF. Picture taken from Refs. [22, 23]. (c) Composite negative stain electron microscopy (EM) image of VWF dimer. Picture taken from Ref. [24]. (d) Illustration of VWF dimer derived from EM pictures taken and modified from Ref. [25].

shown that the average extension of VWF strongly depends on shear rate. VWF extension dramatically changes from a primarily globular to a stretched configuration when a critical shear rate of about $5000\,\mathrm{s}^{-1}$ has been reached [19]. Furthermore, adhesion of a stretched VWF to exposed collagen at a site of injury is also enhanced. Recent numerical simulations and experiments on the formation of aggregates consisting of VWF and colloids in shear flow [33] have confirmed that VWF length, adhesive interactions, and shear rate are the most important factors which govern aggregate size. However, a full understanding of what triggers the unraveling of VWF in the body, has not yet been achieved.

An alteration of components, which participate in the primary haemostasis can lead to extensive bleeding or undesired thrombotic events. One of the most common inherited bleeding disorders is the von Willebrand disease (VWD) with an incidence of up to 1% of the general population [3]. The VWD can be caused by a reduced number of VWF chains (type 1), qualitative changes in their function (type 2), or their complete absence (type 3). The VWD type 2 is related to defects in VWF chains due to mutations resulting in bleeding symptoms of different severity. A different type of blood disorder, thrombotic thrombocytopenic purpura, is caused by the dysfunction of VWF length regulation performed by the enzyme “a disintegrin and metalloprotease with thrombospondin type 1 motif, member 13” (ADAMTS13), which normally cleaves long VWF chains, and therefore controls their length. This dysfunction leads to the occurrence of very long VWF chains in blood plasma. As a result, spontaneous formation of VWF-platelet aggregates may occur and these small platelet clots (thrombi) can damage various tissues and organs due to blood-flow blockages and can lead to myocardial infarction and stroke [34]. Furthermore, VWF influences various other blood components, for instance increases the life time of the blood coagulation protein factor VIII and promotes leucocyte extravasation [35].

In addition, to the natural blood components introduced above, synthetic particles can be injected into the circulatory system for therapeutic or other reasons. For instance, the use of targeted **micro- and nano-carriers** for the delivery of imaging agents and drugs provides a promising strategy for early detection and treatment of diseases, e.g., cancer [36, 37]. However, the determination of the distribution of micro- and nano-carriers in the organism following systemic administration has been identified as one of several major challenges in nanomedicine [38]. Additional to their distribution in the organism, adhesion to specific targeted sites and transport through biological barriers [38–40] has to be considered. Different carrier types have been proposed for drug delivery. Examples are polymer conjugates that are already in clinical use [41,42], fabricated nanoparticles [42,43], and self-assembled structures from lipids or polymers with hydrophilic and hydrophobic fragments forming liposomes, polymersomes, or worm-like micelles [42]. All these carriers differ in shape, size, and deformability.

The role of particle size and shape for the efficient delivery is a multi-faceted problem. Large carriers, with a characteristic diameter (D_c) greater than about 4 µm, may become trapped in the smallest capillaries of the body [44]. Recent experiments suggest that large particles with $D_\mathrm{c} \gtrsim 3\,\mu\mathrm{m}$ are faster removed by the immune system (macrophages) in the reticulo-endothelial system (RES) such as the liver, spleen, and lungs, because they are subject to an enhanced phagocytosis [45,46]. Various experiments [47,48] indicate that the size determines the circulation time of particles. For instance, liposomes of an intermediate size of $D_\mathrm{c} \approx 150 - 200\,\mathrm{nm}$ circulate longer than those with $D_\mathrm{c} < 70\,\mathrm{nm}$ and $D_\mathrm{c} > 300\,\mathrm{nm}$ [47]. However, microfluidic experiments [49] have shown that spheres with the size of 2 µm exhibit a significantly higher adhesion density than particles with a size of 500 nm and 200 nm, while nano-particles possess better internalization properties than micro-particles [40].

Experiments with discoidal particles [45] demonstrated that they accumulate better in the organs than their spherical counterparts. On the one hand, internalization by macrophages appears to be reduced for elongated particles [50]. On the other hand, the internalization into endothelial cells is reduced as well [40]. Additionally, adhesion of different carrier types has been studied experimentally [51,52] and theoretically [53,54], with the result that oblate ellipsoids are subject to stronger adhesion than spheres with the same volume.

In summary, a proper cross-sectional distribution of natural and synthetic blood components is important for accomplishing their particular task. RBCs migrate to the vessel center [55,56], the high velocity region, to ensure an efficient transport of O_2 and CO_2. In contrast, a required pre-condition for adhesion of platelets, drug carriers, VWF as well as WBCs is their localisation close to the wall. Therefore, a quantitative description of their migration to the wall (margination) under realistic blood flow conditions is required to better understand the particular adhesion potential.

1.3. Physical/numerical background

Blood is a typical **soft matter** system. Soft matter embraces materials which are neither a Newtonian liquid nor a solid. Examples of soft matter systems are colloidal suspensions (e.g., ink, milk), polymer solutions, amphiphile mixtures (e.g., soap), gels, self-propelled swimmers (e.g., sperms), but also networks in cells. The relevant length scale of these systems lies in the mesoscopic range, namely from 10 nm to 10 µm. Furthermore, the relevant energy scales of these systems are comparable with the thermal energy $k_\mathrm{B}T$, with the temperature T and the Boltzmann constant k_B. As the name implies, soft materials distort easily. For instance, the shear modulus of a colloidal crystal is 14 orders of magnitude lower than the one of a molecular crystal [57]. Often soft matter systems are composed of a dispersion medium (e.g., a liquid) with a disperse phase (e.g., macromolecular particles) suspended in it. Therefore, the interactions mediated by the solvent play a crucial role in many soft matter systems.

Interactions via the solvent are called hydrodynamic interactions. Hydrodynamics describes the dynamics of fluids. A flow of a simple (viscous) fluid is mainly described by mass, momentum, and energy conservation and the incompressible Navier-Stokes equation (NSE),

$$\begin{aligned} \rho\left(\frac{\partial \mathbf{v}}{\partial t} + (\mathbf{v}\cdot\nabla)\,\mathbf{v}\right) &= -\nabla p + \eta\nabla^2\mathbf{v} + \mathbf{f}_\mathrm{ext}, \qquad (1.1)\\ \nabla\cdot\mathbf{v} &= 0 \end{aligned}$$

with the velocity field $\mathbf{v} = \mathbf{v}(\mathbf{r}, t)$ at the position $\mathbf{r}$, the pressure field $p = p(\mathbf{r}, t)$, the density ρ, the dynamic viscosity η, and an external force $\mathbf{f}_\mathrm{ext} = \mathbf{f}_\mathrm{ext}(\mathbf{r}, t)$. The NSE can be derived by balancing the forces acting on a fluid volume element [58]. Hydrodynamics is the investigation of fluid flow for given geometry, pressure, and temperature. A main distinction is made between flows where the viscous forces and thus the diffusive transport is dominant and the flows where the convective transport is dominant. The Reynolds number characterizes the relative importance of the convective transport with respect to the diffusive one. The Reynolds number Re is the ratio of the typical diffusion time τ_diff and the typical convection time τ_convec,

$$Re = \tau_\mathrm{diff}/\tau_\mathrm{convec} = V_\mathrm{t}L_\mathrm{t}/\nu, \qquad (1.2)$$

with a typical velocity of the system V_t, a typical length scale L_t, and the kinematic viscosity $\nu = \eta/\rho$. For a low Reynolds number ($Re \ll 1$) the diffusive transport prevails and the fluid moves in layers without mixing (laminar), whereas for high Reynolds numbers turbulences occur. For flows with low Reynolds numbers, also called Stokes flow or creeping flow, the non-linear term of the NSE, the convection term, can be neglected $((|\rho(\mathbf{v}\cdot\nabla)\mathbf{v}|)\,(|\eta\Delta\mathbf{v}|)^{-1} << 1)$. Hence, the incompressible NSE simplifies for the steady state to the linear Stokes equation

$$\begin{aligned}\nabla p - \eta\Delta\mathbf{v} &= \mathbf{f}_{\text{ext}}, \\ \nabla\cdot\mathbf{v} &= 0.\end{aligned} \tag{1.3}$$

One solution of the Stokes-Equation is

$$\mathbf{v}(\mathbf{r},t) = \int d\mathbf{r}'\mathbf{f}_{\text{ext}}(\mathbf{r}',t)\mathcal{T}(\mathbf{r}-\mathbf{r}'), \tag{1.4}$$

with the Oseen tensor $\mathcal{T}(\mathbf{r}) = (8\pi\eta r)^{-1}\left(\mathbb{1} + \mathbf{rr}/r^2\right)$, with $r = |\mathbf{r}|$, the unity matrix $\mathbb{1}$, and the boundary conditions $\lim\limits_{r\to\infty}\mathcal{T}(\mathbf{r},t) = 0$ [59]. Since the Oseen tensor is inverse proportional to the position ($\mathcal{T}(\mathbf{r}) \sim 1/r$), the effect of a force is long-ranged.
In the case of moving mesoscopic particles in a fluid, each particle induces a long-ranged flow in the fluid and is influenced by the fluid. Thus, mesoscopic particles experience long-ranged hydrodynamic interactions among each other and with the wall of the container. Consequently, the motion of all particles is coupled.

Due to the complexity of these many-body systems, computer simulations play an important role in the investigation of their behaviour. Simulations can be utilized to better understand experimental results and survey theories. Furthermore, simulations may predict the behaviour of material under conditions which are difficult to explore experimentally, suggest new materials, and deliver new ideas for experiments. Thereby, a variety of simulation methods have been applied to soft matter systems.

The first computer simulation has been performed in 1953 at the Los Alamos National Laboratories in the US. The used method was the Metropolis algorithm of the **Monte Carlo (MC)** method. By random displacements of system particles, the particle distribution corresponds finally to a given probability distribution e.g., the classical Boltzmann distribution [60]. In this way static equilibrium properties such as the structure of the system can be investigated. Systems which have been investigated via MC are, for instance, liquid crystals [61], polymers [62], and magnetic colloids [63].

In order to investigate the dynamics of multi-particle systems the **molecular dynamics (MD)** simulation method was one of the first being used. Particle positions and velocities are calculated from the Newton's equation of motion [60,64]. MD simulations have been applied to simple colloidal systems, as for instance, hard spheres [65].

In MC and the original MD simulation methods the dispersion medium is primarily neglected. However, an immersed particle in a solvent interacts with the solvent molecules that undergoes thermal fluctuations, which leads to a random motion of these mesoscopic particle, called the Brownian Motion [66]. Furthermore, several particles interact hydrodynamically with each other, as discussed above. The difficulty to treat mesoscopic particles and the solvent in the same simulation is the disparity in their length and time scales. In order to resolve the solvent dynamics, small timesteps are needed. Therefore, long simulations would be required to resolve the mesoscopic dynamics as well. Furthermore, a huge amount of particles would be needed to investigate multi-particle systems, since already one dispersed particle would consist of a high number of particles comparable to the size of the fluid molecule. However, the dynamics of the individual solvent molecules are not relevant for the whole soft matter system. For this reason, there exist several simulation approaches to mimic fluid interactions either implicitly or explicitly

For instance, MD is nowadays, widely used for detailed simulations of biological macromolecules [67] including implicit and explicit water models [68],

The **Brownian dynamics (BD)** simulation method implements the Langevin dynamics [69, 70]. Additional to friction and external forces, a random force acts on the particles, mimicing the Brownian motion, which is induced by the solvent molecules. Thus, the motion of the particles is diffusive, but hydrodynamic interactions are not included. However, hydrodynamic interactions can be incorporated by an additional force, given by, for instance, the Rotne-Prager or Oseen tensor, which is then also called the **Stokesian dynamics (SD)** method [71].

In order to explicitly incorporate fluid interactions again two approaches exist, the on-lattice and off-lattice methods. One on-lattice method is the **lattice-gas automata (LGA)**. The speciality of this method is that the particles move from site to site of a lattice. The particles collide if they are on the same lattice side. Collisions are performed in a way such that mass and momentum are conserved [72]. It has been shown that this model fulfils the NSE in the continuum limit by choosing the appropriate parameters [73]. Colloidal systems [74] and polymer systems [75] have been successfully modelled with this method. A drawback of this method is that the Galilean invariance is broken due to the lattice. The **lattice Boltzmann (LB)** method has originally been developed from the LGA and solves the Boltzmann equation on a lattice. Although the fluid is modelled explicitly, in both lattice methods, there were originally no thermal fluctuations included, although there exist now approaches which include fluctuations [72]. Examples for soft matter systems modelled by LB are polymers [76], colloidal suspensions, liquid crystals [77], and blood [78].

One of the off-lattice methods is the **multi-particle collision dynamics (MPC)** simulation method, also called stochastic rotation dynamics (SRD) [72, 79]. It consists of discrete streaming and collision steps. During the streaming step the particles move ballistically. For the collision step the system is divided into different cells. The collision is implemented by a stochastic rotation of the relative velocities of all particles in one collision cell, with respect to the center-of-mass velocity in the cell. The collision cells are shifted before each collision step to ensure Galilean invariance [72]. MPC has been applied, for instance, to polymers, self propelled systems, colloids, vesicle, and blood flow [72, 80, 81].

In 1992, Hoogerbrugge and Koelman [82] introduced another off-lattice method, the **dissipative particle dynamics (DPD)** method, as a combination of MD and the LGA. Then, Español and Warren [83] developed it further, such that the Gibbs canonical ensemble is the equilibrium solution of the corresponding Fokker-Planck equation, leading to a fluctuation-dissipation theorem. In DPD three proposed forces, a conservative, a dissipative, and a random force determine the position and the velocity of the fluid particle by applying Newton's second law. Thereby the fluid particles can be interpreted as a molecular cluster.

Drawbacks of DPD are that the equation of state as well as the viscosity are an outcome of the simulation. Therefore, the **smoothed dissipative particle dynamics (SDPD)** method has been introduced as a combination of smoothed particle hydrodynamics (SPH) with thermal fluctuations included similar to DPD [84]. SPH is a method, which has been originally used in astrophysics and is used to discretize the Navier-Stokes equation. Two approximations are applied in order to obtain numerical solutions of equations of fluid dynamics. First, the quantity, which is to be determined, is replaced by a convolution integral of this quantity and a so called kernel function, and second, the integral is replaced by a discrete sum [85, 86]. The original SDPD formalism lacks angular momentum conservation [84]. However, there exist variations of the SDPD method with angular momentum conservation [87, 88]. The simulation results presented in this work have been produced with the DPD and SDPD methods.

1.4. Blood flow *in silico* and *in vitro*

Numerical simulations have been proven to be a good tool to deliver new insights in complicated systems such as blood flow. *In silico* studies of blood flow can utilize different techniques depending on the domain to be investigated. In large vessels (diameter larger than 500 µm) and for high enough shear rates blood can be treated as a Newtonian fluid with a constant viscosity, due to the high flow rates [89, 90]. With decreasing vessel diameter the fluid behaviour becomes non-Newtonian, but can still be solved by continuum models [89]. However, for vessel sizes smaller than 100 µm, as examined in this work, explicit modelling of RBCs is required [91]. The above introduced simulation methods have been utilized to investigate blood with explicit modelling of blood components under various conditions. Recent research interests range from the properties of single cells in flow to flowing suspensions

A number of experiments [56, 92–94], theoretical approaches [95–98], and simulations [99–104] have shown that RBCs, elastic capsules, and fluid vesicles exhibit a rich dynamical behaviour in shear flow including tank-treading (TT) and tumbling (TB) motion. The TB motion corresponds to a vesicle rotating around its center-of-mass (COM) almost as a rigid body. A TT vesicle in shear flow exhibits a stationary shape with a finite inclination angle with respect to the flow direction, while the membrane and inner fluid is rotating around the COM of the vesicle. A third interesting dynamic of a single vesicle is the swinging (SW) or vacillating-breathing state, which occurs between the TT and TB regimes. An experimental example of Ref. [94] is shown in Fig. 1.4 (α). Essential for the SW state is that the vesicle undergoes shape deformations. Concurrently an oscillating inclination angle is observed. The transition between the modes can primarily be induced by changing the viscosity contrast of the internal and external fluid.

Blood flow takes place in blood vessels, thus the interaction of particles with the wall has to be considered additional to shear flow. Studies in three-dimensional (3D) and two-dimensional (2D) model systems have shown that RBCs and vesicles experience a lift away from a wall due to the hydrodynamic interactions with the wall. This lift force exists due to an asymmetric shape, deformability, and the TT motion. A non-deformable sphere does not experience a lift force in a low Reynolds number flow, due to the time reversibility of the Stokes flow. Rigid non-spherical particles can experience a lift, but tend to tumble in flow which reduces the drift from the wall [105]. The lift force on RBCs and vesicles has been studied experimentally [56,106,107], theoretically [55,105,108], and numerically [104, 109]. The strength of the hydrodynamic lift force F_{L} depends on the size, shape, deformability, distance to the wall, fluid viscosity, and shear rate. Boundary-integral simulations [109] and theoretical studies [105] together with experiments [56] suggest a dependence of the lift force on the vesicle radius R_{v} in 3D as $F_{\mathrm{L}} \sim R_{\mathrm{v}}^{\zeta}$ with

$\zeta = 3$ [56] and $\zeta = 4$ [105,109]. For 2D $\zeta = 0.5$ has been found [55]. Furthermore, the lift force increases with increasing deformability [56]. Vesicles in simple shear flow bound to a wall have been found to detach, see Fig. 1.4 (β) from Ref. [56], and it has been suggest that $F_\mathrm{L} \sim \eta^2\dot{\gamma}^2$ [55,108], with $\dot{\gamma}$ the shear rate. For a vesicle close to the wall at height h_v it has been suggested that $F_\mathrm{L} \sim \eta\dot{\gamma}$ [55,56,109] and $F_\mathrm{L} \sim h_\mathrm{v}^{-2}$ [104,105,109], but also $F_\mathrm{L} \sim h_\mathrm{v}^{-1}$ [56,108]. Close to the wall the force is strongest and decreases with increasing distance. The balance of lift force and gravity leads to a equilibrium distance of the vesicle to the wall. However, under influence of microgravity a drift of vesicles is observed at larger distances from the wall with the lift velocity $v_\mathrm{L} \sim h_\mathrm{v}^{-2}$ [107]. The TT motion contributes to the lift force as follows. If an inclined vesicle is close to the wall, the hydrodynamic interactions with the fluid increase the pressure in the gap between the vesicle and lead to the lift. Concurrently, the pressure is reduced at the two caps of the vesicle [104]; see also Fig. 1.4 (γ). Furthermore, spherical particles experience a lift from the wall in case of an flexible wall, which also breaks the symmetry [110]. In blood flow, the lift force leads the crowding of RBCs in the middle of the channel. Hence, a region close to the wall depleted of RBCs, here called the RBC-free-layer (RBC-FL), develops [111].

In blood vessels the blood components are exposed to Poiseuille flow rather than simple shear flow. In Poiseuille flow migration to the low shear rate and high velocity regime is numerically observed even without a wall [112]. Simulations of single and several RBCs in Poiseuille flow have identified different shapes of RBCs, the discocyte shape, the parachute shape, and the slipper like shape [113–115] and see Fig. 1.5 (α). The occurrence of different shapes depends on the shear rate and the channel size. These shapes have also been found in experiments [116]. Further numerical studies have identified additional RBC shapes like teardrops and fin-tailed spheres in case of sedimentation, due to gravity or centrifugation [81], see also Fig. 1.5 (β). For several RBCs in a channel, additionally to different shapes, different alignments in flow have been observed, as an unordered arrangement of discocyte shapes, axis aligned parachute shapes, and a zig-zag structure of slipper-like shapes [113] as presented in Fig. 1.5 (α).

Furthermore, blood is a non-Newtonian shear thinning fluid. This shear thinning results from RBCs, which aggregate into rouleaux structures for low shear rates (see Fig. 1.5 (γ)) and a break-up of these stacks with increasing shear rate. Experimentally, it has been shown that this aggregation is related to the presence of plasma proteins [117]. In simulations it has been observed that low attraction between the RBCs leads to a good representation of this shear-thinning behaviour and the attraction forces have been estimated to be 2 pN to 7 pN [118].

However, in blood also other components as platelets and WBCs are present. A good first assumption of different blood components are different sized rigid particles. It has been observed that in bidisperse systems of large and small particles, the distribution depends on the overall volume fraction and the volume fraction of the two components [119]. Typically the large particles accumulate in the low shear rate region, due to their larger drift velocity towards the center line. However, for large overall volume fraction and large fraction of small particles, the small particles enrich the center of the channel. Furthermore, the distribution of particles in the channel depends on their deformability. For bidisperse systems of deformable and stiff capsules with the same size a higher fraction of stiffer particles is found close to the wall [119].

WBC are larger and stiffer than RBCs, their count in blood is much smaller, and they have a more spherical shape. Experimental studies *in vivo* and *in vitro* have shown that WBCs marginate as needed to perform their function [121, 122]. However, the margination decreases with increasing shear rate but is less sensitive to the hematocrit. Only for hematocrit values larger than 50 % and low shear rates a drastic increase of margination has been observed. Furthermore, for the hematocrit range 20 % to 30 % the strongest WBC margination occurs, supposedly due to the RBC aggregation [119, 123, 124]. Recent 2D [120] and 3D [125] simulations are in good agreement with experimental results. Furthermore, these simulations provided an explanation for these observations. For hematocrit values below 45 % the space in front of a WBC is empty, but RBCs coming from behind collide with the WBC and push it to the wall. However, for high hematocrit values the RBCs occupy also the space in front of a WBC and thus act as a "springboard" and the WBC is pushed towards the channel center, see Fig. 1.5 (δ). Additional 3D simulations have shown that WBC margination is indeed stronger for the case with aggregating RBCs than without aggregation and that the RBC aggregation increases primarily the margination for the low shear rates [125].

Margination of platelets has been observed *in vivo* [126, 127], as well. *In vitro* experiments in channels from 50 µm to 200 µm with rigid platelet sized beads showed that for a significant number of beads close to the wall the hematocrit has to be larger than 7 % and the number increases with hematocrit [128]. Furthermore, the margination increase with shear rate until an optimal value and decreases afterwards [129]. Numerical studies that focused on platelet margination in 2D [130] and 3D [14, 131, 132] have presented that margination of rigid particles increase with increasing hematocrit. Furthermore, a 2D study showed that the accumulation in the periphery of the blood vessel develops

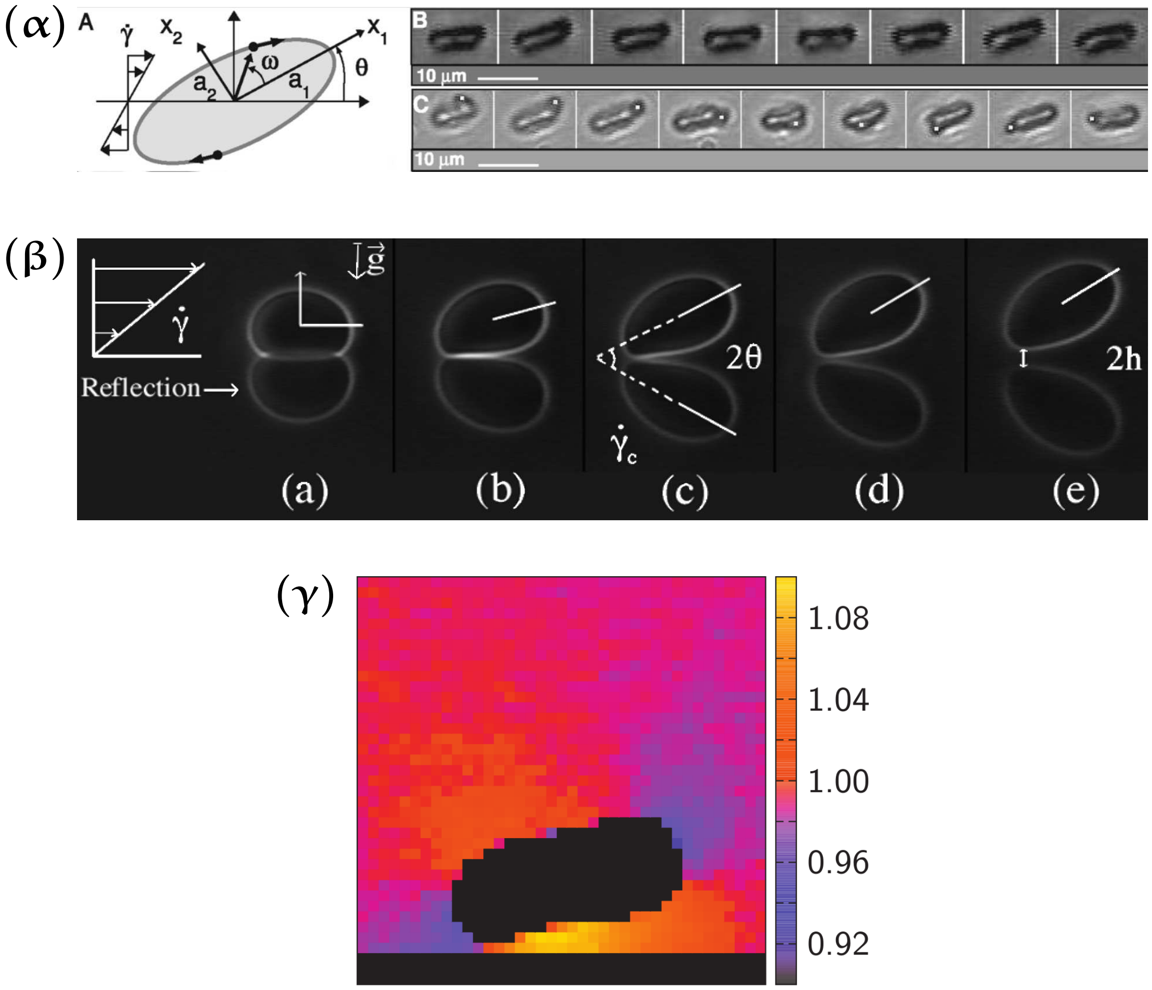

Figure 1.4.: Overview on recent research of vesicle dynamics. (α) Swinging (SW) and tank-treading (TT) of a RBC. (α-A) Schematic drawing of TT ellipsoid in shear flow. (α-B) SW RBC in shear flow. (α-C) Rotation of a bead stuck to the membrane of a RBC showing the TT motion. Picture taken from Ref. [94]. Copyright (2007) by The American Physical Society. (β) Side-view image of a vesicle with radius $31\,\mu\mathrm{m}$ with reflection on the substrate for different shear rates from $0\,\mathrm{s}^{-1}$ to $2.5\,\mathrm{s}^{-1}$ (a-e). Taken from Ref. [56]. Copyright (2002) by The American Physical Society. (γ) Pressure field of a TT vesicle under shear, flow given by the colour code. Taken from Ref. [104]. Copyright (2009) by The American Physical Society.

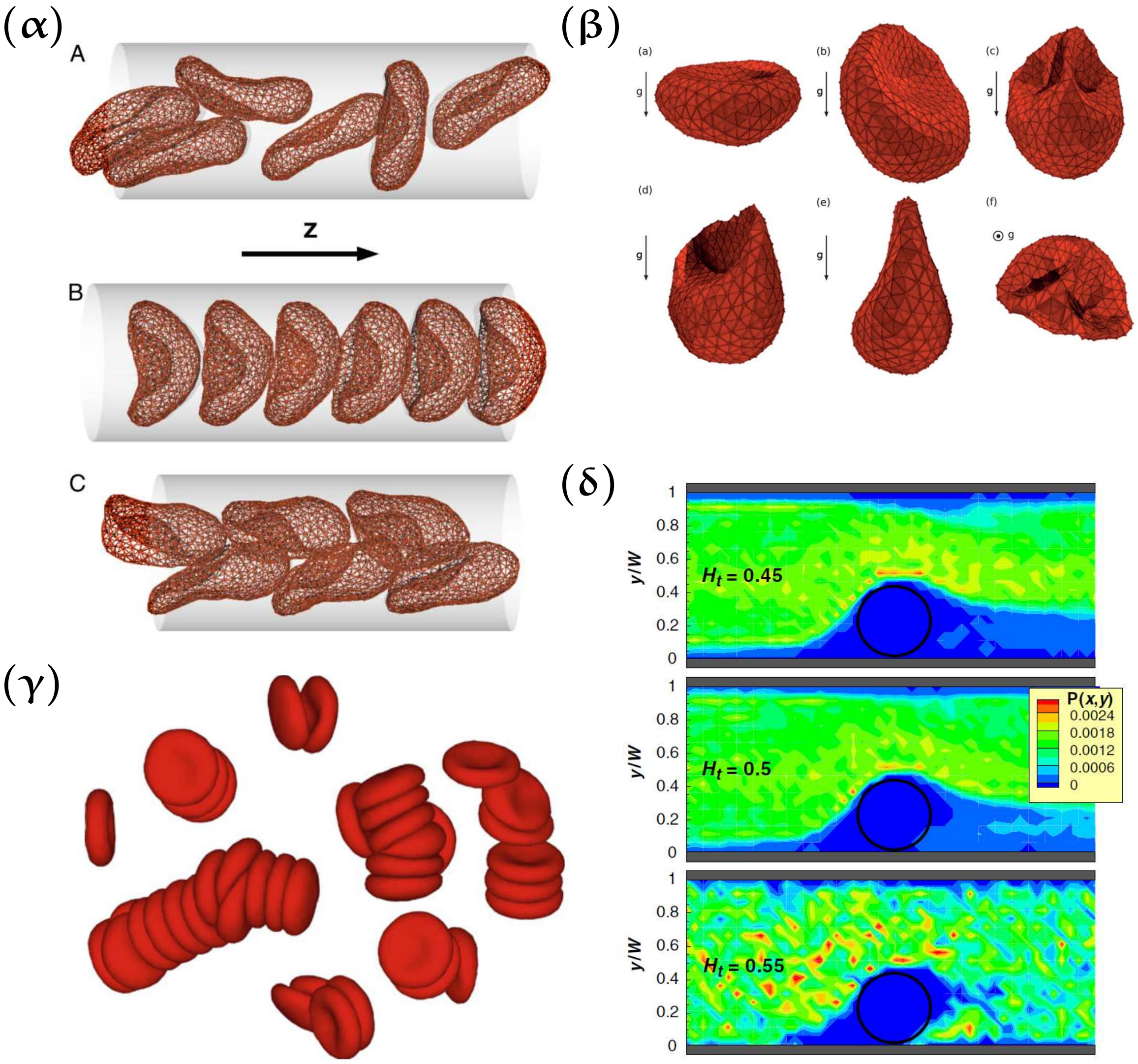

Figure 1.5.: Overview on recent research of blood flow. (α) Snapshots of simulations of RBCs in pressure driven flow at different shear rates and hematocrits. (α-A) Disordered-discocyte phase, (α-B) aligned-parachute phase and (α-C) Zig-zag-slipper phase. Taken from Ref. [113]. Copyright (2009) by the authors. (β) Snapshots from simulations of sedimenting RBCs for different gravities. (β-a) Parachute, (β-b) teardrop, (β-c) fin-tailed sphere, (β-d) asymmetric teardrop, (β-e) symmetric teardrop, and (β-f) same as (β-c) but seen from above. Reproduced from Ref. [81] with permission of The Royal Society of Chemistry. (γ) Snapshot from simulations of aggregating RBCs in shear flow with shear rate $\dot{\gamma} = 0.04\,\mathrm{s}^{-1}$. Taken from Ref. [118]. Copyright (2011) by the authors. (δ) RBC COM distribution around a marginated hard WBC (circle) for various hematocrit values H_t. Taken from Ref. [120]. Copyright (2012) by The American Physical Society.

more quickly for higher shear rates [130]. A theoretical study suggest that the near-wall platelet excess is due to the finite size of platelets [133]. However, 3D simulations explained the platelet margination by expulsion of platelets due to velocity fluctuations in the channel center [14, 131]. Further 3D simulations presented that disc marginate slower than spherical particles [132].

However, several open questions remain. This work sheds light on the dependence of margination of particles on several system parameters such as the hematocrit, shear rate, and the channel size. In addition, the dependence of margination the particle size, shape, and deformability, is considered in this work.

1.5. Outline

In Chapter 2, the simulation techniques DPD and SDPD with and without angular momentum conservation are introduced and compared. In Chapter 3 the employed RBC model is introduced, single RBC and vesicle properties are examined, and characteristics of RBC bulk flow are discussed. In this context, the typical simulation setup is described as well. Chapter 4 comprises of the study of platelet and drug carrier margination in microcirculation. Based on 3D simulations, the size and shape dependence of carrier margination is discussed in detail. Subsequently, 3D and 2D simulations are compared. Furthermore, additional carrier sizes and the influence of the carrier deformability are presented. On the basis of 2D simulations, the dependence of margination and concentration on the channel size is demonstrated. Furthermore, the dependence of the near-wall carrier concentration on hematocrit and carrier size is discussed. Finally, the contributions of direct and hydrodynamic interactions between carriers and RBCs on margination are examined. In addition to the carrier margination, polymer margination is studied in Chapter 5 and compared to margination of carriers. The focus is on the influence of different internal interactions between polymer monomers on margination. Beforehand, the stretching characteristics of these polymers under different conditions are analysed in shear flow, are compared to the stretching behaviour in blood flow, and are compared to the stretching experiments with VWF. Finally, all results are summarized and conclusions are drawn in Chapter 6. Possible prospects for future work are pointed out in Chapter 7.

2. Fluid model

Two particle based hydrodynamic simulation methods, the dissipative particle dynamics (DPD) and the smoothed dissipative particle dynamics (SDPD) method, have been employed to incorporate a fluid in the simulations and are introduced in this chapter. DPD mainly has been utilized for 2D simulations and SDPD for 3D simulations. Considering that the SDPD method originally lacks angular momentum conservation [84], a SDPD version with angular momentum conservation is developed and compared to the original approach.

2.1. Dissipative particle dynamics

In DPD [82, 83], the system is represented by a collection of N_p point particles. These particles interact locally by three pairwise additive forces: a conservative force $\mathbf{F}^\mathrm{C}$, a dissipative or drag force $\mathbf{F}^\mathrm{D}$, and a random $\mathbf{F}^\mathrm{R}$ force. Thus, the total force $\mathbf{f}_i$ on particle i exerted by all other particles j within a selected cut-off region and is given by

$$\mathbf{f}_i = \sum_{j \neq i} (\mathbf{F}^\mathrm{C}_{ij} + \mathbf{F}^\mathrm{D}_{ij} + \mathbf{F}^\mathrm{R}_{ij}). \tag{2.1}$$

The proposed conservative force $\mathbf{F}^\mathrm{C}$ controls the pressure and the fluid compressibility, while the pair of dissipative $\mathbf{F}^\mathrm{D}$ and random force $\mathbf{F}^\mathrm{R}$ defines a local thermostat in order to keep a system equilibrium temperature constant. The DPD forces are local and act only along the separation vector $\mathbf{r}_{ij} = \mathbf{r}_i - \mathbf{r}_j$ of the particles within a selected cut-off radius r_c (see Fig. 2.1). The conservative force is typically [134] taken to be

$$\mathbf{F}^\mathrm{C}_{ij} = \hat{\mathbf{e}}_{ij} \begin{cases} a_{ij}\left(1 - \frac{r_{ij}}{r_\mathrm{c}}\right), & \text{for } \ r_{ij} \leq r_\mathrm{c} \\ 0, & \text{for } \ r_{ij} > r_\mathrm{c} \end{cases} \tag{2.2}$$

where a_{ij} is the maximum repulsion between particle i and particle j, $\hat{\mathbf{e}}_{ij} = \mathbf{r}_{ij}/r_{ij}$ is the normalized separation vector between two particles, and $r_{ij} = |\mathbf{r}_{ij}|$.

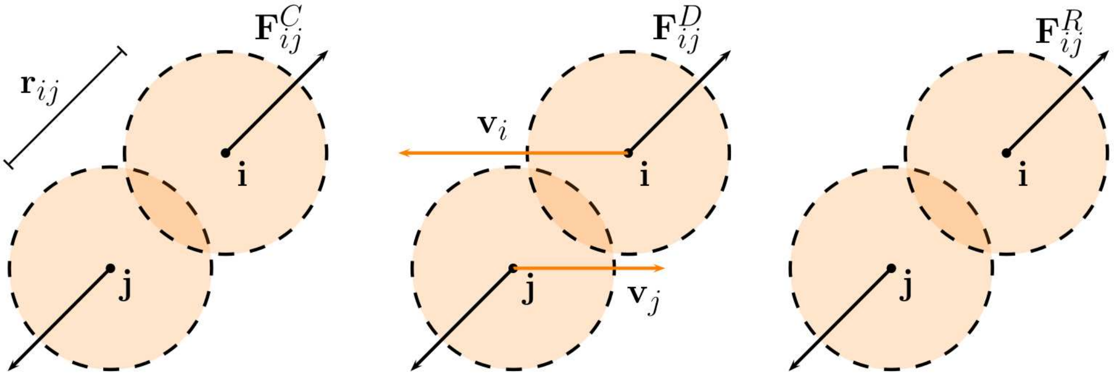

Figure 2.1.: Schematic of the DPD method. All forces act along the direction of the separation vector $\mathbf{r}_{ij}$. A soft repulsive force $\mathbf{F}^{\mathrm{C}}$ determines the system pressure and a dissipative force $\mathbf{F}^{\mathrm{D}}$, which reduces the velocity difference between the particles and a random $\mathbf{F}^{\mathrm{R}}$ force build a thermostat.

The equation of state of a DPD fluid [134] and the speed of sound c_s can be approximated as

$$p = \rho k_{\mathrm{B}} T + \alpha_a a \rho^2 \qquad \text{and} \qquad c_s^2 = \frac{\partial p}{\partial \rho} = k_{\mathrm{B}} T + 2\alpha_a a \rho, \tag{2.3}$$

for densities $\rho > 2$, with p being the pressure, the temperature T, the Boltzmann constant k_{B}, the repulsive coefficient a, and a variable α_a. The compressibility $\beta = \rho^{-1}\partial\rho/\partial p$ is related to the speed of sound as $\beta = (\rho c_s^2)^{-1}$. Thus, in DPD the speed of sound can be controlled by changing the repulsive coefficient a and/or fluid density. However, a significant increase of a may affect the timestep and lead to freezing artefacts [135], while an increase in particle density affects considerably the computational cost.

The dissipative force, defined as

$$\mathbf{F}_{ij}^{\mathrm{D}} = -\gamma \omega^{\mathrm{D}}(r_{ij})(\mathbf{v}_{ij} \cdot \hat{\mathbf{e}}_{ij})\hat{\mathbf{e}}_{ij}, \tag{2.4}$$

reduces the velocity difference $\mathbf{v}_{ij} = \mathbf{v}_i - \mathbf{v}_j$ between two particles, and hence, provides friction in the system. The term $\omega^D(r_{ij})$ is a weight function and γ is the dissipative force coefficient.

The random force in DPD is given by

$$\mathbf{F}_{ij}^{\mathrm{R}} = \sigma \omega_{ij}^{\mathrm{R}} \xi_{ij} dt^{-1/2} \hat{\mathbf{e}}_{ij}, \tag{2.5}$$

where ω_{ij}^R is the weight function, σ is the random force coefficient, and dt is the timestep. The random number ξ_{ij} has to be symmetric ($\xi_{ij} = \xi_{ji}$) to guarantee total momentum conservation. Furthermore, zero mean ($\langle\xi\rangle = 0$) and unit variance is required. Both forces depend only on the relative distance and the relative velocity between two particles to achieve Galilean invariance.

In order to satisfy the fluctuation-dissipation theorem [83], the pair of dissipative and random force has to fulfil the conditions

$$\omega^D(r_{ij}) = \left[\omega^R(r_{ij})\right]^2 \tag{2.6}$$

and

$$\sigma = \sqrt{2k_\mathrm{B}T\gamma}. \tag{2.7}$$

In general, the weight functions can be arbitrarily chosen. However, a typical choice is

$$\omega^D(r_{ij}) = \begin{cases} \left(1 - \frac{r_{ij}}{r_\mathrm{c}}\right)^k, & \text{for} \;\; r_{ij} \leq r_\mathrm{c}, \\ 0, & \text{for} \;\; r_{ij} > r_\mathrm{c}, \end{cases} \tag{2.8}$$

where the exponent $k = 1$ was used in the original DPD method [134]. Other values of k (e.g. 0.25) have been also employed in order to increase the viscosity of a DPD fluid [136, 137].

2.2. Smoothed dissipative particle dynamics

The smoothed dissipative particle dynamics (SDPD) method combines the discretization of the Navier-Stokes equation (NSE) as in the smoothed particle hydrodynamics (SPH) method and the incorporation of thermal fluctuations as in DPD [84].

2.2.1. Smoothed particle hydrodynamics

In the SPH method [86], a field variable $\tilde{g}(\mathbf{r})$ is replaced by the convolution integral of a field $g(\mathbf{r})$ and a kernel function $W(\mathbf{r}, r_h)$ as

$$\tilde{g}(\mathbf{r}) = \int_V g(\mathbf{r}')W(\mathbf{r} - \mathbf{r}', r_h)\, dV', \tag{2.9}$$

where the kernel function has to be differentiable and depends on the distance $|\mathbf{r} - \mathbf{r}'|$ and the smoothing length r_h. In addition, the integral over $W(\mathbf{r} - \mathbf{r}', r_h)$ has to be normalized and the condition $\lim\limits_{r_h \to 0} W(\mathbf{r} - \mathbf{r}', r_h) = \delta\left(\mathbf{r} - \mathbf{r}'\right)$ needs to be satisfied. The convolution integral is discretized using small fluid volumes (or particles) dV such that $\rho(\mathbf{r}')dV' \rightarrow m_j$ with the mass m_j and the mass density $\rho(\mathbf{r}') \rightarrow \rho(\mathbf{r}_j)$ of particle j with the position vector $\mathbf{r}_j$. The discretized convolution integral is then given by

$$\tilde{g}(\mathbf{r}_i) \approx \sum_{j=1}^{N} \frac{m_j}{\rho(\mathbf{r}_j)} g(\mathbf{r}_j) W(|\mathbf{r}_i - \mathbf{r}_j|, r_h), \tag{2.10}$$

where N is the number of particles (Lagrangian discretization points) within the volume V_h characterized by the smoothing radius r_h. The derivatives of the field variable $g(\mathbf{r})$ and of a vector field $\mathbf{G}(\mathbf{r})$, following similar approximation strategies, are described in Appendix A.1. The notations $\rho(\mathbf{r}_j) = \rho_j$, $g(\mathbf{r}_j) = g_j$, and $W(|\mathbf{r}_i - \mathbf{r}_j|, r_h) = W_{ij}$ are used in the following.

Applying the SPH formalism, the continuity equation $d\rho/dt = -\rho \nabla \cdot \mathbf{v}$, with the particle velocity $\mathbf{v}$, becomes (see Eq. (A.11))

$$\frac{d\rho_i}{dt} = \sum_j m_j \mathbf{v}_{ij} \cdot \nabla_i W_{ij}, \tag{2.11}$$

where $\nabla_i W_{ij}$ can be analytically calculated as $\nabla_i W_{ij} = -\mathbf{r}_{ij} F_{ij}$ with a function $F(\mathbf{r}_{ij}) = F_{ij} \geq 0$. Thus, the density ρ_i of particle i is defined by the neighbouring particles located within a sphere of radius r_h as

$$\rho_i = \sum_j m_j W_{ij}. \tag{2.12}$$

2.2.2. SDPD with angular momentum conservation

The first proposed SDPD formulation [84], using a discretization of the NSE, lacks angular momentum conservation, both locally and globally. The lack of angular momentum conservation originates from a translational dissipative force which is proportional to the velocity difference vector and not only to the projection of the velocity difference vector onto the separation vector as in DPD. One possibility to conserve angular momentum is to neglect the perpendicular component of dissipative and random forces resulting in a method formulation very similar to DPD [87].

Here, a spin variable for every particle $\boldsymbol{\omega}_i$ is introduced in order to incorporate angular momentum conservation. In addition, each particle possesses a moment of inertia I_i analogously to the particle mass. The introduced spin variable can be interpreted in two different ways. On the one hand, it is an approach used to recover angular momentum conservation in the SDPD formulation. On the other hand, the spin can be thought of as an effective angular velocity of a fluid volume represented by a particle. However, it should not be confused with a molecular spin. The NSE with spin [138] is given by

$$\rho\frac{d\mathbf{v}}{dt} = -\nabla p + (\eta + \eta_\mathrm{r})\nabla^2\mathbf{v} + \left(\frac{\eta}{3} + \xi_\mathrm{b} - \eta_\mathrm{r}\right)\nabla\left(\nabla\cdot\mathbf{v}\right) + 2\eta_\mathrm{r}\nabla\times\boldsymbol{\omega}, \tag{2.13}$$

where η is the dynamic shear viscosity, ξ_b is the bulk viscosity, η_r is the rotational viscosity, and $\boldsymbol{\omega}$ is the spin angular velocity. Applying the approximations in Eqs. (A.10) to (A.14) and the Newton's second law of motion

$$\mathbf{F} = m\frac{d\mathbf{v}}{dt} \qquad \text{and} \qquad \mathbf{N} = I\frac{d\boldsymbol{\omega}}{dt}, \tag{2.14}$$

with $\mathbf{N}$ the torque, the NSE can be discretized as

$$\begin{aligned}
\mathbf{F}_{ij}^{C} &= \left(\frac{p_i}{\rho_i^2} + \frac{p_j}{\rho_j^2}\right) F_{ij}\mathbf{r}_{ij}, \\
\mathbf{F}_{ij}^{D_T} &= -\left(\frac{5\eta}{3} + 3\eta_\mathrm{r} - \xi_\mathrm{b}\right)\frac{F_{ij}}{\rho_i\rho_j}\mathbf{v}_{ij} - 5\left(\frac{\eta}{3} + \xi_\mathrm{b} - \eta_\mathrm{r}\right)\frac{F_{ij}}{\rho_i\rho_j}\hat{\mathbf{e}}_{ij}(\hat{\mathbf{e}}_{ij}\cdot\mathbf{v}_{ij}), \\
\mathbf{F}_{ij}^{D_R} &= -2\eta_\mathrm{r}\frac{F_{ij}}{\rho_i\rho_j}\mathbf{r}_{ij}\times\left(\boldsymbol{\omega}_i + \boldsymbol{\omega}_j\right).
\end{aligned} \tag{2.15}$$

The conservative force $\mathbf{F}_{ij}^{C}$ controls locally the pressure field in the system. The dissipative force $\mathbf{F}^{D} = \mathbf{F}^{D_L} + \mathbf{F}^{D_R}$ consists of two components. First, a translational friction $\mathbf{F}^{D_T}$ leading to the reduction of the velocity difference between two particles. Second, a rotational friction force $\mathbf{F}^{D_R}$ which acts on the particles' angular velocities, such that a spin of one particle leads to a change in translational and angular velocity of another particle.

The defined set of deterministic forces in Eq. (2.15) can be referred to as a SPH discretization with angular momentum conservation. However, the SDPD method also incorporates consistently thermal fluctuations by appending a random force to the set of forces in Eq. (2.15). Here, the combination of dissipative, rotational, and random forces has to satisfy the fluctuation-dissipation balance. To derive the corresponding relations, a tensor

$$\boldsymbol{\mathcal{T}}_{ij} = A(r_{ij})\mathbb{1} + B(r_{ij})\hat{\mathbf{e}}_{ij}\hat{\mathbf{e}}_{ij} \tag{2.16}$$

is defined similar to the fluid particle model (FPM) framework [139], where $A(r)$ and $B(r)$ are some functions of inter-particle distance r_{ij} with the unity matrix $\mathbb{1}$. The dissipative and rotational forces in Eq. (2.15) can be written in a tensorial form as

$$\mathbf{F}_{ij}^{D_T} = -\boldsymbol{\mathcal{T}}_{ij} \cdot \mathbf{v}_{ij}, \qquad \mathbf{F}_{ij}^{D_R} = -\boldsymbol{\mathcal{T}}_{ij} \cdot \left(\frac{\mathbf{r}_{ij}}{2} \times (\boldsymbol{\omega}_i + \boldsymbol{\omega}_j) \right), \tag{2.17}$$

which implies that $\eta_\mathrm{r} = 5\eta/3 - \xi_\mathrm{b}$,

$$A(r_{ij}) = 4 \left(\frac{5\eta}{3} - \xi_\mathrm{b} \right) \frac{F_{ij}}{\rho_i \rho_j}, \text{ and } B(r_{ij}) = 10 \left(\xi_\mathrm{b} - \frac{2\eta}{3} \right) \frac{F_{ij}}{\rho_i \rho_j}. \tag{2.18}$$

Following the general framework of the FPM [139], the random force can be defined as

$$\mathbf{F}_{ij}^{R} dt = \sqrt{2k_\mathrm{B}T} \left(\tilde{A}(r_{ij}) d\overline{\boldsymbol{\mathcal{W}}}_{ij}^{S} + \frac{\tilde{B}(r_{ij})}{3} \mathrm{tr}[d\boldsymbol{\mathcal{W}}_{ij}] \mathbb{1} + \tilde{C}(r_{ij}) d\boldsymbol{\mathcal{W}}_{ij}^{A} \right) \cdot \hat{\mathbf{e}}_{ij}, \tag{2.19}$$

where $d\boldsymbol{\mathcal{W}}_{ij}$ is a 3×3-matrix of independent Wiener increments, $\mathrm{tr}[d\boldsymbol{\mathcal{W}}_{ij}]$ is the trace of this matrix, $d\overline{\boldsymbol{\mathcal{W}}}_{ij}^{S} = d\boldsymbol{\mathcal{W}}_{ij}^{S} - \mathrm{tr}[d\boldsymbol{\mathcal{W}}_{ij}]\mathbb{1}/3$ is the traceless symmetric part, with the symmetric part $d\boldsymbol{\mathcal{W}}_{ij}^{S} = (d\boldsymbol{\mathcal{W}}_{ij} + d\boldsymbol{\mathcal{W}}_{ij}^{T})/2$, the transposed matrix $d\boldsymbol{\mathcal{W}}_{ij}^{T}$, and $d\boldsymbol{\mathcal{W}}_{ij}^{A} = (d\boldsymbol{\mathcal{W}}_{ij} - d\boldsymbol{\mathcal{W}}_{ij}^{T})/2$ is the antisymmetric part.

In this regard, a Wiener process W_t is defined as a stochastic process, with the following properties [140]: $W_0 = 0$; W_t is a random variable, almost surely everywhere continuous over t; for $s, t > 0$, $W_t - W_s$ is Gaussian with zero mean and variance $t - s$; the increments are independent: for $s_1 \leq t_1 < s_2 \leq t_2$, $W_{t_1} - W_{s_1}$ is independent of $W_{t_1} - W_{t_2}$.

The functions $\tilde{A}(r)$, $\tilde{B}(r)$, and $\tilde{C}(r)$ are related to $A(r)$ and $B(r)$ of the tensor $\boldsymbol{\mathcal{T}}_{ij}$ as

$$\begin{aligned} A(r) &= \frac{1}{2} \left(\tilde{A}(r)^2 + \tilde{C}(r)^2 \right), \\ B(r) &= \frac{1}{2} \left(\tilde{A}(r)^2 - \tilde{C}(r)^2 \right) + \frac{1}{3} \left(\tilde{B}(r)^2 - \tilde{A}(r)^2 \right). \end{aligned} \tag{2.20}$$

For a further simplification of the expression in Eq. (2.19), $\tilde{C}(r) = 0$ is selected, leading to

$$\tilde{A}(r_{ij}) = \left(2 \left(\frac{20\eta}{3} - 4\xi_\mathrm{b} \right) \frac{F_{ij}}{r_i r_j} \right)^{1/2}, \text{ and } \tilde{B}(r_{ij}) = \left(2 \left(17\xi_\mathrm{b} - \frac{40\eta}{3} \right) \frac{F_{ij}}{r_i r_j} \right)^{1/2}. \tag{2.21}$$

The full set of forces for the SDPD method with angular momentum conservation is than given by

$$\begin{aligned}
\mathbf{F}_{ij}^{\mathrm{C}} &= \left(\frac{p_i}{\rho_i^2} + \frac{p_j}{\rho_j^2}\right) F_{ij}\mathbf{r}_{ij}, \\
\mathbf{F}_{ij}^{\mathrm{D_T}} &= -\gamma_{ij}^a \left(\mathbf{v}_{ij} + \frac{\hat{\mathbf{e}}_{ij}\left(\hat{\mathbf{e}}_{ij}\cdot\mathbf{v}_{ij}\right)}{3}\right) - \frac{2\gamma_{ij}^b}{3}\hat{\mathbf{e}}_{ij}\left(\hat{\mathbf{e}}_{ij}\cdot\mathbf{v}_{ij}\right), \qquad (2.22) \\
\mathbf{F}_{ij}^{\mathrm{D_R}} &= -\gamma_{ij}^a \frac{\mathbf{r}_{ij}}{2} \times \left(\boldsymbol{\omega}_i + \boldsymbol{\omega}_j\right), \\
\mathbf{F}_{ij}^{\mathrm{R}} &= \left(\sigma_{ij}^a d\overline{\boldsymbol{\mathcal{W}}}_{ij}^S + \sigma_{ij}^b \frac{1}{3} tr[d\boldsymbol{\mathcal{W}}_{ij}]\mathbb{1}\right) \cdot \frac{\hat{\mathbf{e}}_{ij}}{dt},
\end{aligned}$$

with the coefficients γ_{ij}^a and γ_{ij}^b given by

$$\gamma_{ij}^a = \left(\frac{20\eta}{3} - 4\xi_{\mathrm{b}}\right)\frac{F_{ij}}{\rho_i\rho_j}, \quad \gamma_{ij}^b = \left(17\xi_{\mathrm{b}} - \frac{40\eta}{3}\right)\frac{F_{ij}}{\rho_i\rho_j}, \qquad (2.23)$$

and $\sigma_{ij}^{a,b} = 2\sqrt{k_{\mathrm{B}}T\gamma_{ij}^{a,b}}$. It is important to note that these equations are only valid for $2\eta/3 \leq \xi_{\mathrm{b}} \leq 5\eta/3$, such that the friction coefficients $(\gamma_{ij}^a + 2\gamma_{ij}^b)/3$ and γ_{ij}^a are positive.

Another simplification which can be made is the reduction to a single dissipative parameter $\gamma_{ij} = \gamma_{ij}^a = \gamma_{ij}^b$ such that $\xi_{\mathrm{b}} = 20\eta/21$ and

$$\gamma_{ij} = \frac{20\eta}{7}\frac{F_{ij}}{\rho_i\rho_j}, \qquad \sigma_{ij}^a = \sigma_{ij}^b = \sigma_{ij} = 2\sqrt{k_{\mathrm{B}}T\gamma_{ij}}. \qquad (2.24)$$

The forces of the original SDPD method [84] are very similar to those in Eq. (2.22) with a single dissipative parameter which is $\gamma_{ij} = 5\eta F_{ij}/(3\rho_i\rho_j)$ [84]. Furthermore, the rotational contribution to the dissipative force $\mathbf{F}^{\mathrm{D_R}}$ is excluded, while the conservative force is kept the same.

The SDPD method with angular momentum conservation will be referred to as **SDPD+a** further in text and SDPD method without angular momentum conservation will be called **SDPD–a**.

In both simulation methods, it is important to consider how the mass, and for SDPD+a the moment of inertia, of a fluid particle have to be assigned. For flows with low Reynolds numbers *Re*, which is the main interest of the current study, the viscous forces are much more important than inertial forces and thus, the simulation results are independent of the choice of m and I [88]. However, for high enough *Re*, the particle mass should correspond to the mass of a fluid volume described by a single particle and that the moment of inertia should correspond to that of a sphere with the same volume as a simulated particle [88, 139].

Finally, in both SDPD–a and SDPD+a simulations the Lucy function

$$W(r) = \frac{105}{16\pi r_h^3}\left(1 + 3\frac{r}{r_h}\right)\left(1 - \frac{r}{r_h}\right)^3, \tag{2.25}$$

is used as a kernel function [141], which leads to $F(r) = 315/(4\pi r_h^5)\,(1 - r/h)^2$.

The equation of state in Eq. (2.22) is chosen to be [142]

$$p = p_0\left(\frac{\rho}{\rho_0}\right)^\alpha + b, \tag{2.26}$$

where ρ_0 is the reference density, and the parameters p_0, α, and b can be freely selected. This pressure equation yields the speed of sound $c_s^2 = p_0\alpha/\rho_0$, which can be easily controlled through the above parameters resulting in a good approximation of fluid incompressibility [86, 143].

2.3. Integration

The time evolution of the position $\mathbf{r}$ and the translational velocity $\mathbf{v}$ in DPD, SDPD–a, and SDPD+a, as well as the angular velocity $\boldsymbol{\omega}$ in SDPD+a of a particle i follows Newton's second law as

$$\dot{\mathbf{r}}_i = \mathbf{v}_i, \quad \dot{\mathbf{v}}_i = \sum_j \frac{1}{m_j}\mathbf{F}_{ij}, \quad \dot{\boldsymbol{\omega}}_i = \sum_j \frac{1}{I_j}\mathbf{N}_{ij}, \tag{2.27}$$

with $\mathbf{N}_{ij}$ the torque exerted by particle j on particle i and given by $\mathbf{N}_{ij} = -\mathbf{r}_{ij} \times \mathbf{F}_{ij}/2$. The equations above for all simulation methods are integrated from time t to $t + dt$ with a modified version of the velocity-Verlet algorithm [64] given by

$$\begin{aligned}
\mathbf{r_i}(t + dt) &= \mathbf{r}_i(t) + dt\mathbf{v}_i(t) + \frac{1}{2}(dt)^2\mathbf{f}_i(t) \\
\tilde{\mathbf{v}}(t + dt) &= \mathbf{v}_i(t) + \lambda_\mathrm{v} dt\mathbf{f}_i(t) \\
\mathbf{f}_i(t + dt) &= \mathbf{f}_i(\mathbf{r}_i(t + dt), \tilde{\mathbf{v}}_i(t + dt)) \\
\mathbf{v}_i(t + dt) &= \mathbf{v}_i(t) + \frac{1}{2}dt\left(\mathbf{f}_i(t) + \mathbf{f}_i(t + dt)\right).
\end{aligned} \tag{2.28}$$

The angular momentum is integrated similar to the velocity and in all simulations $\lambda_\mathrm{v} = 0.5$ is employed.

2.4. Boundary conditions

In applications, the fluid is often confined by walls, e.g. planar or cylindrical walls. These walls are modelled by frozen fluid particles with the same structure (e.g., the radial distribution function) as the fluid, while the wall thickness is equal to r_c or r_h depending on the method. This is realized by cutting out the required wall shape from a snapshot of a simulation of the specific fluid. Thus, the interactions of all simulated particles, which are not wall particles, with the wall particles are the same as the interactions with the fluid particles.

Particles are additionally subject to reflection at the fluid-solid interface to prevent wall penetration [144]. In order to verify if a particle would encounter a boundary the collision time with the wall is calculated as $t' = (x^k - x_\mathrm{BC})/(v_\mathrm{BC} - v^k)$, where the parameters $x_\mathrm{BC}, v_\mathrm{BC}$ are the boundary position and boundary speed and v^k, x^k are the normal velocity and the position of a particle, respectively. If $0 \leq t' \leq dt$ the particle would encounter the wall during a timestep of length dt and from the old position $\mathbf{r}(t)$ and old velocities $\mathbf{v}(dt)$, the new position $\mathbf{r}(t+dt)$ and velocity $\mathbf{v}(t+dt)$ are calculated as

$$\mathbf{r}(t+dt) = \mathbf{r}(t)+t'\mathbf{v}(t)+(dt-t')\mathbf{v}(t+dt) \qquad \text{and} \qquad \mathbf{v}(t+dt) = 2\mathbf{v}_\mathrm{BC}(t)-\mathbf{v}(t). \quad (2.29)$$

This reflection rule corresponds to bounce-back reflections. Bounce-back reflections, where the normal and the tangential component of the particle velocity is reversed, are employed, since they provide a better approximation for the no-slip boundary conditions in comparison to specular reflection of particles [145]. Specular reflections, where only the normal component of the velocity is reversed, produce no-slip condition only for high friction [145].

Additionally, a tangential adaptive shear force [144] which acts on the fluid particles in a near-wall layer of thickness r_w is employed to ensure that no-slip boundary conditions are strictly satisfied. This adaptive shear force is given by

$$f_t(\Delta h) = C_k(\Delta v_t)\left(1 - \frac{\Delta h}{r_\mathrm{w}}\right)^4, \qquad (2.30)$$

with the distance Δh from the wall and C_k the adaptive force strength calculated in an iteration via $C_{k+1} = C_k + \alpha_\mathrm{r}\Delta v_t$ where α_r is a relaxation parameter, which can be constant or dynamically calculated. The term $\Delta v_t = v_t^\mathrm{BC} - v_t^\mathrm{est}$ is the difference between v_t^BC, the given velocity of the boundary, and v_t^est, the estimated flow velocity at the boundary. After a number of iterations it converges to $\Delta v_t = 0$ and $f_t^k = \text{const}$.

2.5. Comparison of simulation methods

In comparison with the DPD method, an advantage of SDPD is that transport coefficients, such as the fluid viscosity, can be directly specified, while in DPD they need to be computed in a separate simulation for selected fluid parameters. Furthermore, in SDPD the volume of a fluid particle with mass m and density ρ is clearly defined as $V = m/\rho$, which also determines a physical size of the particle [84, 146]. Additionally, in SDPD the compressibility can be better controlled, since also the pressure equation of state is an input to the simulation and not an outcome.

In order to compare the SDPD–a and SDPD+a methods, first the fluid viscosity and particle density are calculated for several specified viscosities, temperatures, densities, and smoothing lengths. Second, the Taylor-Couette flow with two immiscible fluids is simulated, since recent numerical simulations [147] have shown that the conservation of angular momentum is necessary to obtain correct velocity and torque profiles across immiscible fluids with different viscosities.

2.5.1. Fluid properties

A reverse-Poiseuille flow setup [148] is used to measure the fluid viscosity, where the flow in two halves of a computational domain is driven in opposite directions applying the same force magnitude f per particle. The fluid viscosity is then calculated by averaging the velocity profile over the half of the channel and using the known Poiseuille flow profile, see Eq. (3.16). The velocity profile and the particle density are computed on the fly by averaging the velocity over all particles within a certain distance from the wall and averaging ρ over all particles.

Here, the basic units for the mass, m (e.g., fluid particle mass), length, l, and energy, E, are introduced, since most of the parameters (e.g., temperature, imposed shear, viscosity), which could be used for normalization, are varied. In the simulations they correspond to the standard parameters $m = 1$, $l = 1$, and $E = 1$. The size of a fully-periodic simulation domain has been set to $20l \times 40l \times 10l$, where the flow was driven along the y-axis. Model parameters for the pressure given in Eq. (2.26) have been set to $p_0 = 100E/l^3$, $b = -100E/l^3$, and $\alpha = 7$ [86]. A broad range of the parameter values have been covered in simulations: four different viscosities

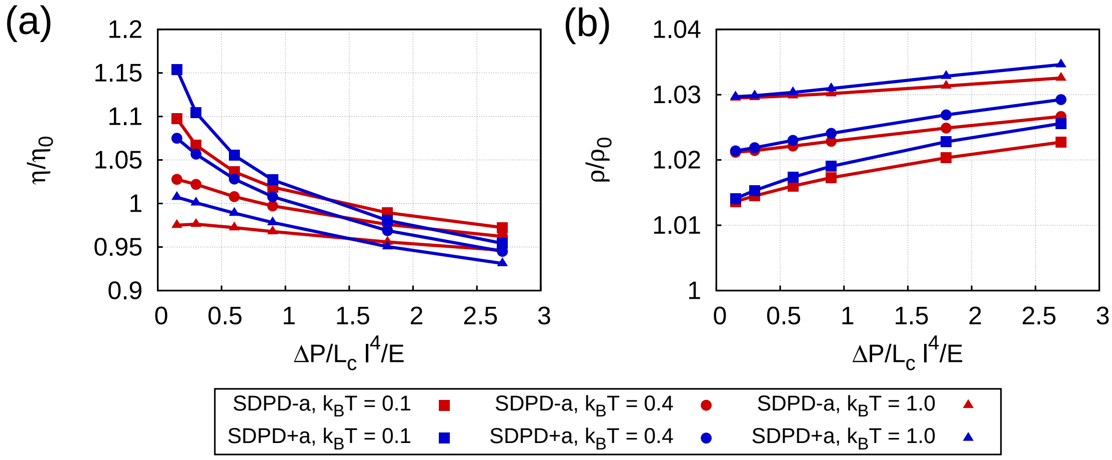

Figure 2.2.: Fluid properties of SDPD+a (blue) and SDPD–a (red) for different temperatures T and pressure gradients $\Delta p/L_\mathrm{c}$, for a channel of length L_c. (a) Measured viscosity η normalized by $\eta_0 = 50\sqrt{mE}/l^2$. (b) Particle density ρ normalized by $\rho_0 = 3m/l^3$. The considered energy levels are $k_\mathrm{B}T \in \{0.1, 0.4, 1\}E$, while $r_h = 1.5l$.
The measured viscosity is larger than η_0 for low and lower for large pressure drops. This effect is more pronounced for lower temperature. The measured density is slightly larger than ρ_0 and is dependent on temperature [88].

$\eta_0 \in \{25, 50, 100, 120\}\sqrt{mE}/l^2$, three energy levels $k_\mathrm{B}T \in \{0.1, 0.4, 1\}E$, two densities $\rho_0 \in \{3, 5\}m/l^3$, and two smoothing lengths $r_h \in \{1.5, 3.0\}l$.

Figure 2.2 (a) displays the measured viscosity η normalized by the specified viscosity η_0 with respect to the applied pressure gradient $\Delta p/L_\mathrm{c} = f\rho_0/m$, for a channel of length L_c, and for a case of $r_h = 1.5l$. The corresponding Reynolds numbers, defined as $Re = \rho\bar{V}W/(2\eta)$, where W is the channel width and $\bar{V}$ the average velocity, are ranging from 0.01 to 4.3. However, simulations with a five-fold increase of particle mass and moment of inertia for $\eta_0 = 25\sqrt{mE}/l^2$, $\rho_0 = 3m/l^3$ demonstrate that the simulation results are hardly affected by the choice of I and m, as presented in Fig. A.1 of Appendix A. For both fluids, SDPD+a and SDPD–a, the measured viscosity is slightly larger than η_0 for small pressure gradients, but smaller than η_0 for large pressure gradients. This effect appears to be more pronounced for a lower temperature. The particle density measurements presented in Fig. 2.2 (b) show a slight deviation from the specified value of $\rho_0 = 3m/l^3$. However, for both SDPD+a and SDPD–a fluids the particle density values are similar.

Figure 2.3 presents similar measurements of fluid viscosity and particle density for a SDPD+a fluid using different ρ_0 and η_0 values. As the particle density is increased, the fluid properties are better approximated resulting in a smaller variation of the measured

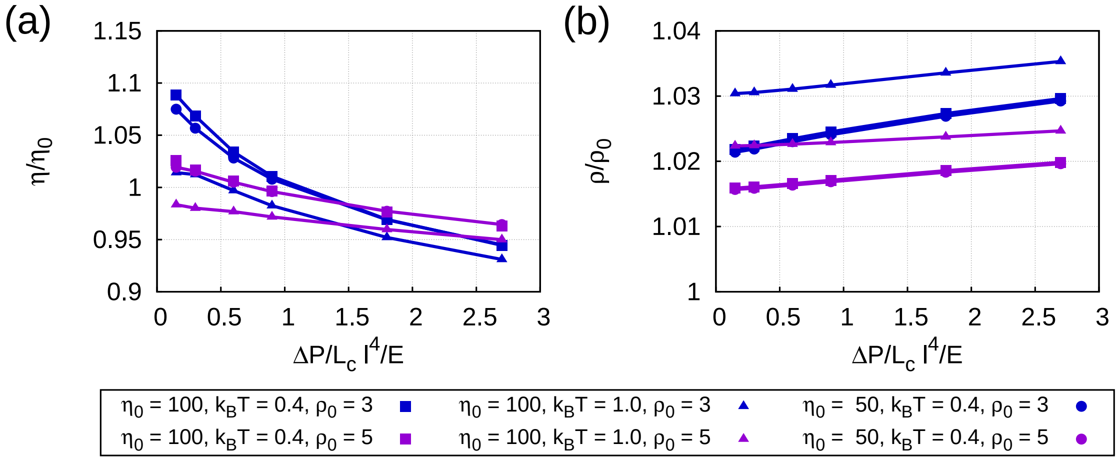

Figure 2.3.: Fluid properties of a SDPD+a fluid with respect to the pressure gradient $\Delta p/L_\mathrm{c}$ for a channel of length L_c and particle densities $\rho_0 = 3m/l^3$ (blue) and $\rho_0 = 5m/l^3$ (purple). (a) Measured viscosity η normalized by $\eta_0 \in \{50, 100\}\sqrt{mE}/l^2$. (b) Particle density ρ normalized by ρ_0. Different energy levels $k_\mathrm{B}T \in \{0.4, 1\}E$ were considered, while $r_h = 1.5l$ [88].
For larger densities the specified viscosity and density are better approximated.

properties from the specified values. A better result obtained for larger densities is due to a larger number of neighbouring particles within the interaction radius r_h, which leads to a better approximation for discretized terms of the NSE. Similar trends are also observed for the SDPD–a fluid; see Fig. A.2. In addition, the simulations demonstrate that the particle density is independent on the specified viscosity, since it is governed by local fluid structure of particles within a radius r_h, which is characterized by the radial distribution function.

Figure 2.4 illustrates the fluid viscosity and particle density of a SDPD+a fluid for different smoothing lengths r_h. With increasing r_h the measured values move closer to the specified ones and the temperature dependence practically vanishes. This effect is again due to a larger number of neighbouring particles within r_h leading to smaller discretization errors for larger r_h values. For a SDPD–a fluid similar results are obtained; see Fig. A.3. However, computational costs may increase considerably for larger r_h, since it is proportional to r_h^3 or to the number of neighbouring particles. Typically it is suggested to use about 50 to 60 neighbouring particles in SDPD [149]. However, slightly smaller values are also possible in simulations if small variations of fluid properties are acceptable.

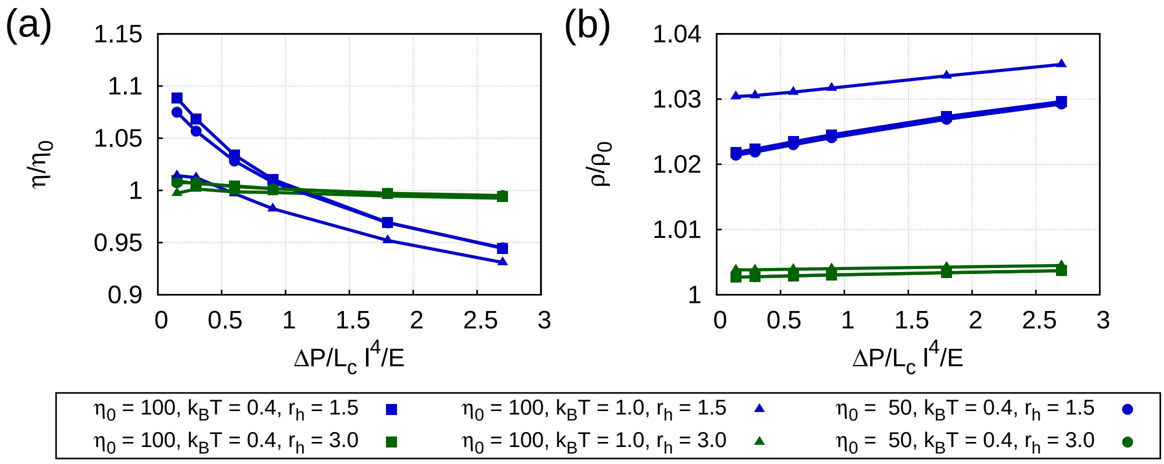

Figure 2.4.: Fluid properties of a SDPD+a fluid for different pressure gradients $\Delta p/L_\mathrm{c}$, for a channel of length L_c and smoothing lengths $r_h = 1.5l$ (blue) and $r_h = 3.0l$ (green). (a) Measured viscosity η normalized by $\eta_0 \in \{50, 100\}\sqrt{mE}/l^2$. (b) Particle density ρ normalized by $\rho_0 = 3m/l^3$. Different energy levels $k_\mathrm{B}T \in \{0.4, 1\}E$ were considered. For larger smoothing lengths specified values are better approximated and differences due to variations of temperature and viscosity vanish [88].

2.5.2. Taylor-Couette flow of two immiscible fluids

Taylor-Couette flow refers to a fluid flow in the gap between two rotating cylinders with the inner and outer radii, R_i and R_o and the inner and outer angular frequencies, Ω_i and Ω_o, respectively as shown in Fig. 2.5. A solution [147] of the incompressible NSE (see Eq. (1.1)) for this problem yields the linear angular velocity profile

$$v_\varphi(r) = Ar + \frac{B}{r}, \tag{2.31}$$

with $R_\mathrm{i} < r < R_\mathrm{o}$ the radial position of the fluid and the corresponding constants

$$A = \frac{\Omega_\mathrm{o} R_\mathrm{o}^2 - \Omega_\mathrm{i} R_\mathrm{i}^2}{R_\mathrm{o}^2 - R_\mathrm{i}^2} \qquad \text{and} \qquad B = \frac{(\Omega_\mathrm{i} - \Omega_\mathrm{o})\, R_\mathrm{o}^2 R_\mathrm{i}^2}{R_\mathrm{o}^2 - R_\mathrm{i}^2}. \tag{2.32}$$

Here, it is also assumed that the system has infinite length in the cylinder-axis direction and the angular velocities are small enough to ensure that no Taylor-Couette instabilities occur. The radial fluid velocity component vanishes, due to symmetry reasons [147].

The inner cylinder can also be replaced by another immiscible fluid such that no mixing between the two fluids at R_i can occur. In this case only the outer cylinder rotates with a constant rotational frequency Ω_o, which leads to the angular velocity $v_\varphi(r) = \Omega_\mathrm{o} r$. Note that these solutions are independent of the viscosity values of the

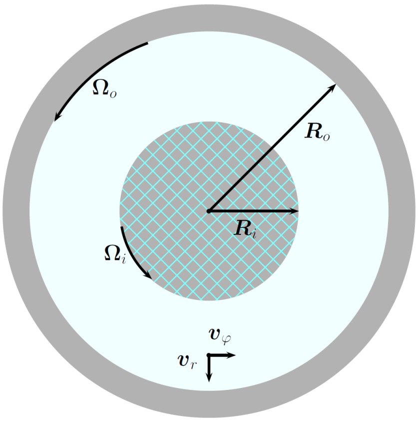

Figure 2.5.: A sketch of two cylinders with radii R_o and R_i where the subscripts 'o' and 'i' denote the outer and inner cylinders, respectively. The gap between cylinders is filled with a fluid coloured in blue. Taylor-Couette flow can be generated by rotation of the outer cylinder with a rotational frequency Ω_o and the inner cylinder with Ω_i. In simulations with two immiscible fluids, the inner cylinder (shaded area) is replaced by another fluid which cannot mix with the fluid inside the gap between two cylindrical surfaces [88].

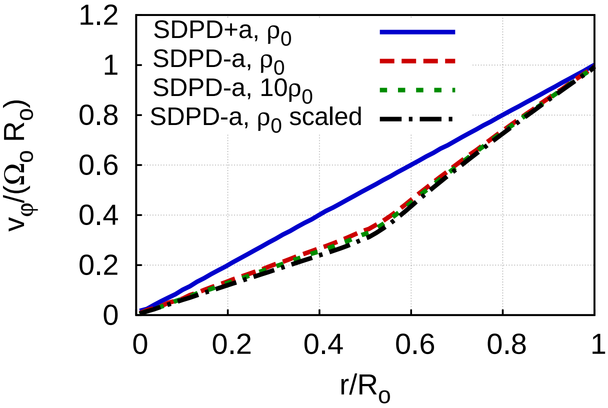

Figure 2.6.: Angular velocity v_φ profiles for the Taylor-Couette flow with two immiscible fluids using both SDPD+a and SDPD–a methods. The radial position r is normalized by the cylinder radius R_o, while the angular velocity is scaled with the cylinder angular velocity $\Omega_\mathrm{o} R_\mathrm{o}$.

The SDPD+a method leads to a correct linear profile, while the SDPD–a method fails to do so, due to violation of angular momentum conservation. The SDPD–a results for different resolution with $\rho = 10\rho_0$ and for a twice larger system size (marked as "scaled") show hardly any dependence on fluid resolution [88].

immiscible fluids.

Here, for both, the SDPD+a and SDPD–a method, the inner and outer fluids had the following parameters $p_0 = 100E/l^3$, $b = -100E/l^3$, $\alpha = 7$, $\rho_0 = 3m/l^3$, $r_h = 1.5l$, and $k_\mathrm{B}T = 0.4E$, while the ratio of fluid viscosities was set to $\eta_\mathrm{i}/\eta_\mathrm{o} = 3$. The computational domain was assumed to be periodic in the cylinder-axis direction, while the cylinder wall was modelled by frozen particles as described in Section 2.4. In order to prevent mixing of the fluids and particle penetration into the wall, specular reflections of particles has been imposed at cylindrical surfaces with $r = R_\mathrm{i}$ and $r = R_\mathrm{o}$. The wall particles were rotated with a constant angular frequency Ω_o in order to generate flow. The corresponding Reynolds number is $Re = \rho\Omega_\mathrm{o}R_\mathrm{o}R_\mathrm{i}/\eta_\mathrm{o} \approx 0.3$.

Figure 2.6 shows angular velocity profiles for the Taylor-Couette flow using both SDPD+a and SDPD–a methods. The SDPD+a simulation properly captures a linear profile of angular velocity, while the SDPD–a method leads to distinct slopes within the regions of different viscosities. This example illustrates the importance of angular momentum conservation and provides a validation for the new SDPD+a approach [88].

A resolution study shows that these results are unaffected by an increase of fluid resolution in the SDPD–a method. Simulations with different densities $\rho \in \{2, 3, 5, 10\}\rho_0$ and a larger system size have led to the same angular velocities (up to a statistical averaging error) as presented in Fig. 2.6. Furthermore, particle mass and inertia do not effect the simulation results as well, as shown in Fig. A.4 for simulations with a two-fold increase/decrease of the mass and moment of inertia.

3. Blood flow simulations

Blood consists of 37 % to 54 % of RBCs by volume, which also represent the majority of cells. In order to model blood flow in small vessels (< 100 µm) it is necessary to model RBCs explicitly in addition to a fluid, which is modelled using the techniques presented in the last chapter. Therefore, in this chapter the applied RBC model is introduced. Furthermore, the dynamics of a single vesicle and RBC in shear flow and flow properties of RBCs in the bulk are discussed.

3.1. Cell model

To model RBCs realistically the viscous as well as the elastic properties, the bending resistance, and the area and volume conservation due to the membrane, the spectrin network, and the cytosol have to be taken into account. Two approaches to describe RBCs have been successfully used so far, a continuum model [150–153] and a network model [153]. In a continuum model, the RBC membrane properties are described by a set of constitutive equations. These equations are than discretized in various ways, for instance by a finite element or boundary integral method [151, 153]. The RBC model introduced here is a network model from Ref. [114].

3.1.1. 3D RBC model

The RBC structure is defined by a 2D triangulated network on a membrane surface which is characterized by a set of point particles p_i, $i \in \{1, ..., N_\mathrm{v}\}$, which are the vertices of the network, see Fig. 3.1.

The vertices are connected by N_s springs and form N_t triangles. The whole potential energy of the system is given by

$$U = U_\mathrm{spring} + U_\mathrm{bending} + U_\mathrm{area} + U_\mathrm{volume}. \tag{3.1}$$

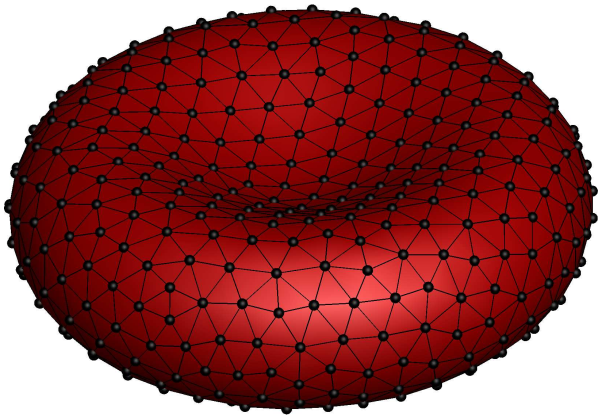

Figure 3.1.: In 3D the RBC consists of a triangulated network drawn in black. The vertices (black dots) are connected by springs with dashpots. Between two adjacent triangles a bending resistance exists and a local and global area, and volume constraints are employed.

The spring potential between vertex pairs,

$$U_{\text{spring}} = \sum_{j=1}^{N_s} k_B T \frac{l_{\text{m}}}{4 l_{\text{p}}} \frac{3x_j^2 - 2x_j^3}{1 - x_j} + \frac{k_p}{l_j}, \tag{3.2}$$

consists of a purely attractive non-linear wormlike chain (WLC) potential and a repulsive potential, where l_j is the length of the spring j, l_{m} is the maximum spring extension, $x_j = l_j / l_{\text{m}} \in (0, 1)$, the persistence length l_{p}, $k_{\text{B}}T$ the energy per unit mass, and k_p the spring constant. By equating the corresponding forces [91] the equilibrium spring length l_0 can be related to the spring constant k_p as

$$k_p = \frac{l_0^m}{l_{\text{p}}} k_B T \left(\frac{1}{4(1 - x_0)^2} - \frac{1}{4} + x_0 \right), \tag{3.3}$$

with $x_0 = l_{\text{m}} / l_0$. Furthermore, the persistence length is determined by the linear shear modulus

$$\mu_0 = \frac{\sqrt{3} k_{\text{B}} T}{4 l_{\text{p}} l_{\text{m}} x_0} \left(\frac{x_0}{2(1 - x_0)^3} - \frac{1}{4(1 - x_0)^2} + \frac{1}{4} \right) + \frac{3\sqrt{3} k_p}{4 l_0^3}. \tag{3.4}$$

The introduced springs mimic the elastic properties of the spectrin network. Additionally a dashpot has to be incorporated in order to take also the membrane viscosity into account. Therefore, an additional dissipative force

$$\mathbf{F}_{ij}^D = -\gamma^T \mathbf{v}_{ij} - \gamma^C (\mathbf{v}_{ij} \cdot \hat{\mathbf{e}}_{ij}) \hat{\mathbf{e}}_{ij} \tag{3.5}$$

and the random force

$$\mathbf{F}_{ij}^{R}dt = \sqrt{2k_B T}\left(\sqrt{2\gamma^T}d\overline{\boldsymbol{\mathcal{W}}}_{ij}^{S} + \sqrt{3\gamma^C - \gamma^T}\frac{tr[d\boldsymbol{\mathcal{W}}_{ij}]}{3}\mathbb{1}\right)\cdot \hat{\mathbf{e}}_{ij} \tag{3.6}$$

are employed. Note that this equation imposes the condition $3\gamma^C \geq \gamma^T$. Accordingly, the membrane viscosity η_m is given by

$$\eta_m = \sqrt{3}\gamma^T + \frac{\sqrt{3}\gamma^C}{4}. \tag{3.7}$$

Furthermore, the bending energy is defined as,

$$U_{\text{bending}} = \sum_{j\in 1\ldots N_s} k_b(1-\cos(\vartheta_j - \vartheta_0)), \tag{3.8}$$

where k_b is the bending constant, ϑ_j is the instantaneous angle between to adjacent triangles having the common edge j, and ϑ_0 is the spontaneous angle. From the Helfrich energy [154]

$$E_c = \frac{\kappa_r}{2}\int_A (C_1 + C_2 - 2C_0)^2\, dA + \kappa_g \int_A C_1 C_2\, dA, \tag{3.9}$$

with the local curvatures C_1, C_2, the spontaneous curvature C_0, and the bending rigidities κ_r and κ_g, for a spherical shell, the model bending constant k_b is related to the macroscopic bending rigidity by $\kappa_r = \sqrt{3}k_b/2$.

The last two terms of Eq. (3.1) are the global and local area, and volume conservation constraints

$$U_{\text{area}} = \frac{k_a(A - A_0^{tot})^2}{2A_0^{tot}} + \sum_{j\in 1\ldots N_t}\frac{k_d(A_j - A_0)^2}{2A_0} \quad \text{and} \quad U_{\text{volume}} = \frac{k_v(V - V_0^{tot})^2}{2V_0^{tot}}, \tag{3.10}$$

with A and V being the total instantaneous global area and volume, and A_0^{tot} and V_0^{tot} the targeted values. The term A_j is the instantaneous area of triangle $j \in \{1, ..., N_t\}$ and A_0 the desired one. The global area, local area, and volume constraint constants are k_a, k_d and k_v, respectively. All input parameters for a typical simulation are presented in Table B.1 of Appendix B.

The RBC is characterized by the effective diameter $D_\mathrm{r} = \sqrt{A_0/\pi}$, where A_0 is the RBC surface area. Typical values for healthy RBCs are $D_\mathrm{r} = 6.5\,\mu\mathrm{m}$, $\eta = 1.2\times 10^{-3}\,\mathrm{Pa\,s}$, and κ_r lies within the range of $50 - 70k_\mathrm{B}T$ for the physiological temperature $T = 37\,^\circ\mathrm{C}$. The RBC is further characterized by the reduced volume $V^* = 6V_0/(\pi D_r^3) = 0.64$, where

V_0 is the enclosed RBC volume in 3D.

3.1.2. Triangulation

For the triangulation, first N_v vertices (points) are distributed on a surface of a sphere. Assuming that every vertex is a point charge, the equilibrated vertex distribution on the surface is used for triangulation. Afterwards, the sphere is conformed to a RBC by applying that the shape of a RBC can be described [91, 155] as

$$z = \pm D_0 \sqrt{1 - \frac{x^2+y^2}{D_0^2}} \left[c_0 + c_1 \frac{x^2+y^2}{D_0^2} + c_2 \frac{(x^2+y^2)^2}{D_0^4} \right], \tag{3.11}$$

with the cell diameter D_0, $c_0 = 0.1035805$, $c_1 = 1.001279$, and $c_2 = -0.561381$. Furthermore, the free energy of the system is minimised by applying the spring and the bending energy and flipping of triangles [156].

3.1.3. 2D RBC model

In addition to the realistic 3D model, a 2D model [120] is introduced, since 2D simulations are computationally cheaper.

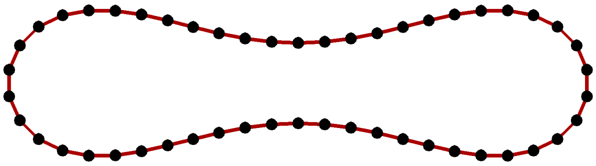

Figure 3.2.: A RBC is modelled as a closed bead-spring chain in 2D. The vertices (black dots) are connected by springs and between two adjacent spring a bending resistance exists. Furthermore, an area conservation constraint is employed.

In 2D, a RBC is modelled as a closed bead-spring chain, see Fig. 3.2. The spring interaction is the same as in Eq. (3.2), the bending potential is

$$U_\text{bending} = \sum_{j \in 1 \ldots N_s} k_b (1 - \cos(\vartheta_j)), \tag{3.12}$$

for the angle ϑ_j between two adjacent springs which have a common vertex j. The area and volume constraint is reduced here to the global area constraint

$$U_\text{area} = \frac{k_a (A - A_0)^2}{2}, \tag{3.13}$$

where A is the instantaneous and A_0 the desired enclosed area.

In 2D the RBC is characterized by the effective diameter $D_\mathrm{r} = L_0/\pi$, where L_0 is the cell contour length. A typical value would be $D_r = 6.1$ µm. The RBC is further characterized by the reduced area $A^* = 4A_0/(\pi D_\mathrm{r}^2) = 0.46$. All input parameters for a typical simulation are presented in Table B.2.

3.2. Single vesicle in shear flow

The described RBC model has been shown to reproduce experimental elasticity measurements [114]. A RBC has been stretched with optical tweezers and its extension has been measured depending on the applied stretching force [157]. Furthermore, single RBCs and vesicles in shear flow possess interesting dynamics, which depend on the viscosity ration of the inner and outer fluid. Thus, simulations of a vesicle in shear flow are presented and used to compare the SDPD+a and SDPD–a simulation method. Beforehand, the implementation of the interactions between fluid and cells is introduced.

3.2.1. Fluid–cell interaction

A RBC or vesicle has to be coupled to the fluid in order to investigate its motion in flow. The coupling is achieved through viscous friction between cell vertices and the surrounding fluid particles, which is implemented via the dissipative and random interactions from the DPD simulation method presented in Eqs. (2.4) and (2.5). The strength γ of the dissipative force F^D for the interaction between a fluid particle and a membrane vertex is computed such that no-slip boundary conditions (BCs) are satisfied. The derivation of γ is based on the idealized case of linear shear flow over a flat plane with area A_p. In a continuum hydrodynamic description, the total shear force exerted by the fluid on the area A_p is equal to $A_p \eta \dot{\gamma_w}$, where η is the fluid's dynamic viscosity and $\dot{\gamma_w}$ is the local wall shear rate. Assuming a discretized plane composed of N_v vertices, the force on a single vertex exerted by the sheared fluid can be found as $F_\mathrm{v} = \int_{V_h} n g(r) F^D dV$, where n is the fluid number density, $g(r)$ is the radial distribution function of the fluid, and V_h is the half sphere volume of fluid above the plane. The total shear force on the area A_p is than equal to $N_A F_\mathrm{v}$. The equality of $N_A F_\mathrm{v} = A_p \eta \dot{\gamma_w}$ results in an expression of the dissipative force coefficient in terms of the fluid density and viscosity, wall density N_A/A_p, and the cut-off radius r_c. Under the assumption of linear shear flow the shear rate $\dot{\gamma_w}$ cancels out. This formulation results in satisfaction of the no-slip

BCs for the linear shear flow over a flat plane. However, it also serves as an excellent approximation for no-slip BCs at the membrane surface [91]. Note that conservative interactions between fluid and membrane particles are turned off, which implies that the radial distribution function is structureless, $g(r) = 1$. In 2D, the surface area is replaced by a line of length L with N_L particles, and the half sphere volume is replaced by the half circle area A_h [91, 158].

3.2.2. Dynamic regimes

Single vesicles and RBCs undergo tank-treading (TT), swinging (SW), and tumbling (TB) motion [56, 92–94, 96–104]. In the TT state vesicles in shear flow exhibits a stationary shape with a finite inclination angle $\theta_\mathrm{i} > 0$ with respect to the flow direction, while the membrane and inner fluid is rotating around the COM of the vesicle, see Fig. 3.3. The TB motion corresponds to rotations as a rigid body. In between the TT and the TB regimes, the SW state occur, where shape oscillations and a concurrently oscillating inclination angle are observed.

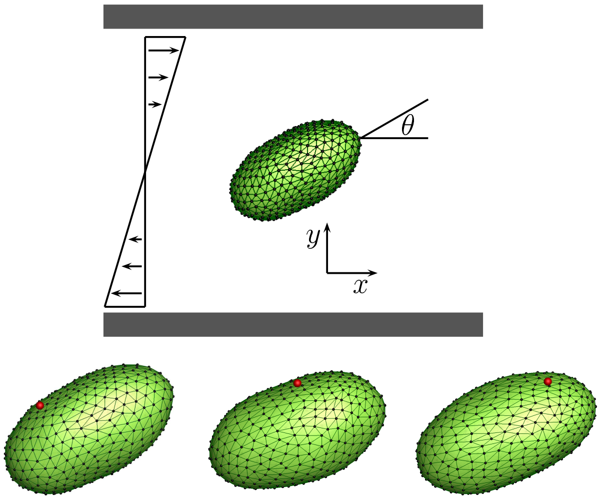

Figure 3.3.: Simulation snapshots of a tank-treading (TT) vesicle in shear flow for the viscosity contrast $\lambda = 2$. (top) A xy-plane view, where the flow is in x-direction. (bottom) For visualization the red sphere is attached to a fixed position on a vesicle in order to demonstrate the TT motion of the membrane. Note that small shape fluctuations are clearly visible [88].

The occurrence of different vesicle motions is governed by shear stresses inside the vesicle. Shear flow has two components, an elongational part which tends to stretch and align a vesicle along the $x = y$ axis with an inclination angle of $\theta_\mathrm{i} = \pi/4$ and a rotational part of the flow which exerts a torque on the vesicle membrane. For low shear stresses between the membrane and the inner fluid this torque leads to the TT motion, whereas increasing shear stresses inside the vesicle result in an effective torque and decrease of the inclination angle. Thus, for large enough inner shear stresses a transition from TT to TB motion occurs.

Keller and Skalak (KS) [95] derived a theory which predicts the TT-to-TB transition for a fixed ellipsoidal shape. Moreover, the KS theory is able to predict the inclination angle θ_i in the vesicle TT regime and is described in detail in Appendix B.2.

Increasing the inner shear stresses means, for instance, increasing the viscosity contrast $\lambda = \eta_i/\eta_o$ between fluids inside and outside the vesicle with viscosities η_i and η_o, respectively. For fluid vesicles the dynamics is very weakly dependent on shear rate, however if elasticity is present, as for RBCs, a TB to TT motion is observed with increasing shear rate if the inner viscosity is low, due to an energy barrier of the TT motion [101].

It is important to note that for simulations with $\lambda > 1$, a simulation method with angular momentum conservation is mandatory. This has been shown for instance for Taylor-Couette flow with two immiscible fluids for both MPC [147] and SDPD+a in Section 2.5.2.

In order to demonstrate this for vesicle simulations, an ellipsoidal vesicle with the shape $(r_1/a_1)^2+(r_2/a_2)^2+(r_3/a_3)^2 = 1$, where $r_i, i \in \{1, 2, 3\}$ are the Cartesian coordinates and a_i are the semiaxes of the ellipsoid, has been simulated. It has a prolate shape with $a_1 > a_2 = a_3$ and an aspect ratio of $a_1/a_2 \approx 1.7$. The ellipsoid is characterized by a reduced volume $V^* = V/(4\pi R_0^3/3)$, where $R_0 = \sqrt{A_0^{tot}/(4\pi)}$ is the effective radius of a vesicle with area A_0^{tot}. An ellipsoidal vesicle with $V^* \approx 0.93$ is employed, since this reduced volume ensures a nearly constant shape in shear flow [97]. Thus, the comparison of simulation results with the KS theory is justified. Note, that in this case the vertices are not connected by springs, but the above introduced bending potential, and area and volume constraints are employed; the parameters are given in Table B.3.

The vesicle is placed in a box of size $L_x = 9.3R_0$ and $L_y = L_z = 5.6R_0$. This box size is large enough to neglect potential finite-size effects as it has been verified in Ref. [97]. Periodic BCs are applied in x- and z-direction, while shear flow is generated by two moving walls in the x-direction with the flow velocity $\mathbf{v} = \dot{\gamma}(y - L_y/2)\hat{\mathbf{e}}_x$ and $\dot{\gamma}$ being the shear rate. Two different strategies are employed to simulate two distinct fluids separated by a membrane. The first method for fluid separation implements bounce-back reflections of fluid particles at the triangle area, similar to the wall-particle interaction described in Section 2.4. This method will be referred to as the 'reflection' method further below. The implementation of fluid particle reflections provides local conservation of momentum, while angular momentum is not strictly conserved at the membrane. Another method for fluid separation considers tracking of fluid particles such that the type, of the particle crossing the membrane, can be altered. Depending on the particle type, the fluid particles interact with different dissipative forces leading to different viscosities. Thus, the type of an outer-fluid particle is changed to the type of an inner-fluid particle if this particle crosses the membrane from outside to inside and vice versa. This method for fluid separation at the membrane leads to local conservation of angular momentum. This method will be referred to as the 'exchange' method.

It has been shown numerically that the inclination angle depends on the Reynolds number $Re = \dot{\gamma}\rho_0 R_0^2/\eta_o$ [104]. Therefore, the system parameters are set such that $Re < 0.1$, to avoid inertial effects. The parameters are presented in Table B.4.

The inclination angle of a TT vesicle in shear flow is calculated by

$$\theta_{\mathrm{i}} = \arctan(u_y/u_x), \tag{3.14}$$

where $\mathbf{u} = (u_x u_y u_z)$ is the eigenvector of the moments of inertia tensor, see Eq. (B.3) of Appendix B, with the smallest eigenvalue. Figure 3.4 (a) compares inclination angles obtained from SDPD simulations of a SDPD+a fluid, a SDPD–a fluid, and from the KS theory for different viscosity ratios λ. The simulation results for the SDPD+a fluid agree very well with the KS theory predictions, while the results using a SDPD–a fluid show a significant overestimation of the inclination angle at large λ. The results for $\lambda = 1$ from both SDPD+a and SDPD–a cases coincide, indicating that angular momentum conservation does not affect simulation results if inner and outer fluids have the same viscosity. The deviations of the SDPD+a results from the KS theory predictions might be due to small shape fluctuations of the vesicle and/or numerical errors, indicated by error bars. Comparison of simulated inclination angles using the 'exchange' and 'reflection' methods for the separation of inner and outer fluids at the membrane is shown in Fig. 3.4 (b). Although the 'reflection' method does not strictly conserve angular momentum at the membrane the corresponding effect on the inclination angle seems to be rather small. Use of the 'reflection' method leads to a slight shift of vesicle inclination angles to smaller values [88].

Furthermore, the TT and TB frequency for a RBC measured from simulations agree with experiments, if a membrane viscosity is chosen. However, with a purely elastic membrane the frequency is overestimated [153].

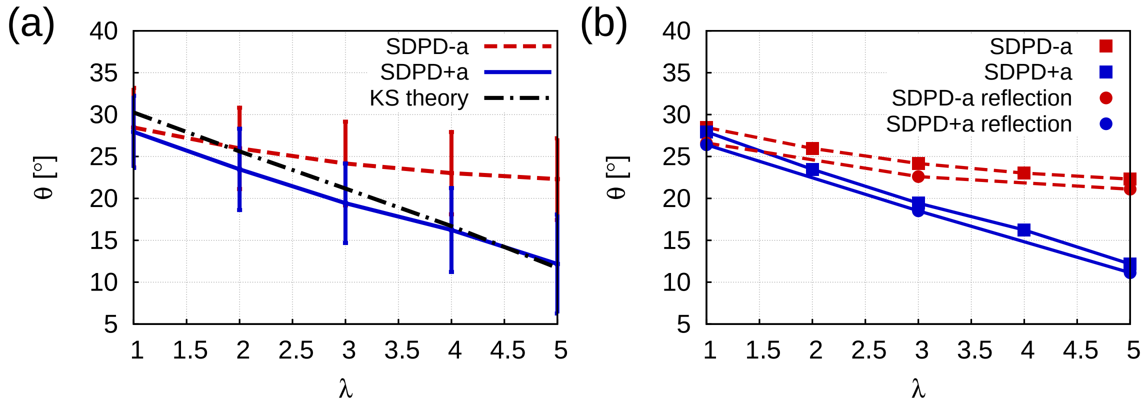

Figure 3.4.: Comparison of inclination angles θ_i of a TT vesicle in shear flow obtained from SDPD+a (blue) and SDPD–a (red) simulations for different viscosity ratios λ. (a) Simulation results, with the 'exchange' method for fluid separation employed, are compared to the KS theory (black). (b) Comparison of the 'exchange' and 'reflection' methods for the separation of inner and outer fluids at the membrane surface.
The inclination angles obtained from SDPD–a simulation differ significantly from the prediction of the KS theory, whereas the results from SDPD+a simulations agree well. Employing the 'reflection' method, which does not strictly conserve angular momentum at the membrane, leads to a small shift to smaller inclination angles [88].

3.3. Blood flow

Clearly, the single-cell properties influence the flow properties of RBCs in bulk flow. Therefore, the arrangement of RBCs in blood flow will be introduced, since this is an important requirement to understand the results of the further presented studies. Also, the implemented interactions between cells and the typical 2D and 3D simulation setup will be is introduced. Additionally, the differences between the DPD and SDPD methods for blood flow simulations will be presented.

3.3.1. Cell–cell interactions

For simulations with more than one RBC, the overlapping of different cells has to be prevented. Therefore, two types of interactions are applied. The first one, is a Lennard-Jones (LJ) repulsion between the cell vertices. The LJ potential

$$U_{\mathrm{LJ}}(r) = 4\epsilon\left(\left(\frac{\sigma_{\mathrm{LJ}}}{r}\right)^{12} - \left(\frac{\sigma_{\mathrm{LJ}}}{r}\right)^{6}\right) \tag{3.15}$$

is truncated at the distance $r_m = 2^{1/6}\sigma_{\mathrm{LJ}}$ at which the potential has its minimum. In order to decrease computational cost the number of vertices can be reduced. For the applied number of vertices solely the LJ repulsion is not sufficient to prevent overlapping. Therefore, bounce-back reflections of the vertices of one cell on the triangle surfaces of the other cells are also assumed, similar to the particle-wall interactions introduced in Section 2.4.

3.3.2. Simulation setup

A typical simulated system corresponds to a cylindrical microvessel in 3D with diameter W and length of $L_\mathrm{c} = 12.3D_\mathrm{r}$ as presented in Fig. 3.5. In 2D, a slit geometry with different widths W and a length $L_\mathrm{c} = 19.5D_\mathrm{r}$ is employed and shown in Fig. 3.6. The focus is on a channel width of $W = 20\,\mu\mathrm{m}$, but smaller and larger ones are also discussed. The wall boundaries are modelled in 3D and 2D as described in Section 2.4. In flow direction, periodic BCs are assumed and blood flow is driven by a constant force applied to all solvent particles, which is equivalent to a prescribed pressure drop. A pressure drop leads to the Poiseuille flow velocity profile

$$v_x(r) = V_0\left(1 - \frac{4r^2}{W^2}\right), \tag{3.16}$$

for a cylindrical channel, with the maximum velocity $V_0^\mathrm{C} = \Delta p W^2/(16 L_\mathrm{c}\eta)$, the dynamic viscosity η, and the pressure drop $\Delta p/L_\mathrm{c} = fn$ defined by the force f on the fluid particles and the number density n. For planar walls in 2D and 3D, the maximum velocity is $V_0^\mathrm{P} = \Delta p W^2/(8 L_\mathrm{c}\eta)$.

In order to characterize the flow strength, a non-dimensional shear rate in both 2D and 3D is defined as

$$\dot{\gamma}^* = \bar{\dot{\gamma}}\tau_\mathrm{RBC} = \bar{\dot{\gamma}}\frac{\eta D_\mathrm{r}^3}{\kappa_r}, \tag{3.17}$$

where κ_r is the bending rigidity, $\bar{\dot{\gamma}} = \bar{v}/W$ is the average shear rate (or pseudo shear rate), and $\bar{v}$ is the average flow velocity computed from the velocity profile, while τ_RBC defines a characteristic RBC relaxation time. The simulated values of $\dot{\gamma}^*$ cover the range of flow rates characteristic for the venular part of microcirculation ($\bar{\dot{\gamma}} \lesssim 80\,\mathrm{s}^{-1}$ for $W \approx 20\,\mu\mathrm{m}$), where it is estimated that $\dot{\gamma}^* \lesssim 90$ in 3D ($\dot{\gamma}^* \lesssim 77$ in 2D), while in arteriolar part the flow rates are larger ($\bar{\dot{\gamma}} \gtrsim 110\,\mathrm{s}^{-1}$ for $W \approx 20\,\mu\mathrm{m}$) with $\dot{\gamma}^* \gtrsim 120$ in 3D [159, 160]. The considered range of shear rates is also relevant for tumor microvasculature, since blood flow velocities in tumors are much reduced in comparison to those under normal conditions, due to large geometric resistance and vessel permeability [161, 162].

In addition to the fluid particles the channel is filled with N_RBC RBCs. The number of

RBCs is computed according to channel hematocrit H_{t}, which corresponds to the volume fraction of RBCs in 3D and to the area fraction of RBCs in 2D. Due to the repulsive LJ interactions between the vertices, a layer of thickness $\sigma_{\mathrm{LJ}}/4$ has been assumed around the RBCs to calculate their effective size and thus to calculate N_{RBC}.

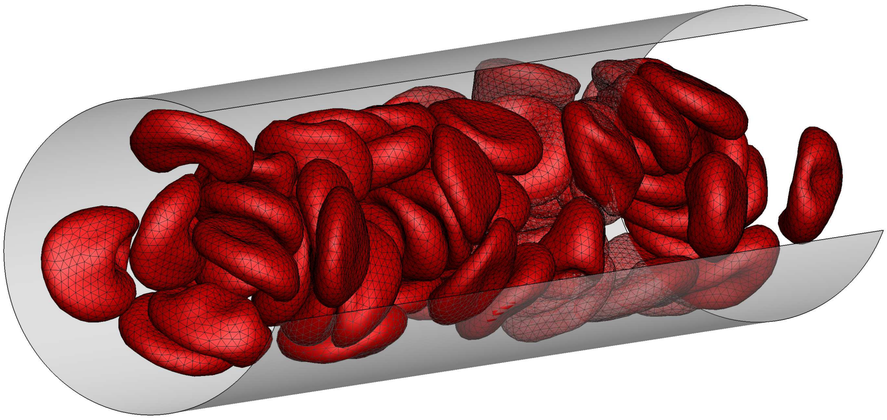

Figure 3.5.: Snapshot of a 3D simulation of blood flow with hematocrit $H_{\mathrm{t}} = 0.3$ in a cylindrical channel with the shear rate $\dot{\gamma}^{*} = 59$. The channel diameter corresponds to $W = 20\,\mu\mathrm{m}$ and the length corresponds to $L_{\mathrm{c}} \approx 80\,\mu\mathrm{m}$. RBCs are coloured in red and the triangulation is shown by the black lines.

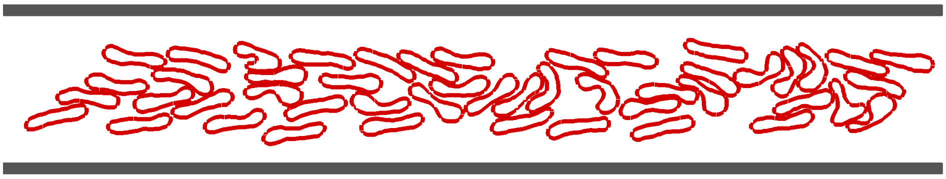

Figure 3.6.: Snapshot of 2D simulation of blood flow with hematocrit $H_{\mathrm{t}} = 0.3$ in a slit geometry with the shear rate $\dot{\gamma}^{*} = 29.3$. The channel width corresponds to $W = 20\,\mu\mathrm{m}$ and the length corresponds to $L_{\mathrm{c}} \approx 118\,\mu\mathrm{m}$. RBCs are coloured in red.

3.3.3. RBC distribution

Due to the hydrodynamic lift, RBCs in blood flow gather in the middle of the channel, where flow velocities are large, which leads to an efficient supply of O_2 and disposal of CO_2. This arrangement leads to a layer close to the wall depleted of RBCs, therefore called the RBC-free-layer (RBC-FL). The exchange of O_2 and CO_2 is mainly performed in the small capillaries with a typical diameter of $5\,\mu\mathrm{m}$ to $8\,\mu\mathrm{m}$ and which have thin walls for this reason. Since the size of the capillaries is comparable to or smaller as the size of the RBCs there is only a small plasma layer between the RBCs and the wall, which is to be overcome by the substances. Furthermore, the RBCs are not equally distributed and the shape and orientation may vary along the cross-section of the channel. Sampling the RBC's cross-sectional center-of-mass (COM) positions in blood flow over time leads to a distribution, which reflects the probability of a RBC to be at a certain radial distance $\Delta r = W/2 - r$ from the wall. These probability distributions are normalized to unity. Figure 3.7 displays such radial COM probability distributions of RBCs for different hematocrit values and average shear rates. In the middle of the channel the local shear rates are lowest, therefore close packing is possible and a peak in the COM distribution is observed. With increasing distance from the wall, the local shear rates increase, which leads to a disturbance of the structure and consequently to a reduced probability. Interestingly, close to the RBC-FL border, the RBCs align with the flow and form a layer, which also leads to a peak in the COM distribution. With increasing hematocrit, the described structure becomes more apparent as presented in Fig. 3.7 (a). Furthermore, with increasing shear rate the packing at the center line increases and the packing close to the RBC-FL shifts to larger distances from the wall, see Fig. 3.7 (b), since the lift force is larger for larger shear rates. Additional to the arrangement, the shape of the RBCs changes along the cross-section. With increasing distance form the wall, the asphericity, the departure from a spherical shape, decreases. RBCs in the middle of the channel even attain a more spherical shape than in equilibrium [163]. Close to the RBC-FL border the asphericity is largest, since cells are subject to the largest shear rates.

Furthermore, the velocity profile changes due to the RBCs, when compared to the flow of fluid alone, with the same pressure drop. The velocity profile for blood flow is more flat in the middle of the channel, as shown in Fig. 3.8, whereas the profiles in the RBC-FL overlap.

A frequently used measure in experiments is the wall shear rate $\dot{\gamma}_w$. For normal Poiseuille flow the wall shear rate and the pseudo shear rate are related by $\dot{\gamma}_w = \zeta\dot{\gamma}^*$ with $\zeta = 8$. However, due to the flatting of the velocity profile for blood flow $\zeta > 8$, depending on the hematocrit.

Fluid compressibility in different methods

In order to test the simulation methods, introduced in the previous chapter, the corresponding COM distributions are compared for similar simulation conditions as hematocrit, shear rate, and fluid viscosity. Figure 3.9 (a) presents the COM distributions of RBCs for $r_h = r_c$, the same hematocrit, shear rate, and viscosity η for the three different

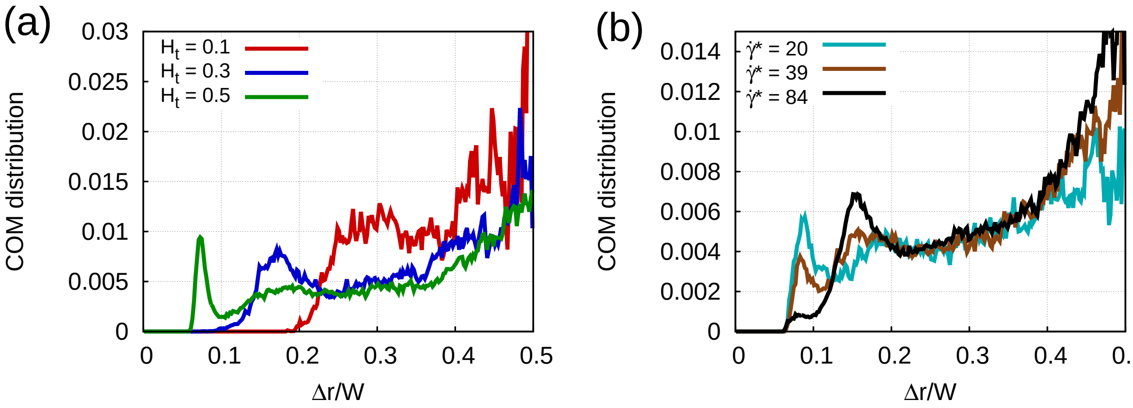

Figure 3.7.: RBC COM distributions depending on the distance Δr to the wall normalized by the channel width W for different hematocrit values The different plots correspond to (a) $\dot{\gamma}^* = 39$ and different hematocrit values: $H_\mathrm{t} = 0.1$ (red), $H_\mathrm{t} = 0.3$ (blue), and $H_\mathrm{t} = 0.5$ (green). (b) At $H_\mathrm{t} = 0.4$ for the shear rates: $\dot{\gamma}^* = 20$ (cyan), $\dot{\gamma}^* = 39$ (brown), and $\dot{\gamma}^* = 84$ (black).

In the middle of the channel the RBCs are closely packed. For increasing local shear rates the structure is disturbed, but close to the wall the RBCs align with the flow and form a layer. With increasing hematocrit, the described structure becomes more pronounced and with increasing shear rate the RBC pack closer in the middle and migrate further away from the wall.

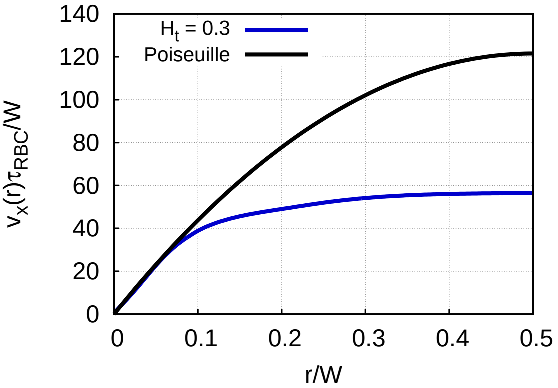

Figure 3.8.: Velocity profile $v_x(r)$ scaled by the RBC relaxation time τ_RBC and the channel width W for the same pressure drop depending on the radial position r for Poiseuille flow (black curve) and blood flow at the hematocrit $H_\mathrm{t} = 0.3$ (blue curve). The pressure drop is defined by the force on the fluid particles $f \approx 165 k_\mathrm{B}T/W$ and the number density $n = 3$.

The blood flow velocity is flattened in the middle and agrees with the Poiseuille flow in the RBC-FL, since the RBCs are gathered in the center.

simulation techniques DPD, SDPD+a, and SDPD–a. The employed fluid parameters are presented in Tables B.5 and B.6. Both SDPD methods agree, since the viscosities inside and outside the RBCs are equal. However, for the DPD method the RBCs are located closer to the wall due to the compressibility of the fluid and therefore, altered hydrodynamic interactions with the wall are observed. For the lower shear rates the distributions from all three methods agree. For 2D simulations a larger fluid density can be applied to treat this compressibility problem, while computational costs still remain manageable. With a number density of $n_{\mathrm{2D}} = 5$ for 2D, instead of $n_{\mathrm{3D}} = 3$ for 3D, the COM distribution agree well in 2D for the DPD and SDPD–a method, since the compressibility is lower.

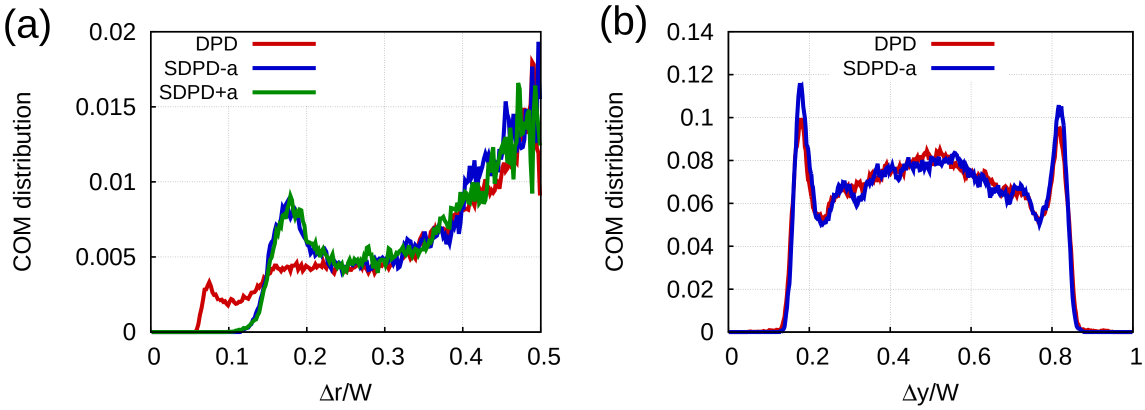

Figure 3.9.: COM distributions depending on the distance Δr to the wall in 3D and Δy in 2D normalized by the channel width W for the different simulation methods DPD (red curves), SDPD–a (blue curves), and SDPD+a (green curve). (a) 3D simulations at $\dot{\gamma}^* \approx 59$ and $H_{\mathrm{t}} = 0.3$. (b) 2D simulations at $\dot{\gamma}^* = 29.7$ and $H_{\mathrm{t}} = 0.45$. The DPD fluid for the 3D simulation is too compressible and leads to incorrect results, whereas the larger density in 2D simulations leads to an incompressible fluid.

3.3.4. Calculation of the RBC-free-layer

The RBC-FL, the region close to the wall depleted of RBCs, is an important characteristic of the RBC arrangement. In order to determine the RBC-FL thickness, the outer edge of the RBC core shown in Fig. 3.10 is measured, which is similar to RBC-FL measurements in experiments [164, 165]. The data is averaged for many RBC snapshots at different times. In 3D, the RBC core edge is measured by projecting RBC vertices onto the xy-plane, leading to a RBC-FL edge similar to that in Fig. 3.10. In addition to the temporal averaging, averaging over different angular orientations (to exploit the cylindrical symmetry of the channel) is also performed.

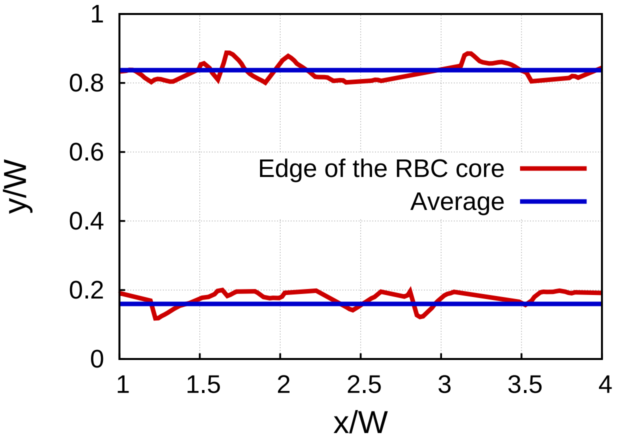

Figure 3.10.: A schematic of a RBC-FL measurement. An example of a RBC-FL edge (red curve) from a 2D simulation at $H_\mathrm{t} = 0.4$ and $\dot{\gamma}^* = 29.7$. The x- and y-positions are normalized by the channel width W. The blue line presents the average of the RBC-FL edge, which defines the RBC-FL thickness.

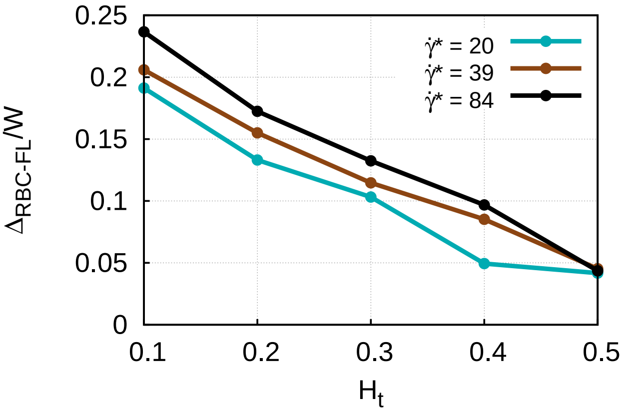

Figure 3.11.: Measurements of 3D RBC-FL thickness $\Delta_{\mathrm{RBC-FL}}$ normalized by the channel diameter W depending on the hematocrit H_t. Different curves correspond to different shear rates $\dot{\gamma}^* = 20$ (cyan), $\dot{\gamma}^* = 39$ (brown), and $\dot{\gamma}^* = 84$ (black).
With increasing hematocrit, the RBC-FL thickness decreases and with increasing shear rate it increases.

The RBC-FL thickness $\Delta_{\mathrm{RBC-FL}}$ depends mainly on the hematocrit but also on the shear rate, as illustrated in Fig. 3.11. The RBC-FL decreases with increasing hematocrit due to the crowded center. Furthermore, with increasing shear rate the RBC-FL increases slightly, due to a larger lift force and the improved packing in the center of the channel. In the limit of very small shear rates ($\dot{\gamma}^* \lesssim 1$), the RBC-FL should almost vanish.

4. Margination of platelets and drug-delivery carriers

The cross-sectional distribution of RBCs is determined by the flow rate and their volume fraction (hematocrit), as discussed in the previous chapter. In particular, the arrangement of RBCs in the middle of the channel is crucial and develops due to a hydrodynamic lift from the wall. The RBC migration towards the channel center leads to a near-wall region depleted of RBCs, which is called the RBC-free-layer (RBC-FL). Since RBCs constitute the majority of cells in blood, their distribution has a high impact on the arrangement of other blood components, such as platelets or synthetic particles, injected into the circulatory system for therapeutic or other reasons. In order to perform a certain task, adhesion of these components to the vessel wall is often required. Hence, they have to migrate to the wall (marginate) to enable adhesion.

In this chapter, the focus is on the investigation of margination of particles, which are considerably smaller and stiffer than RBCs. The dependence of the particle cross-sectional distribution on several relevant parameters is addressed, which include blood flow properties (shear rate and hematocrit), particle characteristics (size, shape, and deformability), and vessel size. Furthermore, a qualitative comparison of 2D and 3D simulations is made. Additionally, the dependence of margination on the channel size is investigated, and the dependence of carrier concentration on channel size, hematocrit, and carrier size is discussed. Finally, to understand the underlying mechanisms of margination, different contributions due to hydrodynamic and direct interactions between the particles and RBCs are examined.

4.1. Size and shape dependence of margination

The margination of different carriers in blood flow is analysed depending on the hematocrit H_t and the normalized average shear rate $\dot{\gamma}^*$, first for spheres of different sizes and second for carriers with ellipsoidal shapes. Moreover, their margination efficiency and rotational dynamics is compared. Finally, the adhesion potential and the favourable shape for drug delivery is discussed.

Figure 4.1 displays the various carrier shapes, emphasizing their different thickness h. All these carriers have been constructed and modelled as described in Section 3.1. The corresponding parameters are presented in Table C.1 and Table C.2 of Appendix C.

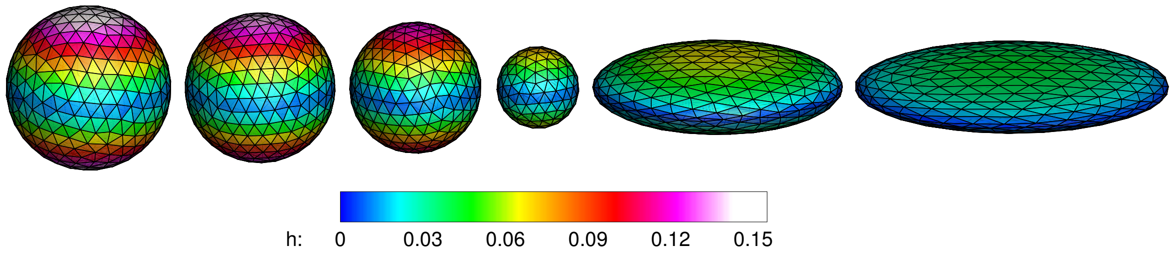

Figure 4.1.: Employed 3D carrier models. Spheres and ellipsoids with triangulated mesh shown in black. The absolute value of the thickness h is given by the colour code: from blue ($h = 0D_\mathrm{r}$) to white ($h = 0.15D_\mathrm{r}$), with the RBC diameter D_r.

4.1.1. Spherical carriers

First, spheres with four different diameters ($D_\mathrm{c} \in \{0.3, 0.28, 0.25, 0.15\}D_\mathrm{r}$), with $D_\mathrm{r} = 6.5\,\mu\mathrm{m}$ being the RBC diameter, are considered. Thereby, a sphere with $D_\mathrm{c} = 0.25D_\mathrm{r}$ has half the volume of the sphere with $D_\mathrm{c} = 0.3D_\mathrm{r}$.

Margination diagrams

Sampling the carrier's cross-sectional COM positions in blood flow over time leads to a distribution, which reflects the probability of a carrier to be at a certain radial distance $\Delta r = W/2 - r$ from the wall. Figure 4.2 displays a radial COM distribution for RBCs and carriers with the diameter $D_\mathrm{c} = 0.25D_\mathrm{r}$, at $H_\mathrm{t} = 0.3$ and $\dot{\gamma}^* \approx 59$. A corresponding snapshot is also presented. In contrast to the RBCs, the carriers migrate into the RBC-FL and remain quasi-trapped there.

One possibility to quantify and compare carrier margination for a wide range of flow and carrier parameters is to calculate the probability of the carrier's COM to be within a certain distance δ away from the wall. Suitable distances would be the RBC-FL thickness or the potential adhesion layer (PAL). The PAL is defined as the region where adhesive interactions between the carrier's surface and the wall would be perceptible. The margination probabilities p_δ are calculated by integrating the COM distributions

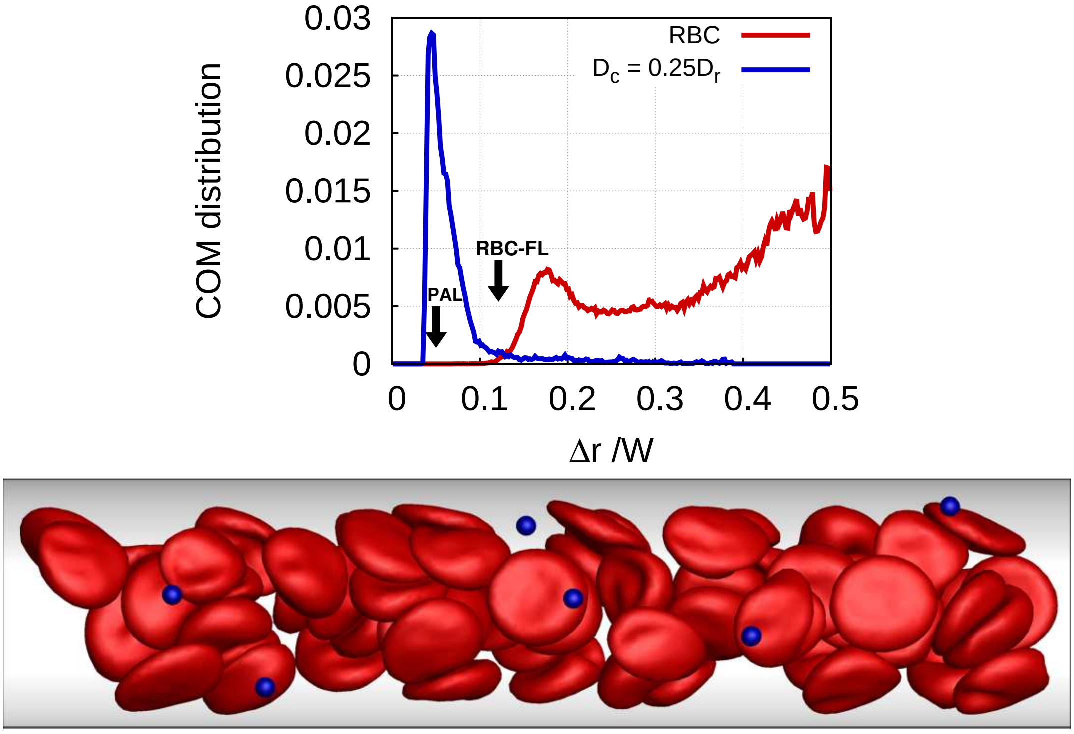

Figure 4.2.: Distribution of different components in blood flow for the shear rate $\dot{\gamma}^* \approx 59$ and the hematocrit $H_\mathrm{t} = 0.3$. (top) Center-of-mass (COM) probability distribution depending on the radial distance Δr to the wall normalized by the diameter W of the channel. The curves correspond to RBCs (red) and spheres with the diameter $D_\mathrm{c} = 0.25 D_\mathrm{r}$ (blue). The black arrows indicate the corresponding RBC-FL and the potential adhesion layer(PAL). (bottom) Corresponding snapshot. RBCs are coloured in red and carriers in blue.
RBCs migrate away from the wall due to a hydrodynamic repulsion (lift force), whereas the carriers are quasi-trapped in the RBC-FL.

$P_{\mathrm{COM}}(r)$ over the particular region as $p_\delta = 2\pi \int_{W/2-\delta}^{W/2} r P_{\mathrm{COM}}(r) dr$. The COM distributions are normalized, such that $p_\delta = 1$ for $\delta = W/2$. The analysis of the margination into the PAL with $\delta_{\mathrm{PAL}} = D_{\mathrm{c}}/2 + s$ is restricted to a distance $s = 200\,\mathrm{nm}$ between the carrier's surface and the wall, due to the resolution of the applied mesoscopic simulation method. Although the distance s is motivated by the receptor-ligand interactions, which occur within several nanometres, the distance of several hundred nanometres becomes relevant for carrier-wall interactions in case of a carrier whose surface is decorated by tethered molecules [166], or for vessels decorated with proteins such as the von Willebrand factor [167]. Both suggested distances depend on the system parameters. The RBC-FL thickness depends on shear rate and hematocrit, as described in Chapter 3, and the PAL on the size of the carriers. Therefore, it is also useful to estimate the margination into a region with a constant thickness independent of all system parameters.

These margination probabilities are then used to construct a so-called margination diagram, in order to compare the margination for a wide range of shear rates and hematocrit values. The margination probability into the RBC-FL (left column) and into the PAL (right column) are displayed in Fig. 4.3 for all considered sizes of spheres. The margination diagrams for a constant region $\delta = 0.31 D_{\mathrm{r}}$ are presented in Fig. C.1 of Appendix C. In all diagrams a high (low) margination probability is depicted in red (blue). Note that the colour scale differs for the different regions. Margination into the RBC-FL has higher probability than margination into the PAL. Thus, for the latter the selected range for the margination probability is different in order to better contrast the dependencies on the hematocrit and shear rate. For the RBC-FL the probability range is chosen as $p^{\mathrm{min}}_{\mathrm{RBC-FL}} = 0.5$ and $p^{\mathrm{max}}_{\mathrm{RBC-FL}} = 1$, and for the PAL, $p^{\mathrm{min}}_{\mathrm{PAL}} = 0$ and $p^{\mathrm{max}}_{\mathrm{PAL}} = 0.7$. The investigation of the margination of the sphere with $D_{\mathrm{c}} = 0.28 D_{\mathrm{r}}$ has shown that for the low hematocrit value $H_{\mathrm{t}} = 0.1$ at all shear rates and for the shear rate $\dot{\gamma}^* = 20$ at all hematocrit values the margination probability is small, therefore, $H_{\mathrm{t}} = 0.1$ and $\dot{\gamma}^* = 20$ are omitted from the margination investigations for the other spheres.

The margination probabilities show a similar dependence on hematocrit and shear rate for all sizes. Primarily, with increasing hematocrit, the margination increases for both choices of margination layer. However, for the sphere with $D_{\mathrm{c}} = 0.3 D_{\mathrm{r}}$ at $H_{\mathrm{t}} = 0.4$ and for the spheres with $D_{\mathrm{c}} = 0.28, 0.25 D_{\mathrm{r}}$ at $H_{\mathrm{t}} = 0.5$, this trend changes and a decrease of margination into the RBC-FL is observed, whereas the margination into the PAL further increases. Figure 4.4 illustrates better that the probability p_{PAL} of margination into the PAL mainly increases rather than decreases at high H_{t}. Diagram cuts are presented for all considered spheres and a shear rate of $\dot{\gamma}^* = 59$. For high shear rates,

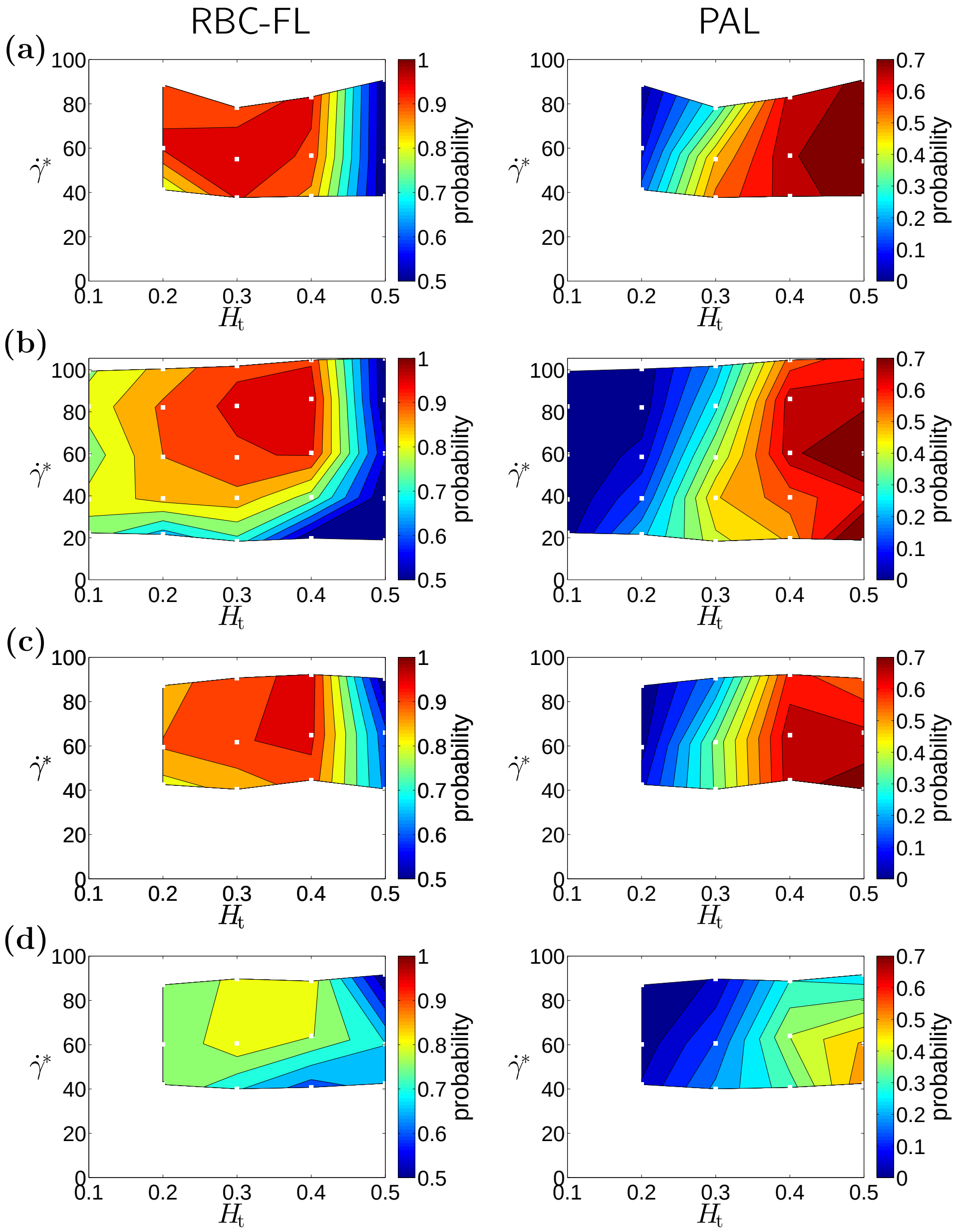

Figure 4.3.: Margination probabilities combined for different hematocrit values H_{t} and shear rates $\dot{\gamma}^*$. Left column: Margination into the RBC-FL. Right column: Margination into the PAL. The four considered sphere diameters D_{c}, compared to the RBC diameter D_{r}, are: (a) $D_{\mathrm{c}} = 0.3D_{\mathrm{r}}$, (b) $D_{\mathrm{c}} = 0.28D_{\mathrm{r}}$, (c) $D_{\mathrm{c}} = 0.25D_{\mathrm{r}}$, and (d) $D_{\mathrm{c}} = 0.15D_{\mathrm{r}}$. The white squares (□) indicate the values of H_{t} and $\dot{\gamma}^*$ for which simulations have been performed. The colour code ranges from blue (low probability) to red (high probability) and is acquired via interpolation.

The margination probability increases with increasing H_{t}. The margination probability into the RBC-FL mainly increases with shear rate, whereas the probability of margination into the PAL decreases. Furthermore, the margination decreases with decreasing size, especially $D_{\mathrm{r}} = 0.15D_{\mathrm{r}}$ possesses a drastically reduced margination probability compared to the other sizes.

a slight decrease may be observed at $H_\mathrm{t} = 0.5$, see Fig. C.2. Comparing the shear-rate dependence of the margination for the two choices of margination layer, considerable differences are observed. The margination probability into the RBC-FL mainly increases with increasing shear rate. Occasionally, a slight decrease of margination for further increasing shear rate may be observed (e.g., $\dot{\gamma}^* \approx 84$, $H_\mathrm{t} = 0.3$). In contrast, the margination into the PAL mainly decreases with increasing shear rate.

Independent of the choice of margination layer, the margination probabilities decrease with carrier size. Especially, for $D_\mathrm{c} = 0.15D_\mathrm{r}$ the margination is drastically reduced compared to the other sizes. Further, the localisation of the carriers is analysed in more detail, to understand not only the detected dependence of margination on hematocrit and shear rate but also the dependence on carrier size.

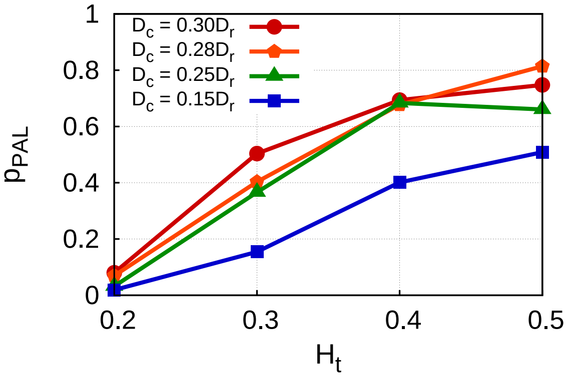

Figure 4.4.: Probability p_PAL of margination into the PAL depending on the hematocrit H_t for an intermediate shear rate $\dot{\gamma}^* \approx 59$. Different curves correspond to different sphere sizes: $D_\mathrm{r} = 0.3D_\mathrm{r}$ (red), $D_\mathrm{c} = 0.28D_\mathrm{r}$ (orange), $D_\mathrm{c} = 0.25D_\mathrm{r}$ (green), and $D_\mathrm{c} = 0.15D_\mathrm{r}$ (blue).
The sphere with $D_\mathrm{c} = 0.15D_\mathrm{r}$ possesses a significantly reduced margination. No significant decrease of margination is observed at high H_t.

Hematocrit dependence

In the majority of cases, an increase of hematocrit results in an increase of margination for all sizes of spheres. With increasing hematocrit, the RBCs are located closer to the wall, as illustrated by the RBC COM distributions in Fig. 4.5 for $\dot{\gamma}^* \approx 84$. In other words, the RBC-FL decreases with increasing hematocrit as presented in Fig. 3.11 of Chapter 3. Simultaneously, the COM distribution of the carriers develops a distinct peak in the RBC-FL. In response to the diminishing RBC-FL thickness $\Delta_\mathrm{RBC-FL}$, the peak of the COM distribution for carriers approaches the wall, becomes sharper, and its height increases.

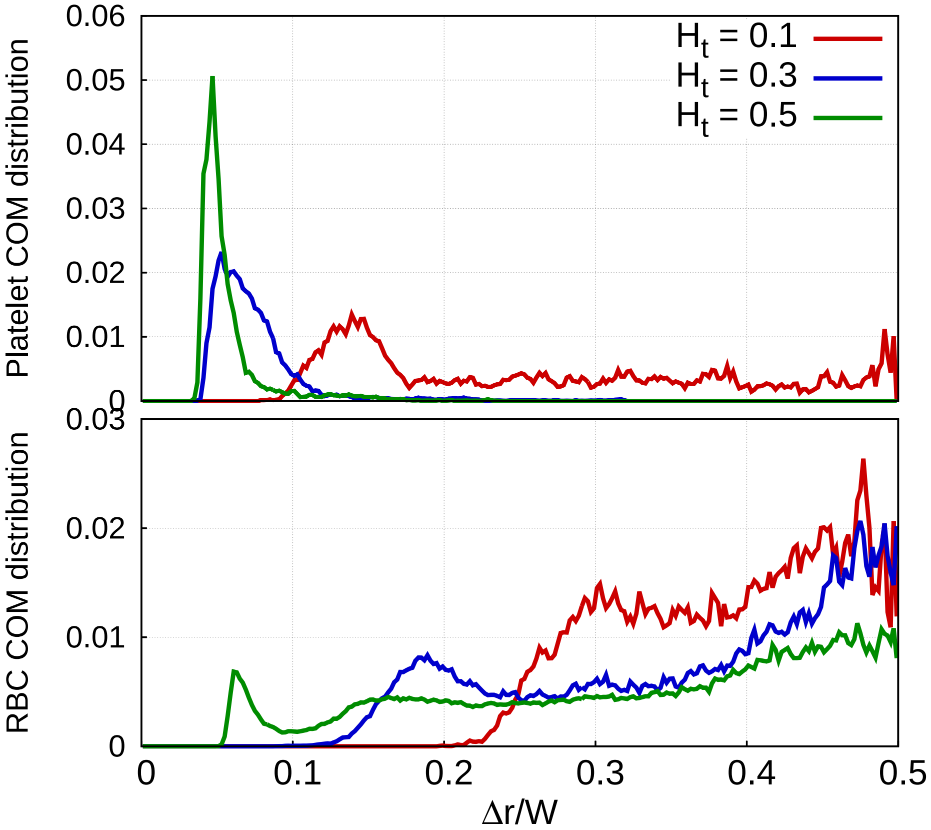

Figure 4.5.: COM probability distributions of a sphere with the diameter $D_\mathrm{c} = 0.28D_\mathrm{r}$ (top) and RBCs (bottom) depending on the radial distance Δr to the wall normalized by the channel diameter W. The curves correspond to the shear rate $\dot{\gamma}^* \approx 84$ and three different hematocrit values $H_\mathrm{t} = 0.1$ (red), $H_\mathrm{t} = 0.3$ (blue), and $H_\mathrm{t} = 0.5$ (green). The RBC COM distribution becomes broader with increasing hematocrit, thus the RBC-FL thickness deceases. With decreasing RBC-FL, the peak of the carrier COM distribution moves closer to the wall, becomes sharper, and higher.

In the following, the distance Δ_MAX of the peak maximum of the COM distribution to the wall and the height $p(\Delta_\mathrm{MAX})$ of the peak are examined. Additionally, the distance of the average COM position in the RBC-FL ($\Delta_{\langle r_\mathrm{RBC-FL}\rangle}$) as well as the distance of the average position in the whole channel ($\Delta_{\langle r\rangle}$) are estimated. The quantities $\langle r_\mathrm{RBC-FL}\rangle$ and $\langle r\rangle$ are the average over all cross-sectional COM positions of all carriers in the RBC-FL, more precisely in a region of thickness $1.05\Delta_\mathrm{RBC-FL}$ and the entire channel for all timesteps, respectively.

Figure 4.6 (a) displays the dependence of Δ_MAX on the hematocrit for two sphere sizes and two shear rates. The considered diameters are $D_{\mathrm{c}} = 0.3D_{\mathrm{r}}$ and $D_{\mathrm{c}} = 0.15D_{\mathrm{r}}$ and the two shear rates are $\dot{\gamma}^* \approx 39$, and $\dot{\gamma}^* \approx 84$. The dotted lines indicate the minimum distances of the COM to the wall that are possible, namely $\Delta_{\mathrm{MAX}}^{\mathrm{min}} = D_{\mathrm{c}}/2$. The peak of the COM distributions reaches the minimum distance for all sphere sizes and shear rates. Indeed, the hematocrit value for which the minimum distance is reached depends mainly on the shear rate but hardly on the size. Higher hematocrit values are necessary for higher shear rates to reach the minimum distance. Once the minimum distance is reached, the maximum height increases further with increasing hematocrit (cf. Fig. 4.7 (c)). The black lines in Fig. 4.6 (a) denote the RBC-FL thickness. At $H_{\mathrm{t}} = 0.5$ the RBC-FL thickness is smaller than the size of the carrier with $D_{\mathrm{c}} = 0.3D_{\mathrm{r}}$. Therefore, the particle center cannot be located in the RBC-FL without deformations of its shape, which is not possible for the considered nearly rigid carriers. Thus, the drastic decrease of margination into the RBC-FL observed in Fig. 4.3 is not due to a reduction of carriers close to the wall, which agrees with the stable margination into the PAL, see Fig. 4.4.

Differences between the various sizes become more apparent after the analysis of the average position in the RBC-FL. The distance $\Delta_{\langle r_{\mathrm{RBC\text{-}FL}} \rangle}$ of the mean position in the RBC-FL from the wall decreases with increasing hematocrit, just like the peak position, as shown in Fig. 4.6 (b). For the sphere with $D_{\mathrm{c}} = 0.3D_{\mathrm{r}}$ the average position in the RBC-FL is closer to the minimum possible distance for both shear rates than for the smaller sphere indicating that the peak for the larger sphere is narrower. The RBC-FL is effectively larger for the smaller spheres, due to their smaller diameter. Smaller spheres can come closer to the wall, as well as to the RBC core, while still being located in the RBC-FL. Therefore, their distribution is broader and their margination into the PAL is less effective.

Interestingly, the increase of the distance $\Delta_{\langle r \rangle}$ of the average position in the entire channel from the wall at $H_{\mathrm{t}} = 0.5$, presented in Fig. 4.6 (c), indicates that the three larger carriers depart from the wall. Carriers that are located close to the RBC-FL border at $H_{\mathrm{t}} = 0.4$ supposedly interact stronger with RBCs at $H_{\mathrm{t}} = 0.5$ and thus get departed; but this seems to be irrelevant for the margination into the PAL, since the number of carriers in the PAL is stable. However, for further increasing H_{t} a reduction of the margination into the PAL is likely. In contrast, the average position of the smallest spheres decreases further at $H_{\mathrm{t}} = 0.5$. Furthermore, a higher percentage of small carriers is still found in the bulk, since the small spheres fit better between the RBCs. Indeed, the curves for the three larger spheres are very similar and the mean

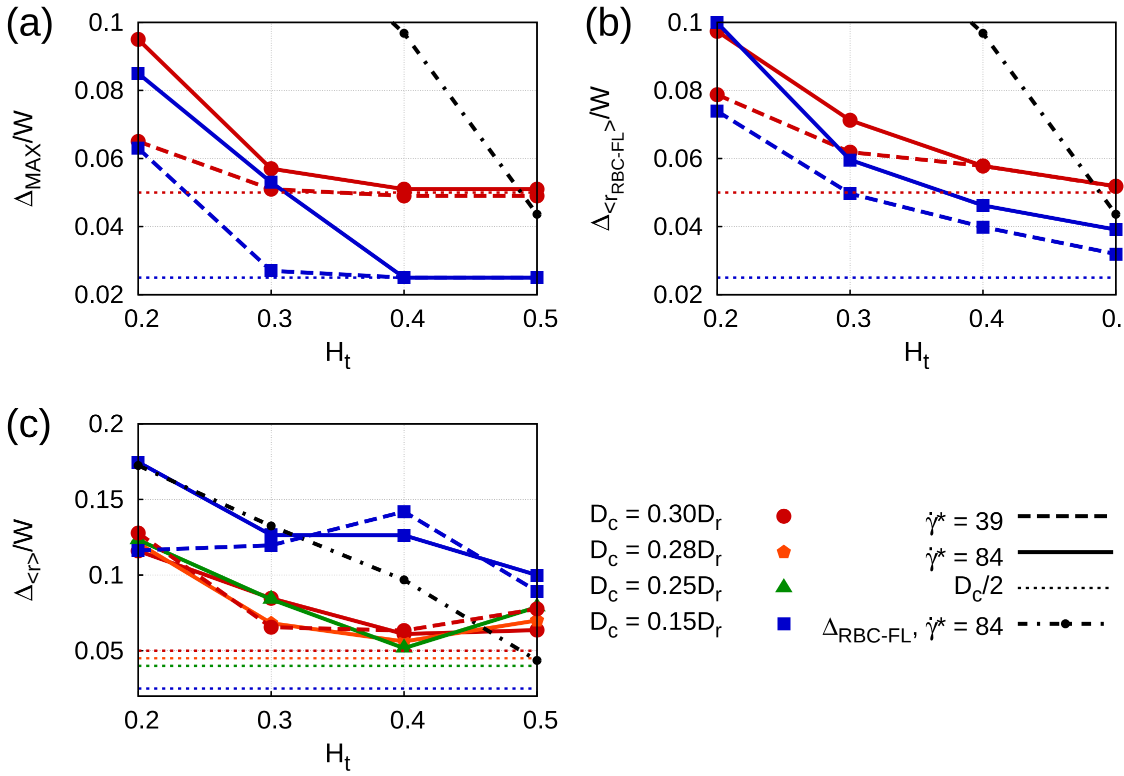

Figure 4.6.: COM distribution characteristics depending on the hematocrit H_t. (a) Distance Δ_MAX of the peak to the wall, (b) distance $\Delta_{\langle r_\mathrm{RBC-FL} \rangle}$ of the mean position in the RBC-FL to the wall , and (c) distance $\Delta_{\langle r \rangle}$ of the mean position in whole channel to the wall. All quantities are normalized by the channel diameter W. Different colours correspond to different sphere sizes: $D_\mathrm{c} = 0.3D_\mathrm{r}$ (red), $D_\mathrm{c} = 0.28D_\mathrm{r}$ (orange), $D_\mathrm{c} = 0.25D_\mathrm{r}$ (green), and $D_\mathrm{c} = 0.15D_\mathrm{r}$ (blue). Different curve types refer to different shear rates: $\dot{\gamma}^* \approx 39$ (dashed) and $\dot{\gamma}^* \approx 84$ (solid). The coloured dotted curves indicate the particular minimum distance to the wall $D_\mathrm{c}/2$ and the black dash-dotted curve the RBC-FL thickness $\Delta_\mathrm{RBC-FL}$.
From $H_\mathrm{t} = 0.1$ to $H_\mathrm{t} = 0.4$ all carriers come closer to the wall. At $H_\mathrm{t} = 0.5$ the three largest spheres are departed from the wall. All measured quantities decrease with increasing shear rate. Although the peak reaches the minimum distance for the sphere with $D_\mathrm{c} = 0.15D_\mathrm{r}$, the average positions differ considerably from the minimum possible distances.

position is located in the RBC-FL, whereas the average position of the smallest sphere is considerably further away from the wall than the RBC-FL border. See also Fig. C.3 for further sphere sizes.

In short summary, it has been observed that RBCs are essential for margination. With increasing hematocrit, the RBC-FL decreases and the margination increases. The smaller the carriers the worse the margination, because smaller carriers fit better in the RBC bulk and their distribution in the RBC-FL are broader. Noteworthy is the significant difference between the carrier with $D_\mathrm{c} = 0.15D_\mathrm{r}$ and the other spheres, for all investigated properties of the system. The three cases $D_\mathrm{c} \in \{0.3, 0.28, 0.25\}D_\mathrm{r}$ just differ slightly, although the volume of the sphere with $D_\mathrm{c} = 0.3D_\mathrm{r}$ is twice the volume of the sphere with $D_\mathrm{c} = 0.25D_\mathrm{r}$. Accordingly, the linear size of a carrier affects the margination properties rather than the volume.

Shear-rate dependence

The distributions of carriers depend not only on the hematocrit, but also on the shear rate, as seen above. The shear-rate dependence stems from the dependence of the RBC-FL thickness on shear rate. In the limit of very small shear rates ($\dot{\gamma}^* \lesssim 1$), the RBC distribution is nearly uniform, and therefore, the RBC-FL and consequently the carrier margination should almost vanish. The increase of shear rate associated with an increase of the RBC-FL thickness, as presented in Fig. 3.11, would explain both observations, the increase of margination into the RBC-FL as well as the decrease of margination into the PAL. For the former case, the margination probability is calculated with respect to a broader channel region, but a broader RBC-FL leads also to a reduction of margination into the PAL as seen before. Nevertheless, taking into account that RBCs are influenced by different shear rates it is reasonable to assume that carriers may be also influenced. Therefore, the distribution characteristics are examined depending on the corresponding RBC-FL thickness $\Delta_{\mathrm{RBC-FL}}$ to exclude the effect of a different RBC-FL thickness for various shear rates.

Figures 4.7 (a) and (b) present the distance Δ_{MAX} of the peak and the distance $\Delta_{\langle r_{\text{RBC-FL}} \rangle}$ of the average position in the RBC-FL from the wall. Despite the new way of plotting, both properties still depend on the shear rate. The deviations are smaller compared to Figs. 4.6 (a) and (b) and are more distinct for the smaller carrier. Additionally, the height $p(\Delta_{\mathrm{MAX}})$ of the maximum, i.e. the probability to find a carrier exactly at the peak position, is clearly reduced at higher shear rates, see Fig. 4.7 (c). Thus, the increase of margination into the RBC-FL is due to the increase of the RBC-FL thickness

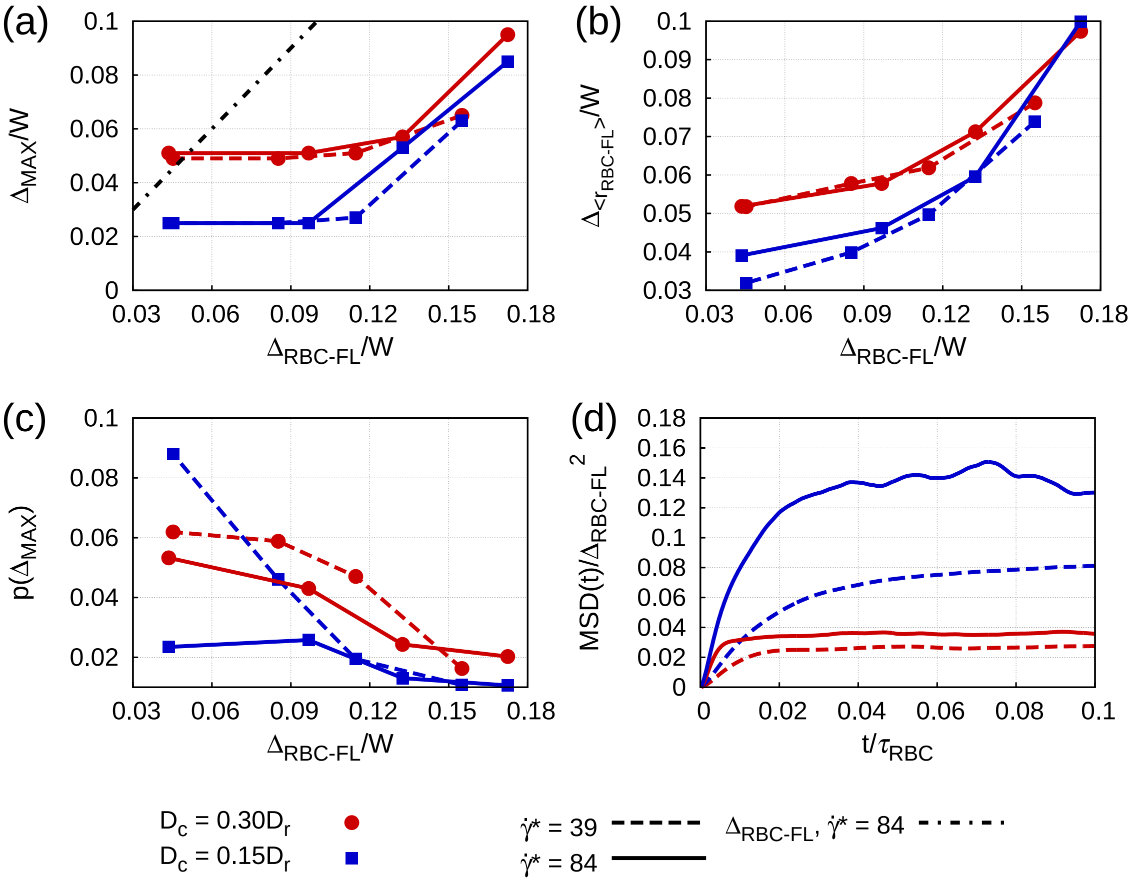

Figure 4.7.: COM distribution analysis depending on the RBC-FL thickness $\Delta_{\mathrm{RBC-FL}}$ and shear rate $\dot{\gamma}^*$. (a) Distance Δ_{MAX} of the peak to the wall, (b) distance $\Delta_{\langle r_{\mathrm{RBC-FL}}\rangle}$ of the mean position in the RBC-FL to the wall, and (c) height $p(\Delta_{\mathrm{MAX}})$ of the peak maximum. All parameters are normalized by the channel diameter W. (d) Time t dependent mean squared displacement $\mathrm{MSD}(t)$ in RBC-FL at hematocrit $H_{\mathrm{t}} = 0.5$. The time is normalized by the RBC relaxation time τ_{RBC}. Different colours correspond to different spheres: $D_{\mathrm{c}} = 0.3D_{\mathrm{r}}$ (red) and $D_{\mathrm{c}} = 0.15D_{\mathrm{r}}$ (blue). The dashed curves refer to the shear rate $\dot{\gamma}^* \approx 39$ and the solid curves to $\dot{\gamma}^* \approx 84$.
All examined distribution characteristics still depend on the shear rate. The influence of shear rate is stronger for the smaller sphere. The increased fluctuation at higher shear rates is observed especially for the small sphere.

$\Delta_{\mathrm{RBC-FL}}$ with increasing shear rate, whereas the reduction of margination into the PAL has additional reasons. See also Figs. C.4 (a) to (c) for further sphere sizes.

The motion of the carriers in radial direction in the RBC-FL is analysed to further understand the shear-rate dependence. Therefore, the mean squared displacement (MSD), given by

$$\mathrm{MSD}(t) = \left\langle \left(r_{\mathrm{RBC-FL}}\left(t + t_0\right) - r_{\mathrm{RBC-FL}}\left(t_0\right) \right)^2 \right\rangle , \tag{4.1}$$

is investigated. The MSD provides a measure for the distance, a carrier diffuses in a given time interval of length t from its original position $r(t_0)$ at time t_0. Figure 4.7 (d) shows the MSD, normalized by the RBC-FL thickness squared to eliminate the effect of different RBC-FL thicknesses, for two shear rates at $H_{\mathrm{t}} = 0.5$. The MSD increases with increasing shear rate. An increase of effective fluctuations explains the reduction of the maximum height and the change of mean position in the RBC-FL. Furthermore, the more pronounced change in fluctuations for the small carriers is in agreement with the stronger influence of the shear rate on the COM distribution. However, this is not the full explanation, since at $H_{\mathrm{t}} = 0.4$ different MSDs for various shear rates are observed only for the smallest carrier, see also Figs. C.4 (d) and (e).

In short summary, the shear-rate dependence of margination of almost rigid carriers is less pronounced than the hematocrit dependence. However, the shear-rate dependence originates from an increase of RBC-FL thickness with increasing shear rate and from effective fluctuations induced by larger shear rates.

4.1.2. Elongated carriers

Non-activated platelets have a disc-like rather than a spherical shape. Therefore, the margination of two elongated shapes is examined. Both carriers are modelled as oblate ellipsoids based on the surface equation $4(x^2 + y^2)/D_{\mathrm{L}}^2 + 4z^2/D_{\mathrm{S}}^2 = 1$, with D_{L} being the long axis diameter and D_{S} being the short axis diameter. The carriers differ in their aspect ratios ($\kappa = D_{\mathrm{L}}/D_{\mathrm{S}}$), but have the same volume as the sphere with the diameter $D_{\mathrm{c}} = 0.3D_{\mathrm{r}}$, see Fig. 4.1. One ellipsoid has the aspect ratio of $\kappa = 3.5$, which corresponds to $D_{\mathrm{L}}^e = 0.47D_{\mathrm{r}}$ and $D_{\mathrm{S}}^e = 0.13D_{\mathrm{r}}$, respectively. The second ellipsoid has an aspect ratio of $\kappa = 7$ ($D_{\mathrm{L}}^d = 0.59D_{\mathrm{r}}$, $D_{\mathrm{S}}^d = 0.09D_{\mathrm{r}}$). For simplicity the carrier with the larger aspect ratio is referred to as “disc”, the other as “ellipsoid”.

Margination diagrams

Figure 4.8 presents the margination probabilities depending on hematocrit and shear rate for carriers of the same volume, the sphere with $D_\mathrm{c} = 0.3D_\mathrm{r}$ (a), the ellipsoid (b), and the disc (c). Please note that the plot employs different colour scales compared to Fig. 4.3. See Fig. C.5 for the margination into a constant region. Both elongated shapes marginate worse into the RBC-FL (left column) than the sphere. For both elongated shapes the probabilities are smaller. However, a similar shear-rate and hematocrit dependence is observed. After an initial increase, a decrease of margination into the RBC-FL with increasing hematocrit is already starting from $H_\mathrm{t} = 0.3$. For the elongated shapes, the margination into the PAL is computed with respect to the long diameter D_L, since for this distance an ellipsoid is able to interact with the wall. However, particles in shear flow perform rotations, thus an interaction with the wall can just happen in a specific time window during the rotation. The PAL margination probabilities for elongated shapes seem to be similar to the margination of the sphere. This is confirmed in Fig. 4.9 which presents the probability p_PAL of margination into the PAL depending on the hematocrit at $\dot{\gamma}^* = 59$ (see also Fig. C.6 for $\dot{\gamma}^* = 39$ and $\dot{\gamma}^* = 84$). At low hematocrit values both elongated shapes marginate slightly better into the PAL than the sphere. However, at high hematocrit values the PAL margination probability decreases for the ellipsoid but not for the disc. The same distribution characteristics as presented above for spheres are compared for the elongated shapes, in order to understand the origin of discrepancies for the different shapes.

Hematocrit dependence

Figure 4.10 (a) displays the COM distributions for both, the disc and the ellipsoid with the corresponding RBC distribution at $\dot{\gamma}^* \approx 84$ and $H_\mathrm{t} = 0.5$. In contrast to the COM distributions observed for spheres, two peaks can be identified for the elongated shapes for some parameter combinations. One peak is close to the peak of the RBCs (peak 1) and one very close to the wall (peak 2). However, for the ellipsoid the second peak is less distinct. A particularly interesting observation is the splitting of the first peak of the disc, with a local minimum exactly at the position of the maximum of the RBC distribution. This has been observed for multiple parameter combinations and indicates that the disc can easily slide between the RBCs.

Figure 4.10 (b) shows for both elongated shapes and two shear rates the distance of the peaks to the wall. Additionally, the minimal distance of the long axis ($D_\mathrm{L}/2$) to

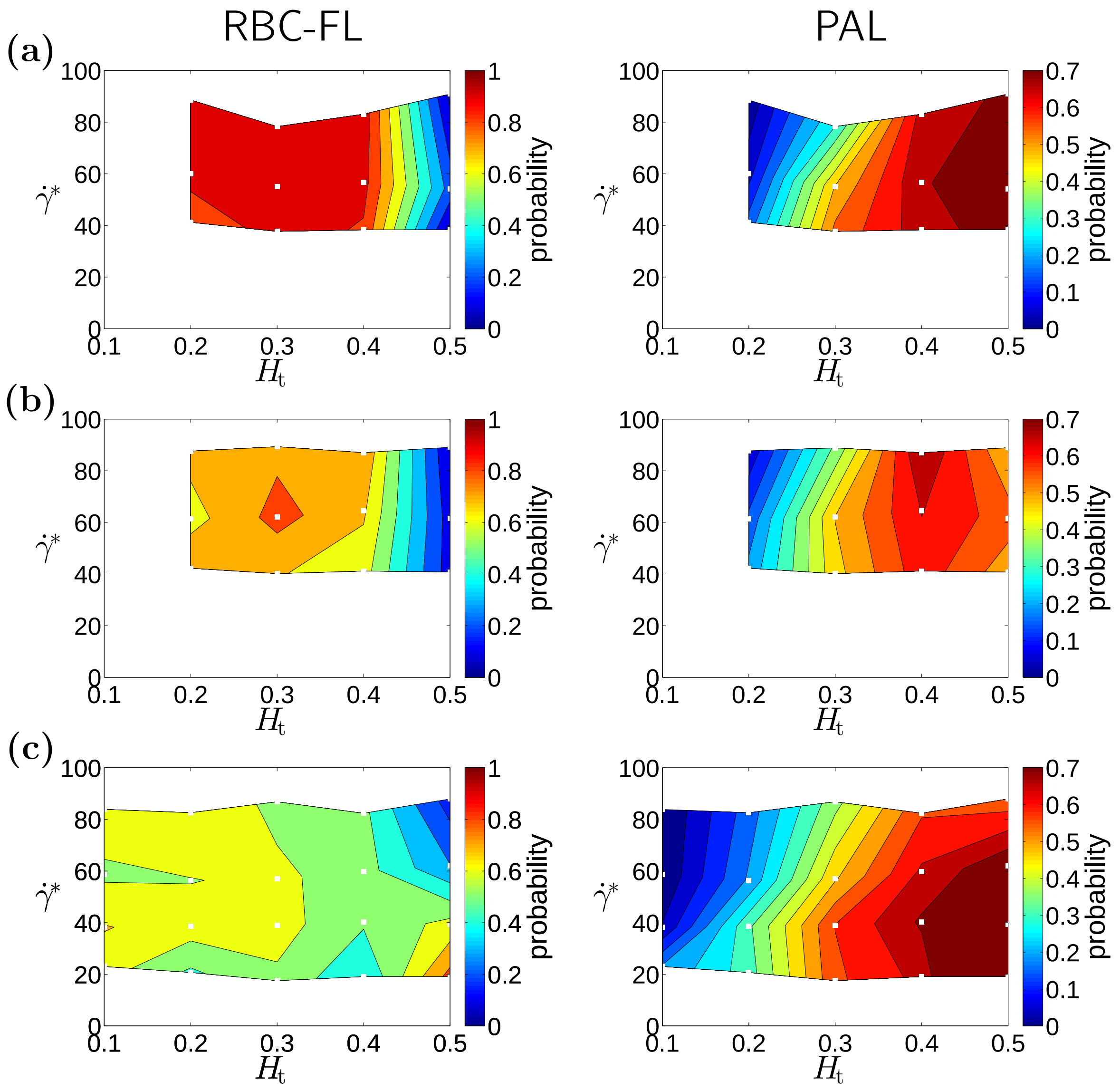

Figure 4.8.: Margination probabilities combined for different hematocrit values H_t and shear rates $\dot{\gamma}^*$. Margination into the RBC-FL (left) and the PAL (right). (a) Sphere with $D_\mathrm{c} = 0.3D_\mathrm{r}$, (b) oblate ellipsoid with a long axis diameter of $D^e_\mathrm{L} = 0.47D_\mathrm{r}$ and a short axis diameter of $D^e_\mathrm{S} = 0.13D_\mathrm{r}$, and (c) oblate ellipsoid ("disc") with $D^d_\mathrm{L} = 0.59D_\mathrm{r}$ and $D^d_\mathrm{S} = 0.09D_\mathrm{r}$. The white squares (□) indicate the values of H_t and $\dot{\gamma}^*$ for which simulations have been performed. The colour code ranges from blue (low probability) to red (high probability) and is acquired via interpolation.

The probability of margination into the RBC-FL is significantly reduced for the elongated shapes. However, the margination into the PAL is similar for the sphere and the disc, but slightly reduced for the ellipsoid.

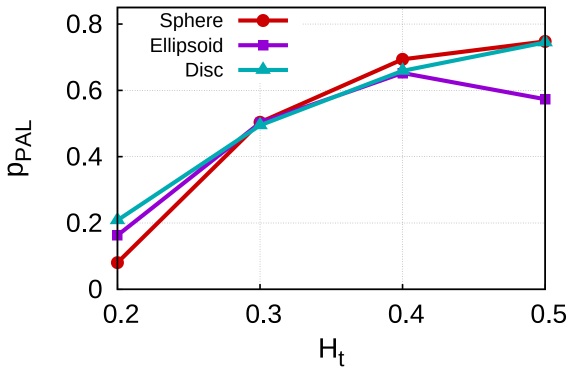

Figure 4.9.: Probability p_{PAL} of margination into the PAL depending on hematocrit H_{t} at an intermediate shear rate $\dot{\gamma}^* \approx 59$. The curves correspond to the sphere with $D_{\mathrm{c}} = 0.3D_{\mathrm{r}}$ (red), the ellipsoid (purple), and the disc (cyan).
At low H_{t} values elongated shapes marginate better. At high H_{t} the disc marginates similar to the sphere, whereas the margination probability of the ellipsoid decreases.

the wall, the minimum distance of the short axis ($D_{\mathrm{S}}/2$), and the RBC-FL thickness are depicted. Already for low hematocrit values the first peak reaches the distance that corresponds to the long axis. Thus, the elongated carriers are close enough to interact with the wall for lower hematocrit values than the spheres (cf. Fig. 4.6 (a)).

However, the first peak is very close to the RBC-FL border for high hematocrit values. Furthermore, the average position in the channel is close to the RBC-FL, as shown in Fig. 4.10 (c). Hence, a reasonable amount of carriers is located outside of the RBC-FL, which explains the low RBC-FL margination probability, especially for the disc. Nevertheless, the thicker ellipsoids are influenced more by RBCs than the thinner discs, since the ellipsoids mean distance $\Delta_{\langle r \rangle}$ decreases for the highest H_{t}. However, the second peak starts to appear for cases with $\Delta_{\mathrm{RBC-FL}} \lesssim D_{\mathrm{L}}/2$ and is located at the minimal possible distance $D_{\mathrm{S}}/2$. An advantage of this second peak is that carriers, located such close to the wall, would be able to interact with adhesive sites on the wall without disturbance by RBCs, as long as $\Delta_{\mathrm{RBC-FL}} \gtrsim D_{\mathrm{S}}/2$. The appearance of a larger second peak for the disc also explains the larger margination probability into the PAL for the disc compared to the ellipsoid.

Shear-rate dependence

In the case of carriers with a spherical shape, the peak height of the COM distributions changes clearly with shear rate (see Fig. 4.7 (c)). In contrast, the height of the peaks depending on the RBC-FL thickness $\Delta_{\mathrm{RBC-FL}}$ for the elongated shapes (presen-

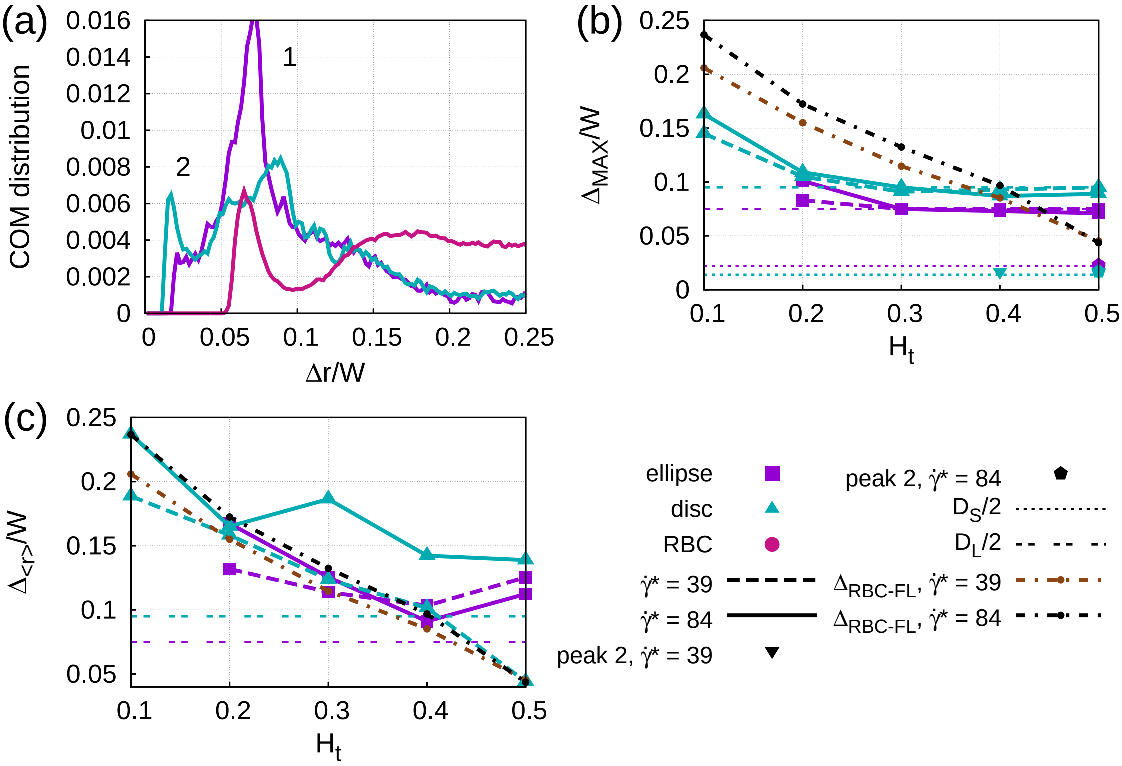

Figure 4.10.: Distribution characteristics depending on hematocrit H_t. (a) COM distributions of carriers with elongated shapes and RBCs (magenta curve) depending on the radial distance Δr from the wall normalized by the channel diameter W. The curves correspond to a shear rate of $\dot{\gamma}^* \approx 84$ and to the hematocrit value $H_\mathrm{t} = 0.5$. (b) Distance Δ_MAX of the peak to the wall, and (c) distance $\Delta_{<r>}$ of the mean position in the whole channel to the wall. The cyan colour correspond to the disc and the purple colour to the ellipsoid. The symbols without lines refer to the second peak. The dashed curve/turned-triangle correspond to $\dot{\gamma}^* \approx 39$ and the solid curve/pentagon to $\dot{\gamma}^* \approx 84$. The dotted and two-fold dashed line correspond to the short axis D_S and the long axis D_L, respectively. The brown and the black dash-dotted lines display the RBC-FL thickness at $\dot{\gamma}^* \approx 39$ (brown) and $\dot{\gamma}^* \approx 84$ (black).
In contrast to the sphere, the COM distributions of the elongated shapes show two peaks. Both peaks are either close to the radius of the long or of the short axis. The ellipsoid shows an increased mean distance at high hematocrit values, which is similar to the sphere.

ted in Fig. 4.11 (a)), is hardly influenced by shear rate. The height of the first peak increases with decreasing RBC-FL thickness, as observed also for spheres. However, when the second peak appears, the height of the first peak decreases. There might be two possible reasons. First, the carriers that have been in the region of the first peak moved to the region of the second peak. Second, since the first peak is close to the RBC-FL border, interactions with RBCs could displace the carriers. Interestingly, the elongated shapes display more stable margination characteristics than the spheres. The height of the first peak as well as the RBC-FL mean-distance presented in Fig. 4.11 (c) hardly depend on shear rate. However, the height of the second peak depends on the shear rate, see Fig. 4.11 (b). Especially for the disc, the height of the second peak is reduced for the two highest shear rates, although the RBC-FL thickness is smaller.

The origin of the shear-rate dependence of the height of the second peak might be related to an increase of effective fluctuations as discussed for the spheres. However, there is a second aspect, which is related to the rotational motion of carriers in shear flow. A spherical carrier is subject to a uniform rotation, while an ellipsoid displays tumbling dynamics. Indeed, an ellipsoid whose COM is closer to the wall than its long axis cannot freely rotate. If the distance to the wall is close to $D_\mathrm{S}/2$ it can hardly change orientation, but for higher distances it is able to swing back and forth. For tumbling, an ellipsoid is forced to move away from the wall to a distance of $D_\mathrm{L}/2$ making a full rotation possible. Figure 4.12, depicts the correlation of the orientation of the disc and the COM distance to the wall. The orientation is described by the angle θ, which is the angle between the short axis of the disc and the radial unit vector. The colour of the curve characterizes the COM distance to the wall. Purple corresponds to a small distance to the wall and yellow to a larger distance. If the carrier is aligned with the flow, the angle is $\theta = 0$ (Figs. 4.12 (b), (d)) and during rotation the angle is $0 < \theta \leq \pi/2$ (Fig. 4.12 (c)). The distance of a carrier located in the region of the first peak, has to increase to reach a certain angle. Hence, after a rotation the carrier is located in the region of the second peak. This is consistent with the observation that the peak is located either at $D_\mathrm{L}/2$ or $D_\mathrm{S}/2$. For higher shear rates the force on the carriers is stronger due to the higher velocity gradient in the near wall region, leading to a higher first peak and a less distinct second peak.

4.1.3. Rotational dynamics of a carrier

The carriers' rotational dynamics influences not only the margination as seen above but also the adhesion efficiency. An analysis of the average angular velocities $\langle \psi \rangle$ of

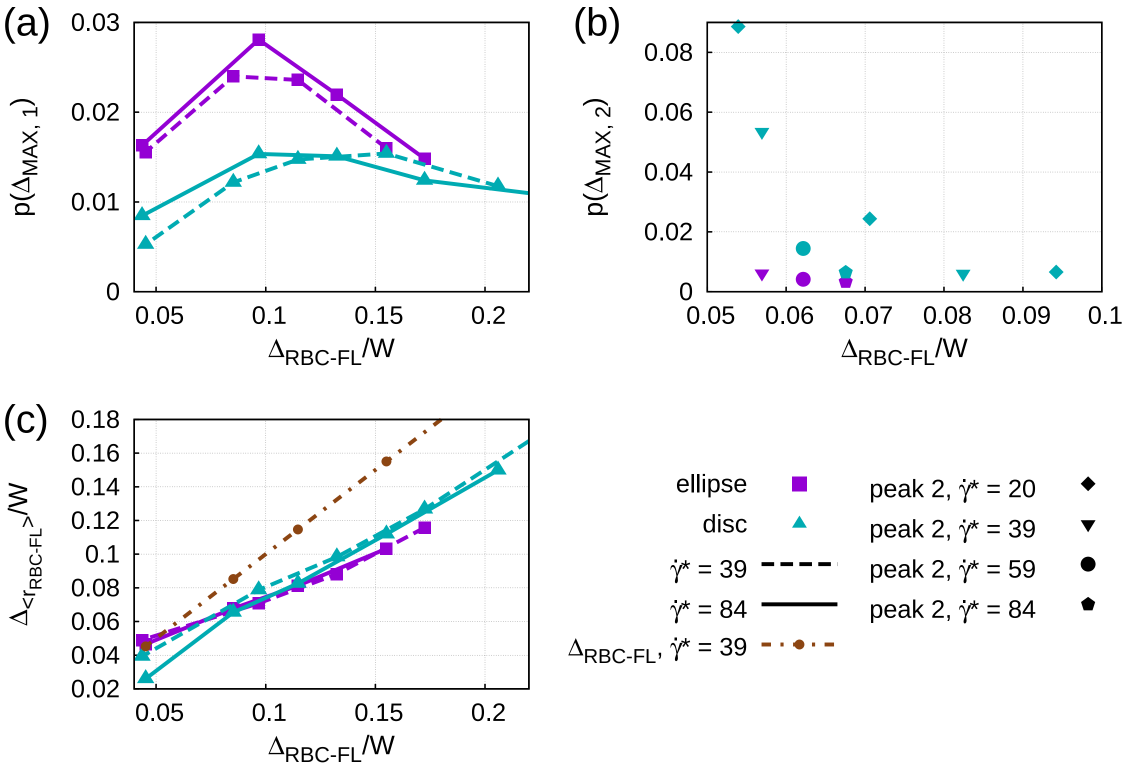

Figure 4.11.: Distribution characteristics for different shapes depending on the RBC-FL thickness $\Delta_{\mathrm{RBC-FL}}$ normalized by the channel diameter W. Comparison of the ellipsoid (purple) and the disc (cyan). (a) Height $p(\Delta_{\mathrm{MAX},1})$ of the first peak at the shear rates $\dot{\gamma}^* = 39$ (dashed curve), and $\dot{\gamma}^* = 84$ (solid curve). (b) Height $p(\Delta_{\mathrm{MAX},2})$ of the second peak at the shear rates $\dot{\gamma}^* = 20$ (diamond), $\dot{\gamma}^* = 39$ (turned-triangle), $\dot{\gamma}^* = 59$ (circle), and $\dot{\gamma}^* = 84$ (pentagon). (c) Distance $\Delta_{\langle r_{\mathrm{RBC-FL}} \rangle}$ of the mean position in the RBC-FL and RBC-FL thickness $\Delta_{\mathrm{RBC-FL}}$ at $\dot{\gamma}^* = 39$ (brown dash-dotted line).
Initially, the first peak increases with decreasing RBC-FL thickness. When the second peak appears the first peak decreases. Only the height of the second peak seems to be dependent on the shear rate.

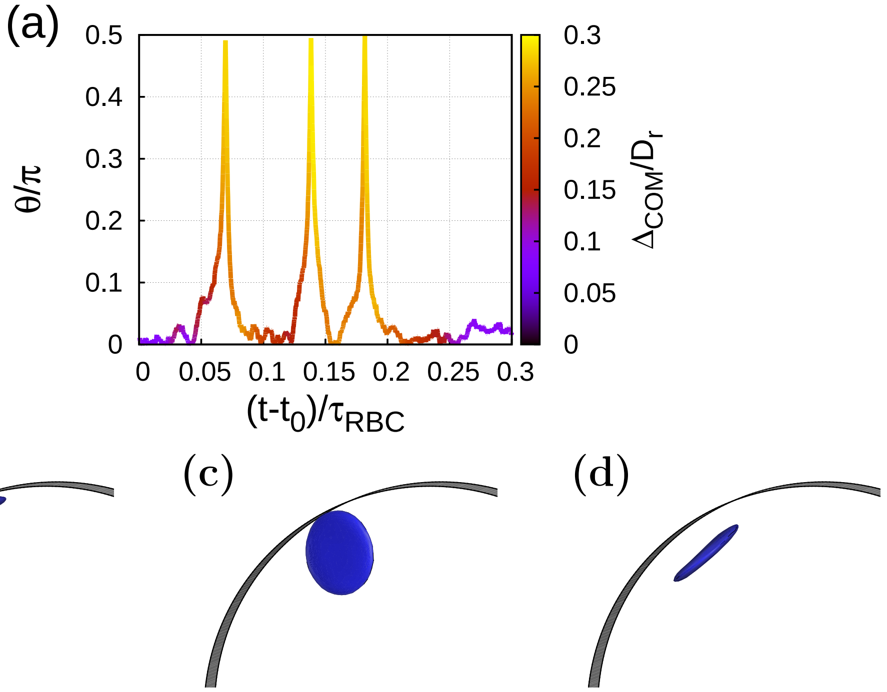

Figure 4.12.: Orientation of a disc in flow. (a) The angle θ between the short axis of the disc and the radial unit vector normalized by π for different times t starting from the simulation time t_0 normalized by the RBC relaxation time τ_{RBC}. The colour of the curve corresponds to the distance Δ_{COM} of the carriers COM to the wall, normalized by the RBC diameter D_{r}. Purple refers to a short distance and yellow to a larger one. (b-d) Snapshots for the disc whose orientation is shown in (a) at times $t/\tau_{\mathrm{RBC}} = 0.005$, $t/\tau_{\mathrm{RBC}} = 0.07$, and $t/\tau_{\mathrm{RBC}} = 0.09$. This example corresponds to the shear rate $\dot{\gamma}^* \approx 39$ and hematocrit $H_{\mathrm{t}} = 0.5$.
Initially, the carrier is close to the wall, but it has to depart from the wall to rotate. After the rotation of 0.5π it has a distance comparable to its long axis $D_{\mathrm{L}}^{d}/2 \approx 0.3 D_{\mathrm{r}}$.

marginated carriers indicates that ellipsoidal carriers rotate considerably slower within the RBC-FL than spherical carriers, see Fig. 4.13. Since the velocity profile in the RBC-FL can be assumed as simple shear flow with the shear rate $\dot{\gamma}_w$, the carriers are expected to rotate with the angular velocity $\psi(t)$ predicted by Jeffery [168, 169]. For an oblate ellipsoid with the long radius $R_\mathrm{L} = D_\mathrm{L}/2$ and the short radius $R_\mathrm{S} = D_\mathrm{S}/2$, the time-dependent angular velocity is given by

$$\begin{aligned} \psi(t) &= \frac{\dot{\gamma}_w}{R_\mathrm{L}^2 + R_\mathrm{S}^2}\left((R_\mathrm{L}\cos(\chi(t)))^2 + (R_\mathrm{S}\sin(\chi(t)))^2\right), \\ \text{with} & \\ \chi(t) &= \arctan\left(\frac{R_\mathrm{L}}{R_\mathrm{S}}\tan\left(\frac{R_\mathrm{L}R_\mathrm{S}\dot{\gamma}_\mathrm{w}t}{R_\mathrm{L}^2 + R_\mathrm{S}^2}\right)\right). \end{aligned} \tag{4.2}$$

Averaging over time leads to

$$\langle\psi\rangle = \frac{\dot{\gamma}_\mathrm{w}}{\kappa + 1/\kappa}, \tag{4.3}$$

with $\kappa = R_\mathrm{L}/R_\mathrm{S}$ being the aspect ratio of major and minor axis. For all spheres $\kappa_\mathrm{s} = 1$ which implies that $\langle\psi_\mathrm{s}\rangle = \dot{\gamma}_\mathrm{w}/2$, while for the ellipsoid $\kappa_\mathrm{e} = 3.5$, and the disc $\kappa_\mathrm{d} = 7$, which results in $\langle\psi_\mathrm{e}\rangle \approx 0.26\dot{\gamma}_w$ and $\langle\psi_\mathrm{d}\rangle \approx 0.14\dot{\gamma}_w$, such that $\langle\psi_\mathrm{d}\rangle < \langle\psi_\mathrm{e}\rangle < \langle\psi_\mathrm{s}\rangle$.

The shear rate $\dot{\gamma}_w$ in the simulation has been derived from the near-wall velocity profiles in the RBC-FL in order to compare with theoretical predictions. The time-dependent angular velocity of the carriers in the simulation has been computed as an average of the angular velocity of all N_v particles (vertices) representing one carrier (see Section 3.1) with $\psi(t) = 1/N_v \sum_{i=1}^{N_v}(\mathbf{r}_i \times \mathbf{v}_i)/|\mathbf{r}_i|^2$ assuming a pure rotation around the axis perpendicular to the vector between channel center and COM of the carrier. $\psi(t)$ has been averaged over all particles and timesteps, to obtain $\langle\psi\rangle$. The results for $\langle\psi\rangle$ in Fig. 4.13 (a) for a sphere are close to the theoretical predictions (see also Fig. C.7 for other sphere sizes). The angular velocities for the ellipsoid in Fig. 4.13 (b) and the disc in Fig. 4.13 (c) are lower than the theoretical predictions. The reduced average angular velocity for the elongated shapes is due to two reasons. First, for a carrier very close to the wall the rotation is suppressed. Second, the rotation is slowed down by interactions with RBCs and the wall. This is illustrated in Fig. 4.13 (d) by a reduced peak angular velocity when the carriers' surface is close to the wall. A lower rotational velocity of a carrier leads to a longer interaction time between the carrier and a wall. Thus, adhesion of elongated carriers is expected to be more efficient than for spheres with a comparable size [158].

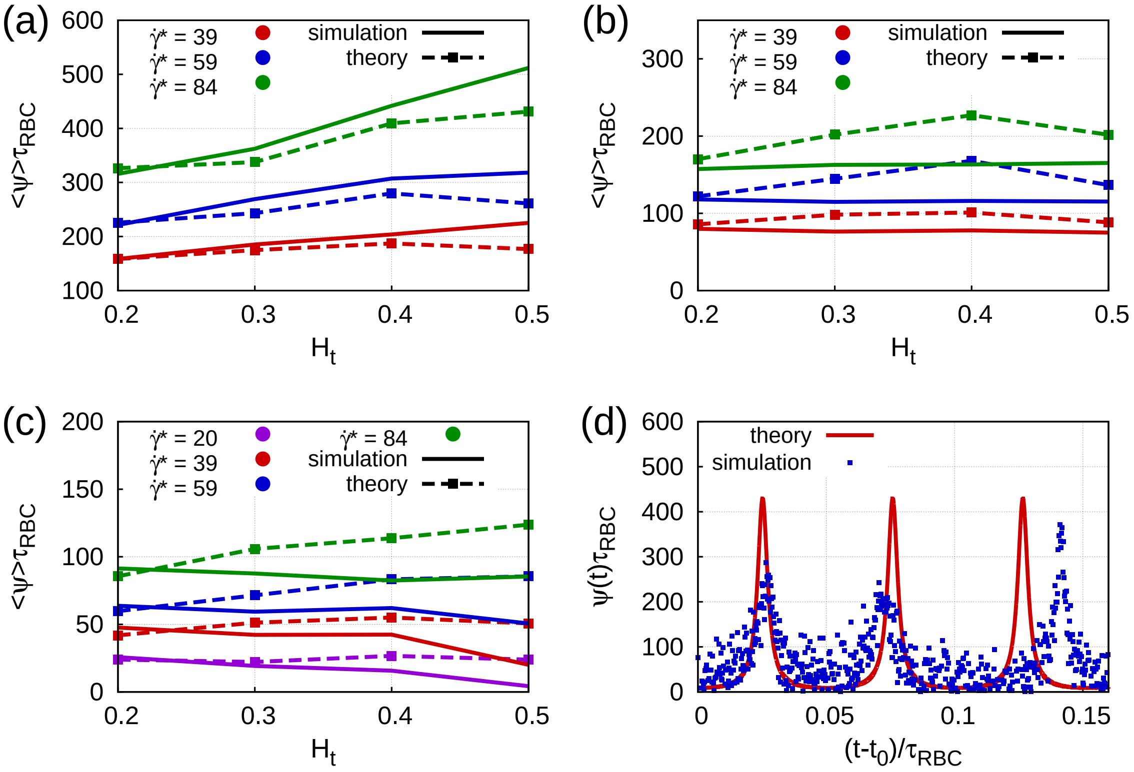

Figure 4.13.: (a-c) Average angular velocities $\langle\psi\rangle$ as given in Eq. (4.3) for (a) the sphere with $D_\mathrm{c} = 0.3D_\mathrm{r}$, (b) ellipsoid, and (c) disc. Solid curves: simulation results and dashed curves: theoretical predictions by Jeffery [168] for the near-wall shear rate estimated from simulations. (d) Time t dependent angular velocity $\psi(t)$ estimated from simulations for $H_\mathrm{t} = 0.4$ and $\dot{\gamma}^* = 39$ (blue dots) starting after the simulation time t_0 and theoretical predictions as given in Eq. (4.2) (red curve). $\langle\psi\rangle$ as well as t are normalized by the RBC relaxation time τ_RBC.
The average angular velocity for the spheres agrees well with the theoretical predictions. For both elongated shapes the angular velocity is smaller than for a sphere and when compared to the theoretical predictions. The difference increases with increasing shear rate. The reduction is due to hindered rotations close to the wall and to a reduced maximum angular velocity stemming from interactions with the RBCs and the wall.

4.1.4. Summary and Discussion

In summary, the margination efficiency of spherical as well as elongated carriers is mainly influenced by the change of the RBC-FL thickness, which is mostly induced by an increase of the hematocrit. With decreasing RBC-FL thickness, the margination efficiency increases. Nevertheless, due to changes in effective fluctuations and rotations, a change of the shear rate also affects margination. Thus, higher shear rates reduce margination.

Comparing spheres with diameters between $D_\mathrm{c} = 0.3D_\mathrm{r}$ and $D_\mathrm{c} = 0.15D_\mathrm{r}$ it is found that, the smaller carriers marginate less. The sphere with $D_\mathrm{c} = 0.3D_\mathrm{r}$, which corresponds to $D_\mathrm{c} = 2\,\mu\mathrm{m}$ shows the most efficient margination. However, for a small RBC-FL thickness, larger spheres could leave the wall due to interactions with the RBCs. This effect increases with size, since for white blood cells [125], modelled as spheres with a diameter of $D_\mathrm{c} = 1.5D_\mathrm{r}$, a strong reduction of margination at $H_\mathrm{t} = 0.5$ has been observed. The crucial factor to determine the margination efficiency seems to be the linear carrier size (diameter). The sphere with $D_\mathrm{c} = 0.15D_\mathrm{r}$ is drastically less marginated than the three larger spheres, although the volume from $D_\mathrm{c} = 0.3D_\mathrm{r}$ to $D_\mathrm{c} = 0.25D_\mathrm{r}$ is twice smaller.

The majority of elongated carriers are located at a distance from the wall comparable with their longest axis, ensuring the possibility of direct interactions with the wall for a broad range of hematocrit values. Furthermore, for a small RBC-FL thickness, where interactions with RBCs could negatively influence the position of the carriers, a considerable fraction of carriers is located at the minimal possible distance securing potential adhesion. Comparing the two investigated elongated shapes, a high aspect ratio seems to be advantageous, since the margination into the PAL is more efficient for the disc, due to the higher fraction of discs at the minimal distance to the wall. The reason is supposedly that the disc can slide easier between RBCs.

Concerning the margination probability into the potential adhesion layer (PAL), the larger sphere and the disc seem to be favourable shapes. An advantage of a sphere over a disc is that the distance of the surface is independent of the orientation. The sphere surface is always close to the wall when it is located in the PAL, whereas discs surface is only close to the wall in a specific time window during rotation. However, compared to a sphere, elongated shapes rotate slower. The rotations are even reduced compared to the theoretical predictions for free shear flow, due to interactions with the wall and the RBCs. Furthermore, the localisation of both elongated carriers seems to be less influenced by changes in shear rate than for spheres. Additionally, for high shear rates and low hematocrit values the disc is more beneficially distributed than the sphere.

Besides, a larger distance to the wall might be favourable under realistic conditions in blood vessels; for instance, carriers may become departed from the wall due to different reasons, such as bifurcations or marginated white blood cells that are in the way. It is likely that a departed disc returns faster to the for adhesion required distance to the wall, since its long axis is larger than for spheres with the same volume and it can slide between the RBCs more easily.

The presented simulation results are in good qualitative agreement with several experimental observations [49, 51, 52, 126, 128, 170]. For example, margination of micro-particles has been observed to be more efficient than that of nano-particles in recent *in vivo* experiments [49, 170]. However, it has to be emphasized that margination in experiments is mainly measured in terms of efficient adhesion. Recent theoretical [53, 54] and experimental [51, 52] studies suggest that ellipsoidal particles possess better adhesion properties than spheres due to a larger contact area for adhesion interactions. Even though margination is a necessary pre-condition for carrier adhesion to vessel walls, carrier margination and adhesion are not equivalent, since carrier adhesion may also depend on other factors (e.g., specific targets, the receptor/ligand density and distribution). It is also interesting to consider the drag force on an ellipsoid or sphere in shear flow near a wall. In case of an ellipsoid close and parallel to a wall, the drag force is found to be smaller than that on a sphere with the same volume, which was estimated in separate simulations of a sphere and an ellipsoid in shear flow with fixed position. Thus, adhered ellipsoidal particles experience a lower drag force due to fluid flow than the corresponding spheres with the same volume [158].

The current knowledge about adhesion of ellipsoidal particles and the presented simulation results on margination give an idea why non-activated platelets have a disc like shape. Similar to platelets, an elongated disc-like shape seems to be favourable for therapeutic agents as well. However, a further requirement for efficient drug delivery includes particle transport through vessel walls, interstitial space, and cell membranes. For instance, particle internalization by endothelial cells and intracellular trafficking is more efficient for spherical sub-micron particles, rather than for micron-size carriers with an ellipsoidal shape [40].

As a consequence, the concept of multi-stage drug delivery [6, 36], where a larger micro-particle incorporates a number of small nano-carriers, seems to be very promising. In this way, margination and carrier delivery or adhesion to a specific target within the microvasculature could be achieved using micro-particles, which would then be followed by the release of nano-particles into the tissue [158].

4.2. Simulations of carriers in two-dimensional model systems

Two-dimensional (2D) simulations with adequate statistics consume less computational time and hence costs than 3D simulations. For extensive studies, it is beneficial to first perform 2D simulations to narrow the parameter range down to the most interesting one. In order to trust 2D results with respect to the prediction of properties in 3D, it has to be checked for some example cases that 2D simulations provide the correct qualitative description or to recognize possible discrepancies. Therefore, in this chapter results of 2D and 3D simulations are compared. In addition, 2D simulation results for additional carrier sizes and deformabilities are discussed.

4.2.1. Comparison of 2D and 3D simulations

The considered 2D shapes, namely circles and an ellipse, have similar diameters as the spheres and the disc in 3D. The RBC diameter in 2D is defined as $D_\mathrm{r} = L_0/\pi$, with L_0 being the RBC contour length. The RBC diameter in 2D is taken to have a value of $D_\mathrm{r} = 6.1\,\mu\mathrm{m}$. The 2D RBCs are simulated according to the model described in Section 3.1.3 and the model parameters are given in Table B.2 of Appendix B. The shear rate $\dot{\gamma}^*$ is calculated as in Eq. (3.17), with respect to the 2D fluid parameters, provided in Table B.5. The carriers comprise of a number of connected particles as the RBCs, which are constrained to maintain a rigid configuration. Information about the number of particles per carrier and the number of carriers in several simulations is given in Table C.3.

As described in Section 3.3.2, in 2D a slit geometry, as shown in Fig. 4.14, is used while in 3D a cylindrical channel is employed. The width W of the 2D channel and the diameter of the cylinder are equal. Additionally to the interactions with the walls described in Section 2.4, the carriers experience a repulsive interaction with the channel walls, which is implemented through the repulsive part of the Lennard-Jones (LJ)-9-3 potential,

$$U_\mathrm{LJ93}(r) = \epsilon \left[\frac{2}{15} \left(\frac{\sigma_\mathrm{LJ}}{r} \right)^9 - \left(\frac{\sigma_\mathrm{LJ}}{r} \right)^3 \right] \quad \text{for} \quad r < r_m, \tag{4.4}$$

where r is the distance, r_m is the distance at which the potential reaches its minimum, σ_LJ is the range, and ϵ is the strength. This potential is derived by integrating the LJ-12-6 potential in Eq. (3.15) over a 3D half-space [171, 172]. The LJ-9-3 potential is softer then the usual LJ-12-6 potential. The minimum of this potential is at a particle distance of $r_m = (6/15)^{1/6}\sigma_{\mathrm{LJ}}$. Accordingly, this repulsion has to be taken into account for the calculation of the margination into a region of thickness δ' by $\delta = \delta' + r_m$. Here, r_m has been chosen for simplicity as an effective diameter of the carriers. However, for a more accurate, but also more difficult determination of an effective hard sphere diameter of particles interacting by a LJ-9-3 potential for instance the Barker-Henderson equation [173] or the method of Andersen, Weeks, and Chandler [172, 174] could be used. Due to the symmetry of the 2D system, the COM distributions are averaged over the half width of the channel. Consequently, the margination probability p_δ is calculated similar to 3D, as $p_\delta = 2\int_0^\delta P_{\mathrm{COM}}(y)dy$.

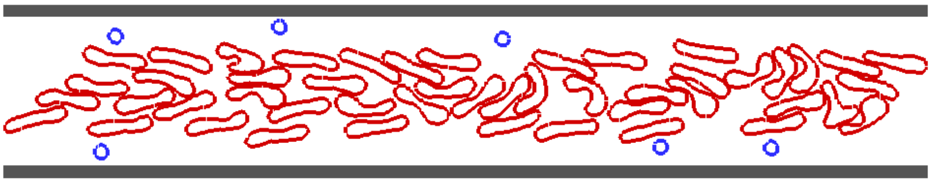

Figure 4.14.: Snapshot of a 2D simulation for $H_{\mathrm{t}} = 0.3$, $\dot{\gamma}^* = 29.3$, and a carrier with the diameter $D_{\mathrm{c}} = 0.3D_{\mathrm{r}}$. RBCs are coloured in red and carriers in blue.

Margination diagrams

Figure 4.15 presents the 2D margination probability diagrams for the margination into the RBC-FL and PAL. The considered circle diameters are $D_{\mathrm{c}} \in \{0.3, 0.22, 0.15\}D_{\mathrm{r}}$, and the ellipse has a long axis diameter of $D_{\mathrm{L}} = 0.63D_{\mathrm{r}}$ and a short axis diameter of $D_{\mathrm{S}} = 0.09D_{\mathrm{r}}$. Thus, the ellipse and the sphere with $D_{\mathrm{c}} = 0.22D_{\mathrm{r}}$ enclose a similar area. As in 3D, the margination probability increases with increasing hematocrit, independent of the considered margination layers. No reduction of margination into the RBC-FL for high hematocrit values is observed, except for the ellipse (see Fig. 4.15 (d)). An initial increase of margination is observed for increasing shear rate. Especially Fig. 4.15 (a) shows that for very low shear rates no adequate margination is observed. However, the shear-rate dependence of the margination into the RBC-FL is less pronounced than in 3D. The probability of margination into the PAL is reduced with increasing shear rate as in 3D. Similar to 3D simulations, a decrease of margination is found for decreasing carrier size, for both choices of margination layer. The margination into the RBC-FL for the ellipse (Fig. 4.15 (d)) is clearly reduced compared to a circle with the same area (Fig. 4.15 (b)). Nevertheless, in 3D the deviation of margination for a sphere and a disc is more distinct. The probability of margination into the PAL for the ellipse, again computed based on its long axis, is even larger than for the circle with a similar area.

The qualitative comparison of margination diagrams implies a good agreement of 2D and 3D simulations. This applies to the shear rate, hematocrit, and size dependence of margination. Furthermore, the comparison of diagrams indicates that roughly $\dot{\gamma}^*_{\mathrm{3D}} \approx 1.2\dot{\gamma}^*_{\mathrm{2D}}$ [158]. However, small differences are observed, particularly for the carriers with an elongated shape. Therefore, the COM distribution characteristics are compared in more detail, first for the RBCs and than for the carriers to better understand those differences.

2D RBC-free-layer

In 2D, the given hematocrit values correspond to the area fraction of RBCs, while H_{t} in 3D corresponds to the volume fraction. Figure 4.16 presents the RBC-FL thickness $\Delta_{\mathrm{RBC-FL}}$ for 2D and 3D depending on the H_{t} value. For the same hematocrit value the RBC-FL thickness is smaller in 3D than in 2D. After shifting the 2D curves by $H^s_{\mathrm{t}} \approx 1.7$ they overlap with the 3D curves. This is due to the cylindrical curvature of the 3D geometry which makes the close-packing of the RBCs less efficient. This observation explains the higher probabilities for the margination into the RBC-FL for high hematocrit values in 2D, since the RBC-FL thickness is larger than the considered carrier sizes. In the previous chapter, it has been shown that the RBC-FL thickness has a strong influence on the carrier distribution. Consequently, the distribution characteristics have to be compared for the same RBC-FL thickness $\Delta_{\mathrm{RBC-FL}}$, in order to relate 2D and 3D simulation results.

Carrier distribution characteristics

The distance of the peak of the COM distribution to the wall, Δ_{MAX}, and the mean position in the whole channel, $\Delta_{\langle \mathrm{r} \rangle}$, for 2D and 3D simulations with $\dot{\gamma}^*_{2D} = 29.7$ and $\dot{\gamma}^*_{\mathrm{3D}} = 59$, respectively, are presented in Figs. 4.17 (a) and (b) (for other shear rates see Fig. C.8). These measurements corroborate that 2D and 3D COM distributions possess similar characteristics. Some differences are mainly observed for the small carriers (green curves). In 2D a smaller RBC-FL thickness is required for the peak maximum to reach the minimal distance, a distance corresponding to the radius of the carrier. On the contrary, the 2D carriers are on average located closer to the wall, than in 3D. Additionally, the carriers with $D_{\mathrm{c}} = 0.3D_{\mathrm{r}}$ remain close to the wall in 2D, while the

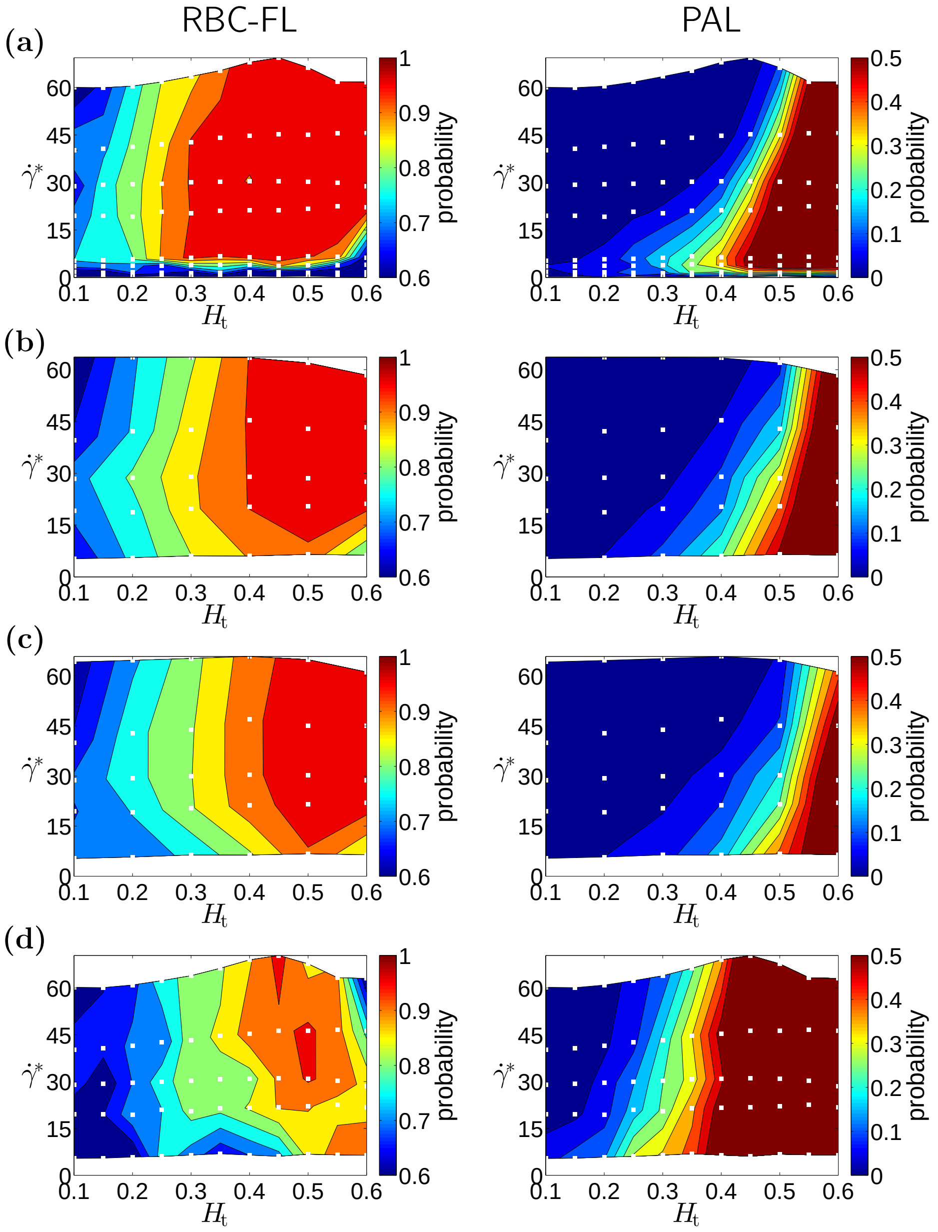

Figure 4.15.: Margination probability combined for different hematocrit H_t and shear rates $\dot{\gamma}^*$. The diagrams correspond to the margination into the RBC-FL (left column) and the PAL (right column). The considered carriers are circles with the diameters of (a) $D_\mathrm{c} = 0.3D_\mathrm{r}$, (b) $D_\mathrm{c} = 0.22D_\mathrm{r}$, (c) $D_\mathrm{c} = 0.15D_\mathrm{r}$, and (d) an ellipse with the long and short diameter of $D_\mathrm{L} = 0.63D_\mathrm{r}$ and $D_\mathrm{S} = 0.09D_\mathrm{r}$, respectively. The white squares (□) indicate the values of H_t and $\dot{\gamma}^*$ for which simulations have been performed. The colour code ranges from blue (low probability) to red (high probability).

The margination diagrams show qualitatively a similar dependence on H_t, $\dot{\gamma}^*$, and carrier size and shape as in 3D. The main difference is the more pronounced margination into both choices of margination layer for the ellipse. Especially the margination into the PAL is even larger for the ellipse compared to the sphere with the same enclosed area $D_\mathrm{c} = 0.22D_\mathrm{r}$.

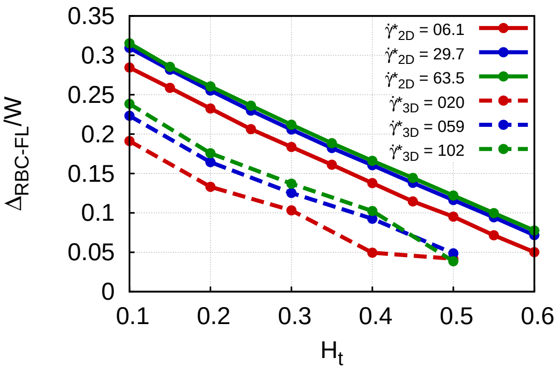

Figure 4.16.: Comparison of the RBC-FL thickness $\Delta_{\mathrm{RBC-FL}}$ normalized by the channel diameter/width W depending on the hematocrit H_{t} for 2D (solid curves) and 3D (dashed curves) simulations. The curve colours correspond to the shear rates, $\dot{\gamma}^*_{2D} = 6.1$ (red), $\dot{\gamma}^*_{2D} = 29.7$ (blue), $\dot{\gamma}^*_{2D} = 63.5$ (green), $\dot{\gamma}^*_{3D} = 20$ (red), $\dot{\gamma}^*_{3D} = 59$ (blue), and $\dot{\gamma}^*_{3D} = 102$ (green).
At the same H_{t} value the RBC-FL thickness in 3D is smaller than in 2D due to a less efficient packing of RBCs in the 3D cylindrical geometry.

carriers depart from the wall in 3D. On the one hand, it is easier for the small spheres to fit between the RBCs in 3D, due to a looser packing of the RBCs; on the other hand the looser packing supposedly increases the interactions with the RBCs close to the RBC-FL. Even though the small carriers, which are located in the RBC-FL, are more effectively pushed to the wall, the larger carriers depart from the wall for high hematocrit values.

The different packing of RBCs also leads to a distinct distribution of the discs in 2D and 3D. For 2D simulations no clear coexistence of two peaks can be identified, and instead, the one peak is approaching the wall with decreasing RBC-FL as presented in Fig. 4.17 (c). Accordingly, the full mean position in 2D is considerably closer to the wall, see Fig. 4.17 (d), which leads to the increased probability of margination into the RBC-FL as well as into the PAL. For some shear rates and hematocrit values, long tails of the distribution, either to closer distances to the wall or into the bulk are observed (see Fig. 4.18). These curves are similar to those distributions in 3D when the second peak develops or the first peak almost vanishes. In 3D, the discs can more easily slide between the RBCs, and may stay even at a distance which is outside of the RBC-FL. In 2D, the discs are more hindered by the RBCs. Therefore, they are pushed more to the wall after a rotation, leading to one distinct peak which approaches the wall.

In conclusion, 2D margination simulations are able to properly capture carrier margination in blood flow. Differences, that are observed by comparing the COM distributions,

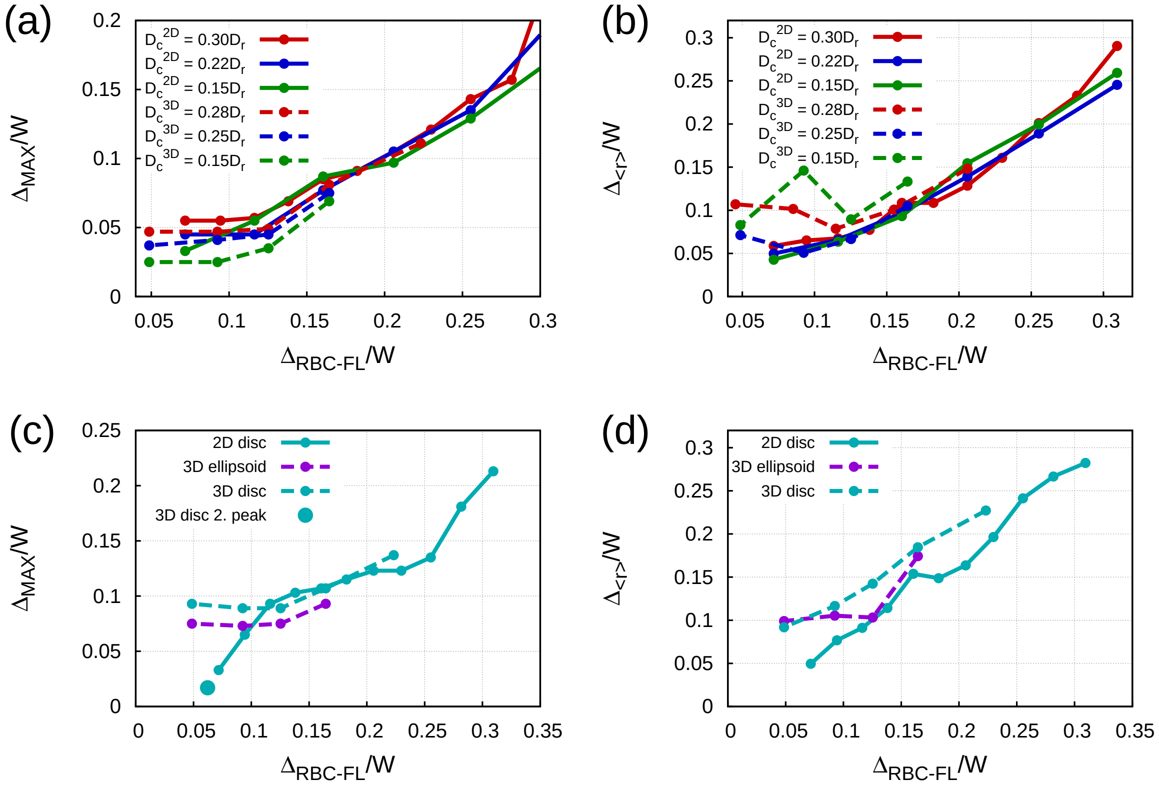

Figure 4.17.: Comparison of carrier distribution characteristics in 2D and 3D. (a) Distance Δ_{MAX} of the peak of the COM distribution and (b) the distance $\Delta_{<r>}$ of the mean position in the whole channel to the wall normalized by the channel width/diameter W for round carriers. In 2D, the examined carrier sizes are $D_{\mathrm{c}}^{2\mathrm{D}} = 0.3D_{\mathrm{r}}^{2\mathrm{D}}$ (red), $D_{\mathrm{c}}^{2\mathrm{D}} = 0.22D_{\mathrm{r}}^{2\mathrm{D}}$ (blue), and $D_{\mathrm{c}}^{2\mathrm{D}} = 0.15D_{\mathrm{r}}^{2\mathrm{D}}$ (green), while in 3D, $D_{\mathrm{c}}^{3\mathrm{D}} = 0.28D_{\mathrm{r}}^{3\mathrm{D}}$ (red), $D_{\mathrm{c}}^{3\mathrm{D}} = 0.25D_{\mathrm{r}}^{3\mathrm{D}}$ (blue), and $D_{\mathrm{c}}^{3\mathrm{D}} = 0.15D_{\mathrm{r}}^{3\mathrm{D}}$ (green). (c) Distance Δ_{MAX} of the peak of the COM distribution and (b) the distance $\Delta_{<r>}$ of the mean position in the whole channel to the wall for ellipse (purple) and disc (cyan). The different curves correspond to 2D (solid) and 3D (dashed) simulations. The considered shear rates are $\dot{\gamma}^*_{2\mathrm{D}} = 29.7$ for 2D and $\dot{\gamma}^*_{3\mathrm{D}} = 59$ for 3D.

The carrier distribution characteristics of 2D and 3D simulations are rather similar. However, for the round carriers, some deviations are observed for small carriers. For elongated shapes, in 3D a second peak occurs, whereas in 2D the peak approaches the wall. All observations can be explained by the looser packing of the RBCs in 3D.

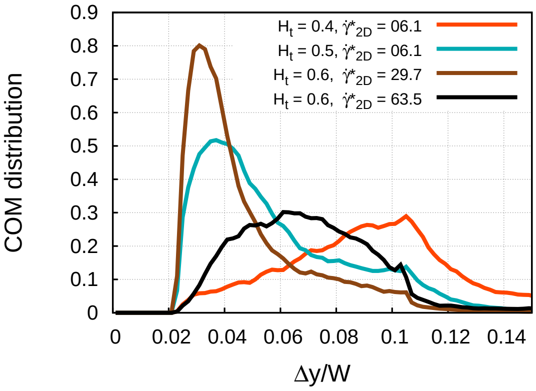

Figure 4.18.: COM distributions depending on the COM distance Δy to the wall normalized by the channel width W. The different curves correspond to different combinations of hematocrit H_t and shear rate $\dot{\gamma}^*$.
The presented distributions are the distributions which are closest to exhibit two peaks.

correspond to the different packing of RBCs in 2D and 3D simulations.

4.2.2. Complementary 2D simulations

The margination probability of two additional sizes of circles is investigated; smaller and larger than the already considered ones. Furthermore, the influence of deformability of the carrier on the margination is examined.

Large and nano carriers

The largest considered carrier has a diameter of $D_\mathrm{c} = 0.6D_\mathrm{r}$ and the nano-carrier a diameter of $D_\mathrm{c} = 0.04D_\mathrm{r}$. In order to simulate such a small carriers, they have been modelled as single particles with a LJ-6-12 repulsion with the range $\sigma_\mathrm{LJ} = D_\mathrm{c}$ (see Eq. (3.15)) from each other and from the vertices, which model the RBCs.

Figure 4.19 presents the probability of margination into the RBC-FL and the PAL for these two carrier sizes. A low margination probability is found for both choices of margination layer for the nano-carrier. Nonetheless, an increase of margination with increasing hematocrit is detected. The margination is reduced at high hematocrit values for the large carrier, because its radius is larger than the RBC-FL thickness. The probability of margination into the PAL is high for a broad range of hematocrit values.

Additionally, Fig. 4.20 (a) demonstrates that the PAL margination probability p_PAL for the large carrier either remains similar for a thin RBC-FL or even decreases ($\dot{\gamma}^* = 6.1$). This shows that the carrier moves away from the wall through interactions with RBCs

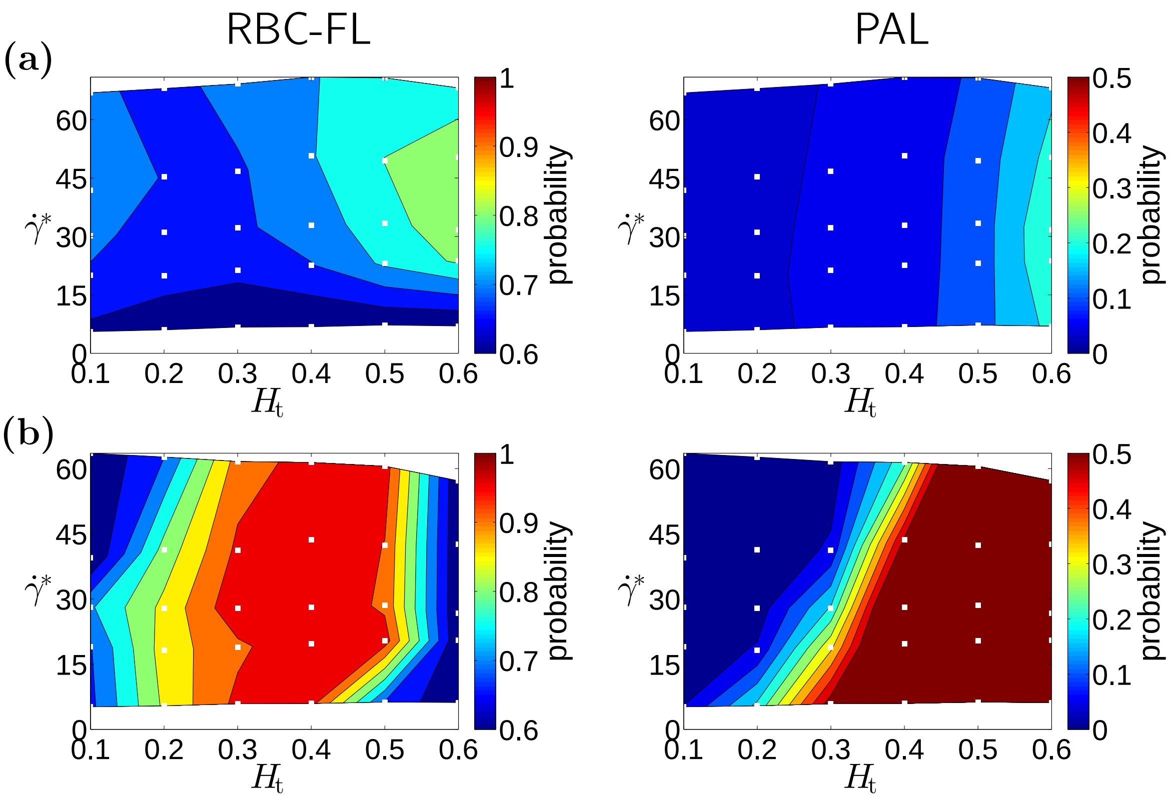

Figure 4.19.: Margination probability diagrams for the RBC-FL (left) and the PAL (right) for different spherical carriers with the diameters $D_\mathrm{c} = 0.04D_\mathrm{r}$ (a) and $D_\mathrm{c} = 0.6D_\mathrm{r}$ (b). The white squares (□) indicate the values of H_t and $\dot{\gamma}^*$ for which simulations have been performed. The colour code ranges from blue (low probability) to red (high probability).
The nano-carrier possesses a low margination for both choices of margination layer. The carrier with $D_\mathrm{c} = 0.6D_\mathrm{r}$ shows a reduced margination into the RBC-FL compared to a carrier with $D_\mathrm{c} = 0.3D_\mathrm{r}$ for the high hematocrit values. However, the large carrier shows a strong margination into the PAL.

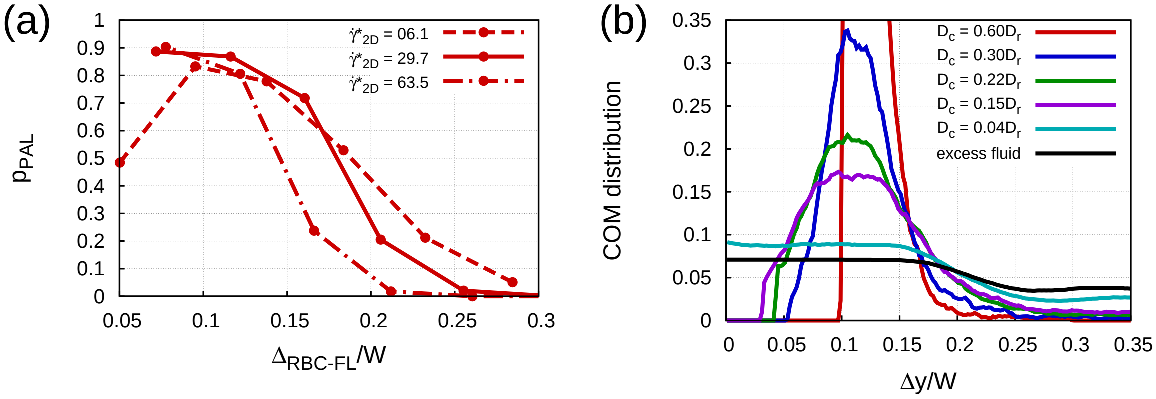

Figure 4.20.: Distributions of different sized 2D carriers. (a) Margination probability p_{PAL} into the PAL for the carrier with size $D_{\mathrm{c}} = 0.6D_{\mathrm{r}}$ depending on the RBC-FL thickness $\Delta_{\mathrm{RBC-FL}}$ normalized by the channel width W for three shear rates $\dot{\gamma}^* = 6.1$ (dashed curve), $\dot{\gamma}^* = 29.7$ (solid curve), and $\dot{\gamma}^* = 63.5$ (dot-dashed curve). (b) COM distributions depending on the COM distance Δy to the wall for different carrier sizes, that can be distinguished by different colours. The considered hematocrit is $H_{\mathrm{t}} = 0.4$ and the shear rate is $\dot{\gamma}^* = 29.7$

For small $\Delta_{\mathrm{RBC-FL}}$ a decrease or no further increase of p_{PAL} is observed for the large carrier. The nano-carrier is distributed similar to the excess fluid volume. The smaller the carrier, the broader and flatter the COM distribution in the RBC-FL becomes.

due to its large size. In 3D, the influence of RBCs on the carriers is stronger, due to the cylindrical curvature of the channel. Thus, the carrier would be even more displaced from the wall. Figure 4.20 (b) presents COM probability distributions for different sizes of circular carriers depending on the COM distance Δy to the wall. With decreasing size the distributions become broader and flatter, because the RBC-FL is effectively larger, leading to a decreased number of carriers close to the wall. In particular, the distribution of the nano-carrier is flat with no distinct peaks in the RBC-FL.

From simulation snapshots the distribution of the excess fluid volume of flowing RBCs has been computed. It characterizes the plasma distribution in the channel, which can be inferred from the RBC density distribution. Interestingly, the nano-carrier distribution is very similar to the excess fluid volume. The carrier distribution is slightly higher in the RBC-FL and accordingly lower in the channel center, due to the excluded volume interactions between nano-carriers and RBCs. Especially for high hematocrit values the effect of the excluded volume becomes stronger which leads to 84% margination for $H_{\mathrm{t}} = 0.5$. The further reduced margination into the PAL is due to the small diameter of the nano-carrier.

Soft carriers

Platelets are known to be more rigid than RBCs [8,14]. However, several proposed therapeutic agents are considerably less rigid, such as polymer conjugates and liposomes [42]. As discussed in Chapters 1 and 3, the deformability of RBCs is one reason for the hydrodynamic lift from the wall. Hence, it is interesting to investigate the influence of the hydrodynamic lift on the margination of a soft carrier. Thus, a soft circle with $D_\mathrm{c} = 0.3D_\mathrm{r}$ has been modelled by a number of particles connected by springs as described in Section 3.1.3 and parameters for the springs, area and bending constraint coefficients are exactly the same as for RBCs given in Table B.2.

Figure 4.21 presents the margination diagrams for the RBC-FL and the PAL for soft carriers compared to the rigid one. The margination probabilities for both choices of margination layer are slightly reduced for the soft carrier. However, for low shear rates the margination into the PAL is slightly better for the soft carrier.

The peak position (see Fig. 4.22 (a)) of the rigid carrier is closer to the wall for the majority of cases and reaches the minimum possible distance for a lower RBC-FL thickness $\Delta_\mathrm{RBC-FL}$. However, for low shear rates and small RBC-FL thicknesses, when the minimal distance is reached, the soft carrier deforms and comes closer to the wall than the rigid one. Accordingly, the margination into the PAL is reduced for the soft carrier as long as it is not compressed to the wall, see Fig. 4.22 (b). Thus, this deformable carrier is subject to a hydrodynamic repulsion from the wall as the RBCs. In contrast to the RBCs, the carriers have originally a circular shape and are subject to less interactions with other blood components, which reduces the strength of the deformations. As discussed in Section 1.4 the suggested size dependence of the lift force in 2D is $F_\mathrm{L} \sim D_c^{1/2}$. Thus, the lift force is expected to be reduced for the smaller carriers compared to the RBCs and margination still occurs. However, the margination of even more flexible particles, such as polymers, is discussed in Chapter 5.

4.2.3. Summary

The comparison of carrier margination in 2D and 3D simulations shows that the dependence of margination on hematocrit, shear rate, carrier size, and carrier shape is qualitatively similar. Even COM distribution characteristics for circles and spheres are comparable. Slight discrepancies are caused by the different packing of RBCs in 2D and 3D. The different packing leads to a smaller RBC-FL thickness in 3D compared to 2D for the same hematocrit. Therefore, the properties have to be compared for the same

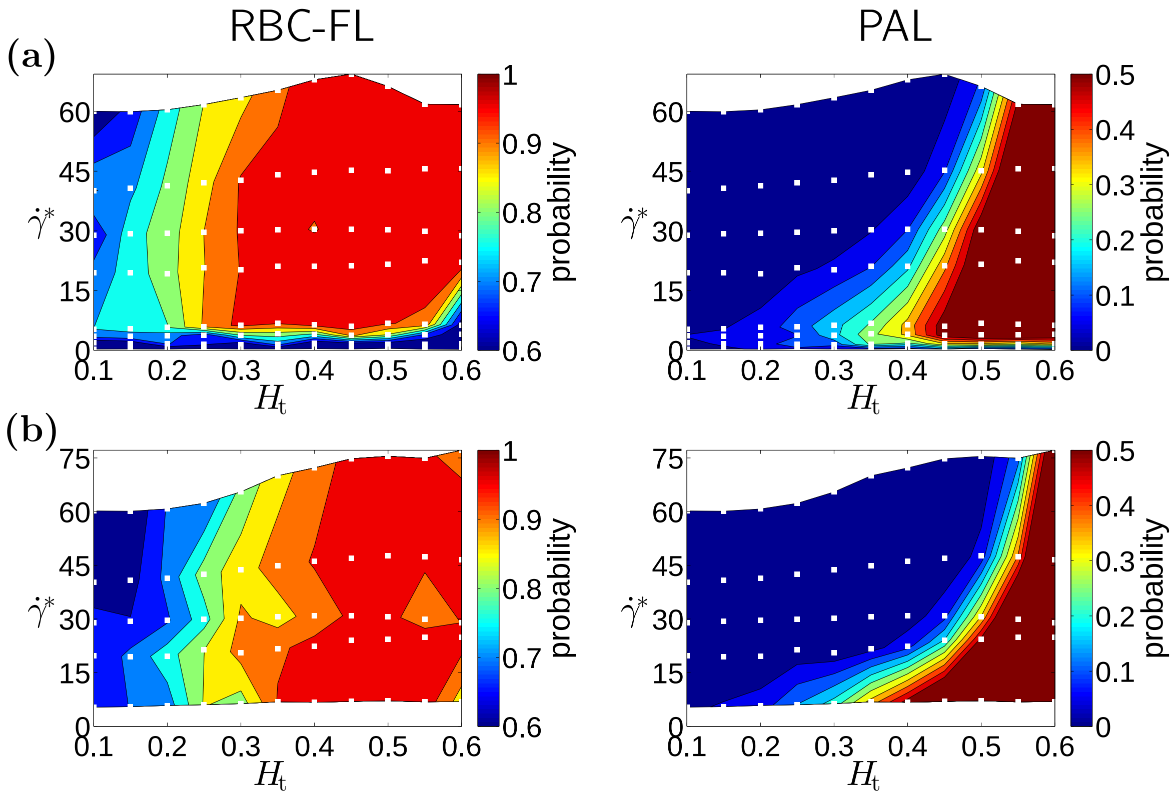

Figure 4.21.: Margination probability diagrams for the RBC-FL (left column) and PAL (right column). The circle with $D_\mathrm{c} = 0.3 D_\mathrm{r}$ is constrained to (a) a rigid configuration or (b) is deformable as a RBC. The white squares (□) indicate the values of H_t and $\dot{\gamma}^*$ for which simulations have been performed. The colour code ranges from blue (low probability) to red (high probability).
For both choices of margination layer the deformable carrier marginates less than the rigid one, due to a hydrodynamic repulsion from the wall.

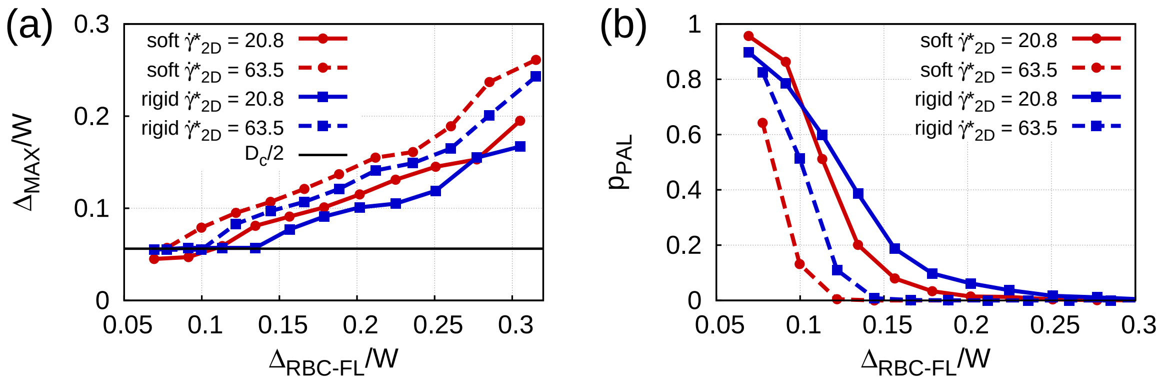

Figure 4.22.: 2D distribution characteristics for a deformable carrier. (a) Distance Δ_{MAX} of the peak of the COM distribution from the wall and (b) probability p_{PAL} of margination into the PAL depending on the RBC-FL thickness $\Delta_{\mathrm{RBC-FL}}$, scaled by the channel width W; comparison of a deformable carrier (red circles) and a rigid carrier (blue squares), both with the diameter $D_{\mathrm{c}} = 0.3D_{\mathrm{r}}$. Considered are two shear rates, namely $\dot{\gamma}^* = 20.8$ (solid curves) and $\dot{\gamma}^* = 63.5$ (dashed curves).
The peak for the soft carrier is further away from the wall. Only for a thin RBC-FL and a low shear rate the soft carrier deforms and is thus closer to the wall. Accordingly, the margination into the PAL is lower for the soft carrier as long as it is not deformed.

RBC-FL thickness rather than the same hematocrit. Furthermore, small carriers as well as elongated carriers can slide less easily among RBCs in 2D than in 3D, leading to a decreased average distance to the wall, whereas interactions of carriers in the RBC-FL with RBCs are less strong. Additionally, in 2D elongated carriers do not distribute at two distinct distances from the wall, but move continuously closer to the wall with decreasing RBC-FL thickness. Apart from these differences, 2D simulations capture the carrier margination properly.

Further 2D simulations indicate that carriers with a size of a few nanometres are distributed similar to the excess fluid volume and thus do not possess a significant margination. However, for carriers with a diameter larger than 3 µm to 4 µm an increased departure from the wall at high hematocrit values is expected, due to interactions with the RBCs.

Furthermore, deformable carriers are subject to a hydrodynamic lift forces and repulsion from the wall. Hence they are less marginated than rigid carriers of the same size. Additionally, in 3D a further decrease of margination for deformable carriers is likely, since the looser packing of RBCs in 3D might enable the deformable carrier to squeeze between the RBCs more easily.

4.3. Channel-size dependence

In addition to the channel size of $W = 3.28D_\mathrm{r}$ considered so far, in this section, channels with double and half the previous width are investigated, shown in Fig. 4.23, to ascertain that the observed dependencies of margination on hematocrit, shear rate, and carrier size are a general feature. Furthermore, according to the decrease of the RBC density with decreasing channel size, called Fåhræus-effect [175], the dependence of carrier (platelet) density on the channel size, hematocrit, and carrier size is also examined.

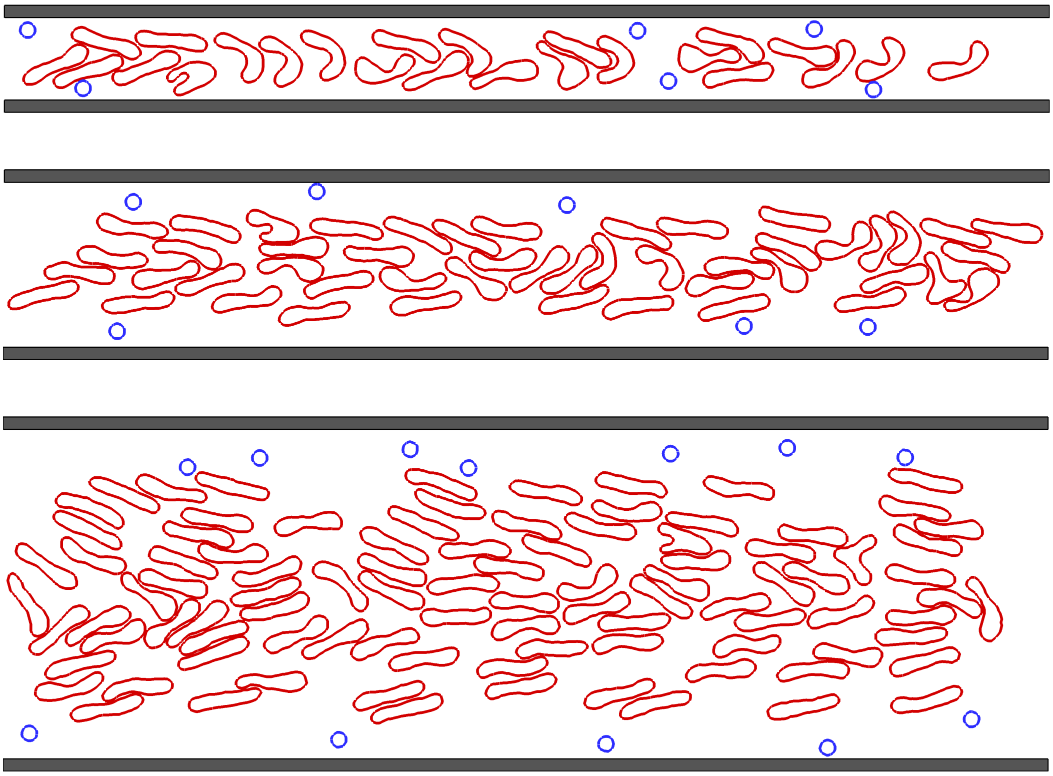

Figure 4.23.: Snapshots for different channel sizes with different widths W: (top) $W = 1.64D_\mathrm{r}$, (middle) $W = 3.28D_\mathrm{r}$, and (bottom) $W = 6.56D_\mathrm{r}$. All snapshots correspond to the hematocrit $H_\mathrm{t} = 0.3$, the shear rate $\dot{\gamma}^* \approx 29.7$, and carriers with the size $D_\mathrm{c} = 0.3D_\mathrm{r}$. The RBCs are coloured in red and carriers in blue.

4.3.1. Margination

The comparison of margination diagrams for all three channel sizes for carriers with $D_\mathrm{c} = 0.3D_\mathrm{r}$, see Fig. 4.24, indicates that the dependence of margination on hematocrit and shear rate remains similar for different channel sizes. Figure 4.25, presenting the margination diagrams for the carrier with $D_\mathrm{c} = 0.15D_\mathrm{r}$, supports this proposition. Additionally, a reduction of margination for both choices of margination layer is observed for the smaller carriers for all three channel sizes.

Although the hematocrit, shear-rate, and carrier-size dependence is similar in all channels, differences in margination efficiency are observed. The margination into the RBC-FL is reduced for both, the smaller channel and the bigger channel compared to the channel with $W = 3.28D_\mathrm{r}$. On the other hand, the margination into the PAL is the highest for $W = 1.63D_\mathrm{r}$ and decreases with increasing channel size.

The reduced margination at low hematocrit values for $W = 1.64D_\mathrm{r}$ is due to the RBC distribution. For these low hematocrit values and the considered shear rates, the RBCs are localized in the middle of the channel, their small axis is aligned with the flow, and they have a parachute shape as presented in Fig. 4.26. This alignment and shape of RBCs has been also observed experimentally [176] and numerically in 3D simulations [113, 177]. The carriers are almost uniformly distributed with a slight peak close to the wall, due to the absence of the alignment of RBCs that constitutes a barrier for the carriers.

The decrease of margination into the RBC-FL at high hematocrit values is due to the reduced RBC-FL thickness for the smaller channel, displayed in Fig. 4.27 (a). For high hematocrit values the RBC-FL thickness is comparable to or smaller than the carrier size. The small RBC-FL thickness is also the reason for the low margination at the lowest shear rate.

The reduction of margination into the RBC-FL for the channel with $W = 6.56D_\mathrm{r}$ is related to the distribution of the RBCs, as well. With increasing channel size, the RBC-FL thickness increases, as shown in Fig. 4.27 (a). However, the RBC-FL thickness does not change linearly with the channel diameter, it increases less strong. Hence, the RBCs occupy a larger percentage of the channel. This is confirmed by the RBC COM distributions at $H_\mathrm{t} = 0.4$ and $\dot{\gamma}^* = 63.5$ for all channel sizes in Fig. 4.27 (b). Thus, for the wide channel, the RBC density is reduced. This facilitates the movement of carriers between the RBCs, especially for low hematocrit values and small carrier sizes. A detailed comparison of the probability of margination into the RBC-FL for different channel sizes and the carrier size $D_\mathrm{c} = 0.3D_\mathrm{r}$, presented in Fig. 4.28 (a), illustrates that the probabilities for the channels widths $W = 3.28D_\mathrm{r}$ and $W = 6.56D_\mathrm{r}$ are very similar. However, the probability is indeed lower for the carrier with size $D_\mathrm{c} = 0.15D_\mathrm{r}$ in the channel with $W = 6.56D_\mathrm{r}$ at low hematocrit values, see Fig. C.9 (a). At intermediate hematocrit values all probabilities are similar.

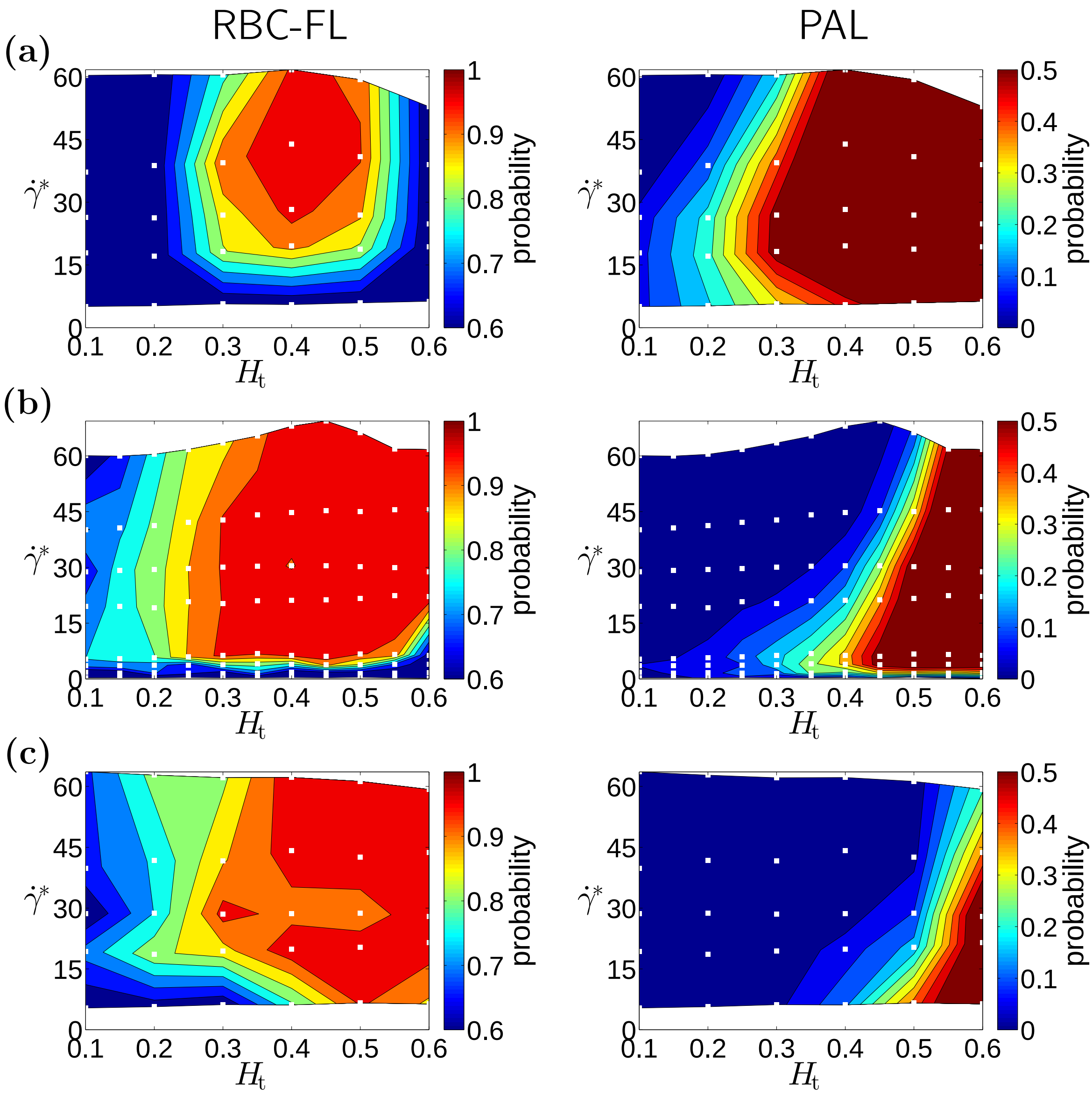

Figure 4.24.: Margination probabilities for different hematocrit H_t and shear rates $\dot{\gamma}^*$ for carrier with the diameter $D_\mathrm{c} = 0.3D_\mathrm{r}$. The diagrams correspond to the margination into the RBC-FL (left column) and the PAL (right column), for three channel sizes. The considered channel widths are (a) $W = 1.64D_\mathrm{r}$, (b) $W = 3.28D_\mathrm{r}$, and (c) $W = 6.56D_\mathrm{r}$. The white squares (□) indicate the values of H_t and $\dot{\gamma}^*$ for which simulations have been performed. The colour code ranges from blue (low probability) to red (high probability) and is acquired via interpolation.
The same dependence of margination on H_t and $\dot{\gamma}^*$ is observed for all channel sizes. The margination into the RBC-FL is reduced for $W = 1.64D_\mathrm{r}$ as well as for $W = 6.56D_\mathrm{r}$ compared to $W = 3.28D_\mathrm{r}$. The margination into the PAL is highest for the smallest channel and decreases with increasing channel size.

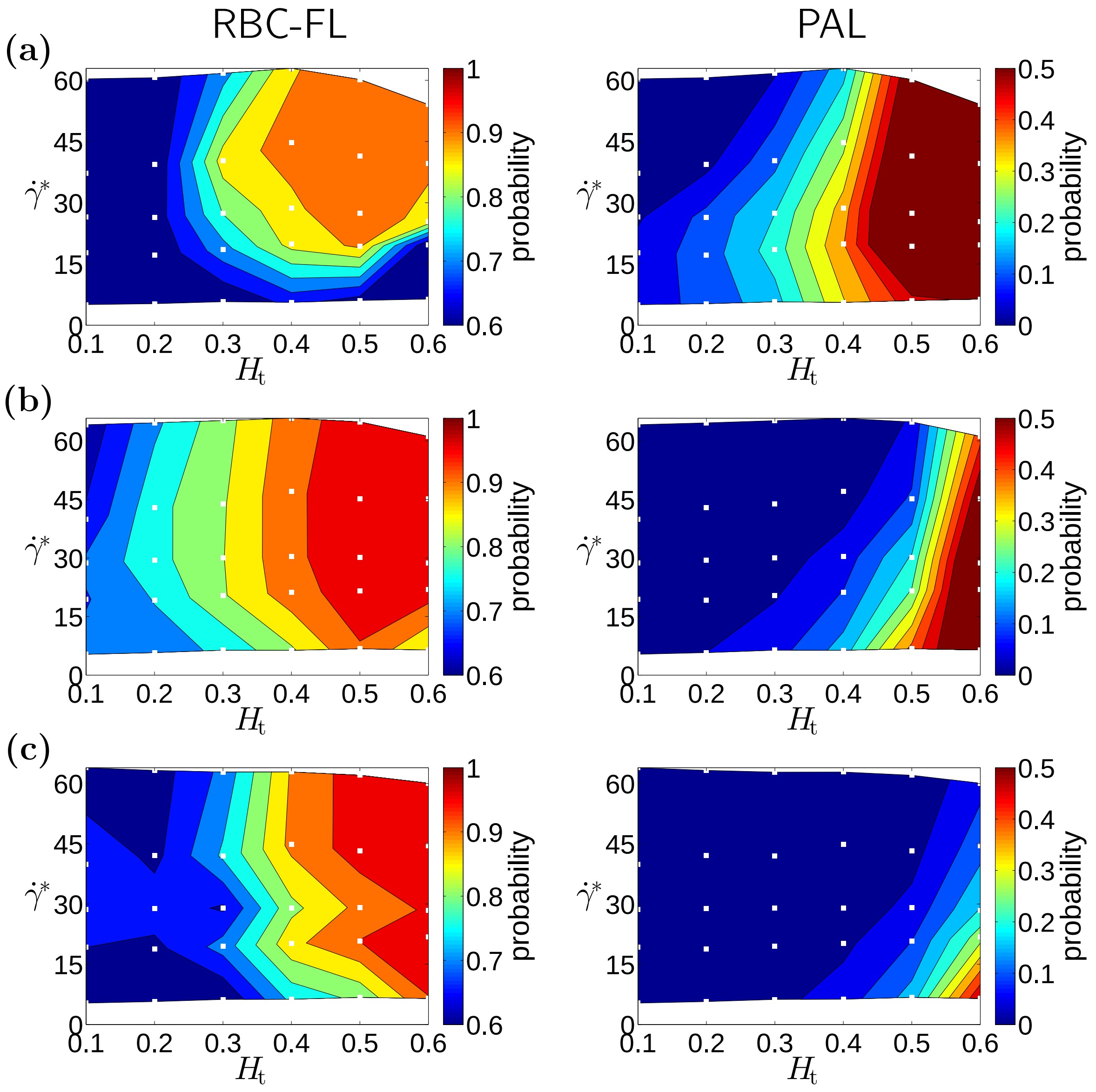

Figure 4.25.: Margination probabilities for different hematocrit H_t and shear rates $\dot{\gamma}^*$ for carrier with the diameter $D_c = 0.15D_r$. The diagrams correspond to the margination into the RBC-FL (left column) and the PAL (right column), for three channel sizes. The considered channel widths are (a) $W = 1.64D_r$, (b) $W = 3.28D_r$, and (c) $W = 6.56D_r$. The white squares (□) indicate the values of H_t and $\dot{\gamma}^*$ for which simulations have been performed. The colour code ranges from blue (low probability) to red (high probability) and is acquired via interpolation.
The same dependence of margination on H_t and $\dot{\gamma}^*$ is observed for all channel sizes. Compared to the margination of the carrier with size $D_c = 0.3D_r$ (Fig. 4.24), the margination is reduced for the smaller carrier for all channel sizes. Exceptions are the cases where the carrier with $D_c = 0.3D_r$ does not fit into the RBC-FL, whereas the carrier with $D_c = 0.15D_r$ fits.

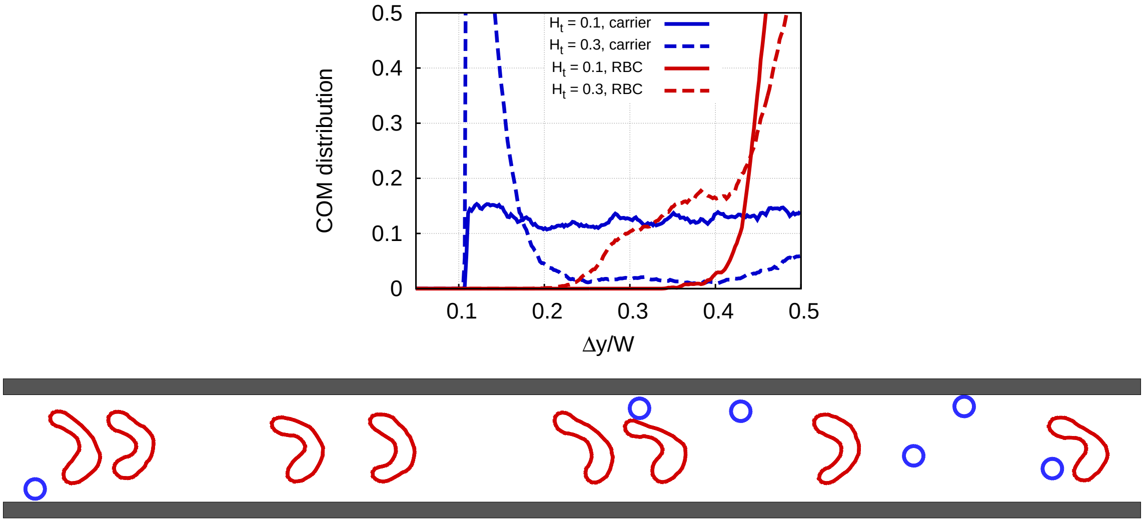

Figure 4.26.: RBC (red) and carrier (blue) distribution in a channel with $W = 1.64D_\mathrm{r}$. (top) COM distribution depending on the distance Δy to the wall normalized by the channel width W for the hematocrit values $H_\mathrm{t} = 0.1$ (solid curve) and $H_\mathrm{t} = 0.3$ (dashed curve). (bottom) Snapshot for $H_\mathrm{t} = 0.1$. The snapshot for $H_\mathrm{t} = 0.3$ is shown in Fig. 4.23. The considered shear rate is $\dot{\gamma}^* = 29.7$ and carrier size is $D_\mathrm{c} = 0.3D_\mathrm{r}$.
At low H_t the RBCs are aligned, all in the same way, in the middle of the channel. Hence, RBCs do not form a barrier for the carriers and the carriers are uniformly distributed in the channel.

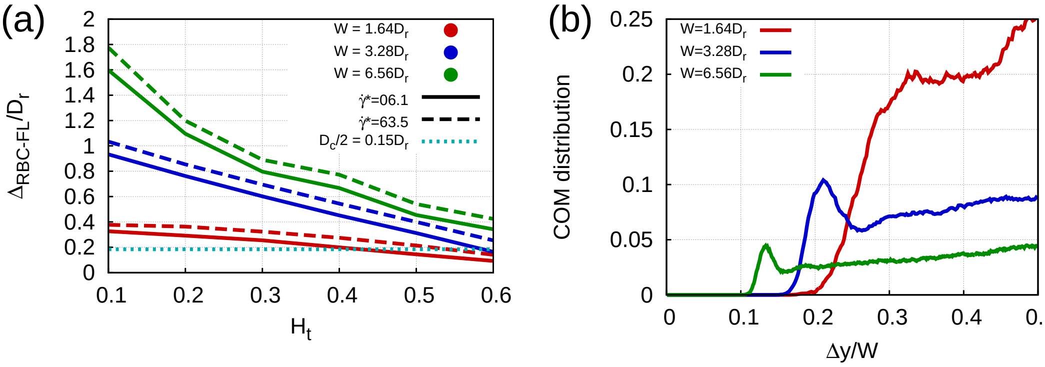

Figure 4.27.: Comparison of RBC distributions for different channel sizes. (a) The RBC-FL thickness $\Delta_\mathrm{RBC-FL}$, scaled by the RBC diameter D_r, over the hematocrit H_t. The considered carrier size $D_\mathrm{c} = 0.3D_\mathrm{r}$ is depicted by the cyan dotted line. (b) COM distribution of RBCs for different channel width, depending on the distance Δy to the wall, scaled by the channel width W. The considered shear rates are $\dot{\gamma}^* = 6.1$ (dashed curves) and $\dot{\gamma}^* = 63.5$ (solid curves). The considered channel width are $W = 1.64D_\mathrm{r}$ (red curves), $W = 3.28D_\mathrm{r}$ (blue curves), and $W = 6.56D_\mathrm{r}$ (green curves).
The RBC-FL thickness increases with increasing channel size but scales by another factor than the vessel size. The wider the vessel, the higher the percentage of the channel which RBCs occupy.

The reduction of margination into the PAL for the channel with $W = 6.56D_{\mathrm{r}}$ is due to the wider RBC-FL thickness and the associated broader carrier distributions in the RBC-FL, leading to a reduced number of carriers close to the wall. Although the carrier COM distribution possesses a distinct peak in the RBC-FL, the peak reaches, if at all, the minimal distance only for the highest hematocrit value (exception: $\dot{\gamma}^* = 6.1$), see Fig. C.10.

In the channel with $W = 1.64D_{\mathrm{r}}$, carriers can be outside of the RBC-FL while still being located close to the wall, due to the small channel width and collisions with RBCs. Therefore, the probability of margination into the PAL is increased, hence adhesion is likely to be most efficient in narrow channels. Nevertheless, a more detailed comparison of the probability of margination into the PAL between the channels with $W = 1.64D_{\mathrm{r}}$ and $W = 3.28D_{\mathrm{r}}$ illustrates that for $D_{\mathrm{c}} = 0.3D_{\mathrm{r}}$ and high hematocrit values the margination probability decreases for the narrow channel. Carriers are departed from the wall supposedly due to interactions with RBCs. A similar effect has been observed for the large carrier size $D_{\mathrm{c}} = 0.6D_{\mathrm{r}}$ at a channel width $W = 3.28D_{\mathrm{r}}$. Additionally, it has to be considered that for the same hematocrit value the packing in 3D is less efficient, leading to smaller RBC-FL thicknesses as discussed in the previous section. Smaller RBC-FL thicknesses might in turn cause a reduced margination into the PAL for the channel with $W = 1.64D_{\mathrm{r}}$, whereas for the channel with $W = 6.56D_{\mathrm{r}}$ the margination might be increased. Furthermore, a different shear-rate dependence is observed for the channel width $W = 1.64D_{\mathrm{r}}$ that has not been resolved in the diagrams, as shown for $D_{\mathrm{c}} = 0.3D_{\mathrm{r}}$ in Fig. 4.28 (b) and for $D_{\mathrm{c}} = 0.15D_{\mathrm{r}}$ in Fig. C.9 (b). For $W = 3.28D_{\mathrm{r}}$, the margination probability is lowest for the highest shear rate. At low hematocrit values this is also true for the channel with $W = 1.64D_{\mathrm{r}}$. However, for higher hematocrit values the probability is higher at higher shear rates.

The RBC as well as the carrier distribution change for a wider channel of width $W = 9.84D_{\mathrm{r}}$. A maximum is observed in the middle of the channel for the RBC COM distribution, due to close packing of RBCs that is even larger than the peak close to the RBC-FL border, see Fig. 4.29. The peak close to the wall disappears [163] for even larger channel sizes. Due to the larger RBC-FL thickness, that is $\Delta_{\mathrm{RBC-FL}} = 0.77D_{\mathrm{r}}$, faster carriers can easily overtake the slower carriers that are close to the wall, which leads to the formation of two lanes of moving carriers. Consequently, a double peak appears in the COM distribution with a distance of the two local maxima of about a carrier diameter.

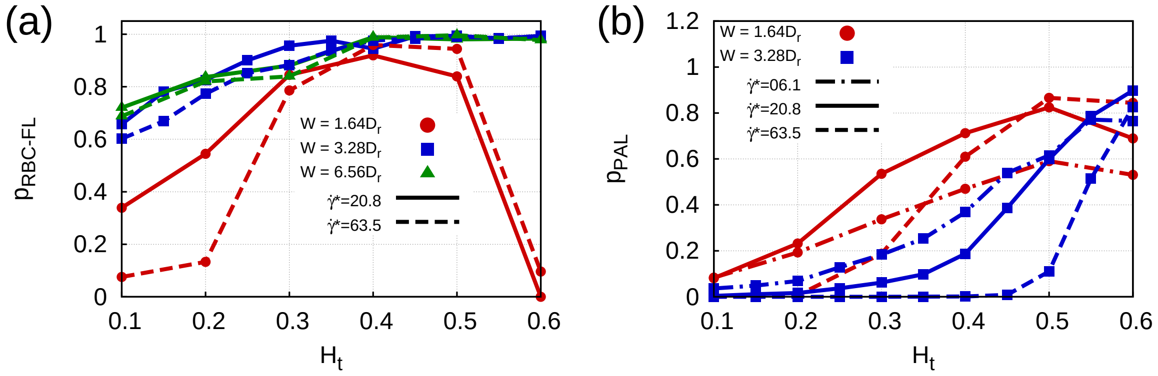

Figure 4.28.: (a) Margination probability $p_{\mathrm{RBC-FL}}$ into RBC-FL and (b) margination probability p_{PAL} into the PAL depending on hematocrit H_{t} for a carrier of size $D_{\mathrm{c}} = 0.3D_{\mathrm{r}}$. Different curve colours correspond to different channel sizes: $W = 1.64D_{\mathrm{r}}$ (red), $W = 3.28D_{\mathrm{r}}$ (blue), and $W = 6.56D_{\mathrm{r}}$ (green). Different shear rates correspond to different curve types: $\dot{\gamma}^* = 6.1$ (dot-dashed), $\dot{\gamma}^* = 20.8$ (solid), and $\dot{\gamma}^* = 63.5$ (dashed).

The $p_{\mathrm{RBC-FL}}$ differs slightly between $W = 3.28D_{\mathrm{r}}$ and $W = 6.56D_{\mathrm{r}}$ at low H_{t}. For $W = 1.64D_{\mathrm{r}}$, $p_{\mathrm{RBC-FL}}$ decreases at low as well as high H_{t}. For $W = 1.64D_{\mathrm{r}}$, p_{PAL} increases with shear rate for biological relevant hematocrit values, whereas it decreases with increasing shear rate for $W = 3.28D_{\mathrm{r}}$.

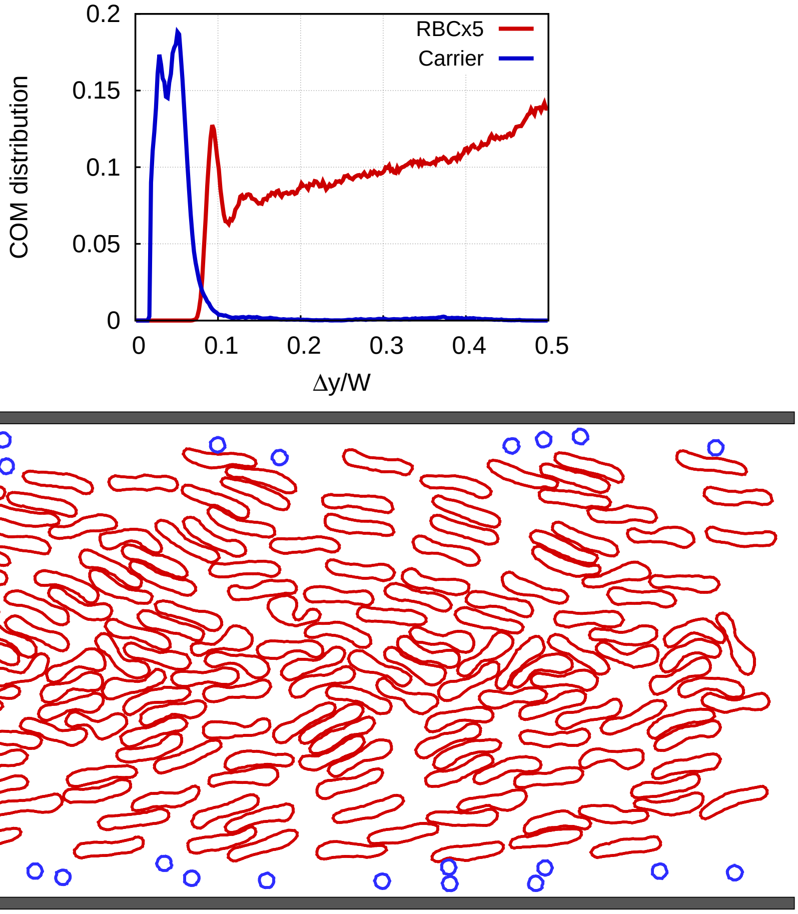

Figure 4.29.: Distribution of RBCs (red) and carriers with $D_\mathrm{c} = 0.3D_\mathrm{r}$ (blue) in a channel width $W = 9.84D_\mathrm{r}$. (top) COM distribution depending on the distance Δy to the wall, scaled by the channel width W. The RBC COM distributions has been scaled by a factor 5. The considered hematocrit value is $H_\mathrm{t} = 0.4$ and the shear rate is $\dot{\gamma}^* = 29.7$. (bottom) A corresponding snapshot is shown.

For the RBC COM distribution a maximum in the middle of the channel is observed that is even larger than the peak close to the RBC-FL border. The carrier distribution splits into two peaks with one carrier diameter difference, because faster carriers can easily overtake slower carriers in the wide RBC-FL.

4.3.2. The 'reverse' Fåhræus effect

So far, the carrier margination probability, the probability for a carrier to be close to the wall, has been discussed. Clearly, strong margination is likely to enhance particle adhesion. However, the density of the carriers also influences the adhesion probability; the higher the density the higher the probability. Therefore, the dependence of carrier density on channel and carrier size is discussed.

Robin Fåhræus found already in 1929, almost a hundred years ago, in *in vitro* blood flow experiments [175] that RBCs flow faster than the average flow. Therefore, the average concentration of RBCs in human blood decreases with decreasing vessel diameter. Concurrently, the RBC velocity increases in narrow channels. For a discussion of this issue, the tube hematocrit and the discharge hematocrit have to be introduced. The tube hematocrit H_t, referred earlier to as hematocrit, is the volume fraction of RBCs inside the channel. The discharge hematocrit H_d corresponds to the volume fraction of RBCs leaving the channel per unit time. Both, H_t and H_d can be found from the RBC cross-sectional density profile $H(r)$, as

$$\pi R^2 H_\mathrm{t} = 2\pi \int_0^R H(r) r dr \tag{4.5}$$

$$\pi R^2 \bar{V} H_\mathrm{d} = 2\pi \int_0^R H(r) v(r) r dr, \tag{4.6}$$

with $R = W/2$, the average velocity $\bar{V} = 2R^{-2}\int_0^R v(r) r dr$, and the cross-sectional velocity profile $v(r)$ [163].

The Fåhræus effect is related to the existence of the RBC-FL. In wide channels the RBC-FL thickness is negligible compared to the tube diameter and the RBC distribution is uniform, therefore $H_\mathrm{t} \simeq H_\mathrm{d}$. In *in vitro* experiments, it has been shown that $H_\mathrm{d}/H_\mathrm{t} = 1$, for channels with $W \gtrsim 0.5 - 1\,\mathrm{mm}$ [178,179]. In narrow channels the RBCs gather in the high-velocity region, the channel center, and therefore pass the channel faster than the average flow, so that $H_\mathrm{d} > H_\mathrm{t}$.

In Fig. 4.30, a closed system is sketched, consisting of a wide channel (A) with the cross sectional area A^A that splits into two narrow channels (B), which have the same diameter and cross sectional area $A^\mathrm{B} = A^\mathrm{A}/2$. From the mass conservation and the continuity equation it follows

$$Q^\mathrm{A} = 2Q^\mathrm{B} \tag{4.7}$$

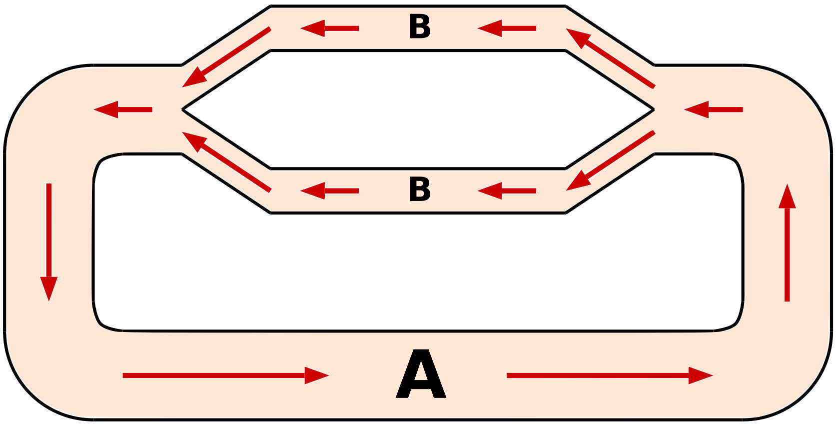

Figure 4.30.: Sketch of a channel system to illustrate the Fåhræus effect.

for the flow rate $Q = \bar{V}A$. Equation (4.7) applies also for the flow rates of RBCs alone, Q_{RBC}, which are defined by the integral on the right hand side of Eq. (4.6). Therefore, from $H_d^A \bar{V}^A A^A = 2H_d^B \bar{V}^B A^B$ and $\bar{V}^A A^A = 2\bar{V}^B A^B$ follows $H_{\mathrm{d}}^{\mathrm{A}} = H_{\mathrm{d}}^{\mathrm{B}}$ for the discharge hematocrits. For the wide channel it can be assumed $H_{\mathrm{t}}^{\mathrm{A}} \simeq H_{\mathrm{d}}^{\mathrm{A}}$ and for the narrow channel $H_{\mathrm{d}}^{\mathrm{B}} > H_{\mathrm{t}}^{\mathrm{B}}$, which results in $H_{\mathrm{t}}^{\mathrm{A}} > H_{\mathrm{t}}^{\mathrm{B}}$. Thus, the RBC volume fraction is larger in the wider channel.

The change of the tube hematocrit depends generally on tube diameter, hematocrit, and shear rate. Theoretically, a solution for the fraction of tube and discharge hematocrit can be derived by assuming a constant RBC distribution in the channel up to the distance $\Delta_{\mathrm{RBC-FL}}$ from the wall

$$H(r) = \begin{cases} H_0, & \text{if } 0 \leq r \leq W/2 - \Delta_{\mathrm{RBC-FL}} \\ 0, & \text{if } W/2 - \Delta_{\mathrm{RBC-FL}} < r < W/2\,. \end{cases} \tag{4.8}$$

Then, from the Poiseuille law the ratio

$$\frac{H_{\mathrm{t}}}{H_{\mathrm{d}}} = \frac{1}{2 - (1 - 2\Delta_{\mathrm{RBC-FL}}/W)^2}, \tag{4.9}$$

is obtained, where the shear-rate and the hematocrit dependence enters via the RBC-FL thickness $\Delta_{\mathrm{RBC-FL}}$. From several experiments [179, 180], a more realistic dependence of the ratio of tube and discharge hematocrits on channel size and hematocrit has been derived, neglecting the shear rate dependence, since experiments showed that the influence of shear rate in the range of shear rates appearing in the microcirculation is small [179]. The ratio of tube and discharge hematocrit is given by

$$\frac{H_\mathrm{t}}{H_\mathrm{d}} = H_\mathrm{d} + (1 - H_\mathrm{d})\left(1 + 1.7e^{-0.3W} - 0.6e^{-0.01W}\right), \tag{4.10}$$

and is shown in Fig. 4.31 (a). For channels with diameters comparable or smaller to the diameter of one RBC, the RBC density increases with decreasing channel size, due to a different RBC alignment compared to wider channels and the negligible RBC-FL.

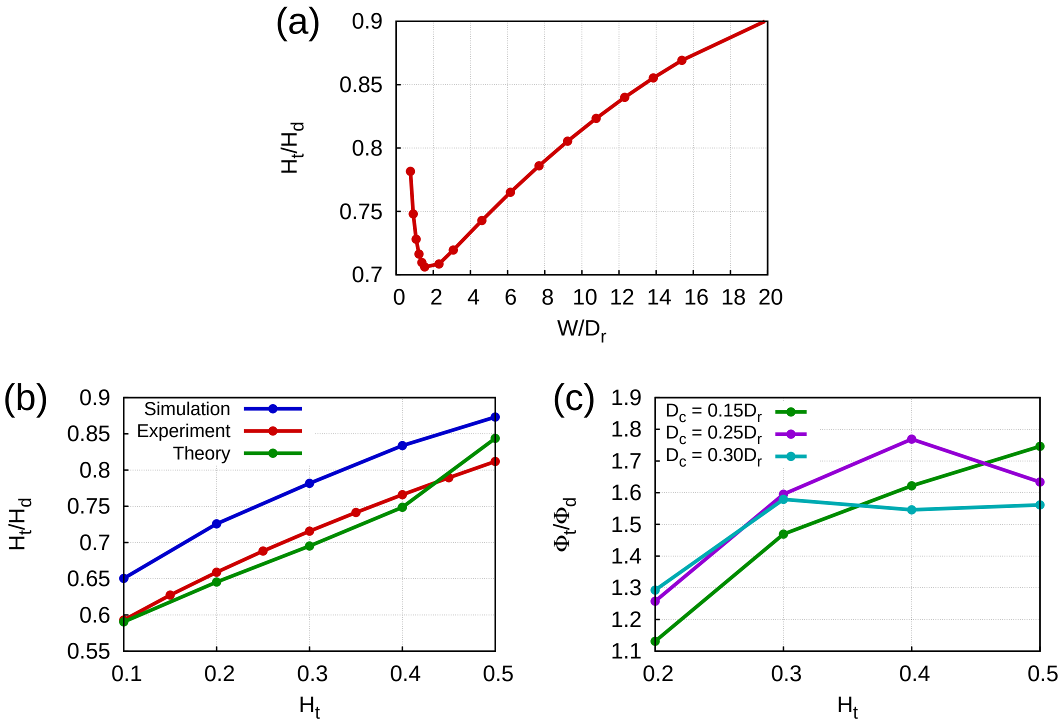

Figure 4.31.: Fåhræus and 'reverse' Fåhræus effect in 3D. (a) Dependence of ratio of tube and discharge hematocrit $H_\mathrm{t}/H_\mathrm{d}$ on vessel diameter W scaled by the RBC diameter D_r as given in Eq. (4.10) calculated for $H_\mathrm{t} = 0.35$. (b) Dependence of ratio of tube and discharge hematocrit, $H_\mathrm{t}/H_\mathrm{d}$, on H_t calculated from Eq. (4.10) (red curve), from theory, Eq. (4.9), with $\Delta_\mathrm{RBC-FL}$ estimated from the simulations (green curve), and directly from simulations at the shear rate $\dot{\gamma}^* = 59$ (blue curve) for $W = 3.1D_\mathrm{r}$. (c) Ratio $\Phi_\mathrm{t}/\Phi_\mathrm{d}$ of the tube and the discharge volume fraction of spherical carriers with different diameters: $D_\mathrm{c} = 0.15D_\mathrm{r}$ (green), $D_\mathrm{c} = 0.25D_\mathrm{r}$ (purple), and $D_\mathrm{c} = 0.3D_\mathrm{r}$ (cyan) for $W = 3.1D_\mathrm{r}$.
With decreasing channel size the RBC density decreases. With increasing hematocrit the differences between H_t and H_d decreases and $H_\mathrm{t} < H_\mathrm{d}$. For carriers $\Phi_\mathrm{t} > \Phi_\mathrm{d}$ and with increasing hematocrit the difference increases. $\Phi_\mathrm{t}/\Phi_\mathrm{d}$ depends on the carrier size.

Similar to the two hematocrits, H_t and H_d, the tube volume fraction Φ_t and discharge volume fraction Φ_d of carriers can be defined (see Eqs. (4.5) and (4.6)), with $\Phi(r)$ being the carrier density profile. In contrast to RBCs, smaller carriers are quasi-trapped in the low velocity region of the RBC-FL. Therefore, the small carriers are expected to pass a channel slower than the average flow, which would lead to $\Phi_\mathrm{t} > \Phi_\mathrm{d}$. This is opposite to the behaviour of RBCs and is thus called the 'reverse' Fåhræus effect.

Contrary to *in vivo* and most *in vitro* conditions, where the discharge hematocrit is specified for instance by the feed hematocrit [179] and the tube hematocrit is measured [163], the tube hematocrit in the presented *in silico* studies is an input to the simulations.

Hence, the discharge hematocrit and the discharge volume fraction have to be calculated from the velocity and the density profiles, using Eqs. (4.5) and (4.6). For the RBCs the density distributions have been computed from simulation snapshots, since the density distribution depends on the orientation of the RBCs. The density distribution of spherical carriers has been calculated from their COM distributions. Thus, the probability to find the center at a certain radial position has been redistributed with respect to the size of the sphere and the spherical shape.

Figure 4.31 (b) presents the ratio $H_\mathrm{t}/H_\mathrm{d}$ for the case of $W = 3.1D_\mathrm{r}$ and $\dot{\gamma}^* = 59$ depending on the tube hematocrit H_t. The results from simulations are within 10% error of the experimental measurements. Furthermore, insertion of the RBC-FL thickness from the simulations into Eq. (4.9), leads to good theoretical predictions. The slightly lower theoretical values are due to an overestimation of H_d, since the peak in the COM distribution close to the RBC-FL, has been neglected. As expected, $H_\mathrm{t}/H_\mathrm{d} < 1$ and with increasing H_t the ratio increases and consequently the difference between H_t and H_d decreases. With increasing hematocrit, the width of the RBC distribution increases, due to packing restrictions in the middle of the channel. This observation agrees with experimental *in vitro* results [178], where $H_\mathrm{t}/H_\mathrm{d}$ has been measured for several discharge hematocrit values. These experiments further demonstrate that this effect subsides with increasing channel size.

Likewise, $\Phi_\mathrm{t}/\Phi_\mathrm{d} > 1$ as expected, and the difference increases further with increasing tube hematocrit, according to the increase of margination at high hematocrit values. Thus, the density of carriers near the wall increases with increasing hematocrit. For the small carriers, $\Phi_\mathrm{t}/\Phi_\mathrm{d}$ increases at all considered hematocrit values, whereas $\Phi_\mathrm{t}/\Phi_\mathrm{d}$ remains constant for the bigger carriers, since they cannot come closer to the wall, due to their size. Through this restriction, higher velocities are weighted more for the larger carriers and Φ_d does not decrease further. In other words, for larger carriers the density cannot increase further.

In the limit of very small H_t values, $\Phi_\mathrm{t}/\Phi_\mathrm{d} \lesssim 1$ is expected, since in the case of more than one carrier in the channel, the majority of carriers will gather close to the channel center. In the limit of very large H_t values, the space the RBCs occupy increases and concurrently the RBC-FL decreases. Hence, $H_\mathrm{t}/H_\mathrm{d}$ approaches unity and $\Phi_\mathrm{t}/\Phi_\mathrm{d}$ is expected to decrease to a value close to unity as well, since no margination may occur similar to simulations with non-deformable (rigid) RBCs, which do not form a RBC-FL [132].

Two-dimensional (2D) simulations were employed to examine the effect of the channel size. In 2D, the tube and discharge hematocrits are defined as

$$\begin{aligned} WH_\mathrm{t} &= \int_0^W H(y)dy \\ W\bar{V}H_\mathrm{d} &= \int_0^W H(y)v(y)dy, \end{aligned} \tag{4.11}$$

with $\bar{V} = \int_0^W v(y)dy/W$. As in 3D, Φ_t and Φ_d are defined accordingly. The density distribution of RBCs has been calculated from snapshots, and the carrier density distribution from the COM distributions.

Figure 4.32 (a) presents the ratio of H_t and H_d for five channel sizes $W/D_\mathrm{r} \in \{1.64, 2.46, 3.28, 6.56, 9.84\}$. As expected from the theoretical consideration and experimental predictions in Fig. 4.31 (a), H_t and H_d become similar with increasing channel size. At high H_t, the channels with $W = 3.28D_\mathrm{r}$ and $W = 1.64D_\mathrm{r}$ possess similar values which agrees with the experimental predictions. However, for $W = 1.64D_\mathrm{r}$ at low H_t, $H_\mathrm{t}/H_\mathrm{d}$ is even larger than for $W = 6.54D_\mathrm{r}$. The reason for these high values is the special orientation of RBCs at this tube hematocrit, presented in Fig. 4.26. The localization of the RBC center in the middle, the alignment of the short axis in flow direction, and the biconcave shape leads to a density distribution with a local minimum in the middle of the channel as shown in Fig. 4.33. Hence, lower velocities are weighted more and thus H_d is reduced, since the middle of the channel is the region with the highest velocity. With increasing H_t the density distribution becomes more uniform and H_d increases.

Figure 4.32 (b) presents, for the channel size $W = 3.26D_\mathrm{r}$, the comparison of the tube and the discharge volume fraction of carriers with different sizes depending on the tube hematocrit. As in 3D, the increase of density with increasing tube hematocrit is stronger for smaller carriers. For larger carrier sizes, the curve levels off, due to their

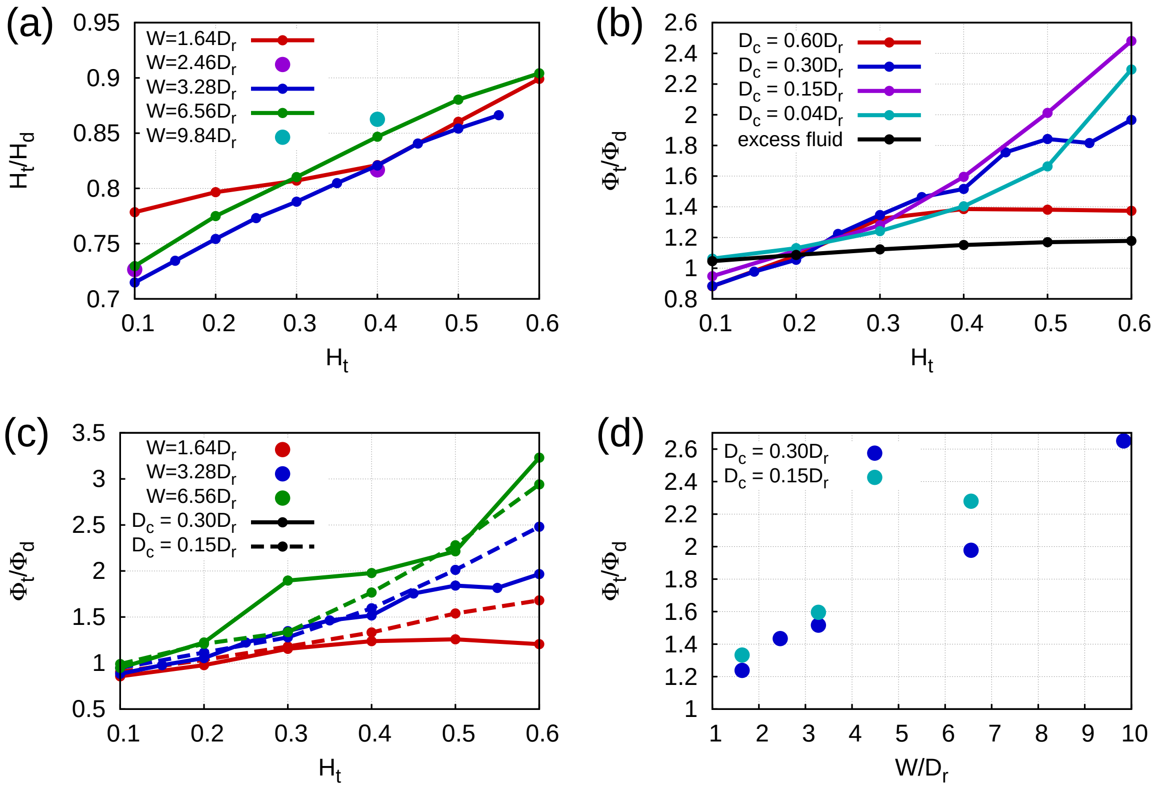

Figure 4.32.: Fåhræus and ‘reverse’ Fåhræus effect in 2D. (a) Dependence of the ratio of tube hematocrit H_t and discharge hematocrit H_d on H_t for different channel sizes at the average shear rate $\dot{\gamma}^* = 29.7$. (b) Dependence of the ratio of tube Φ_t and discharge volume fraction Φ_d on H_t for different carrier sizes at the average shear rate $\dot{\gamma}^* = 29.7$. (c) $\Phi_\mathrm{t}/\Phi_\mathrm{d}$ dependence on H_t for different channel sizes and two carrier sizes at the average shear rate $\dot{\gamma}^* = 29.7$. (d) $\Phi_\mathrm{t}/\Phi_\mathrm{d}$ dependence on channel size W normalized by the RBC diameter D_r for the carrier with diameter $D_\mathrm{c} = 0.3D_\mathrm{r}$ and at the average shear rate $\dot{\gamma}^* = 29.7$.
For high hematocrit values and narrow channels $\Phi_\mathrm{t}/\Phi_\mathrm{d}$ is larger for smaller carriers. The differences vanishes with increasing channel size. Although carriers pass the channel slower than the average flow their density increases with increasing channel size.

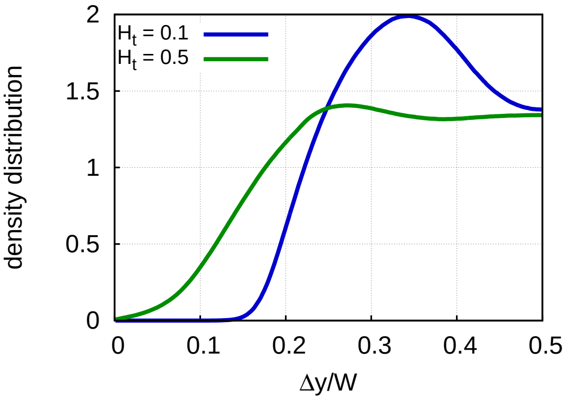

Figure 4.33.: Density distribution of RBCs depending on the distance to the wall Δy in a channel with $W = 1.64D_\mathrm{r}$ and $\dot{\gamma}^* = 29.7$. The curves correspond to different hematocrit values; $H_\mathrm{t} = 0.1$ (blue) and $H_\mathrm{t} = 0.5$ (green).
At low hematocrit values the RBC localization in the middle of the channel and the alignment of the small axis with the flow direction, their biconcave shape leads to a density distribution with the maximum away from the center.

larger diameter. The larger the carrier, the smaller the increase of $\Phi_\mathrm{t}/\Phi_\mathrm{d}$ with H_t. However, for the excess fluid volume only a slight density increase is observed while the nano-carriers exhibit a considerable increase of density near the wall, due to the excluded-volume interactions with the RBCs.

The comparison of different channel sizes for the carriers with $D_\mathrm{c} = 0.3D_\mathrm{r}$ and $D_\mathrm{c} = 0.15D_\mathrm{r}$ are presented in Fig. 4.32 (c). For all channel sizes, the small carries exhibit a higher ratio of Φ_t and Φ_d, which means that for high hematocrit values the density of small carriers would be higher for a similar discharge volume fraction. However, with increasing channel size the differences between the carrier sizes diminish.

Noteworthy is the increase of $\Phi_\mathrm{t}/\Phi_\mathrm{d}$ with channel size as shown in Fig. 4.32 (d), although the ratio of H_t and H_d already increases. It follows that the carrier tube volume fraction increases with channel size similar to the tube hematocrit. The reason here is that the RBC-FL increases for increasing channel size, but not proportionally to the channel diameter. The ratio of RBC-FL thickness and the channel size decreases with increasing channel size. However, it remains unclear what happens for even wider channels. For wider channels, the RBC distribution is constant over the cross section, but a RBC-FL still exists. The RBC-FL thickness compared to the channel width is negligible, but provides still the possibility of margination. As long as the carrier are properly marginated, $\Phi_\mathrm{t}/\Phi_\mathrm{d}$ will increase with increasing channel size. However, with increasing channel size the fraction of the channel the RBCs occupy increases, which might lead to a decrease of the local RBC density although the RBC volume fraction increases. Furthermore, it has been shown that the alignment of RBCs with the flow next to the RBC-FL vanishes with increasing channel size [163], which promotes escaping the RBC-FL for wider channels. Additionally, margination times have to be taken into account. For wider channels also the time increases the carriers need to marginate. Therefore, it may be unlikely that in vessels wider than 1 mm the carrier distribution reaches a steady state. Thus, a decrease of $\Phi_\mathrm{t}/\Phi_\mathrm{d}$ may be likely with further increasing channel width.

4.3.3. Summary

Comparing the margination into the RBC-FL and the PAL for channels of width W in the range $1.64D_\mathrm{r}$ to $6.56D_\mathrm{r}$, a similar hematocrit and carrier size dependence of margination is observed. For the narrowest channel, an increase of margination into the PAL is observed with increasing shear rate, whereas a decrease is observed for the other channel sizes. However, besides the highest hematocrit value, the margination into the PAL is highest for the narrow channel and decreases with increasing channel size. Especially for the widest channel with $W = 6.56D_\mathrm{r}$ the PAL margination is drastically reduced, due to the larger available space in a broader RBC-FL. For the narrowest channel and the highest hematocrit value of $H_\mathrm{t} = 0.6$, the carriers are displaced from the wall through interactions with RBCs, and thus the PAL margination is reduced. It has to be pointed out that this effect is expected to be more pronounced in 3D. However, the RBC tube hematocrit decreases with decreasing channel size, which is known as the Fåhræus effect. Thus, the carrier should remain marginated.

In contrast to RBCs, which pass a narrow channel faster than the average flow, the carriers pass the channel slower. This leads to a tube volume fraction which is larger than the discharge volume fraction, here introduced as a ‘reverse’ Fåhræus effect. Nevertheless, an increase of carrier density is observed with increasing channel size, for the examined channel sizes with the largest channel of width $W = 9.84D_\mathrm{r}$, because the RBC-FL thickness does not increase linearly with the channel width. This is an advantage, because with increasing channel size the margination decreases, but through a higher density the adhesion probability may not be strongly effected. Furthermore, for the biologically relevant hematocrit values, the density of smaller carriers is higher in the considered channels, under the assumption of the same discharge volume fraction. The difference diminishes with increasing channel size and is expected to be even smaller for the smaller carriers with a further increase of channel size. However, the density increase may compensate for the decrease of margination for smaller carriers. Thus, the system might not be very sensitive to a change in carrier or platelet size, which vary between 2 µm and 5 µm in diameter [8]. A decrease of carrier density for even wider channels may be possible due to lower local RBC density, missing RBC layer close to the RBC-FL, due to alignment with the flow, and longer margination times.

In conclusion, from the margination point of view, adhesion is likely to happen preferably in channels of size $10 - 20\,\mu\mathrm{m}$ rather than in wider ones. The density increase of carriers for wider channels and smaller carriers may compensate for the margination reduction for increasing channel sizes and decreasing carrier sizes. However, the effect is not very pronounced, thus nano-particles can not be considered for a sufficient adhesion. Furthermore, to determine an appropriate size for therapeutic particles, the delivered volume has to be considered rather than the number of carriers, which again favours micron-sized carriers.

4.4. Margination mechanism

Platelets and carriers appear to be quasi-trapped in the RBC-FL. Although platelets are located in the RBC-FL, there exists a probability to escape from the RBC-FL, as seen for some platelet trajectories in Fig. 4.34 (a). To analyse this behaviour, Figs. 4.34 (b) and (c) present the time which platelets need in order to cross the RBC-FL border depending on their COM position in the channel. Three hematocrit values and three shear rates have been investigated. Initially the platelets are located either inside or outside the RBC-FL. For platelets, which are initially located inside the RBC-FL, the time has been tracked until it has crossed a distance of $1.15\Delta_{\mathrm{RBC-FL}}$ to the wall, with $\Delta_{\mathrm{RBC-FL}}$ being the RBC-FL thickness. Platelets, which are initially located outside the RBC-FL, were tracked until they crossed the distance $0.85\Delta_{\mathrm{RBC-FL}}$ from the wall. By measuring the time until the platelet crossed a larger and smaller distance than $\Delta_{\mathrm{RBC-FL}}$, respectively it can be assumed to detect real crossing events and exclude small fluctuations. These measurements have been performed for 2D simulations, due to a large number of simulations, which are required to gain sufficient statistics. Clearly, platelets remain in the RBC-populated region for considerable shorter times than they remain in the RBC-FL. The time they need for a crossover depends on the hematocrit and the shear rate. The hematocrit hardly influences the time platelets stay outside the RBC-FL. However, hematocrit influences the time platelets stay inside the RBC-FL. For an intermediate hematocrit value platelets remain longest in the RBC-FL, since for low hematocrit values the platelets can easily slide between the RBCs, whereas for high hematocrit values the RBC-FL decreases, which also favours crossing. The higher the shear rate, the quicker the carriers reach the RBC-FL and the quicker they can leave it. However, the time until a platelet leaves the RBC-FL depend more strongly on the shear rate than the time that is needed to enter the RBC-FL.

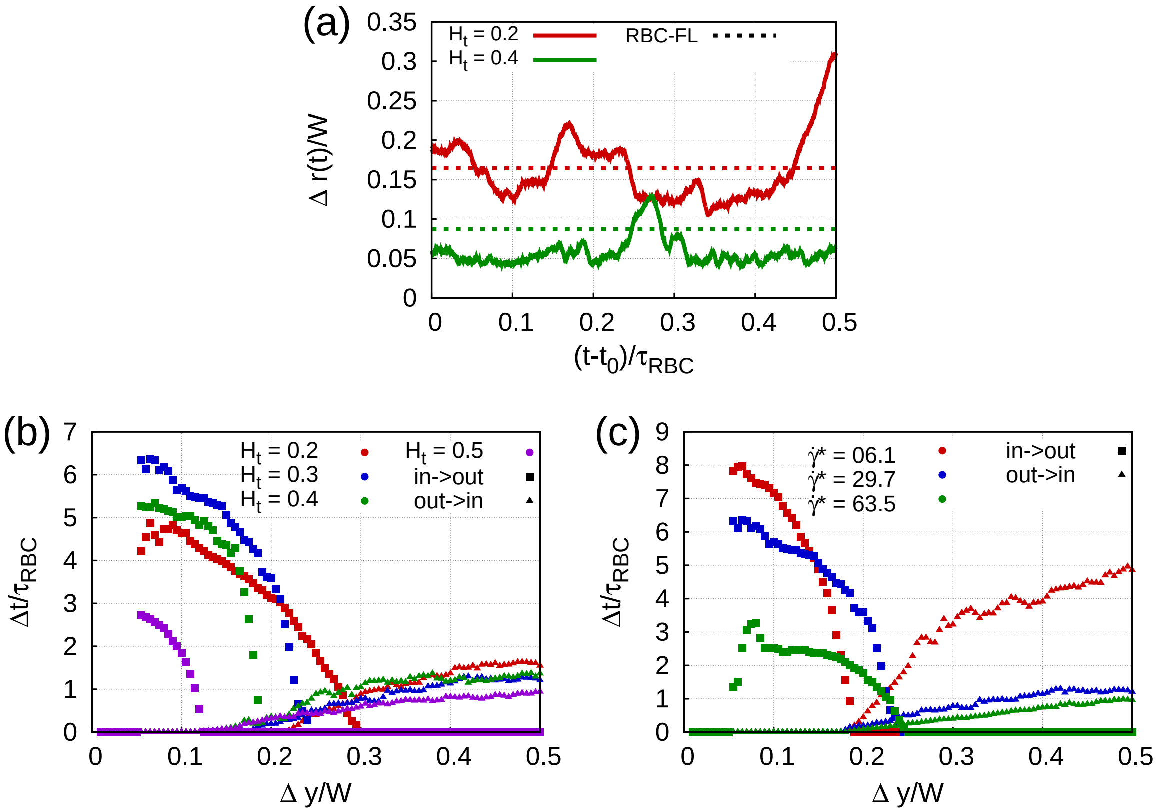

Figure 4.34.: (a) Trajectory $\Delta r(t)$ of a sphere with $D_\mathrm{c} = 0.28 D_\mathrm{r}$, normalized by the channel width W started from the time t_0, and depending on the time t normalized by the RBC relaxation time τ_RBC. The different curves correspond to two hematocrit values $H_\mathrm{t} = 0.2$ (red) and $H_\mathrm{t} = 0.4$ (green). The RBC-FL border is denoted by the dashed lines. (b, c) Measurements of the time Δt for a 2D circular carrier of size $D_\mathrm{c} = 0.3 D_\mathrm{r}$ required to cross the RBC-FL border depending on the COM distance Δy to the wall. (b) Different curves correspond to different H_t: $H_\mathrm{t} = 0.2$ (red), $H_\mathrm{t} = 0.3$ (blue), $H_\mathrm{t} = 0.4$ (green), and $H_\mathrm{t} = 0.5$ (purple). (c) Different curves correspond to different average shear rates $\dot{\gamma}^*$: $\dot{\gamma}^* = 6.1$ (red), $\dot{\gamma}^* = 29.7$ (blue), and $\dot{\gamma}^* = 63.5$ (green). Carriers are able to cross the RBC-FL border and escape from the RBC-FL. Carriers remain in the RBC-FL for longer times than they need to marginate.

Up to now, investigations of the dependence of carrier and platelet margination on a large number of system parameters have been reported. However, the question what makes a carrier stay longer in the RBC-FL than in the RBC populated region remains unacknowledged. It is now obvious that the RBC distribution has a strong impact on the platelet distribution. For instance, the hematocrit has to be high enough, such that the center of the channel is sufficiently populated and RBCs form a barrier for the platelets. On the other hand, a wide enough RBC-FL is required, otherwise platelet margination diminishes. This has been discussed above and observed in experiments [128] at high hematocrit values and low shear rates. Further numerical studies monitored a decrease of particle margination for RBCs with a high viscosity ratio between the inner and the outer fluids, for which the RBC-FL decreases [132].

Different theoretical and numerical studies have been performed to understand the underlying mechanism of margination. The finite size of platelets influences their distribution [133]. However, 2D lattice Boltzmann simulations [130] suggested that pure volume exclusion is not sufficient to explain platelet margination. For pure volume exclusion a uniform platelet distribution within the available space was expected, but has not been observed. Theoretical calculations predict that rebound collisions between the marginated platelets and RBCs play a role [181]. Furthermore, the lateral diffusion of platelets varies in radial direction, due to interactions with RBCs [130, 182]. A proposed mechanism is related to velocity fluctuations, which depend on the radial position in the channel [14, 131]. However, in addition to the lateral diffusion, an additional drift to the RBC-FL border is required to achieve a consistent platelet near-wall excess [130]. This drift is suggested to be due to hydrodynamic interactions with the tank-treading RBCs.

Numerical simulations are used to better understand the influence of direct (excluded-volume) and hydrodynamic interactions between platelets and RBCs, respectively. On account of this, one of these two interactions is turned off and changes in the COM distributions are monitored. First, simulations, where direct (excluded-volume) interactions between platelets and RBCs are turned off, are compared to simulations with direct interactions turned on and to simulations without RBCs. Second, simulations with hydrodynamic simulations turned off are compared to the original simulations.

4.4.1. Excluded-volume interactions turned off

The distribution of platelets in Poiseuille flow in the absence of RBCs depends on the particle type and the Reynolds number Re. Deformable particles and rigid particles with an asymmetric shape experience a lift from the wall [183–185]. According to the Stokes equation in Eq. (1.3), rigid spherical particles undergo no lateral migration across the streamlines due to time reversibility [184]. For higher Reynolds numbers inertia effects have to be taken into account. Inertia leads to gathering of spherical particles at a distance of $0.6R$ from the axis, which is called the Segré-Silberberg effect [186–188]. In the considered simulations the Reynolds number is defined as $Re = \bar{\dot{\gamma}}\rho W^2/\eta$. For the 3D simulations with $W = 3D_\mathrm{r}$ it is $0.05 \leq Re \leq 0.26$. Therefore, inertial effects can be neglected.

For a monodisperse suspension of particles, mutually hydrodynamic interactions between the particles induce motion across a stream line. On the one hand each particle rotates in shear flow [168] and induces and circulatory velocity field around itself inducing a drag force [189]. On the other hand, when particles in a shear flow, which move with different velocities, overtake each other, their velocity fields lead to lateral displacements what leads to shear-induced diffusion [189]. The steeper the velocity gradient, the stronger is this effect. Hence, particles in Poiseuille flow close to the wall change their lateral position more often than particles close to the center, where they consequently remain longer. This effect is called shear-induced migration [190–192].

COM distributions of platelets in a fluid with RBCs and a fluid without RBCs are compared to evaluate the influence of hydrodynamic interactions between RBCs and platelets on the platelet distribution. Therefore, the repulsive LJ interaction between RBCs and platelets, and the reflections of platelets on the RBC surface are turned off. In this way RBCs and carriers do not "see" each other, but they are suspended in the same fluid. These simulations have been performed for spheres with the diameter $D_\mathrm{c} = 0.28D_\mathrm{r}$, $D_\mathrm{c} = 0.15D_\mathrm{r}$, and the ellipsoid with the long and short axis diameter, $D_\mathrm{L} = 0.47D_\mathrm{r}$ and $D_\mathrm{S} = 0.13D_\mathrm{r}$, respectively. The compared distributions are computed after the same number of timesteps has passed and are averaged over the same number of timesteps. This condition is kept for all simulation results which will follow. Furthermore, the RBC distributions are compared to the previous simulations to ensure that there are no changes, see Fig. C.11.

Figure 4.35 shows that the carriers in the fluid with RBCs remain closer to the wall, even in the RBC-FL, than the carriers in the fluid without RBCs. The simulations have been performed for the hematocrit $H_\mathrm{t} = 0.3$ and two pressure gradients that were induced by the force $f' = fk_\mathrm{B}T/W$ on the fluid particles. Indeed, this effect is hardly observed for small spheres with $D_\mathrm{c} = 0.15D_\mathrm{r}$ and is strongest for the ellipsoid. This indicates that for hydrodynamic interactions with the RBCs the shear-induced migration is slower, especially for carriers with large extensions. Hence, this effect is likely to increase the time a carrier remains in the RBC-FL.

An obvious difference between the simulations are the different velocity profiles, for

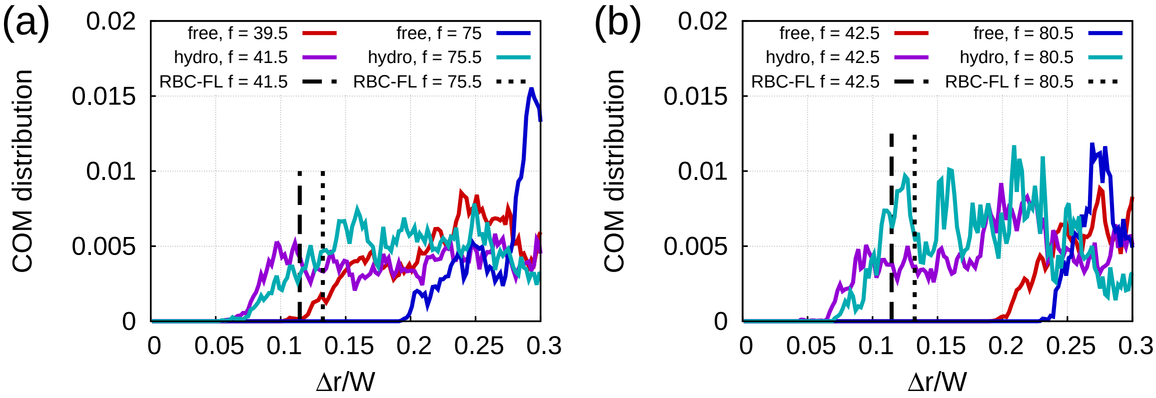

Figure 4.35.: Influence of hydrodynamic interactions on carrier distribution for (a) a sphere with $D_\mathrm{c} = 0.28 D_\mathrm{r}$ and (b) an ellipsoid. COM distributions for free flowing carriers in Poiseuille flow (red, blue) and carriers flowing in a fluid together with RBCs, but carriers and RBCs do not directly interact (purple, cyan). Two different pressure gradients are examined. The force on the fluid particles is $f' = f k_\mathrm{B} T / W$.
With hydrodynamic interactions the shear-induced migration is slower, since carriers partially remain in the RBC-FL.

the cases with and without RBCs, as also discussed in Section 3.3.3. The velocity profile for the simulations with RBCs is flattened in the center due to the RBCs. Such a velocity profile can be fitted by

$$v_x(r) = a \left(1 - \left(\frac{r}{R}\right)^b\right), \tag{4.12}$$

with a and b being two fitting parameters and the radial position r and the radius of the channel $R = W/2$. The values obtained for a flow with $H_\mathrm{t} = 0.4$ and $\dot{\gamma}^* = 39$ are $a = 0.264$ and $b = 4.89$. In the former discussed simulations a constant force is applied to all fluid particles to mimic a pressure drop. In order to investigate the effect of the different velocity profiles, the fluid particles in separate simulations are restricted to a given velocity in flow direction, given by Eq. (4.12). The minimal distance to the wall is not changed by the different velocity profiles, as presented in Fig. 4.36. Hence, the velocity profile can be excluded as to be a reason for the different COM distributions of carriers in a fluid together with RBCs and a fluid without RBCs.

In a next step, platelets were restricted to stay in a near-wall region, since it has been suggested [130] that the hydrodynamic interactions influence mainly the distribution of platelets close to the RBC-FL. Therefore, the platelets have been constrained by a LJ-9-3 repulsion (see Eq. (4.4)) at a distance similar to the RBC-FL thickness, whereas the RBCs were unaffected. Without RBCs, carriers come as close to the wall

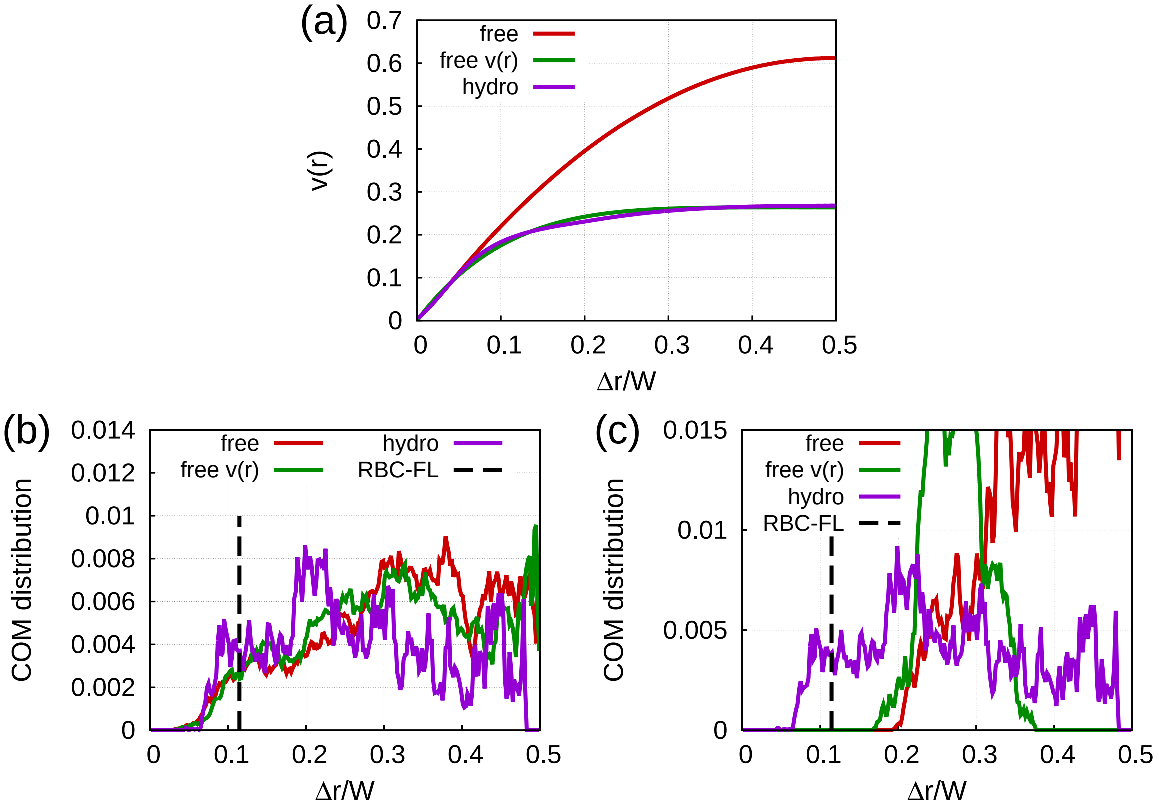

Figure 4.36.: Influence of velocity profile on carrier distribution. (a) Velocity profile $v(r)$ depending on the distance Δr to the wall normalized to the channel width W for the simulations with the carriers free in the channel with normal Poiseuille flow (red), in a fluid with velocity profile as given from Eq. (4.12) (green), and in a fluid with RBCs, but excluded-volume interactions are turned off (purple). Comparison of COM distributions of (b) a sphere with $D_{\mathrm{c}} = 0.15 D_{\mathrm{r}}$ and (c) an ellipsoid. All curves are based on an applied force of $f' \approx 45 k_{\mathrm{B}} T / W$

The velocity profile can be excluded as to be a reason for the different COM distributions of carriers in a fluid without RBCs and a fluid with RBCs.

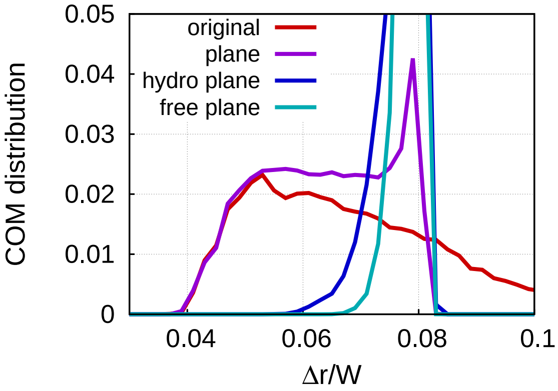

Figure 4.37.: COM distributions of a sphere with $D_\mathrm{c} = 0.28 D_\mathrm{r}$ for the original setup (red), platelets confined to the RBC-FL (purple), platelets confined to the RBC-FL and interactions with RBCs tuned off (blue), and platelets confined to a region of thickness comparable with the RBC-FL, but in a fluid without RBCs (cyan). All curves are for a pressure gradient induced by a force of $f' \approx 75 k_\mathrm{B} T/W$.
The distribution close to the wall develops due to the direct interactions with the RBCs and is only slightly influenced by hydrodynamic interactions.

as possible, because of the shear-induced migration, as presented in Fig. 4.37. However, for a fluid with RBCs, but excluded-volume interactions turned off, a slight shift of the curve is observed. To verify that the restriction does not change the distribution, simulations have been performed with the restriction for the platelets, while platelet and RBC interactions were turned on. Apart from the distance near to the barrier, these simulation results agree well with the results from the original simulation. It means that the hydrodynamic interactions close to the wall have only a weak influence on the platelet distribution. Thus, the platelet distribution is mainly generated by the direct interactions (collisions) with RBCs.

4.4.2. Hydrodynamic interactions turned off

With the former simulations, the effect of hydrodynamic interactions in and close to the RBC-FL has been studied. Additionally, different simulations have been performed to examine the influence of hydrodynamic interactions in the RBC populated region. Hence, the hydrodynamic interactions have been turned off, while excluded-volume interactions between RBCs and platelets by a LJ repulsion and reflections were considered. Therefore, two different background fluids have to be defined in the same simulation. One fluid interacts specifically with the RBCs and another fluid with the carriers, without interactions between the two fluids. The two fluids are driven by the same forces emulating the same pressure gradient.

First, COM distributions after a short simulation time are compared. For all carrier types, a larger number of carriers remained outside the RBC-FL for the simulations without hydrodynamic interactions, whereas the carriers in the normal simulations are already marginated, see Fig. 4.38 (top). However, the effect seems to be the weakest for the small carrier. This is confirmed by comparing the COM distributions after a considerably longer simulation time in Fig. 4.38 (bottom). The curves for the carrier with $D_\mathrm{c} = 0.15 D_\mathrm{r}$ are similar for both types of simulations. However, for the sphere with $D_\mathrm{c} = 0.3 D_\mathrm{r}$ and the ellipsoid, a reasonable number of carriers still remained in the RBC populated region. Thus, hydrodynamic interactions speed the margination up.

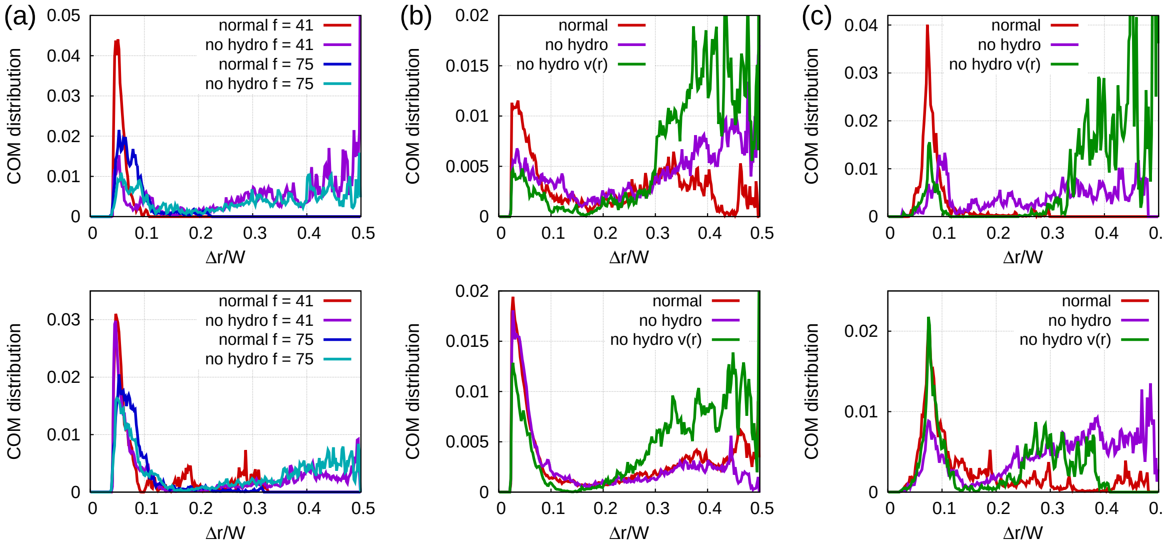

Figure 4.38.: Carrier COM distributions for (a) a sphere with $D_\mathrm{c} = 0.28 D_\mathrm{r}$, (b) $D_\mathrm{c} = 0.15 D_\mathrm{r}$, and (c) an ellipsoid. Compared are simulations with and without hydrodynamic interactions. The curves are averaged after a short simulation time (top) and a longer simulation time (bottom).
Without hydrodynamic interactions the carriers remain longer in the center of the channel. The effect is stronger for larger carriers.

The observations above agree well with force measurements on 2D carriers depending on the COM position. For these measurements, the center of a carrier was constrained by a harmonic potential to a specific distance to the wall and the force on the center has been measured in the course of a simulation. As presented in Figs. 4.39 (a,b), the carriers experience a positive force (a force in the direction to the wall) in the RBC populated region. The force vanishes in the middle of the channel and becomes negative close to the RBC-FL. The force increases with increasing hematocrit and average shear rate. The force measurements correspond to a potential for the carrier with a local minimum in the middle of the channel center and in the RBC-FL; see a shape estimation in Fig. 4.39 (c). Hence, in the channel as well as in the RBC-FL a high percentage of carriers should be expected, which is indeed observed for simulations without hydrodynamic interactions.

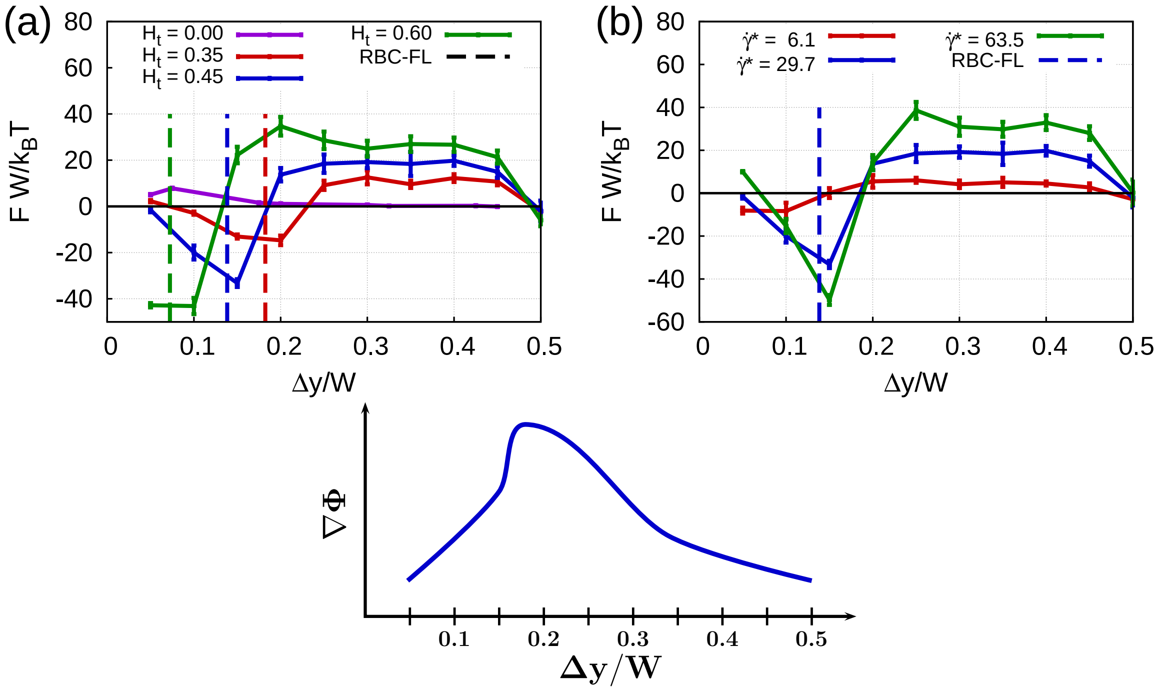

Figure 4.39.: Force on a carrier constrained by a harmonic potential at a specific distance Δy to the wall normalized by the channel width W. (a) Hematocrit has been varied with $\dot{\gamma}^* = 29.7$, (b) the average shear rate $\dot{\gamma}^*$ has been varied at $H_\mathrm{t} = 0.45$, and (c) a shape estimation of the corresponding potential.
The force on the carriers increases with increasing hematocrit and increasing shear rate. The forces predict that carriers are likely to stay in the RBC-FL, but also in the middle of the channel. This corresponds to the case without hydrodynamic interactions.

4.4.3. Summary

The following different simulation setups were used to investigate the influence of direct and hydrodynamic interactions between platelets and RBCs on the platelet distribution:

- Fluid without RBCs, normal Poiseuille flow.
- Fluid without RBCs, with velocity profile similar to simulations with RBCs.
- Fluid with RBCs, without direct (excluded-volume) interactions between RBCs and platelets.

- Fluid with RBCs, without direct interactions, platelets confined to RBC-FL.
- Fluid with RBCs, with direct interactions, platelets confined to RBC-FL.
- Separate fluids for RBCs and platelets, with direct interactions.
- Original, fluid with RBCs, with direct interactions, all cells free in the channel.

The comparison of simulations of platelets in a fluid without RBCs and with RBCs, but excluded-volume interactions turned off, indicate that with hydrodynamic interactions the shear-induced migration is slower and thus may increase the time platelets remain close to the wall. Furthermore, simulations of platelets confined to the RBC-FL, compared for a fluid without RBCs, a fluid with RBCs but direct interactions turned off, and with direct interactions turned on, indicate that the distribution in the RBC-FL is mainly induced by direct interactions (collisions) with the RBCs. However, simulations, with hydrodynamic interactions between platelets and RBCs turned off, show that the hydrodynamic interactions speed up the transport of platelets to the RBC-FL. The carriers with larger sizes are effected stronger by the missing hydrodynamic interaction, since the smaller spheres fit better between the RBCs, and thus collide less often with them and can more easily find a path between the RBCs towards the RBC-FL. It can be hypothesized that the flow around the RBCs guides the carriers through the available space past the RBCs. The flow reduces collisions and speeds up the transport to the RBC-FL, which fits well with the diverse times carriers need to enter or leave the RBC-FL. Furthermore, the flow around the RBCs is likely to influence also the orientation of the ellipsoid such that it fits better in between the RBCs. Additionally, the proposed induced fluctuations in the solvent which accelerate the margination process [14, 131] might be a reason as well. In order to separate the different mechanisms, further studies are required.

5. Von Willebrand factor stretching in simple shear and blood flow

At high shear rate regimes, e.g., in the microcirculation, the interaction of von Willebrand factor (VWF) and platelets is essential for a successful performance of the primary haemostasis. For instance, if wall shear rates exceed approximately $1500\,\mathrm{s}^{-1}$, platelet velocities are too high for direct binding and their adhesion is practically mediated by VWF [15]. Experiments have shown that the stretching of VWF triggers platelet as well as VWF adhesion to the vessel wall. However, the triggers, which lead to VWF unfolding in case of an injury, are still not fully identified. Therefore, the extension of a free-flowing and tethered VWF in simple shear flow is studied.

Another important aspect of primary haemostasis process is the availability of all necessary components near the site of injury, which is affected by their distribution within the vessel cross-section. As presented above in Chapter 4, platelets are subject to margination. However, more deformable blood components experience a stronger hydrodynamic lift, as observed numerically for polymers [193,194]. Furthermore, polymers can be used as therapeutic agents [41]. Therefore, the margination of polymers with different internal interactions in blood flow is also investigated.

5.1. Von Willebrand factor model

As proposed in literature [195], the VWF is modelled as a bead-spring chain with a monomer radius a_m, see Fig. 5.1, with an attractive interaction between its monomers. The interaction potential is given by

$$\frac{U}{k_BT} = \kappa_\mathrm{s} \sum_{i=1}^{N_\mathrm{m}-1} (r_{i+1,i} - 2a_\mathrm{m})^2 + \epsilon \sum_{ij} \left(\left(\frac{2a_\mathrm{m}}{r_{i,j}} \right)^{12} - 2 \left(\frac{2a_\mathrm{m}}{r_{i,j}} \right)^{6} \right), \tag{5.1}$$

where $r_{i,j} = r_i - r_j$ is the distance between two beads i and j. The first part of the potential corresponds to a harmonic spring between neighbouring beads with an equilibrium spring length of $2a_\mathrm{m}$ and the spring constant κ_s. In order to keep the distance of neighbouring monomers essentially constant, $\kappa_\mathrm{s} = 200k_\mathrm{B}Ta_\mathrm{m}^{-2}$ has been chosen in all presented simulations. The second part of the potential corresponds to a Lennard-Jones (LJ) interaction with the strength ϵ and the distance $2a_\mathrm{m}$ at which the potential reaches its minimum. On the one hand, the LJ interaction imposes excluded-volume interactions between the beads for bead distances $r_{i,j} < 2a_\mathrm{m}$. On the other hand, additional attractive interactions between the beads are included for bead distances of $r_{i,j} > 2a_\mathrm{m}$. The properties of two polymer types are explored. One polymer type (repulsive) employs only the repulsive part of the LJ interaction. The other polymer type (attractive) is modelled with the attractive part of the LJ potential, and the attraction strength is varied.

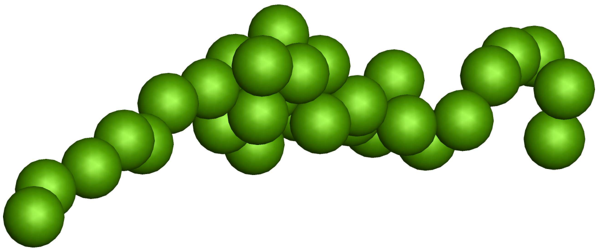

Figure 5.1.: Model of VWF as flexible polymer, described as a bead-spring chain. Snapshot from a 3D simulation.

5.2. Single von Willebrand factor in solvent

The velocity profile close to a vessel wall is approximately a simple shear flow. Hence, the behaviour of the introduced polymer types is investigated in simple shear flow. The focus is on the stretching of chains tethered to the wall and the effect of a platelet attached additionally to the chain. However, first, static properties and the stretching of free-flowing polymers in simple shear flow are compared to theory, other numerical investigations, and experiments.

5.2.1. VWF in equilibrium

The radius of gyration R_g, the second moment of the mass distribution, is a measurement to define a characteristic size of a polymer chain [196]. It is given by

$$\langle R_g^2 \rangle = \frac{1}{N_\mathrm{m}} \sum_{i=1}^{N_\mathrm{m}} (r_i - r_\mathrm{COM})^2 = \frac{1}{N_\mathrm{m}^2} \sum_{i=1}^{N_\mathrm{m}-1} \sum_{j=i+1}^{N_\mathrm{m}} (r_i - r_j)^2, \tag{5.2}$$

where r_i is the position of monomer i and r_COM is the mean position of all monomers. This characteristic size scales with the number of monomers N_m as

$$R_g \propto N_\mathrm{m}^\nu. \tag{5.3}$$

The exponent ν depends on the quality of the solvent. In a good solvent, the chain is swollen and behaves similar to a polymer chain with excluded-volume interactions between the segments. For a good solvent, the Flory theory yields the Flory exponent $\nu = 3/(d+2)$, where d is the dimension and which is exact for 1, 2 and 4 dimensions. Thus, in a 2D system for a good solvent the Flory exponent is $\nu = 3/4$. In a 3D system it is $\nu \approx 3/5$ [197] and experimental measurements yield $\nu = 0.588$ [198]. In a poor solvent the polymer chain is collapsed. The smallest globule can be achieved when monomers arrange in a close-packed configuration corresponding to $\nu = 1/d$. This leads to $\nu = 1/3$ for a 3D and $\nu = 1/2$ for a 2D system. The boundary between a good and a poor solvent is called theta solvent. In a theta solvent the polymer behaves similar to an ideal polymer chain with $\nu = 1/2$ in 2D and 3D. For an ideal chain, the attractive and repulsive interactions between the monomers are balanced, hence the connections between the beads describe a random walk. Interestingly, a 2D coiled polymer configuration in a poor solvent behaves as an ideal chain.

Numerically, the radius of gyration has been estimated in the course of a simulation and averaged over all timesteps after equilibration. The simulations have been performed in a periodic box with a length of $L_\mathrm{B} > 4R_g$, since it has been suggested that for these box sizes finite size effects can be neglected [199]. 2D simulations have been performed for polymers, which bead size corresponds to $a_\mathrm{m} = 0.3\,\mu\mathrm{m}$, with the number of beads $N_\mathrm{m} \in \{17, 26, 34, 42, 60, 80, 100\}$, and with the attraction strengths between the beads $\tilde{\epsilon} = \epsilon k_\mathrm{B}T$, with $\epsilon \in \{0.1, 0.5, 1, 1.25, 1.5, 2, 2.5, 4\}$. The curves in Fig. 5.2 show that changing the LJ interaction is the same as changing the quality of the solvent. With increasing ϵ the radius of gyration decreases. For high ϵ the curves for different N_m

overlap, since the average radius of gyration squared is normalized by $N_\mathrm{m}a_\mathrm{m}^2$ and for a poor solvent $R_g^2 \propto N_m$. The repulsive polymer behaves as a polymer chain in a good solvent. The configuration the attractive polymer adopts, depends on the interaction strength ϵ. With increasing attraction strength ϵ the exponent ν decreases. For high enough ϵ a close-packed configuration is reached. For the same polymer model in 3D similar results are obtained, see Fig. D.1 of Appendix D.

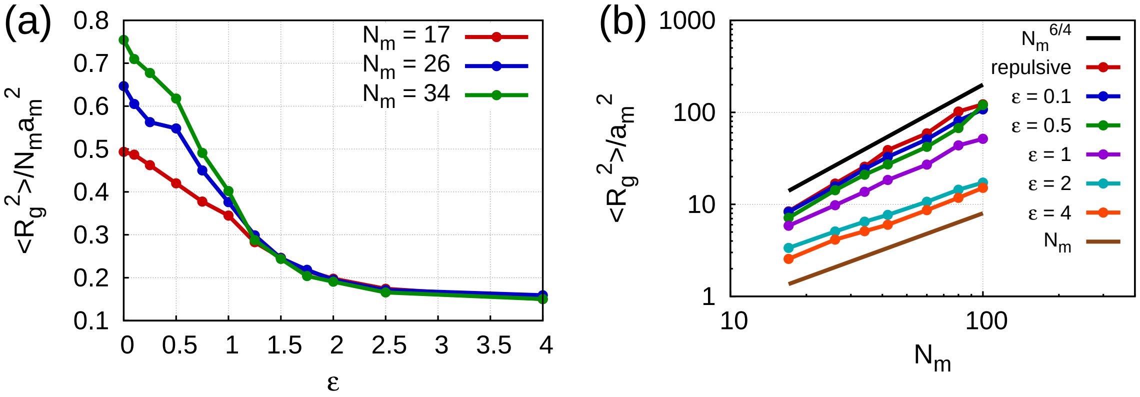

Figure 5.2.: Measurements of the 2D average radius of gyration squared $\langle R_g^2 \rangle$ of a polymer chain. (a) $\langle R_g^2 \rangle$ is normalized by $N_\mathrm{m}a_\mathrm{m}^2$, with N_m being the number of beads and the bead radius a_m, depending on the attraction strength $\tilde{\epsilon} = \epsilon k_\mathrm{B}T$. Different curves correspond to different chain lengths: $N_\mathrm{m} = 17$ (red), $N_\mathrm{m} = 26$ (blue), and $N_\mathrm{m} = 34$ (green). (b) Logarithm of $\langle R_g^2 \rangle$ depending on the number of beads compared to the expected scaling from theory. Different curves correspond to different monomer interactions. The radius of gyration for a repulsive polymer behaves as a flexible polymer in a good solvent and for increasing attraction strength the polymer coil is almost closed packed, as a polymer in a poor solvent.

For further investigations, a polymer with $N_\mathrm{m} = 26$ is employed whose contour length corresponds to $L = 15.6\,\mu\mathrm{m}$. This value has been motivated by the length of ULVWF [19]. For the attractive polymers, the two attraction strengths $\epsilon = 2$ and $\epsilon = 4$ have been employed, since the ϵ that corresponds to the theta-solvent is close to unity.

For these attraction strengths the polymers possess a nearly collapsed configuration. The radii of gyration for the employed polymers are on average: $\langle R_g \rangle = 4.1a_\mathrm{m}$ for $\epsilon = 4$, $\langle R_g \rangle = 4.5a_\mathrm{m}$ for $\epsilon = 2$, and $\langle R_g \rangle = 8.1a_\mathrm{m}$ for the repulsive polymer.

5.2.2. Free VWF in simple shear flow

In a next step, the stretching behaviour of the polymer chains in simple shear flow, depending on the shear rate, is examined. Therefore, the simulation setup consists of a slit geometry as for blood-flow simulations. The fluid parameters are also the same as in blood-flow simulations and are presented in the second row of Table B.5. The length of the channel in flow direction is $L_\mathrm{c} = 233.3a_\mathrm{m} = 4.49L$ and the width $W = 66.6a_\mathrm{m} = 1.28L$. In flow direction periodic boundary conditions are employed, whereas in the perpendicular direction, the fluid is confined by two walls. The simple shear flow has been obtained by moving these two walls in opposite directions with the same velocity magnitude. The shear rate $\dot{\gamma} = \Delta v/W$, with Δv being the velocity gradient between the walls, is normalized by the characteristic time scale $\tau = a_\mathrm{m}^2\eta/k_\mathrm{B}T$ to characterize the flow strength.

The behaviour of the free polymer has been examined for different distances to the wall. Therefore, the COM position y_COM of the polymer has been trapped at the distance y_COM to the wall by the spring potential

$$U_\mathrm{COM} = k_s(y_\mathrm{COM} - y_0)^2, \tag{5.4}$$

with the spring strength $k_s = 115.2k_\mathrm{B}T/a_\mathrm{m}^2$.

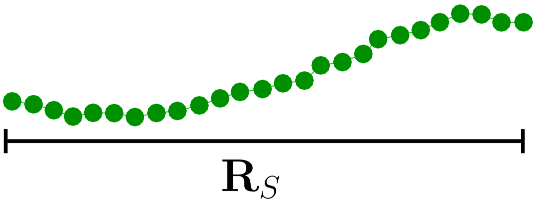

Figure 5.3.: Sketch of the measurements of the polymer extension R_S in flow direction.

A polymer in shear flow undergoes a periodic stretch-and-tumble motion [200]. The polymer extends, due to the different velocities to which different parts of the polymer are exposed to. The extension is followed by a tumbling that results in a partial collapse. The stretching of the polymer is measured as the extension in flow direction R_S, depicted in Fig. 5.3. Furthermore, for all presented results it has been surveyed that the extension is due to unfolding and that the bonds do not stretch. The bond probability distributions for some example cases are presented in Fig. D.2.

Figures 5.4 (a) and (b) display the time-dependent change of R_S for two polymer types, each for two shear rates. An increase in shear rate leads to an increase of the rotational velocity. This change can be identified through the similar frequencies of extension peaks for the repulsive polymer in Fig. 5.4 (a), since the time is scaled by the shear rate. The attractive polymer with $\epsilon = 4$ displays on average a lower extension than the repulsive polymer. Furthermore, at low shear rates it maintains a globular configuration.

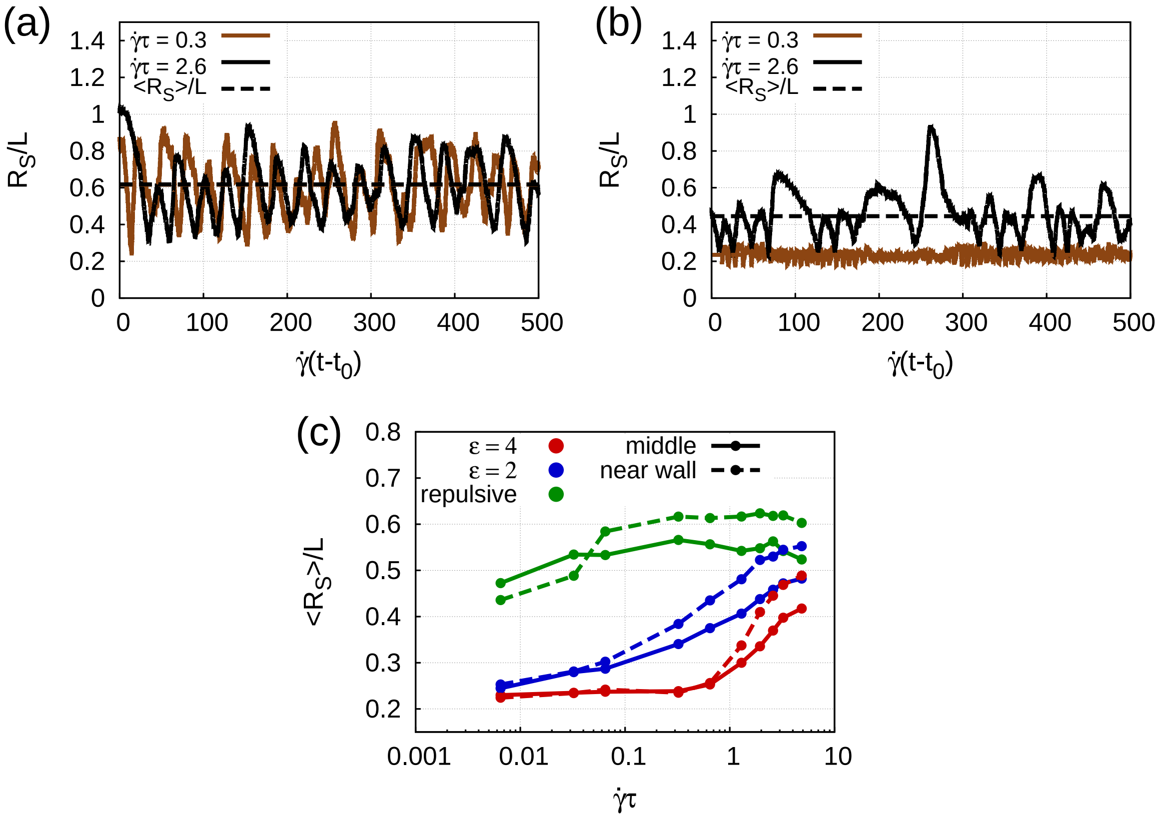

Figure 5.4.: Extension of polymer chains with different internal interactions. (a, b) Time-dependent extension R_S of a polymer chain for two shear rates $\dot{\gamma}\tau = 0.325$ (brown) and $\dot{\gamma}\tau = 2.6$ (black) for (a) the repulsive polymer chain and (b) an attractive polymer chain with $\epsilon = 4$. The extension is scaled by the length of the chain and the time t, starting from time t_0, is normalized by the shear rate $\dot{\gamma}$. The dashed lines show the corresponding averaged values. (c) Average extension $\langle R_S \rangle$ for all polymer types, the repulsive polymer (green), the attractive polymer with $\epsilon = 2$ (blue) and $\epsilon = 4$ (red) depending on the normalized shear rate $\dot{\gamma}\tau$. The solid curves correspond to the COM trapped at the middle of the channel and the dashed curves to the COM at $y_0 = 0.15W$, with W being the channel width.
For attractive polymers a critical shear rate has to be reached before unfolding events are observed. The critical shear rate depends on the attraction strength.

Figure 5.4 (c) presents the averaged extension $\langle R_S \rangle$ for these polymer types with respect to the normalized shear rate $\dot{\gamma}\tau$. For the investigated range of shear rates, the extension of the repulsive polymer shows a weak dependence on the shear rate, while the attractive polymers remain collapsed up to a critical shear rate. It has been observed in this study and other 3D numerical studies based on Stokesian dynamics [195] that especially for the attractive polymer the stretching starts with protrusions which emerge from the globule. If the force is high enough, the protrusions are pulled apart. For low shear rates the forces are too small to overcome the attractive forces acting on the protrusions from the globule. Thus, the critical shear rate as well as the width of globular-to-stretched transition strongly depends on ϵ. Furthermore, the polymer extension is more pronounced if it is located close to a wall [201], shown for a polymer trapped at a distance to the wall of $y_{\mathrm{COM}} = 0.15W$. For all polymer types an increase of extension is observed close to the wall. However, for the attractive polymers still a critical shear rate has to be exceeded to enable stretching. The lower the attraction strength, the larger is the change of the critical shear rate. The more pronounced extension of the VWF close to the wall increases the interaction probability with platelets and the subendothelium while prohibits it in the bulk, where it is unwanted. A comparison of the extension behaviour of the polymer to experimental results [19] indicates that the polymer model with $\epsilon = 4$ is most suitable to model the VWF.

The unfolding and folding depend on the shear rate and the viscosity, because those quantities mainly determine the time a protrusion exists and the force on the protrusion. The polymer extension has been measured for different fluid viscosities and shear rates, to validate that the extension of the globule is mainly dependent on the stress $\varsigma = \eta\dot{\gamma}$, and is independent of the particular viscosity of the fluid. Indeed, a good agreement of the curves in Fig. 5.5 confirms that the average extension depends mainly on the stress. The observed deviations for low viscosities are due to restrictions of the DPD simulation method. For too high velocities the fluid becomes compressible and the results may be unphysical [137].

Since the activity of the VWF depends strongly on its length, the stretching of polymers consisting of three different number of beads $N_{\mathrm{m}} \in \{17, 26, 42\}$ are compared for an attractive polymer with $\epsilon = 4$ in the middle of the channel and close to the wall. Interestingly, the ratio of the average extension and the polymer length is decreasing with increasing polymer size, see Fig. 5.6 (a). Nevertheless, the real extension of the longer chain is larger, which could promote platelet binding, see Fig. 5.6 (b). The larger polymer also seems to be effected more when placed near a wall, such that the change

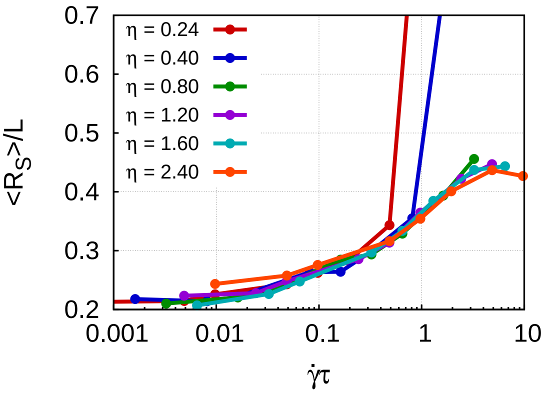

Figure 5.5.: Average extension $\langle R_S \rangle$ of an attractive polymer with $\epsilon = 2$ normalized by the polymer length L and depending on the normalized shear rate $\dot{\gamma}\tau$. Different curves correspond to different fluid viscosities $\tilde{\eta} = \eta k_{\mathrm{B}} T dt a_{\mathrm{m}}^{-2}$, with dt being the simulation timestep and a_{m} the bead radius.
The polymer extension depends mainly on the stress $\eta\dot{\gamma}$. Deviations from the expected curve for low viscosities are due to the compressibility of the DPD fluid.

of extension close to the wall increases with increasing chain length. However, all polymers were held at the same COM distance to the wall. Since the larger polymer has a larger radius of gyration, it is subject to stronger interactions with the wall. It can be expected that the small chain would show a similar dependence if it were held at a similar distance compared to its radius of gyration.

5.2.3. Tethered VWF in simple shear flow

The stretching of polymer chains with one end tethered to the wall is examined, to incorporate the adhesion of plasmatic VWF, but also the ULVWF stored in the subendothelium and the Weibel-Palade bodies, which are released in the case of an injury and remain tethered there [167, 202]. Therefore, the last bead at one end of the polymer chain has been fixed to the position $y = 0$ and has been moved with the same velocity as the wall.

In comparison to a free polymer, the attachment to the wall results in an increased extension of both repulsive and attractive polymers for the same shear rate, as presented in Figs. 5.7 (b-d). For the attractive polymers adhered to the wall, the critical shear rates for stretching are about one order of magnitude lower than that for a free chain. This is due to a different dynamics of a free and attached chain. The free polymer generally exhibits a cyclic transition between an extended and a globular conformation during its rotation in shear flow, while the rotation of an attached polymer is frustrated.

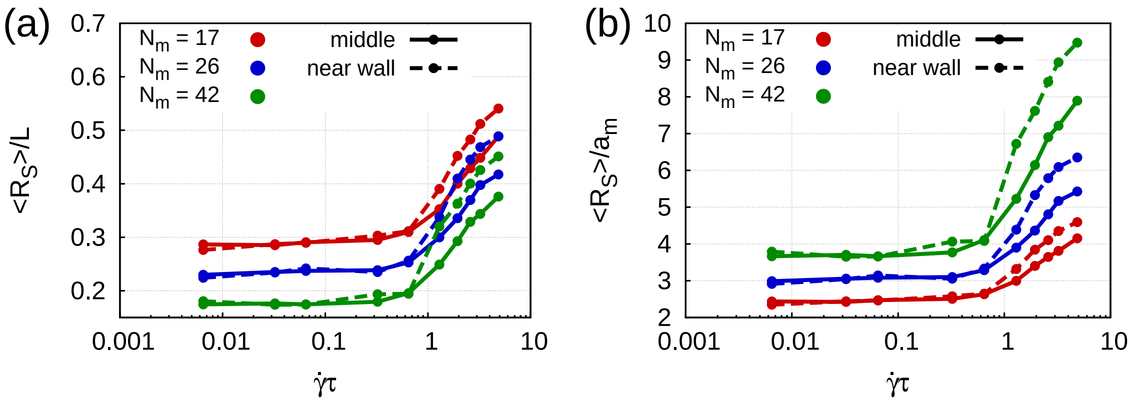

Figure 5.6.: Average extension $\langle R_S \rangle$ of the attractive polymer with $\epsilon = 4$ (a) scaled by the polymer length L and (b) scaled by the monomer radius a_m. The considered bead numbers of the chains are $N_\mathrm{m} = 17$ (red), $N_\mathrm{m} = 26$ (blue), and $N_\mathrm{m} = 42$ (green). The position of the COM of the polymer is either fixed to the middle of the channel (solid curves) or fixed to the distance $y_0 = 0.15W$ from the wall, with the channel width W (dashed curves).
The larger the chain the smaller is the ratio of the extension and its length, but the larger is the ratio of extension and the monomer radius.

Therefore, the attached polymer is quasi-stationary extended and the extension of the polymer is given by the competition between the stretching forces and the attractive forces. Thus, adhesion of the VWF to the wall is identified as a trigger for extension. Furthermore, this explains the advantage of the released and tethered ULVWF strings, which might be able to stretch and thus expose binding sites for the prevailing shear rate, while plasmatic VWF remains collapsed.

In addition, platelet adhesion to the VWF further facilitates its stretching. The platelet consists of connected beads which are constrained to a rigid configuration and it has a diameter of $D_\mathrm{c} = 0.12L$. The platelet has been fixed to the free end of the polymer by trapping it between the last two beads of the polymer chain, see Fig. 5.11. The excluded-volume interactions between the beads of the polymer and the platelet prevent the escaping of the platelet. The springs between the platelet beads and the polymer beads, respectively, are strong enough to prevent stretching of the beads. Interestingly, platelet adhesion mainly influences the extension of the attractive polymers. For them the critical shear rate is considerably further decreased. Thus, adhesion of platelets of the VWF may facilitate the extension of the VWF and following makes adhesion of further platelets and VWF possible.

The average density distribution depending on the x- and the y-position in the channel are measured to characterize the configuration of the polymer chains under these differ-

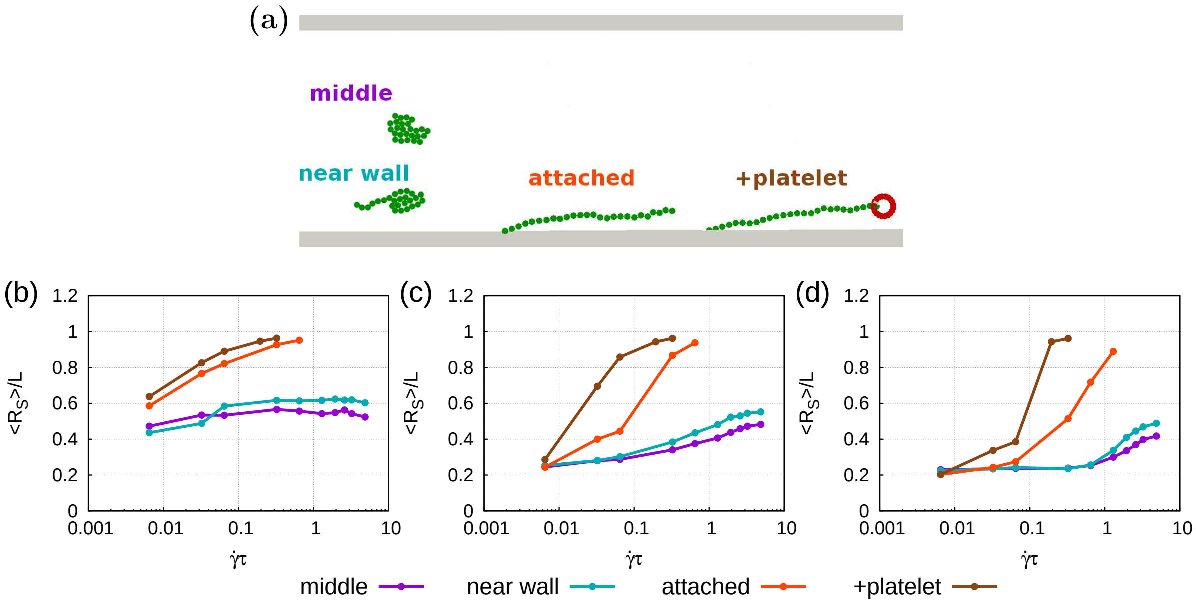

Figure 5.7.: Average extension $\langle R_S \rangle$ of polymers normalized by the polymer length L depending on the normalized shear rate $\dot{\gamma}\tau$ for a polymer coil in the middle of the channel (purple), at a COM position $y_0 = 0.15W$ (cyan), attached to the wall (orange), and attached to the wall with an adhered platelet (brown). (a) Assembled snapshots of polymers in simulations, (b) repulsive polymer, and (c,d) attractive polymers with (c) $\epsilon = 2$, and (d) $\epsilon = 4$.
Tethering of the polymer to the wall and the adhesion of a platelet increases the polymer extension drastically. By tethering the polymer the critical shear rate for extension is reduced by about one order of magnitude.

ent conditions. The density distributions in Fig. 5.8 for tethered polymer chains and in Fig. 5.10 for tethered polymer chains with an attached platelet are for all considered polymer types (horizontal) and for three different normalized shear rates $\dot{\gamma}\tau = 0.0065$ (a), $\dot{\gamma}\tau = 0.065$ (b), and $\dot{\gamma}\tau = 0.325$ (c). These density distributions have been calculated from simulation snapshots. Thus, the bead positions have been analysed such that the tethered bead is always located at $x = 0$.

The repulsive polymer chain possesses large fluctuations for low shear rates, which becomes evident by the broad density distribution and low local densities. A snapshot for the case $\dot{\gamma}\tau = 0.0065$ is shown in Fig. 5.9 (a). With increasing shear rate, fluctuations are reduced, the chain remains in a narrower y-range, and the local density increases. The attractive polymers are collapsed for the low shear rates. For $\epsilon = 4$ and $\dot{\gamma}\tau = 0.0065$, the globule is even symmetric with the center at the x-position of the tethered bead. The polymer with $\epsilon = 2$ shows higher fluctuations than $\epsilon = 4$. This becomes apparent by the lower local densities and broader distributions. With increasing shear rate, a part of the loose end remains collapsed, whereas the chain closer to the tethered point becomes stretched. For $\dot{\gamma}\tau = 0.325$ the distribution for the repulsive polymer and the attractive polymer look rather similar, whereas the attractive polymer with $\epsilon = 4$ is still partially coiled. Comparison of the cases $\epsilon = 2$ at $\dot{\gamma}\tau = 0.065$ and $\epsilon = 4$ at $\dot{\gamma}\tau = 0.325$ shows that the coil configurations are different. The distribution looks more round for the polymer with $\epsilon = 2$, whereas it looks more rectangular for $\epsilon = 4$. This is confirmed by the snapshots presented in Figs. 5.9 (b) and (c). The polymer chain for $\epsilon = 4$ is folded in three layers, whereas for $\epsilon = 2$ the chain is wound-up.

The force on the chain beads close to the globule is determined by the friction of the globular polymer part and the adhesion strength of the polymer coil. On the one hand, the adhesion strength determines the force that is needed to pull the globule apart. On the other hand, comparison of Fig. 5.9 (b) and Fig. 5.9 (c) indicates that the coil for $\epsilon = 2$ has a more spherical shape and experiences higher velocity gradients which increase the friction force. For instance, the drag on a sphere, the Stokes friction $F_{St} = 6\pi\eta R v$, is proportional to the velocity v and the radius R of a sphere. The applied LJ attraction is short ranged, since at distances larger than three bead diameters the potential vanishes. Therefore, it is beneficial that the polymer with strong internal interactions does not form a spherical shape but a layered configuration, since this shape induces less friction. In addition, with increasing shear rate, the number of layers is reduced.

With an attached platelet, the polymer configurations change. The polymers reach larger y-positions, due to the finite extension of the platelet and thus are exposed to

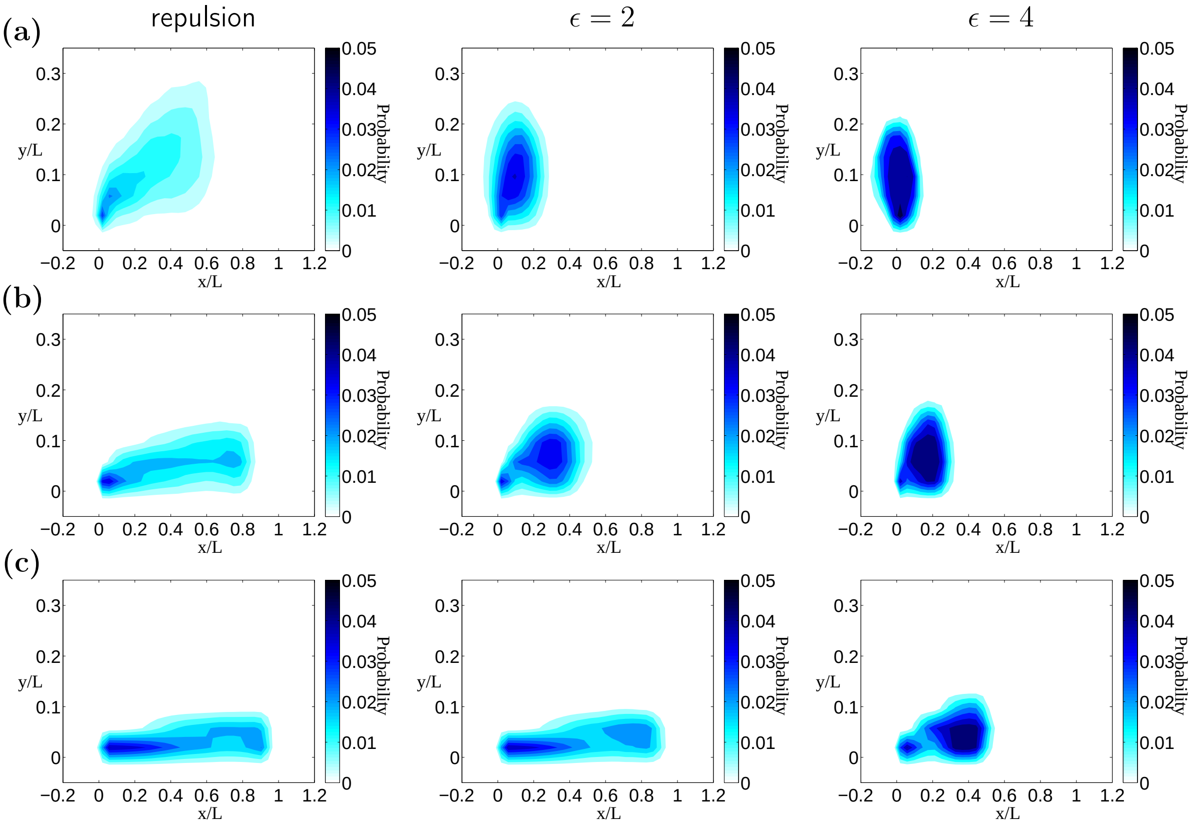

Figure 5.8.: Density probability distribution depending on the x- and y-coordinate, both scaled by the length of the polymer L. The colour code ranges from white (low probability) to blue (large probability). The tethered bead has always the position $x = 0$. Different columns correspond to different polymer types: (left) repulsive, (middle) attractive with $\epsilon = 2$, and (right) $\epsilon = 4$. Different columns correspond to different shear rates (a) $\dot{\gamma}\tau = 0.0065$, (b) $\dot{\gamma}\tau = 0.065$, (c) and $\dot{\gamma}\tau = 0.325$.
Less attraction corresponds to broader distributions. For high shear rates the distribution of the repulsive polymer and the attractive polymer with $\epsilon = 2$ are similar.

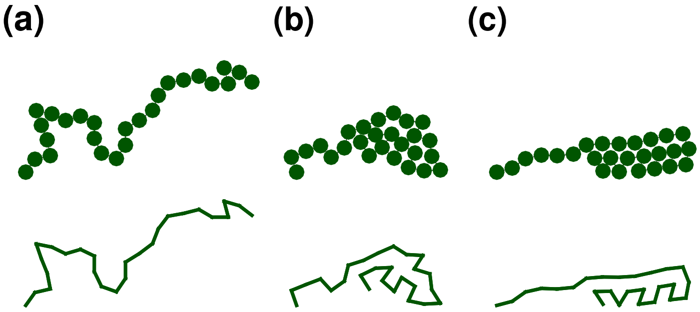

Figure 5.9.: Polymer snapshots for tethered polymers showing (top) the chain beads and (bottom) the bonds to illustrate the folding. (a) Repulsive polymer at $\dot{\gamma}\tau = 0.0065$, (b) attractive polymer with $\epsilon = 2$ at $\dot{\gamma}\tau = 0.065$, and (c) $\epsilon = 4$ at $\dot{\gamma}\tau = 0.325$.
The attractive polymer with $\epsilon = 2$ shows a more circular configuration while with $\epsilon = 4$ the polymer is folded similar to a rectangular block.

larger flow velocities which additionally increase the friction in addition to that already induced by the existence of the platelet. For the repulsive polymer, the density profiles are more narrow in the diagonal direction, which indicates that fluctuations are suppressed. Beside the low shear rate, the distributions for the repulsive and the attractive polymer with $\epsilon = 2$ are rather similar. For $\epsilon = 4$ at low shear rates, the polymer is still coiled but the globule is forced to higher x-values, due to the presence of the platelet. With increasing shear rate not only the chain portion between the tether point and the globule but also a short part between the globule and the attached platelet are stretched. Furthermore, the globular part is less ordered and therefore more round, due to induced fluctuations by the platelet, see Fig. 5.11.

The second row in Fig. 5.9 already indicates that the globular part of the polymer chains have an interesting internal structure. A deeper insight into the structure of the globules is given by the average y-position of the various beads depending on the bead number n, presented in Fig. 5.12 for all the polymer types, different shear rates, and with and without an attached platelet. For the platelet-free repulsive polymer, the polymer chain protrudes more into the channel the further the bead is away from the tethering point. Only the highest bead numbers show a decrease, due to fluctuations of this beads. For the platelet-free attractive polymers, the oscillations indicate the folding of the polymer chain into the globule. The broad variations for the $\epsilon = 2$ polymer indicate that the beads follow a circular path. For $\epsilon = 4$ smaller variations are observed indicating an additional zig-zag structure. Interestingly, the highest point is always the first maximum. The chain folds under the stretched chain to reduce friction. The decreasing values with increasing shear rate indicate that the globule consists of less rows with increasing shear rate. For the polymers with attached platelet the profiles confirm that the chain with $\epsilon = 4$ shows a similar profile than $\epsilon = 2$ without the platelet. The chain possesses less zig-zag structure, but is ordered more circular. Furthermore, the chains for $\epsilon = 2$ at very low shear rates and $\epsilon = 4$ at intermediate shear rates are almost stretched but the beads still form a zig-zag structure, see also Fig. 5.11 (b).

Experiments indicated that stretching of VWF triggers the adhesion of VWF to the wall, but also adhesion of platelets to the VWF [19, 29–32]. The reason is that due to stretching the dimer domains become exposed facilitating the binding [203]. Numerically, this process is too complex to simulate on an atomistic level, since realistic simulations of subdomains of the dimer require already immense computational effort [204]. In the presented coarse-grained simulations it seems plausible to correlate possible adhesion to the angle between two bonds to incorporate the conformational change. This angle is

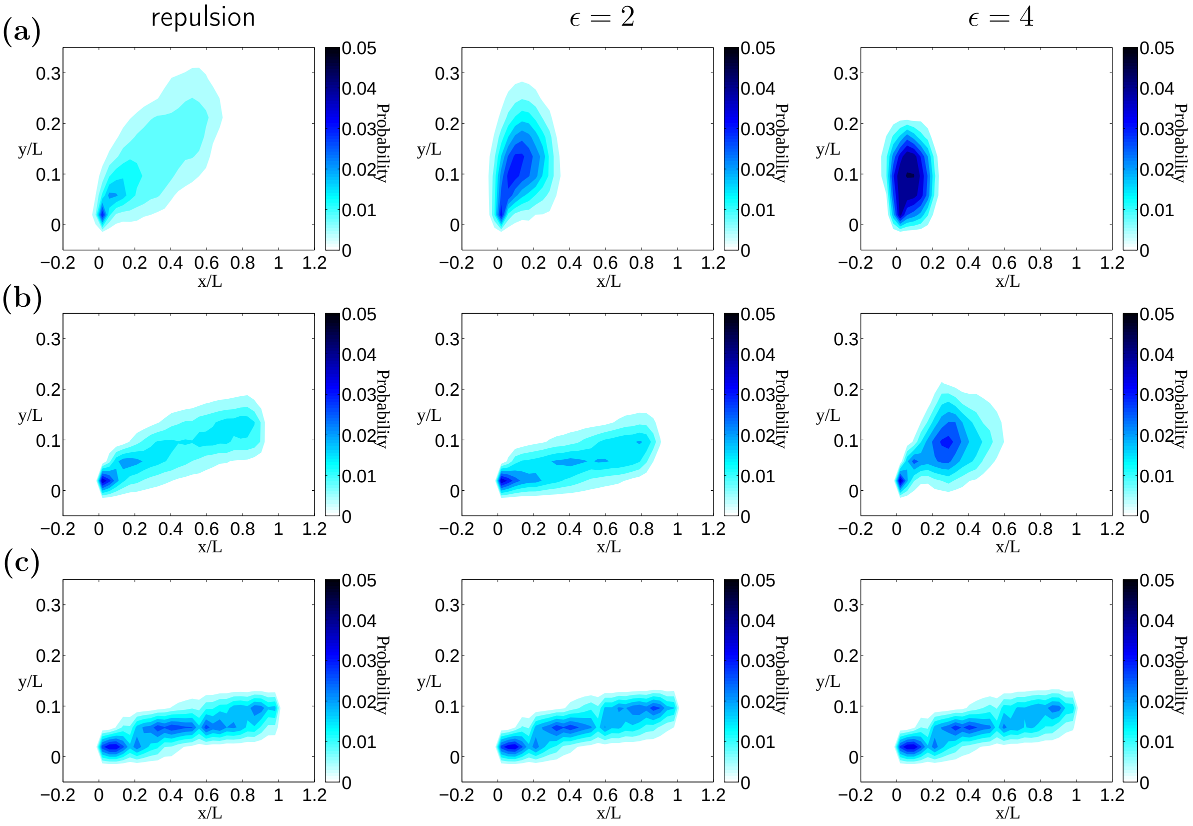

Figure 5.10.: Density probability distribution depending on the x- and y-coordinate, both scaled by the length of the polymer L. The colour code ranges from white (low probability) to blue (large probability). The tethered bead has always the position $x = 0$. Different columns correspond to different polymer types: repulsive (left), attractive with $\epsilon = 2$ (middle), and $\epsilon = 4$ (right). Different rows correspond to different shear rates (a) $\dot{\gamma}\tau = 0.0065$, (b) $\dot{\gamma}\tau = 0.065$, and (c) $\dot{\gamma}\tau = 0.325$.
Adhesion of a platelet leads to further extension of all polymers. For an intermediate shear rate the attractive polymer with $\epsilon = 4$ is more fluctuating than without a platelet and the profile looks similar to the polymer with $\epsilon = 2$ without a platelet. They experience higher velocity gradients and for the highest shear rate all three polymer configurations look similar

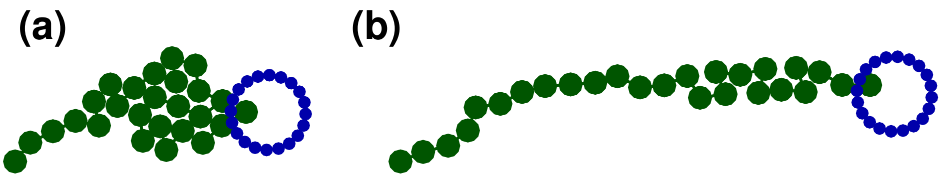

Figure 5.11.: Snapshots of a polymer with an attached platelet for the attractive polymer with $\epsilon = 4$ at two shear rates (a) $\dot{\gamma}\tau = 0.0325$ and (b) $\dot{\gamma}\tau = 0.065$.
The globule looks more round than without a platelet, and although the chain is almost stretched, the beads order in a zig-zag structure. A similar configuration as in (b) is observed for the attractive polymer with $\epsilon = 2$ at shear rate $\dot{\gamma}\tau = 0.0325$.

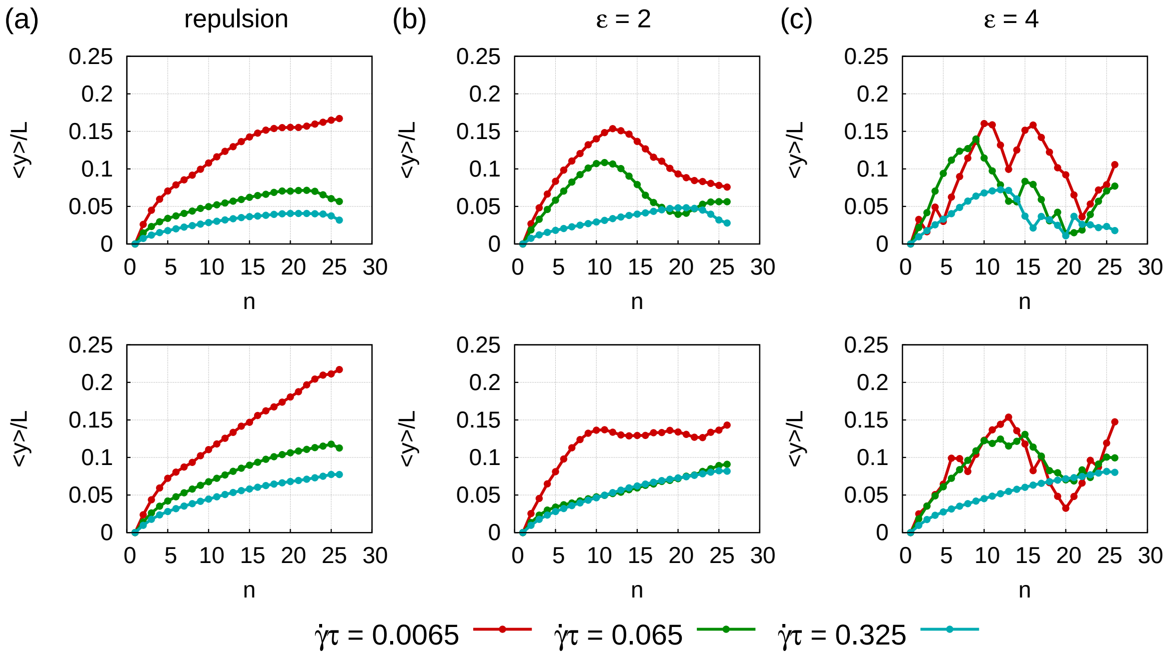

Figure 5.12.: Average y-position scaled by the polymer length L for all beads with number n for (a) the repulsive polymer, (b) the attractive polymer with $\epsilon = 2$, and (c) the attractive polymer with $\epsilon = 4$. (top) The polymers are tethered with one end to the wall and (bottom) additionally a platelet is attached to the free end of the chain. Different curves correspond to different normalized shear rates: $\dot{\gamma}\tau = 0.0065$ (red), $\dot{\gamma}\tau = 0.065$ (green), and $\dot{\gamma}\tau = 0.325$ (cyan).
With adhered polymer the configuration of the attractive polymer with $\epsilon = 4$ is similar to the one of the polymer with $\epsilon = 2$ without an attached platelet.

calculated with the aid of the trigonometric relation $\cos(\varphi) = (l_{12}^2 + l_{23}^2 - l_{13}^2)/(2l_{12}l_{23})$, with l_{ij} being the distance between the beads i and j, where the beads 1 and 2, and 2 and 3 are connected by bonds. Figure 5.13 presents the angle probability distribution, for different shear rates and configurations. For the repulsive polymer the probability increases with increasing angle. However, with increasing shear rate the difference between small and large angles increases. For attractive polymers at low shear rates, which model the VWF, the lowest angle has the highest probability. With increasing shear rate the angle distribution shifts to larger angles. For the stretched configurations, all angles are close to 180°. The three distinct peaks, which can be identified for the attractive polymers, are at the three angles $\varphi = 60°, 120°$ and $180°$. This peaks are due to the packing of the particles as depicted in Fig. 5.14.

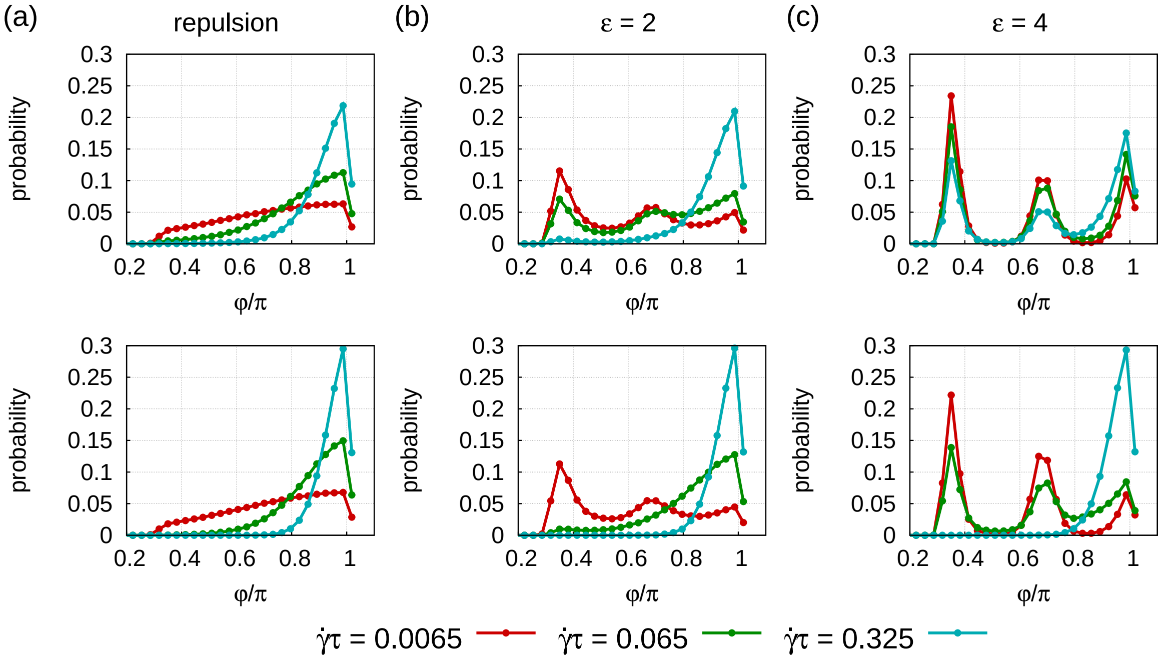

Figure 5.13.: Probability distribution of angles φ between neighbouring bonds scaled by π for (a) the repulsive polymer, (b) the attractive polymer with $\epsilon = 2$, and (c) the attractive polymer with $\epsilon = 4$. (top) The polymers are tethered with one end to the wall and (bottom) additionally a platelet is attached to the free end of the chain. Different curves correspond to different normalized shear rates: $\dot{\gamma}\tau = 0.0065$ (red), $\dot{\gamma}\tau = 0.065$ (green), and $\dot{\gamma}\tau = 0.325$ (cyan).
For the repulsive polymer the largest angles have always the highest probability. For the repulsive polymers the largest probability shifts from low to large angles with increasing shear rate. The peaks occur at $60°$, $120°$, and $180°$, due to the packing of the attractive polymers, see Fig. 5.14.

So far, averaged properties have been considered to shed light on the configuration

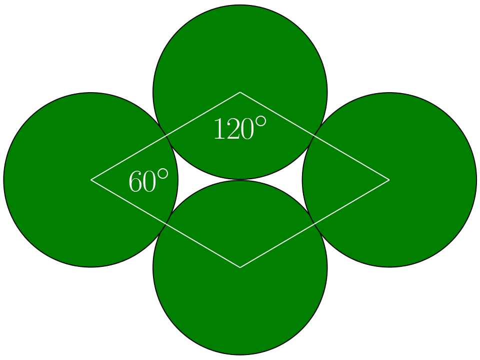

Figure 5.14.: Illustration of the angle distribution in the polymer coil with peaks at 60°, 120°, and 180°.

of the polymers. However, examining the time-dependent extensions of the adhesive polymers, considerable fluctuations can be observed at long timescales. Some example cases are presented in Fig. 5.15. This indicates that the permanent competition between the friction and the adhesion force leads to an alternating extension with time. However, to investigate those fluctuations in more detail much longer simulations are needed, which is out of the scope of this work.

5.2.4. Summary

The inclusion of an attractive interaction between the beads of a bead-spring polymer chain leads to close-packed polymer globules. Under simple shear flow, the polymers with attractive interactions possess a stress-dependent cyclic stretching, in contrast to a polymer with just excluded-volume interactions between the beads. The stronger the attraction, the larger is the critical shear rate, at which protrusions can lead to unfolding of the chain and the steeper is the transition from coiled to stretched. The polymer, modelled with the strongest attraction strength $\epsilon = 4$ is an appropriate model for the VWF, as the shear-rate dependent extension indicates. Furthermore, longer chains stretch to longer conformations.

By tethering one end of the polymer to the wall, the critical shear rate reduces by one order of magnitude and larger extensions are observed. Adhesion of a platelet to the free end further decreases the critical shear rate and increases the extension. Although, both examined attractive polymers, which were modelled with different attraction strengths, were almost closed packed under static conditions, under simple shear flow the configuration and the extension behaviour is considerably different. For low shear rates, the polymer with the adhesion strength $\epsilon = 2$ possess more roundish and loose configuration,

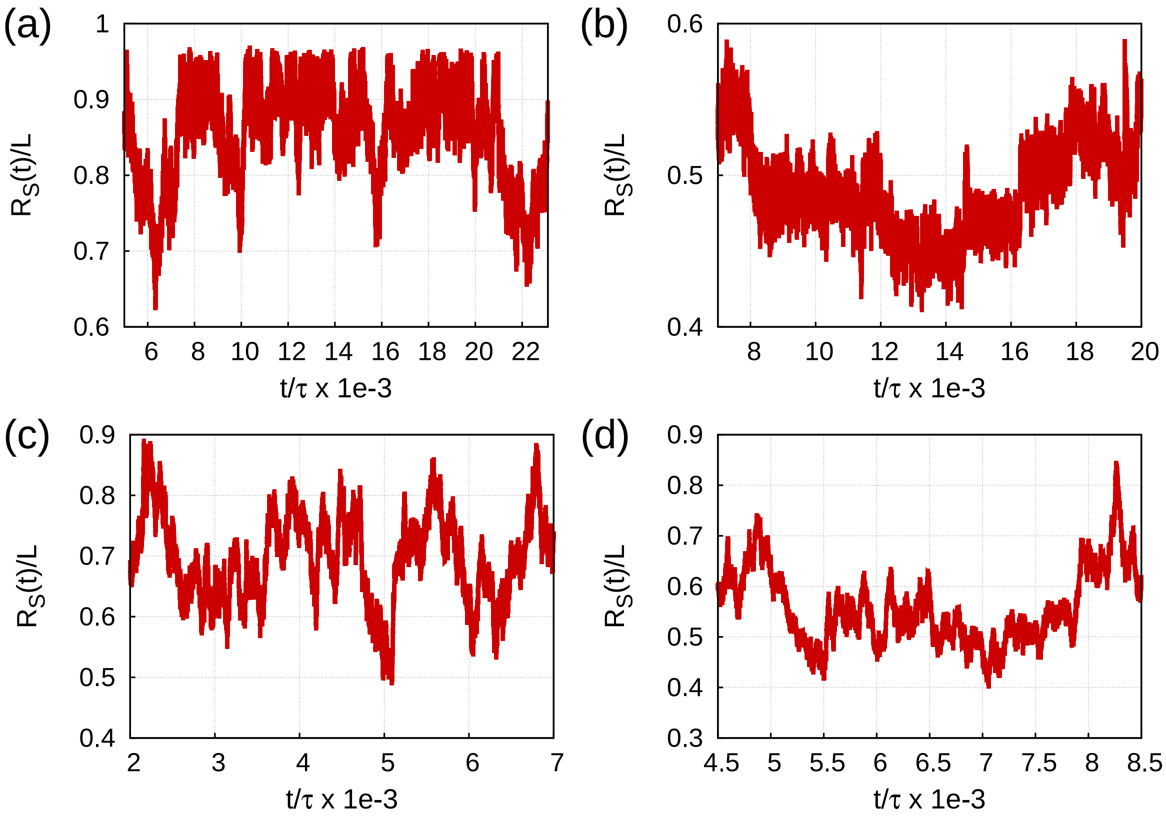

Figure 5.15.: Examples for variations of the time-dependent extension $R_S(t)$ of tethered attractive polymer chains at different normalized shear rates $\dot{\gamma}\tau$. (a) $\epsilon = 2$, $\dot{\gamma}\tau = 0.325$, (b) $\epsilon = 4$, $\dot{\gamma}\tau = 0.325$, (c) $\epsilon = 2$, $\dot{\gamma}\tau = 0.0325$ with attached platelet, and (d) $\epsilon = 4$, $\dot{\gamma}\tau = 0.0325$ with attached platelet. The extension is normalized by the polymer length L and the time t by the typical system time τ.
At long timescales large alternating fluctuations of the extension are observed.

whereas the polymer with the strong adhesion strength $\epsilon = 4$ has a more rectangular folded configuration. For higher shear rates, the configuration of the polymer with $\epsilon = 2$ possess configurations similar to a polymer with only excluded-volume interactions between the beads. For an attached platelet, the configuration of the polymer with the $\epsilon = 4$ is similar to the polymer with $\epsilon = 2$ without an attached platelet.

As a result, the following scenario can be sketched to describe the primary haemostasis. Due to an injury, collagen is exposed to the blood and/or stored ULVWF is released. Since the released ULVWF is still anchored to the vessel wall, it unfolds although the plasmatic VWF remains in its almost globular configuration. Therefore, platelets as well as the plasma VWF can bind. Close to the wall the VWF is able to stretch, which increases the binding probability. With a bound platelet which also slides along the VWF, stretching proceeds further and other VWF and platelets can bind more easily. This leads to onset of the whole cascade. This fits to experimental results where platelet adhesion is mediated by plasma VWF alone, but needed a considerable longer time compared to the case with wall-bound VWF [205]. However, not considered in this work is that for larger lesions the flow close to the wall changes. The elongational part of the flow is likely to become important. It has been shown that elongational flow promotes further stretching of plasmatic VWF [206] and thus adhesion to the wall and to platelets.

Furthermore, incorporation of adhesion of VWF to the wall and of platelets to the VWF would require an adhesion potential which depends on the angle between two neighbouring bonds, since especially for the attractive polymers the angle distribution shifts from small to large angles for increasing shear rate. Although adhesion is out of the scope of this work, it should be mentioned that recent numerical studies suggest catch bonds [207,208] as an appropriate interaction mechanism. Furthermore, for chains tethered to the wall, slow alternating extensions are observed which might be interesting for further studies.

5.3. Von Willebrand factor margination

Sufficient extension of VWF, to provide adhesion of VWF and platelets to the wall, occurs close to the vessel wall and is increased by VWF adhesion, as seen above. Experimental [209,210], numerical, and theoretical studies [211–214] have shown that flexible as well as semiflexible polymers [215] in a dilute suspension undergo cross-stream migration in simple shear and Poiseuille flow. In low confinement, where the channel width is larger than the radius of gyration ($W/R_g > 5$), the polymers migrate to the channel center for both, simple shear and Poiseuille flow, due to hydrodynamic interactions with the walls. In simple shear flow a peak in the middle of the channel develops, whereas for Poiseuille flow they possess a symmetric double peak for large Péclet numbers, due to the different extension and diffusivity for different shear rates [209–215]. The Péclet number is the ratio of the convective to the diffusive transport rate [58]. In strong confinement, where the channel width is smaller or comparable to the radius of gyration ($W/R_g \leq 5$), the polymers migrate to the channel wall, since the hydrodynamic interactions with the wall, which lead to migration to the center, are screened [212, 213]. However, in blood flow the VWF has to marginate to the wall even in low confinement. Hence, the focus in this section is to elucidate how the margination of polymers changes for different blood-flow conditions and polymer types. Furthermore, the stretching of the polymer is analysed and the polymer margination is compared to platelet margination.

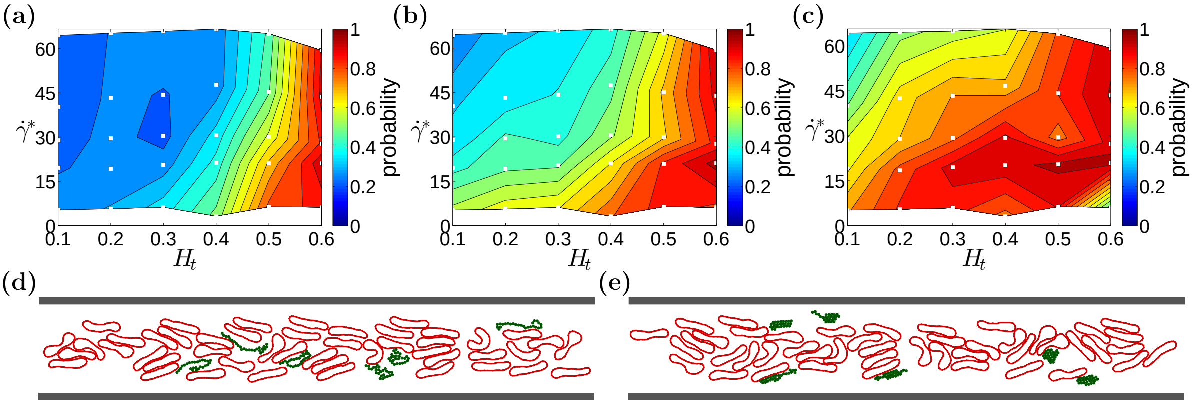

Figure 5.16.: Margination diagrams and snapshots for the (a,d) repulsive polymer, (b) the attractive polymer with $\epsilon = 2$, (c,e) and $\epsilon = 4$. The white squares (□) indicate the values of H_t and $\dot{\gamma}^*$ for which simulations have been performed. The colour code ranges from blue (low probability) to red (high probability) and is acquired via interpolation. Both snapshots are for the system parameters $H_\mathrm{t} = 0.3$ and $\dot{\gamma}^* \approx 29.7$.
The attractive polymer with $\epsilon = 4$ marginates drastically better than the other two. The snapshots indicate that the margination is related to the stretching of the polymers. The repulsive polymer fits better between the RBCs in the bulk and can come closer to the RBCs at the RBC-FL border.

Figure 5.16 presents the polymer margination into the RBC-FL depending on the hematocrit and shear rate $\dot{\gamma}^*$ in a channel of width $W = 3.28D_\mathrm{r}$ for the repulsive polymer and the attractive polymers with $\epsilon = 2$ and $\epsilon = 4$, respectively. The margination probability is clearly highest for the attractive polymer with $\epsilon = 4$ than for the other ones for all shear rates and for $H_t < 0.5$. For large hematocrit values also for the attractive polymer with $\epsilon = 2$ and the repulsive polymer notable margination is observed. The margination probability of the attractive polymer with $\epsilon = 2$ is higher than that for the repulsive polymer especially for low shear rates. However, the margination for $\epsilon = 2$ is closer to the repulsive polymer than to the $\epsilon = 4$ polymer. The snapshots in Figs. 5.16 (d) and (e) at $H_\mathrm{t} = 0.3$ and $\dot{\gamma}^* = 29.7$ illustrate that the extension of the polymers change. The more flexible the polymer, the larger is the lift force from the wall and the lower is the margination. Additionally, the extension of the polymer determines how well the polymer can slide between the RBCs and it defines the distance the polymer can have to the RBCs, if it is located close to the RBC-FL. The comparison of the polymer margination diagrams with the platelet margination diagrams in Fig. 4.15 shows that the polymer margination is more influenced by changes of the average shear rate. With increasing average shear rate the margination decreases. This is likely to be due to the increase of local shear rates which extend the polymer and change the polymer configuration.

For a more quantitative analysis of the polymer extension in blood flow, Fig. 5.17 presents the extension of the polymer depending on the distance of the COM position to the wall. The extension of the repulsive polymer differs only slightly for different shear rates, which explains why the margination of this polymer type is almost independent of shear rate. With increasing hematocrit, the COM of the polymer approaches closer the wall where the polymer also stretches more. However, for larger distances from the wall a change of hematocrit seems to have no considerable effect. For the attractive polymers, an increase of stretching with increasing hematocrit as well as shear rate is found. The effect is more pronounced for the polymer with stronger attraction. These observations illustrate the reduced margination for increasing shear rates. A less globular polymer experiences a higher lift force and due to the stretching the polymer fits better in between the RBCs and also can come closer to the RBCs if it is located in the RBC-FL. At higher shear rates the differences for different H_t become more pronounced, whereas for high hematocrit values the difference between different shear rates is less pronounced. Noteworthy is the drop of extension close to the RBC-FL before the extension increases drastically, that is monitored for all three polymers.

Figure 5.18 compares the extension of the three polymer types for two hematocrit values and two shear rates. For low hematocrit values the repulsive polymer is most stretched over the whole channel and changes only slightly for different distances to the wall. However, the attractive polymer with $\epsilon = 4$ exhibits a clear increase with decreasing distance to the wall. With increasing hematocrit and shear rate, the differ-

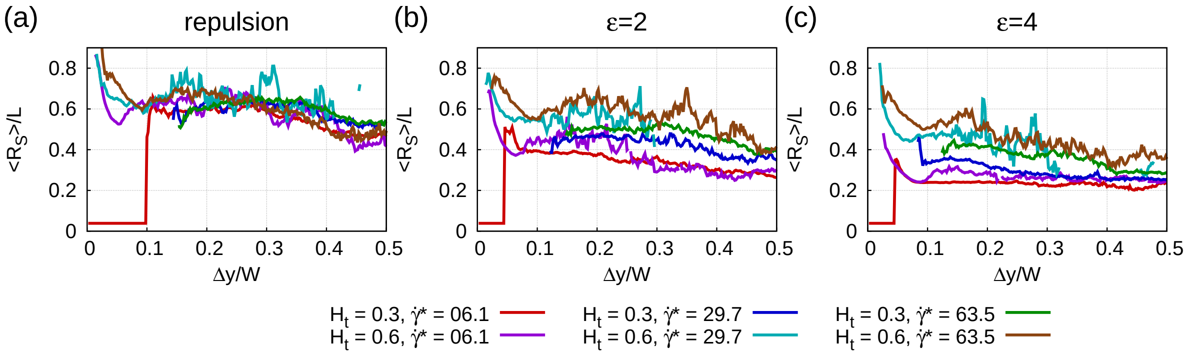

Figure 5.17.: Average extension $\langle R_S \rangle$ normalized by the polymer length L depending on the distance Δy of the COM position to the wall normalized by the channel width W for the (a) repulsive polymer, (b) the attractive polymer with $\epsilon = 2$, and (c) the attractive polymer with $\epsilon = 4$. Different curve colours correspond to different combination of hematocrit values ($H_\mathrm{t} \in \{0.3, 0.6\}$) and average shear rates $\dot{\gamma}^* \in \{6.1, 29.7, 63.5\}$. For all polymer types the extension increases drastically in the RBC-FL. The stronger the attraction, the more the extension depends on the hematocrit and the shear rate.

ences between the polymer types diminish. Especially for the shear rate $\dot{\gamma}^* = 63.5$ and $H_\mathrm{t} = 0.6$, the curves for the repulsive polymer and the attractive polymer with $\epsilon = 2$ overlap. However, for all cases the attractive polymer with $\epsilon = 4$ is less extended in the bulk but can extend to similar lengths in the RBC-FL.

In order to examine the elongation of the polymer depending on the local shear rate in blood flow, the channel is divided into several layers in y-direction. For every layer a local shear rate is estimated from the velocity profile assuming simple shear flow in this region. The measured extension is then associated with the shear rate of the layer the COM is located in. In Fig. 5.19 the extension of a polymer depending on the local shear rate in blood flow is compared to the extension in simple shear flow. For the repulsive polymer the extensions in blood flow are similar to those in simple shear flow. However, for the attractive polymers the extension is increased. This indicates that interactions with RBCs favour stretching, since the largest values correspond to high hematocrit values. The effect is more pronounced the higher the local shear rate and the stronger the attraction strength is.

Finally, the VWF COM distributions are compared to each other and to the distributions of circular platelets with a diameter of $D_\mathrm{c} = 0.15$. As in Chapter 4 the distance of the peak (Fig. 5.20) and the distance of the mean position in the channel (Fig. 5.21) to the wall are examined. The distance of the peak as well as the mean position in the whole channel to the wall is for the attractive polymer with $\epsilon = 4$ at low shear rates

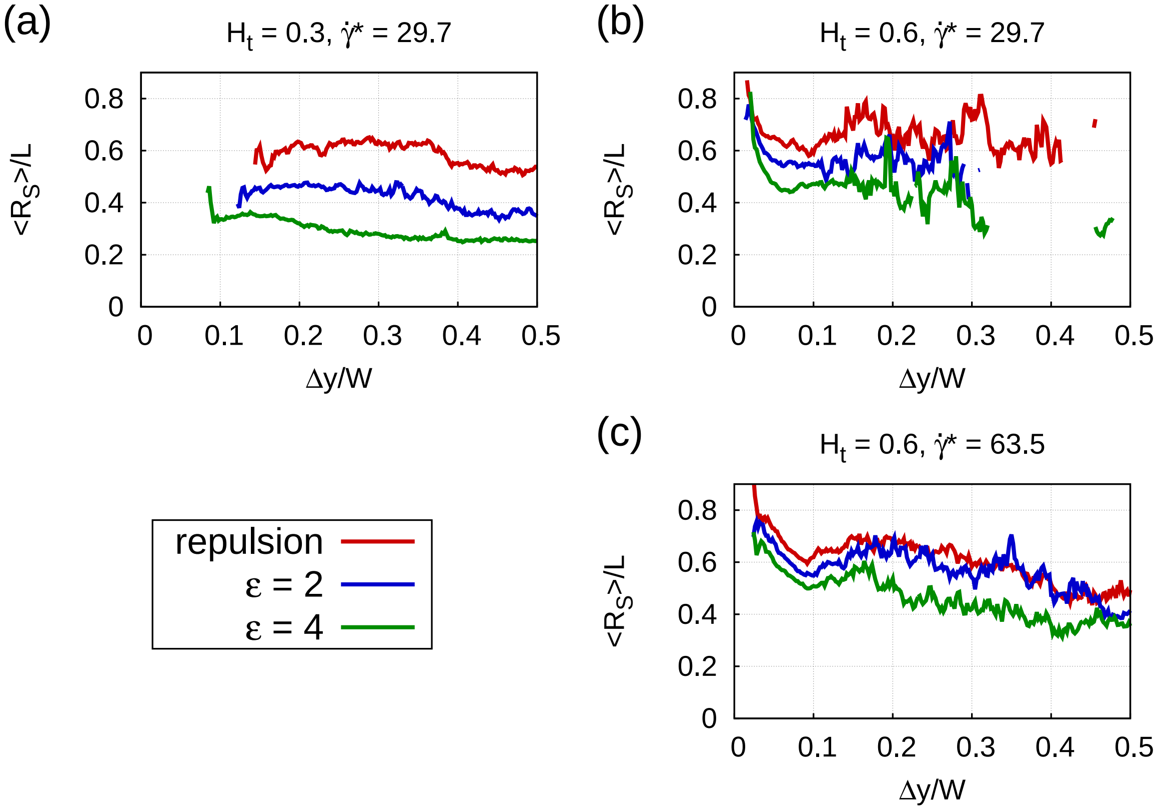

Figure 5.18.: Average extension $\langle R_S \rangle$ normalized by the polymer length L depending on the COM position Δy for the repulsive polymer (red curves), the attractive polymer with $\epsilon = 2$ (blue curves), and $\epsilon = 4$ (green curves). Only data points are shown, which have been estimated by averaging at least 500 values. The different plots correspond to the system parameters (a) $H_\mathrm{t} = 0.3$, $\dot{\gamma}^* = 29.7$, (b) $H_\mathrm{t} = 0.6$, $\dot{\gamma}^* = 29.7$, and (c) $H_\mathrm{t} = 0.6$, $\dot{\gamma}^* = 63.5$.
For the attractive polymer with $\epsilon = 4$ the difference between extension in the bulk and close to the wall is largest. However, with increasing H_t and $\dot{\gamma}^*$ the polymer extension becomes similar for the different polymer types.

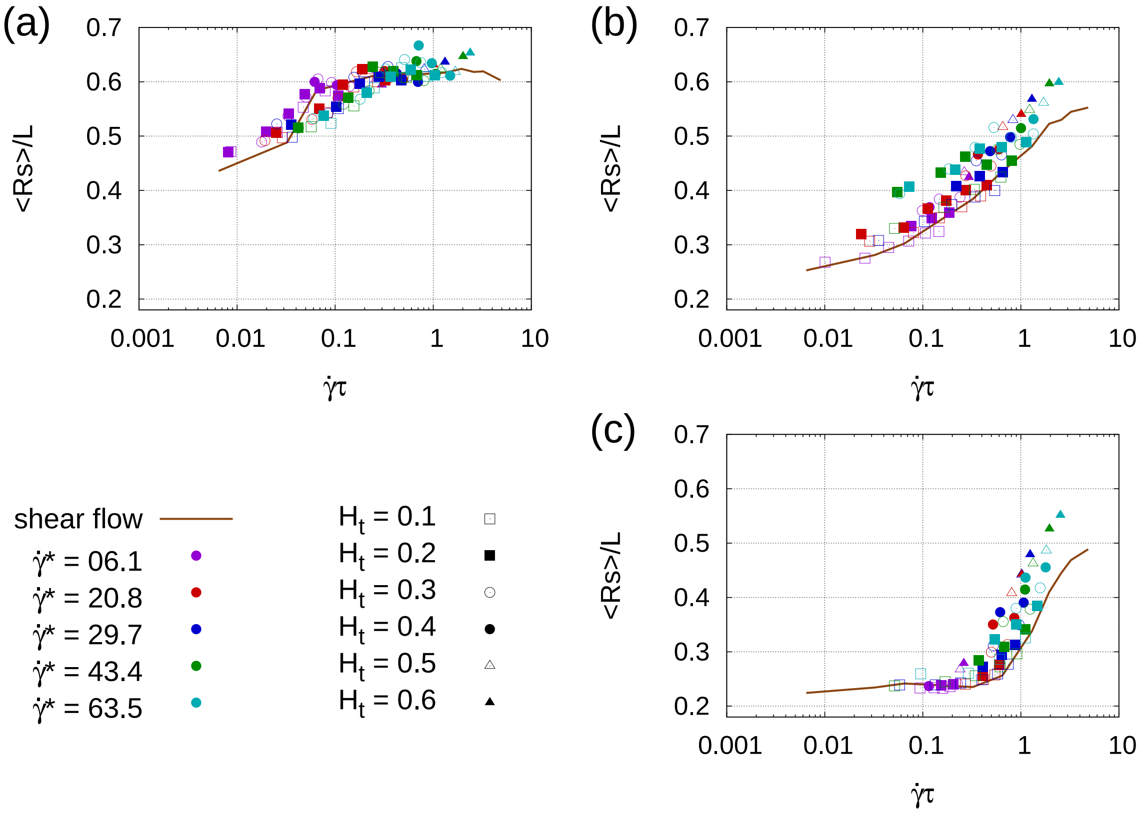

Figure 5.19.: Comparison of average polymer extension $\langle R_S \rangle$ normalized by the polymer length L depending on the (local) scaled shear rate $\dot{\gamma}\tau$ compared for different average shear rates (symbols) and simple shear flow (brown curve) for (a) the repulsive polymer, (b) the attractive polymer with $\epsilon = 2$, (c) and the attractive polymer with $\epsilon = 4$. For the repulsive polymer the extension in blood flow is similar to the extension in shear flow. For the attractive polymers, as the hematocrit increases, the stretching increases in blood flow compared to simple shear flow, due to interactions with the RBCs.

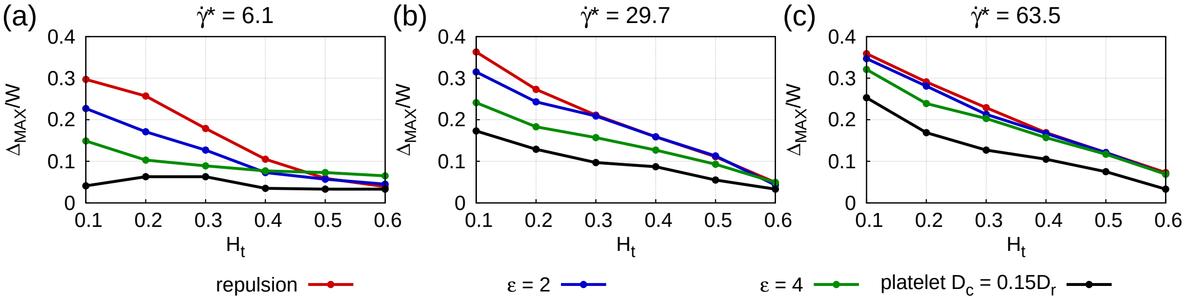

Figure 5.20.: Distance Δ_{MAX} of peak position to the wall normalized by the channel width W. Comparison between the repulsive polymer (red), the attractive polymer with $\epsilon = 2$ (blue), $\epsilon = 4$ (green), and a circular platelet with $D_{\mathrm{c}} = 0.15 D_{\mathrm{r}}$ (black) at three different shear rates (a) $\dot{\gamma}^* = 6.1$, (b) $\dot{\gamma}^* = 29.7$, and (c) $\dot{\gamma}^* = 63.5$.
With increasing shear rate the distance of the peak position to the wall for all polymer types become similar. For low shear rates the attractive polymer with $\epsilon = 4$ is close to the smallest platelet.

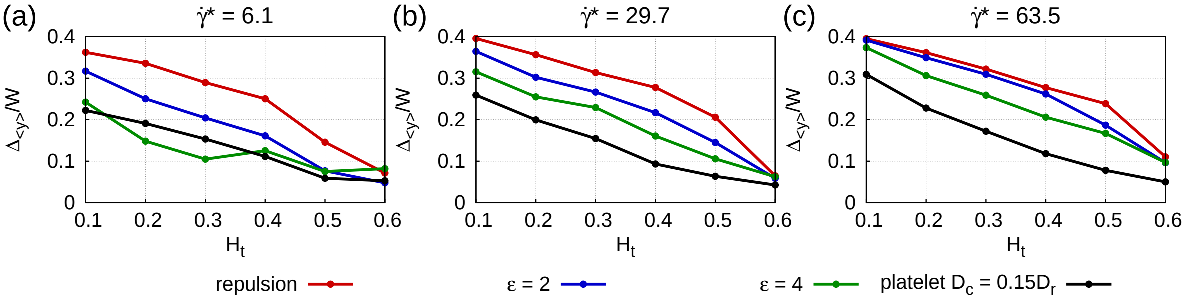

Figure 5.21.: Distance $\Delta_{\langle r \rangle}$ of the mean position in the whole channel from the wall normalized by the channel width W. Comparison between the repulsive polymer (red), the attractive polymer with $\epsilon = 2$ (blue), $\epsilon = 4$ (green), and a circular platelet with $D_{\mathrm{c}} = 0.15 D_{\mathrm{r}}$ (black) at three different shear rates (a) $\dot{\gamma}^* = 6.1$, (b) $\dot{\gamma}^* = 29.7$, and (c) $\dot{\gamma}^* = 63.5$. With increasing shear rate the distance of mean position to the wall fro all polymers become similar. For low shear rates the attractive polymer with $\epsilon = 4$ is very similar to the platelet.

similar to the small platelet. With increasing shear rate the distances increase like for the platelet. However, the changes are more drastic for the polymer, due to the stronger lift force. Consequently, the polymers have similar distributions for high shear rates and are thus considerable further away from the wall than the platelet. One reason is that the lift force scales as $F_{\mathrm{L}} \sim \dot{\gamma}$ [56, 109] as discussed in Section 1.4. However, this applies to all particles, but the higher the shear rate the more the attractive polymers are extended, as seen above. Thus, the shape is less symmetric and also the flexibility increases which leads to an increased lift force [56]. Furthermore, the extension in y-direction of the polymer decreases, the polymers can more easily squeeze between the RBCs and in the RBC-FL they can come closer to the RBC.

5.4. Summary

Strong attractive interactions between the polymer beads increase drastically the margination. Thus, the globule form of the VWF does not only prevent spontaneous binding of platelets in the bulk, but also takes care that the plasmatic VWF is marginated. Furthermore, the polymer with strong attractive interactions stretches considerably close to the wall, due to interactions with the RBCs which is even slightly more efficient than in simple shear flow but is still coiled in the bulk. Therefore, adhesion to collagen can be provided if needed. However, it has to be pointed out that the examined polymer length correspond to the ULVWF. The average size of plasmatic VWF has been found to be about 6 dimers [216], which corresponds to a length of about 420 nm. Considering that the size distribution exhibits an exponential dependence [216], it is expected that especially the longer chains are closer to the wall than the smaller ones, which are expected to be distributed more uniformly similar to the nano-carrier investigated in Section 4.2. This conclusion is also consistent with the increased activity of longer VWF chains, for instance in the thrombotic thrombocytopenic purpura disease [34]. Longer chains marginate better and thus, a higher number of chains is located close to the wall. Close to the wall a polymer with strong internal interactions stretches considerably and clot formation is highly promoted.

6. Summary and Conclusion

In this thesis, a systematic *in silico* study of the migration of various blood components to the wall in blood flow, which is called margination, has been presented. Applying two particle-based and full-hydrodynamic simulation methods, blood has been modelled as a mixture of fluid, RBCs, and different blood components.

The two utilized methods are the DPD method [82, 83] for 2D simulations and the SDPD method with angular momentum conservation [84, 88] for 3D simulations. DPD has been shown to model a solvent with low enough compressibility for the applied parameters and SDPD with angular momentum conservation has been demonstrated to properly capture the single dynamics of vesicles [88]. Considered blood components are platelets, drug carriers, and the protein called von Willebrand factor (VWF). The margination of WBCs has been investigated elsewhere [120, 121, 125], but has been considered in discussions.

RBCs have a biconcave shape, platelets are small discs, and for drug carriers a huge variety of shapes is possible [41–43]. RBCs, platelets, and carriers are all modelled as triangulated networks, involving the viscoelastic properties, area conservation, bending resistance, and volume conservation, due to the lipid bilayer, the spectrin network, and inner cytosol [114, 153, 156]. In 2D simulations the RBCs and carriers/platelets are modelled as closed bead-spring chains with a bending resistance and an area conservation constraint [120]. In both dimensions, platelets and carriers are stiffer than RBCs similar to experimental measurements [8, 14]. In 3D simulations the carriers are faintly deformable and in 2D simulations they are completely rigid. The VWF has been modelled as a bead-spring polymer chain [195], employing a harmonic spring between the neighbouring beads. In addition, all monomers are subject to a volume exclusion, but may also experience an additional attraction, due to different cut-off distances of a truncated Lennard-Jones (LJ) interaction between all monomers.

Blood flow simulations have been performed in a cylindrical channel for a wide range of normalized average shear rates $\dot{\gamma}^*$ and volume fraction of RBCs, the hematocrit. In 3D a straight cylindrical vessel with the diameter of 20 µm has been used, in 2D a slit geometry with different widths. The examined hematocrit values are 10 % to 60 %, whereas the natural human hematocrit lies in the range of 37 % to 54 % [1], but assumes smaller values in narrow channels. The considered shear rate ranges from $\dot{\gamma}^* = 20$ to $\dot{\gamma}^* = 99$ and covers the flow rates which are characteristic for the venular part of microcirculation with $\dot{\gamma}^* \lesssim 90$, while in the arteriolar part the flow rates are higher with $\dot{\gamma}^* \gtrsim 120$ [159, 160]. Furthermore, the considered shear rates are also relevant for tumor microvasculature, since blood flow velocities in tumors are much reduced [161, 162].

In flow, RBCs experience a hydrodynamic lift force from the wall, due to their asymmetric shape and deformability [55, 56, 104–109]. Consequently, in blood flow RBCs gather in the middle of a channel and close to the vessel walls a region depleted of RBCs develops, called the RBC-free-layer (RBC-FL). Hence, margination is analysed in terms of the probability that a particle (platelet, carrier, VWF) is located in the RBC-FL and in terms that the carrier is located in the potential adhesion layer (PAL), a region close to the wall where a direct interaction of the particle surface with the wall may be possible. These probabilities have been calculated from the center-of-mass (COM) probability distribution. Furthermore, these particle distributions are analysed in more detail, considering the peak position of the COM distribution, the average position in the RBC-FL, and the average position in the whole channel.

By 3D simulations, the margination of different shapes has been examined, including four spheres with diameters between 1 µm to 2 µm and two oblate ellipsoids with the long axis diameters 3.1 µm and 3.9 µm, and different aspect ratios (3.5, 7). By 2D simulations a similar sized ellipse and similar sized circles are investigated. Additionally, the margination of other particle sizes (diameter: 0.25 µm and 3.7 µm) and the influence of particle deformability has been examined for a channel of 20 µm width in 2D.

The comparison of 2D and 3D simulations indicates that indeed the dependence of margination on the hematocrit, shear rate, carrier size and shape in 2D is qualitatively similar to the dependence observed in 3D. However, 3D simulation results have to be compared to higher hematocrit values in 2D, since different packing of RBCs leads in 2D to a larger RBC-FL thickness for the same hematocrit. Furthermore, for the ellipse with the highest aspect ratio the dynamics is different in 2D and 3D. Nevertheless, the results of both simulations in both 2D and 3D can be interpreted together in order to draw conclusions.

RBCs are essential for the occurrence of margination. The margination efficiency of weakly deformable particles is mainly determined by the hematocrit. The larger the hematocrit, the smaller the RBC-FL thickness and the more efficient is the margination –

as long as the RBC-FL is not considerably smaller than the particle radius. However, the shear rate influences the margination as well. Initially, the margination increases with increasing shear rate, due to the developing inhomogeneous RBC distribution. After reaching a certain shear rate, an increase of shear rate leads to a reduced margination, since with increasing shear rate the RBC-FL increases and effective fluctuations reduce the margination efficiency. Moreover, the more deformable the particles, the stronger is the influence of the shear rate on the margination efficiency. An increased deformability leads to a decreased margination with increasing shear rate.

An important result is that margination decreases with decreasing carrier size. More precisely, for spheres the linear size determines mainly the margination efficiency, because a sphere ($D_\mathrm{c} = 2\,\mu\mathrm{m}$) marginates almost similar to a sphere with half the volume, but the sphere with half the diameter marginates drastically less. Moreover, nanocarriers ($D_\mathrm{c} = 250\,\mathrm{nm}$) distribute similar to the plasma and thus do not possess a significant margination. Indications are found that spheres with diameters larger than 3 µm to 4 µm might be departed from the wall, similar to what has been shown for WBCs [120, 125].

The simulation results agree with experimental measurements [49, 51, 52, 126, 128, 170]. *In vitro* an increase of margination with increasing hematocrit [128] has been observed. Moreover, with increasing shear rate an increase of margination has been observed followed by a decrease of margination with increasing shear rate after an optimal shear rate value has been reached [129]. Furthermore, microfluidic experiments [49] have shown that spheres with the size of 2 µm exhibit a significantly higher adhesion density than particles with a size of 500 nm and 200 nm.

The study indicates that micron-particles with either a spherical shape or an ellipsoidal shape with a high aspect ratio, such as platelets, are favourable for margination. The flat disc with an aspect ratio of 7 shows a similar margination into the PAL with respect to the long axis compared to a sphere with the same volume. An ellipsoid with smaller aspect ratio but same volume possess less margination. This is due to the fact that at high hematocrit values a high enough fraction of flat carriers is located with their COM at a distance from the wall similar to their small radius. Moreover, the angular velocity of ellipsoids is reduced in blood flow compared to a sphere and even theoretical predictions, and the drag force on an ellipsoid close to the wall is smaller than the drag on a sphere. Other theoretical and experimental studies [51–54] have shown that ellipsoidal particles exhibit better adhesion properties than spheres, due to a larger contact area for adhesion interactions. Taking these results into account, an ellipsoidal shape may be profitable for drug carriers, although the surface of an rotating ellipsoid is only close enough to the wall for possible adhesion in a small time window during the rotation. These results, combined with the observations that particle internalization by endothelial cells and intracellular trafficking is more efficient for spherical sub-micron particles, rather than for micron-size carriers with an ellipsoidal shape [40], promote the concept of multi-stage drug delivery [6, 36], where a larger micro-carrier incorporates a number of small nano-particles which are, after adhesion of the micro-carrier to the wall, released into the tissue.

In order to study the effect of channel size, the margination in channels with four other sizes (width: 10 µm, 15 µm, 40 µm, and 60 µm) has been presented in 2D. The above described hematocrit, shear rate, and carrier-size dependence of margination is similar for all examined channel sizes. However, margination has been shown to be most efficient for narrow vessels ($\lesssim 20\,\mu\text{m}$ in 2D), since the RBC-FL thickness increases with increasing channel size and consequently margination into the PAL is reduced.

With the channel size also the concentration of RBCs and carriers changes. RBCs pass the channel faster than the average flow, thus the tube hematocrit, the volume fraction of RBCs in the specific channel, is smaller than the discharge hematocrit, the volume fraction leaving the channel per unit time. With increasing channel size, the tube and the discharge hematocrit become more similar. It follows that the RBC concentration increases with increasing channel size, which is called the Fåhræus effect [175]. Accordingly, the concentration change of carriers with changing hematocrit, carrier size, and channel size has been discussed, by examining their tube and the discharge volume fraction. In contrast to the RBCs, carriers are localised close to the wall and thus they pass a channel slower than the average flow, introduced as a 'reverse' Fåhræus effect. With increasing hematocrit the carrier density increases, because the margination improves. However, the RBC-FL thickness does not increase linearly with the channel diameter, it increases less. Therefore, the density of carriers increases with increasing channel size similar to the RBC density. Consequently, the density increase could compensate for a reduced margination in larger channels. Similarly, size fluctuations may be balanced, because the tube volume fraction of smaller carriers is larger assuming the same discharge volume fraction.

In order to understand the process of margination, the contribution of direct and hydrodynamic interactions between platelets and RBCs on margination has been examined. Therefore, either the excluded-volume or the hydrodynamic interactions between the platelets and RBCs have been turned off. It has been shown that the shear-induced migration close to the RBC-FL is slower for platelets, which hydrodynamically interact with RBCs, since platelets experiencing hydrodynamic interactions with RBCs are located closer to the wall. Furthermore, hydrodynamic interactions seem to speed up the migration from the center to the RBC-FL by guiding the path between the RBCs, since without hydrodynamic interactions more carriers remain outside the RBC-FL than with hydrodynamic interactions. However, the platelet distribution in the RBC-FL is mainly determined by excluded-volume interactions and collisions with RBCs.

In order to understand the trigger of VWF extension in case of an injury, the chain extension of polymers in simple shear flow is investigated, with respect to different shear rates and internal monomer interactions. The mainly investigated chain length corresponds to $L = 15.6\,\mu\mathrm{m}$. The following configurations have been examined: a polymer with its COM fixed in the middle of the channel, its COM fixed close to the wall, with one end attached to the wall, and additionally to the wall attachment decorated with one platelet. The main focus has been on the last two configurations.

Strong attractive interactions between the beads of a polymer lead to a globule stretching transition at a critical shear rate as observed in experiments [19]. The less adhesive the monomers, the lower the shear-rate dependence on the polymer configuration. Adhesion of one end of the polymer to the wall decreases the critical shear rate for stretching by an order of magnitude, leads to longer configurations, and adhesion of a platelet leads to even further stretching. This indicates that adhesion of VWF triggers stretching. Furthermore, released and tethered ULVWF is able to extend, whereas the soluble VWF remains coiled. Thus, the release of ULVWF triggers the aggregate formation by providing binding sides for platelets and soluble VWF.

The margination efficiency of the repulsive and attractive polymers is examined and compared to the margination efficiency of rigid carriers. In addition, the stretching dependence of VWF on hematocrit, normalized average shear rate, polymer position, and local shear rate in blood flow is investigated. Polymers with strong attractive interactions marginate drastically better than these with low attractive interactions. Furthermore, the margination of the examined polymers depends much stronger on shear rate and is less than for rigid carriers. For higher local shear rates, the polymer coil becomes more flexible and deforms and thus, margination is reduced. The stronger the internal interactions, the more apparent is the dependence of extension on hematocrit and the normalized average shear rate. With both, increasing hematocrit and shear rate, larger elongations are observed. The stretching is strongest in the RBC-FL, since the local shear rates are highest there and the polymer has free space. Therefore, the probability of spontaneous platelet plug formation is suppressed in the channel, but at the same time adhesion of soluble VWF to the wall has a certain probability in case of an injury.

As a concluding remark, this *in silico* study of margination in this thesis presents new insights about the dependence of margination of blood components such as platelets, von Willebrand factor, and drug carriers on blood flow properties (hematocrit, shear rate), particle properties (size, shape, deformability), and channel width, but also about the dependence of particle density on these properties, and about margination mechanisms. Thus, a further piece is added to the big puzzle of understanding haemostasis and developing early detection and therapy strategies for diseases as, for instance, cardiovascular diseases and cancer.

7. Outlook

The simulations results obtained so far provide interesting new insights about margination and thus, a good theoretical basis for further studies. For future work, two different directions are conceivable.

First, margination is a requirement for adhesion to the wall, but is not equivalent, since adhesion ability may also depend on receptor/ligand density and distribution. Therefore, the incorporation of adhesive interactions between the carriers and the wall would provide a possibility to compare quantitatively simulations with experiments and shed light on further important parameters.

Moreover, the intricate interplay between the different blood components can be investigated by including attractive interactions of VWF to the wall and platelets to VWF. For instance, the effect of hematocrit, shear rate, soluble and wall-bound VWF on the platelet plug formation can be examined. Figure 7.1 presents a sketch of a simulation taking all important components into account.

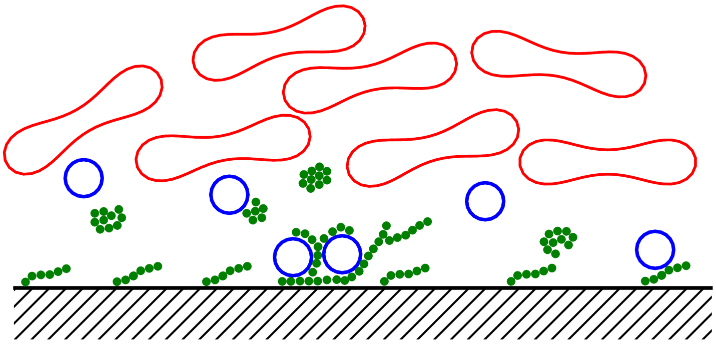

Figure 7.1.: Sketch of further investigations. Future work could include attractive interactions between platelets and VWF with the wall and attractive interactions between VWF and platelets.

One suggestion for adhesive interactions is to model the dependence of stretching of VWF and improved adhesion by correlating the adhesion strength to the angle between the two neighbouring bonds. Furthermore, catch bonds have been suggested for both, appropriate VWF-platelet and VWF-wall interaction [207, 208]. Studying systems with soluted VWF and platelets of different concentration in shear flow might lead to an understanding of the early stage of shear-dependent aggregation formation not only for normal VWF but also for mutations.

Second, this study sheds light on the margination dependence on a multiplicity of parameters in a simplified geometry. After this, different additional aspects could be considered leading to a more realistic environment. One aspect is the geometry of a healthy, but also of an injured blood vessel. A second aspect is to take further properties of blood into account. Different system properties that could be included in simulations are listed below.

More realistic blood vessels

Blood vessels are not rigid, they are comprised of elastic tissue and muscles and are different for different vessel types [1]. Furthermore, the endothelium is covered by a so-called endothelial surface layer (ESL) with a thickness of 0.3 µm to 1 µm and with glycocalyx, macromolecules attached to the plasma membrane, with a thickness of some tens of nanometers [217, 218]. The ESL impedes the plasma flow, increasing the flow resistance and leading to very low tube hematocrit values compared to the bulk hematocrit [217, 218]. These properties could also influence the margination properties.

Bifurcations and junctions

Another interesting feature are bifurcations and junctions, which may affect the platelet adhesion ability. The microvascular network consists of short segments ($\sim$ 400 µm to 800 µm) linked by bifurcations. Depending on the flow velocity and the geometry of the daughter branches, RBCs and plasma can be unevenly distributed in the daughter branches, leading to a heterogeneity. Thereby, larger vessels with higher volume flow lead to an increased hematocrit [218]. If one of the daughter vessels is only perfused by plasma and void of RBCs, this is called ‘plasma-skimming’ [219, 220]. Thus, at bifurcations and junctions the margination may not only diminish, but also the carrier density in the various channels may be changed as for RBCs.

Pulsatile flow

Another very controversial topic is the influence of pulsatile flow in microcirculation. The question is, whether a pulsatile flow exists in microcirculation and what impact it has. This topic is mainly discussed in the context of the development of acute and chronic cardiac support systems. Some studies suggest that pulsatile flow exists in microcirculation and that it improves the velocity of cells in the capillaries and increases the number of perfused capillaries compared to non-pulsatile perfusion [221, 222]. However, if pulsatile flow is important in microcirculation the pulsation might also effect carrier margination and VWF extension.

Altered flow in case of injury

Concerning blood clotting in case of an injury, it may be taken into account that the flow initially changes, due to the lesion and subsequently, due to the formed blood clot [223]. For instance, it has been suggested that elongational flow is likely to increase the stretching VWF [206, 224] and thus, adhesion to the wall and to platelet would be reinforced. Furthermore, the narrowing and widening of blood vessels, called vasoconstriction and vasodilation, respectively is involved in the primary haemostasis [1].

Aggregation of RBCs

Moreover, blood is a 'shear-thinning' fluid, meaning that the viscosity decreases with increasing shear rate. On the one hand, RBCs deform in response to high shear stresses. On the other hand, for low shear rates RBCs aggregate into so-called rouleaux formations, comparable to a stack of coins [117]. This aggregation is mediated by plasma proteins and a strong increase of these aggregations is observed associated with diseases as atherosclerosis, AIDS, and diabetes [118]. With increasing shear rate, these fragile piles break up, which is the major cause of the shear-thinning [220]. An observed impact of aggregation, for instance on WBC margination, is an increase of margination for high hematocrit values and low shear rates assuming that the aggregation represents an additional expulsion force, but also leads to an increase of the RBC-FL [125] and would also have an impact on carrier margination.

Appendices

Appendix A.

Fluid model

A.1. Smoothed dissipative particle dynamics

Here, the calculations of derivatives of field variables similar to those in SPH [86] are summarized.

Using Eq. (2.10), the first derivative of a field $\tilde{g}$ can be approximated as

$$\left(\frac{\partial \tilde{g}}{\partial x}\right)_i \approx \sum_{j=1}^{N} \frac{m_j}{\rho_j} g \frac{\partial W_{ij}}{\partial x_i}, \tag{A.1}$$

where the notations are identical to those in the main text of Chapter 2. A disadvantage of this approximation is that the derivative does not vanish for $\tilde{g}$ being a constant function. Therefore, a better approximation is given by

$$\frac{\partial \tilde{g}}{\partial x} = \frac{1}{\phi}\left(\frac{\partial(\tilde{g}\phi)}{\partial x} - \tilde{g}\frac{\partial \phi}{\partial x}\right), \tag{A.2}$$

where ϕ has to be a differentiable function. Following Eq. (A.1),

$$\left(\frac{\partial \tilde{g}}{\partial x}\right)_i \approx \frac{1}{\phi_i} \sum_{j=1}^{N} \frac{m_j}{\rho_j} \phi_j \left(g_j - g_i\right) \frac{\partial W_{ij}}{\partial x_i}. \tag{A.3}$$

is obtained. When $\phi = 1$, Eq. (A.3) reduces to

$$\left(\frac{\partial \tilde{g}}{\partial x}\right)_i \approx \sum_{j} \frac{m_j}{\rho_j} g_{ji} \frac{\partial W_{ij}}{\partial x_j}, \tag{A.4}$$

where $g_{ji} = g_j - g_i$. In Eq. (A.3), $\phi = \rho$ can also be selected, yielding an approximation for the first derivative as

$$\left(\frac{\partial \tilde{g}}{\partial x}\right)_i \approx \frac{1}{\rho_i} \sum_j m_j g_{ji} \frac{\partial W_{ij}}{\partial x_i}. \tag{A.5}$$

The choice for different discretizations ($\phi = 1$ or $\phi = \rho$) may depend on the problem of interest. For instance, when different interacting fluids with large density ratios are considered, it has been shown that the approximation in Eq. (A.3) with $\phi = 1$ is more accurate than that with $\phi = \rho$, because ρ in Eq. (A.4) is included directly inside the sum [86, 225]. Furthermore, if only a single fluid is employed, an approximation $\rho_i \approx \rho_j$ can be used making the above choices for ϕ equivalent.

There exists another definition for the first derivative,

$$\frac{\partial \tilde{g}}{\partial x} = \phi \left(\frac{\partial}{\partial x} \left(\frac{\tilde{g}}{\phi} \right) + \frac{\tilde{g}}{\phi^2} \frac{\partial \phi}{\partial x} \right), \tag{A.6}$$

leading to

$$\left(\frac{\partial \tilde{g}}{\partial x}\right)_i \approx \phi_i \sum_{j=1}^{N} \frac{m_j}{\rho_j} \left(\frac{g_j}{\phi_j} + \frac{g_i}{\phi_i^2} \phi_j \right) \frac{\partial W_{ij}}{\partial x_i}. \tag{A.7}$$

A choice of $\phi = 1$ leads to

$$\left(\frac{\partial \tilde{g}}{\partial x}\right)_i \approx \sum_{j=1}^{N} \frac{m_j}{\rho_j} \left(g_j + g_i \right) \frac{\partial W_{ij}}{\partial x_i}, \tag{A.8}$$

while for $\phi = \rho$ Eq. (A.7) becomes

$$\left(\frac{\partial \tilde{g}}{\partial x}\right)_i \approx \rho_i \sum_{j=1}^{N} m_j \left(\frac{g_j}{\rho_j^2} + \frac{g_i}{\rho_i^2} \right) \frac{\partial W_{ij}}{\partial x_i}. \tag{A.9}$$

The above defined approximations can be used to also approximate the other differential operators of the Navier-Stokes equation (NSE). For instance, using Eq. (A.5) the gradient of $\tilde{g}(\mathbf{r})$ can be approximated as

$$(\nabla \tilde{g})_i \approx -\frac{1}{\rho_i} \sum_j m_j g_{ij} \nabla_i W_{ij}, \tag{A.10}$$

where $g_{ij} = g_i - g_j$. Similarly, the divergence and the curl of a vector field $\tilde{\mathbf{G}}(\mathbf{r})$ are discretized as

$$\left(\nabla \cdot \tilde{\mathbf{G}}\right)_i \approx -\frac{1}{\rho_i}\sum_j m_j \mathbf{G}_{ij} \cdot \nabla_i W_{ij}, \tag{A.11}$$

$$\left(\nabla \times \tilde{\mathbf{G}}\right)_i \approx -\rho_i \sum_j \frac{m_j}{\rho_i \rho_j}\left(\mathbf{G}_j + \mathbf{G}_i\right) \times \nabla_i W_{ij}. \tag{A.12}$$

The second derivatives are then given by

$$\left(\nabla\left(\nabla \cdot \tilde{\mathbf{G}}\right)\right)_i \approx -\sum_j m_j \frac{F_{ij}}{\rho_i \rho_j}\left(5\hat{\mathbf{e}}_{ij}\left(\hat{\mathbf{e}}_{ij} \cdot \mathbf{G}_{ij}\right) - \mathbf{G}_{ij}\right) \tag{A.13}$$

and

$$\left(\nabla^2 \tilde{g}\right)_i \approx -2\sum_j m_j \frac{F_{ij}}{\rho_i \rho_j} g_{ij}, \tag{A.14}$$

where $\hat{\mathbf{e}}_{ij} = \mathbf{r}_{ij}/r_{ij}$ is the unity vector along the separation direction of particles i and j [84].

A.2. Comparison of simulation methods

Regarding the simulations presented in Section 2.5, a number of simulations were performed to verify that the simulation results are independent of the choice for particle mass and moment of inertia for low enough Re numbers. Figure A.1 illustrates that the effect of both mass and moment of inertia on the measured viscosity can be neglected for the studied range of flow Re numbers [88].

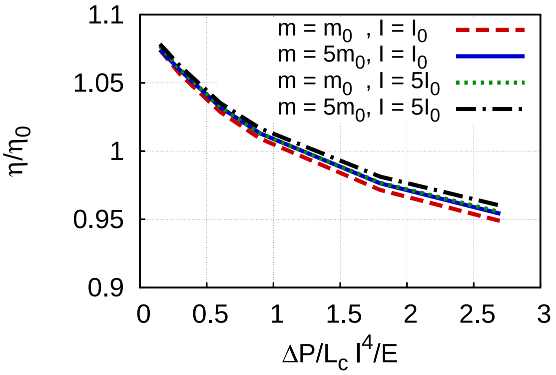

Figure A.1.: Dependence of fluid properties on mass and moment of inertia. Measured viscosity η, scaled by $\eta_0 = 25\sqrt{mE}/l^2$ depending on the pressure gradient $\Delta P/L_\mathrm{c}$, with L_c being the channel length for different mass and moment of inertia values. The density is $\rho_0 = 3m/l^3$.
Although both, mass and moment of inertia, are varied, the measured values of η are hardly affected [88].

Additional to measurements of fluid properties for a SDPD+a fluid presented in Figs. 2.3 and 2.4 of Section 2.5, Figs. A.2 and A.3 show the measured fluid viscosity and density of a SDPD–a fluid, depending on the pressure drop, input viscosity, input density, and temperature. Similar to SDPD+a, the fluid properties are better approximated for an increased particle density, see Fig. A.2. Furthermore, with increasing smoothing length r_h the measured values are closer to the specified ones and the temperature dependence practically vanishes, see Fig. A.3.

A similar test for the Taylor-Couette flow using both SDPD–a and SDPD+a methods have been performed to verify that simulation results are independent of the choice of particle mass and moment of inertia for low enough Re numbers. Figure A.4 illustrates that for all choices of mass and moment of inertia the measured angular velocity profiles agree.

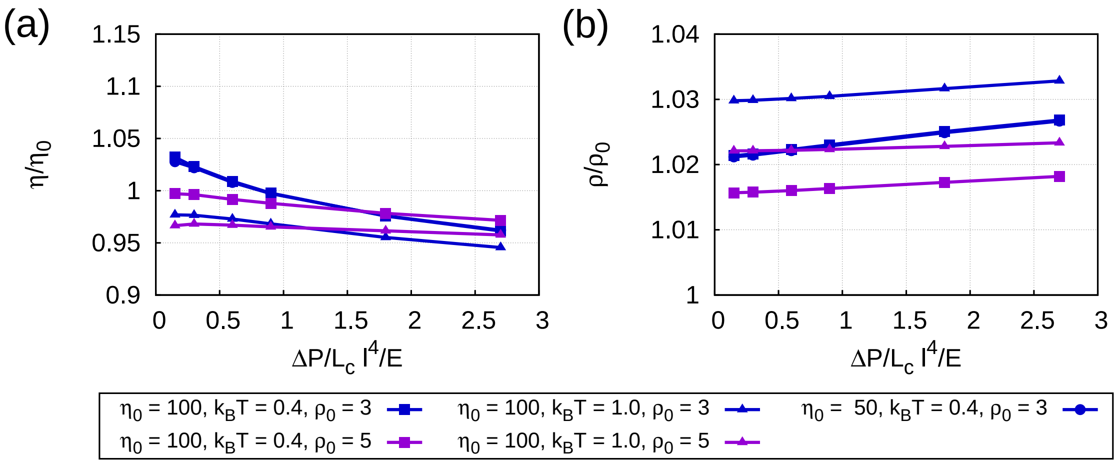

Figure A.2.: Fluid properties of a SDPD–a fluid for different pressure gradients $\Delta p/L_\mathrm{c}$, for a channel of length L_c and particle densities $\rho_0 = 3m/l^3$ (blue) and $\rho_0 = 5m/l^3$ (purple). (a) Measured viscosity η normalized by $\eta_0 \in \{50, 100\}\sqrt{mE}/l^2$. (b) Particle density ρ normalized by ρ_0. Different energy levels $k_\mathrm{B}T \in \{0.4, 1\}E$ were considered, while $r_h = 1.5l$. This plot corresponds to Fig. 2.3.

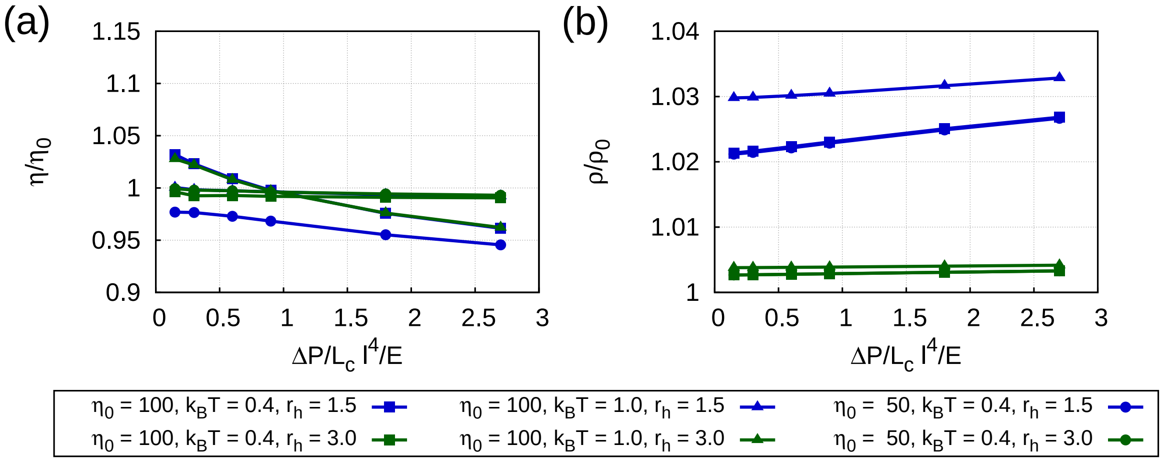

Figure A.3.: Fluid properties of a SDPD–a fluid for different pressure gradients $\Delta p/L_\mathrm{c}$, for a channel of length L_c and smoothing lengths $r_h = 1.5l$ (blue) and $r_h = 3.0l$ (green). (a) Measured viscosity η normalized by $\eta_0 \in \{50, 100\}\sqrt{mE}/l^2$. (b) Particle density ρ normalized by $\rho_0 = 3m/l^3$. Different energy levels $k_\mathrm{B}T \in \{0.4, 1\}E$ were considered. This plot corresponds to Fig. 2.4.

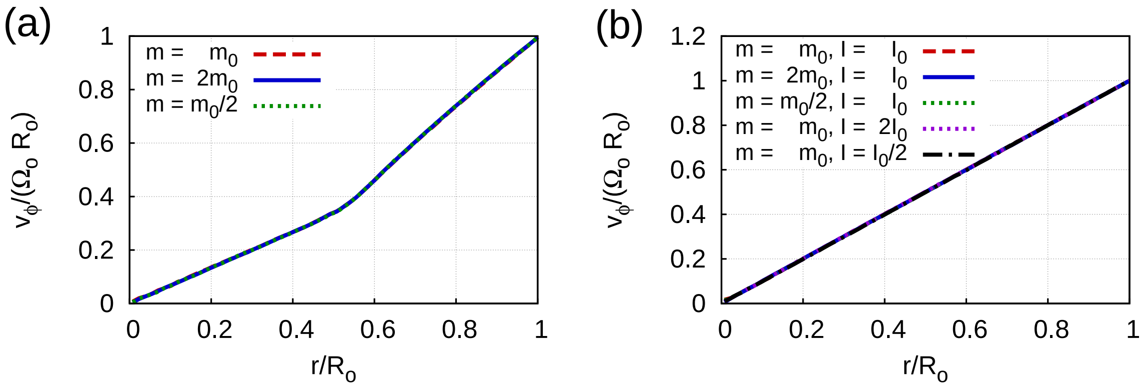

Figure A.4.: Angular velocity v_ϕ profiles for the Taylor-Couette flow with two immiscible fluids using both (a) SDPD–a and (b) SDPD+a methods for different mass m and moment of inertia I. The radial position r is normalized by the cylinder radius R_o, while the angular velocity is scaled with the cylinder angular velocity $\Omega_o R_o$.
For all masses and moments of inertia the same results are obtained [88].

Appendix B.

Blood flow simulations

B.1. Cell model

Tables B.1 and B.2 present the RBC model parameters for the 3D and 2D model, respectively, which have been introduced in Section 3.1.1. For Table B.1 the given parameters correspond to Eqs. (3.2), (3.5) to (3.8), and (3.10). For Table B.2 the parameters correspond to Eqs. (3.2), (3.12), and (3.13).

	N_v	l_m	Y	ϑ_0	κ_r	A_0^{tot}	V_0^{tot}	k_d	k_a	k_v	η_m
unit	1	l_0	µN/m	rad	k_BT	µm^2	µm^3	k_BT/D_r^2	k_d	D_r/k_d	$k_\mathrm{B}T\tau/D_\mathrm{r}^2$
value	500	2.2	18.9	0	70	133	92.5	42250	49	325	122.7

Table B.1.: 3D RBC model parameters corresponding to Section 3.1.1. N_v is the number of vertices per cell, l_m is the maximum spring extension, and l_0 is the spring length set to the value of the initially triangulated membrane surface. Y is the Young's modulus, ϑ_0 is the spontaneous angle between two adjacent faces. κ_r is the macroscopic bending rigidity. A_0^{tot} is the desired cell area and V_0^{tot} is the cell volume, while k_d is the local area constraint coefficient, k_a is the global area constraint coefficient, and k_v is the volume constraint coefficient. The desired area A_0 of the triangles is set to the value of the initial membrane triangulation. The membrane viscosity η_m is derived by Eq. (3.7) with $\gamma^C = 21.8 k_\mathrm{B}T\tau_\mathrm{RBC}/D_\mathrm{r}^2$ and $\gamma^T = 65.4 k_\mathrm{B}T\tau_\mathrm{RBC}/D_\mathrm{r}^2$.

	N_v	l_m/l_0	L_0/µm	ϑ_0	$\kappa_r/k_\mathrm{B}T$	A_0/µm^2	$k_a/(k_\mathrm{B}T/D_r^2)$
RBC	50	2.2	19.22	0	50	13.6	37210

Table B.2.: 2D RBC model parameters corresponding to Section 3.1.3. N_v is the number of vertices forming a cell, l_m is the maximum spring extension, and l_0 is the initial spring length. L_0 is the cell's contour length, ϑ_0 is the spontaneous angle between two neighbouring bonds, κ_r is the macroscopic bending rigidity, A_0 is the desired cell area, and k_a is the area constraint coefficient.

B.2. Single vesicle in shear flow

The Keller and Skalak (KS) theory assumes a fixed ellipsoidal shape $(r_1/a_1)^2 + (r_2/a_2)^2 + (r_3/a_3)^2 = 1$, where $r_i, i \in \{1, 2, 3\}$ are the Cartesian coordinates and a_i are the semiaxes of the ellipsoid. The motion of a vesicle is derived by considering energy balance between the energy supplied by the fluid and the energy which dissipates on the membrane and inside the vesicle. This balance leads to a differential equation given by

$$\frac{d\theta_\mathrm{i}}{dt} = \frac{1}{2}\dot{\gamma}\left(B\cos(2\theta_\mathrm{i}) - 1\right), \tag{B.1}$$

where $\dot{\gamma}$ is the shear rate. If $B > 1$, the vesicle is in the tank-treading (TT) regime, and hence, a steady inclination angle can be found as $\theta_\mathrm{i} = 0.5\arccos(1/B)$, where B is a function of vesicle shape and viscosity contrast given by

$$\begin{aligned} B &= f_0\left(f_1 + \frac{1}{f_1}\frac{1}{1 + f_2(\lambda - 1)}\right), \\ f_0 &= \frac{2}{a_1/a_2 + a_2/a_1}, \\ f_1 &= 0.5\left(a_1/a_2 - a_2/a_1\right), \\ f_2 &= 0.5g(\alpha_1^2 + \alpha_2^2), \\ g &= \int_0^\infty (\alpha_1^2 + s)^{-3/2}(\alpha_2^2 + s)^{-3/2}(\alpha_3^2 + s)^{-1/2}\,ds, \\ \alpha_i &= \frac{a_i}{(a_1a_2a_3)^{1/3}}. \end{aligned} \tag{B.2}$$

Note that the vesicle's membrane viscosities are not considered here.

The moment of inertia tensor $\boldsymbol{\mathcal{I}}$, which is used to compute the inclination angle of a vesicle in Eq. (3.14), by using the eigenvalues of this tensor, is given by

$$\boldsymbol{\mathcal{I}} = \begin{pmatrix} y^2 + z^2 & -xy & -xz \\ -xy & x^2 + z^2 & -yz \\ -xz & -yz & x^2 + y^2 \end{pmatrix}. \tag{B.3}$$

Tables B.3 and B.4 show the cell model parameters corresponding to Eqs. (3.8) and (3.10) and the fluid parameters corresponding to Eq. (2.26), used in 3D simulations of a single vesicle in shear flow presented in Section 3.2.2.

$k_d/(k_BT/R_0^2)$	$k_a/(k_BT/R_0^2)$	$k_v/(k_BT/R_0^3)$	κ_r/k_BT	$\dot{\gamma}\tau_\mathrm{v}$
1145	11450	12256	21.7	0.36

Table B.3.: Vesicle parameters in units of energy $k_\mathrm{B}T$ and effective vesicle radius R_0 corresponding to Eq. (3.8) and Eq. (3.10). k_d is the local and k_a the global area constraint coefficient, k_v is the volume constraint coefficient, κ_r is the bending rigidity, and $\dot{\gamma}$ is the shear rate normalized by a characteristic vesicle relaxation time $\tau_\mathrm{v} = \eta_o R_0^3/\kappa_r$, with η_o being the outer fluid viscosity.

p_0	ρ_0	α	b	r_c	η_0	n	k_BT
100	3.0	7	100	1.5	20.0	3	0.4

Table B.4.: SDPD fluid parameters used in 3D simulations of a single vesicle in shear flow for SDPD–a and SDPD+a corresponding to Section 3.2.2. p_0, ρ_0, α, and b are model parameters that correspond to Eq. (2.26). η_0 is the desired outer dynamic viscosity, n is the number density, and $k_\mathrm{B}T$ is the energy unit. The measured (real) outer fluid viscosity η for SDPD–a is $\eta_{-\mathrm{a}} = 20.2$ and for SDPD+a it is $\eta_{+\mathrm{a}} = 19.9$.

B.3. Blood flow

Table B.5 shows the fluid parameters of the DPD fluid corresponding to Eqs. (2.2), (2.4), and (2.5) and measured properties for 3D and 2D simulations used in blood flow simulations, which are presented in Sections 3.3.3, 4.2, and 4.3 and Chapter 5. Table B.6 shows the fluid parameters corresponding to Eq. (2.26) for the SDPD fluid employed for 3D simulations, which are presented in Section 3.3.3 and Chapter 4.

D		m	a	γ	r_c	k	n	k_BT	η
2D	$\dot{\gamma}^* \leq 20$	1	40	10	1.5	0.3	5	1	72.2
2D	$\dot{\gamma}^* > 20$	1	40	20	1.5	0.3	5	1	144.4
3D	all $\dot{\gamma}^*$	1	4	22	1.5	0.1	3	0.1	104.3

Table B.5.: DPD fluid parameters used in 2D and 3D simulations. m is the mass of a fluid particle, a and γ are the conservative and dissipative force coefficients, respectively. r_c is the interaction cut-off radius, k is an exponent for the dissipative-force weight function, n is the number density of fluid particles, $k_\mathrm{B}T$ is the energy unit with k_B being the Boltzmann constant and T temperature, and η is the measured fluid's dynamic viscosity.

p_0	ρ_0	α	b	r_c	η_0	n	k_BT	η
100	3.0	7	80	1.5	100.0	3	0.4	109.2

Table B.6.: SDPD fluid parameters used in 3D simulations. p_0, ρ_0, α and b are model parameters. η_0 is the desired dynamic viscosity, n is the number density, k_BT is the energy unit, and η is the measured (real) fluid viscosity.

Appendix C.

Margination of platelets and drug-delivery carriers

C.1. Size and shape dependence of margination

Table C.1 presents the carrier model properties, corresponding to Eqs. (3.2), (3.8), and (3.10), which have been used for all 3D simulations presented in Chapter 4.

l_m/l_0	$Y/(\mathrm{\mu N/m})$	θ_0	$\kappa_r/k_\mathrm{B}T$	$k_d/(k_\mathrm{B}T/D_\mathrm{r}^2)$	k_a/k_d	$k_v D_\mathrm{r}/k_d$
2.2	189	θ_0^l	866	422500	50	3250

Table C.1.: 3D carrier model parameters that are similar for all carriers. l_m is the maximum spring extension and l_0 is the spring length set to the value of the initially triangulated membrane surface. Y is the Young's modulus, θ_0 is the spontaneous angle between two adjacent faces set to θ_0^l being the angles of the initially triangulated shape. The macroscopic bending rigidity κ_r. k_d is the local area constraint coefficient, k_a is the global area constraint coefficient, and k_v is the volume constraint coefficient. The description of the model can be found in Section 3.1.

Table C.2 gives an overview over the number of vertices per carrier and the number of carriers per 3D simulation. The ellipsoids are characterized by a effective diameter defined as $D_\mathrm{c} = \sqrt{A_0^{tot}/\pi}$.

In Section 4.1 margination diagrams have been presented for the two different choices of margination layer, namely the RBC-FL and PAL, which depend on system properties. Therefore, the margination diagrams for a constant region of width $\delta = 0.31 D_\mathrm{r}$ for 3D simulations of the four spherical carriers are presented in Fig. C.1. Similar hematocrit and shear rate dependence on margination is observed as for the two other choices of margination layer.

Shape	$D_\mathrm{c}/D_\mathrm{r}$	N	N_v
Sphere	0.3	6	350
Sphere	0.28	6	350
Sphere	0.25	10	300
Sphere	0.15	20	150
Ellipsoid	0.36	6	350
Ellipsoid	0.43	6	350

Table C.2.: 3D carrier model parameters. D_c is the diameter for the spheres and the effective diameter $D_\mathrm{c} = \sqrt{A_0^{tot}/\pi}$ of the ellipsoids. N is the number of carriers per simulation and N_v is the number of vertices per carrier, see Section 3.1 for details.

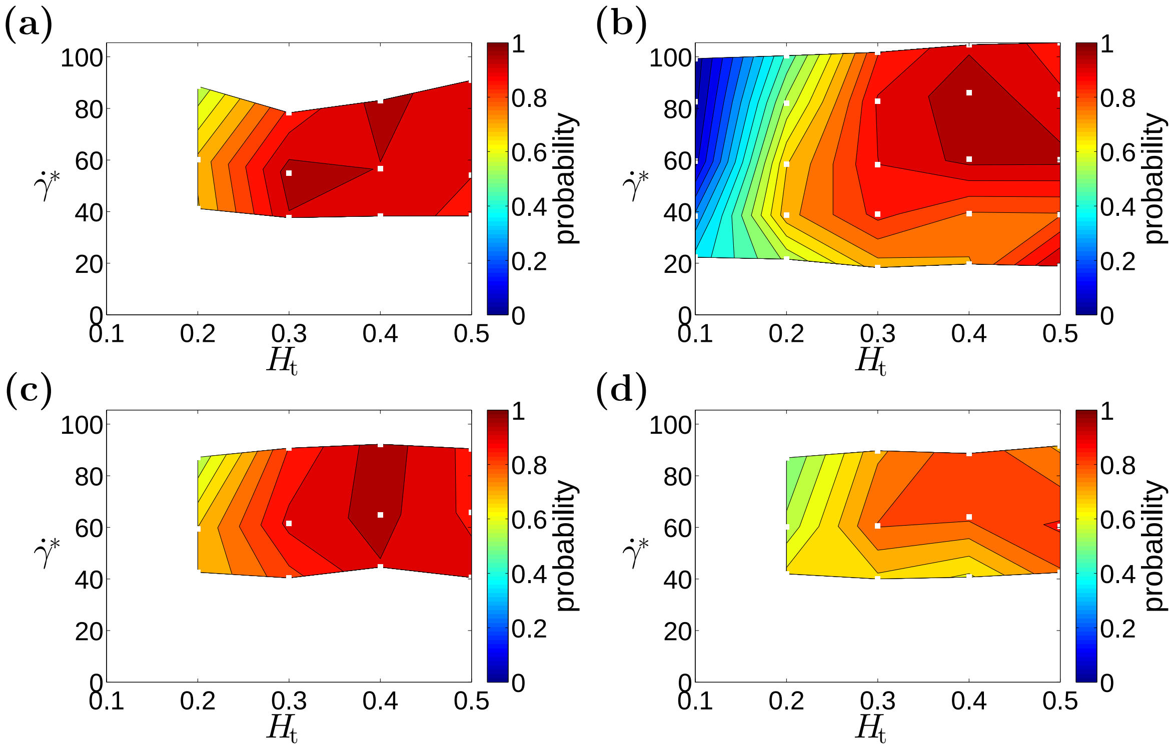

Figure C.1.: Margination probability for carrier margination into a region with constant distance $\delta = 0.1W = 0.31D_\mathrm{r}$ depending on the hematocrit H_t and the shear rate $\dot\gamma^*$. The considered spheres have the diameter: (a) $D_\mathrm{c} = 0.3D_\mathrm{r}$, (b) $D_\mathrm{c} = 0.28D_\mathrm{r}$, (c) $D_\mathrm{c} = 0.25D_\mathrm{r}$, and (d) $D_\mathrm{c} = 0.15D_\mathrm{r}$. The white squares (□) indicate the values of H_t and $\dot\gamma^*$ for which simulations have been performed. The colour code ranges from blue (low probability) to red (high probability).

The margination increases with increasing H_t apart from $H_\mathrm{t} = 0.5$ for the three largest spheres. Initially the margination increases with increasing shear rate, but for high shear rates it starts to decrease. The margination is similar for the three largest sizes but for $D_\mathrm{c} = 0.15D_\mathrm{r}$ margination is considerably reduced. All observations are in agreement with the observations made for the margination into the RBC-FL and the PAL in Fig. 4.3.

Corresponding to Fig. 4.4, which shows the margination probability into the PAL for $\dot{\gamma}^* \approx 59$ for all four spheres, Fig. C.2 presents the margination probability into the PAL for $\dot{\gamma}^* \approx 39$ and $\dot{\gamma}^* \approx 84$. Figure C.2 also shows a significantly reduced margination for the smallest carrier and shows slight decreases of the margination probability for $H_\mathrm{t} = 0.5$ at $\dot{\gamma}^* \approx 84$.

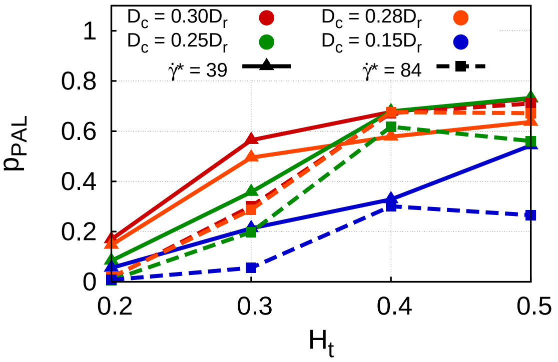

Figure C.2.: Probability p_PAL of margination into the potential adhesion layer (PAL) depending on the hematocrit H_t at $\dot{\gamma}^* \approx 39$ (triangles–solid curves) and $\dot{\gamma}^* \approx 84$ (squares–dashed curves). Different colours correspond to different sphere sizes: $D_\mathrm{c} = 0.3D_\mathrm{r}$ (red), $D_\mathrm{c} = 0.28D_\mathrm{r}$ (orange), $D_\mathrm{c} = 0.25D_\mathrm{r}$ (green), and $D_\mathrm{c} = 0.15D_\mathrm{r}$ (blue).
The sphere with $D_\mathrm{c} = 0.15D_\mathrm{r}$ possesses a significantly reduced margination. For $\dot{\gamma}^* \approx 84$ slight decreases of p_PAL are observed for $H_\mathrm{t} = 0.5$

Figure C.3 shows the carrier distribution characteristics dependent on the hematocrit of spherical carriers similar to Figs. 4.6 (a) and (b), but for carriers with the diameters $D_\mathrm{c} = 0.22D_\mathrm{r}$ and $D_\mathrm{c} = 0.25D_\mathrm{r}$. Similar to Fig. 4.6 (a) with increasing hematocrit the peak maximum reaches the minimum distance. However, the distance of the mean position in the RBC-FL to the wall is for both carriers further away from the minimal position compared to the carrier with $D_\mathrm{c} = 0.3D_\mathrm{r}$ in Fig. 4.6 (b) and also further away for the smaller carrier.

Figure C.4 shows the carrier distribution characteristics dependent on the RBC-FL thickness of spherical carriers similar to Figs. 4.7 (a) to (d), but for carriers with the diameters $D_\mathrm{c} = 0.22D_\mathrm{r}$ and $D_\mathrm{c} = 0.25D_\mathrm{r}$. A similar dependence on the RBC-FL thickness, shear rate, and carrier size of the measured properties is observed as in Figs. 4.7 (a) to (d). Additional, it shows the mean squared displacement at $H_\mathrm{t} = 0.4$ in Fig. C.4 (e) for all carriers, where only a shear rate dependence is observed for the smallest carrier in contrast to Fig. 4.7 (d) and Fig. C.4 (d).

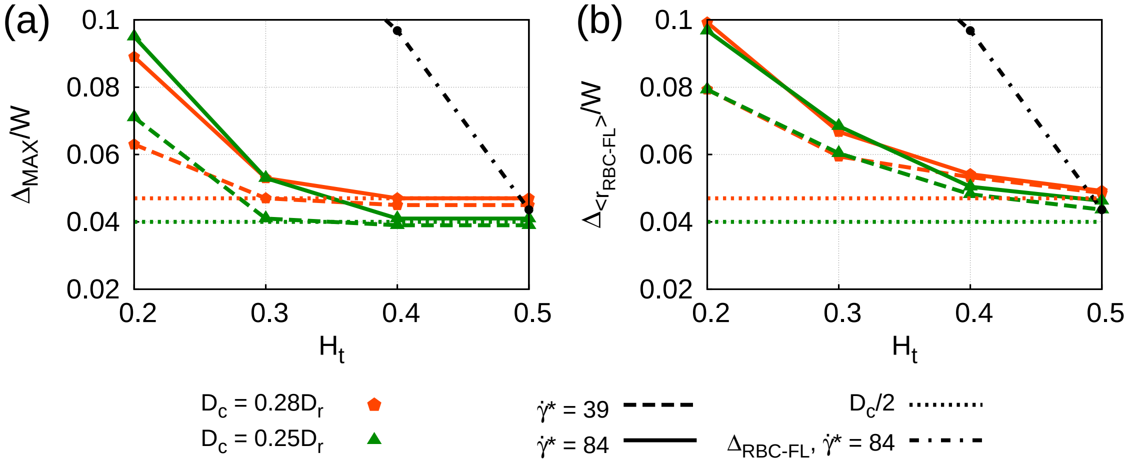

Figure C.3.: COM distribution characteristics depending on H_t. (a) Distance of the peak to the wall, Δ_MAX and (b) distance $\Delta_{\langle r_\mathrm{RBC-FL}\rangle}$ of the mean position in the RBC-FL to the wall Both quantities are normalized by the channel diameter W. Different curve colours correspond to different sphere sizes: $D_\mathrm{c} = 0.28D_\mathrm{r}$ (orange) and $D_\mathrm{c} = 0.25D_\mathrm{r}$ (green) Different curve types refer to different shear rates: $\dot{\gamma}^* \approx 39$ (dashed) and $\dot{\gamma}^* \approx 84$ (solid). The coloured dotted curves indicate the particular minimum distance to the wall $D_\mathrm{c}/2$ and the black dash-dotted curve the RBC-FL thickness $\Delta_\mathrm{RBC-FL}$ for $\dot{\gamma}^* \approx 84$.

With increasing H_t the peak maximum reaches the minimum distance, similar to the results shown in Fig. 4.6,. Furthermore, $\Delta_{\langle r_\mathrm{RBC-FL}\rangle}$ is further away from the minimal position for the smaller carrier.

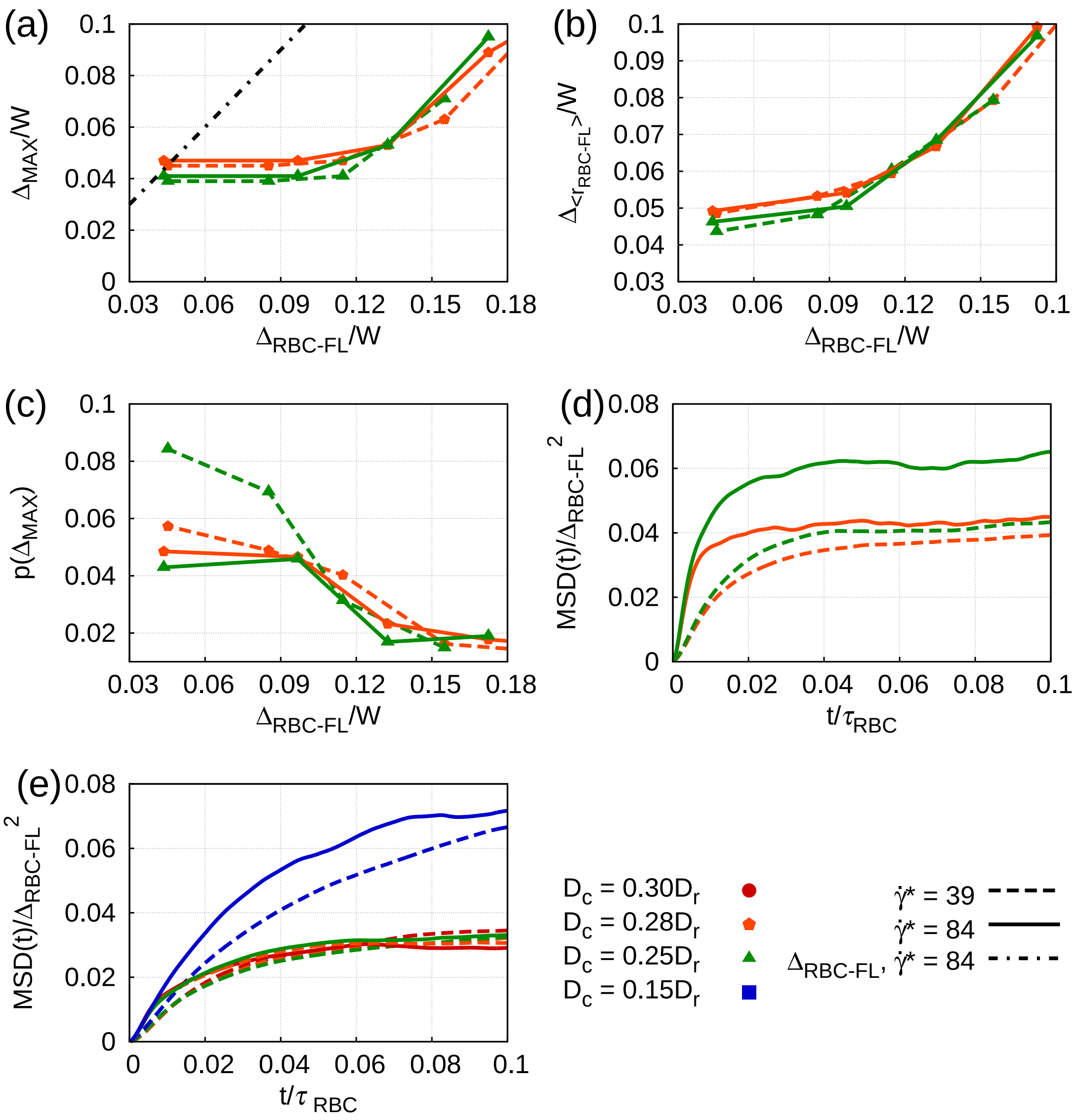

Figure C.4.: COM distribution analysis depending on the RBC-FL thickness $\Delta_{\mathrm{RBC-FL}}$ and shear rate $\dot{\gamma}^*$. (a) Distance of the peak to the wall, Δ_{MAX}, (b) distance $\Delta_{\langle r_{\mathrm{RBC-FL}}\rangle}$ of the mean position in the RBC-FL to the wall, and (c) height of the peak maximum $p(\Delta_{\mathrm{MAX}})$. These parameters are normalized by the channel diameter W. (d) Time t dependent mean squared displacement $\mathrm{MSD}(t)$ in RBC-FL at hematocrit $H_{\mathrm{t}} = 0.5$. (e) $\mathrm{MSD}(t)$ in RBC-FL at hematocrit $H_{\mathrm{t}} = 0.4$. The time is normalized by the RBC relaxation time τ_{RBC}. Different curves correspond to different sphere diameters: $D_{\mathrm{c}} = 0.3D_{\mathrm{r}}$ (red), $D_{\mathrm{c}} = 0.28D_{\mathrm{r}}$ (orange), $D_{\mathrm{c}} = 0.25D_{\mathrm{r}}$ (green), $D_{\mathrm{c}} = 0.15D_{\mathrm{r}}$ (blue). The dashed curves refer to the shear rate $\dot{\gamma}^* \approx 39$ and the solid curves to $\dot{\gamma}^* \approx 84$. The black dash-dotted curve the RBC-FL thickness $\Delta_{\mathrm{RBC-FL}}$ for $\dot{\gamma}^* \approx 84$..

At $H_{\mathrm{t}} = 0.4$ a deviating MSD for different shear rates is only observed for the carrier with $D_{\mathrm{c}} = 0.15D_{\mathrm{r}}$. Hence, a change in fluctuations does not fully explain the shear rate dependence of margination.

Figure C.5 presents the margination probability of the ellipsoid and the disc into a constant distance of thickness $\delta = 0.31 D_\mathrm{r}$. Also here, a similar hematocrit and shear rate dependence of margination is observed as in Figs. 4.8 (b) and (c).

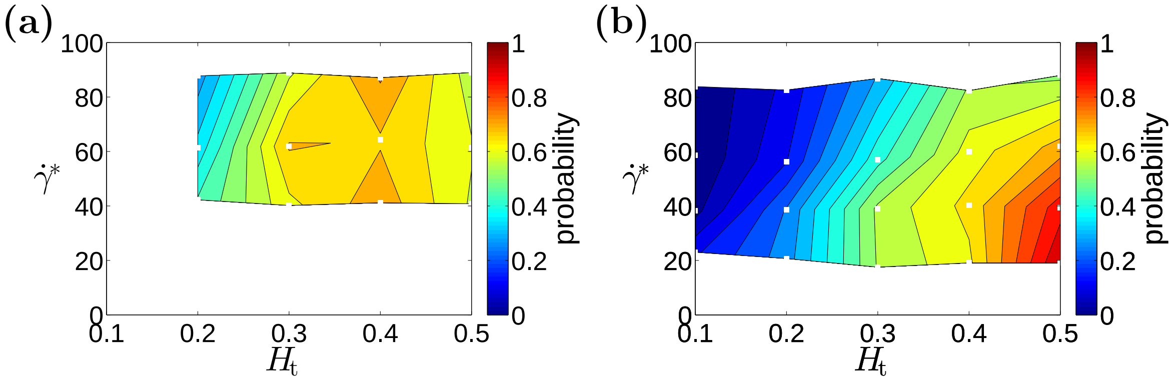

Figure C.5.: Margination probability into a region with constant distance $\delta = 0.1W = 0.31 D_\mathrm{r}$ depending on the shear rate $\dot{\gamma}^*$ and hematocrit H_t. The white squares (□) indicate the values of H_t and $\dot{\gamma}^*$ for which simulations have been performed. The colour code ranges from blue (low probability) to red (high probability).
Compared to Fig. C.1 (a) the margination in the constant region is reduced for elongated shapes, since δ is just slightly larger than the long axis radius of the considered shapes. For high H_t the margination for the disc is higher, because a high second peak occurs, see Fig. 4.10. The margination dependence on H_t and $\dot{\gamma}^*$ is similar to the margination into the two other choices of margination layer shown in Figs. 4.8 (b) and (c).

Figure C.6 presents the margination probability into the PAL for all three carriers with the same volume (sphere, ellipsoid, and disc) for the shear rates $\dot{\gamma}^* = 39$ and $\dot{\gamma}^* = 84$, corresponding to Fig. 4.9, which shows the margination probability for the shear rate $\dot{\gamma}^* = 59$. For the highest shear rate not only the margination probability for the ellipsoid, but also for the disc decreases for $H_\mathrm{t} = 0.5$, whereas for the lowest shear rate the margination probability for the disc is larger than for the sphere at all hematocrit values.

Corresponding to Figs. 4.13 (a) to (c), Fig. C.7 presents the angular velocity of the three spheres with the diameter of $D_\mathrm{c} = 0.28 D_\mathrm{r}$, $D_\mathrm{c} = 0.25 D_\mathrm{r}$, and $D_\mathrm{c} = 0.15$ depending on hematocrit and shear rate. The measured angular velocities agree with the theoretical predictions by Jeffery [168].

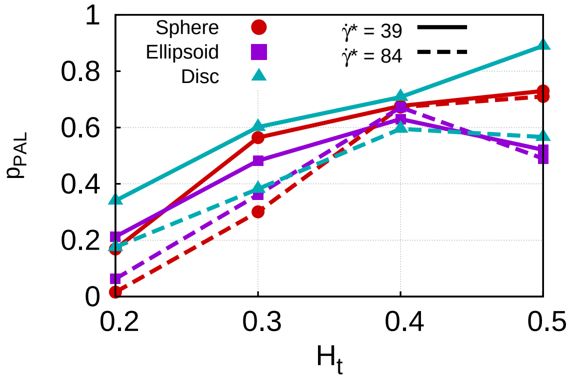

Figure C.6.: Probability p_{PAL} of margination into the PAL depending on hematocrit H_{t}. Curve colours correspond to the sphere with $D_{\mathrm{c}} = 0.3D_{\mathrm{r}}$ (red), ellipsoid (purple), and disc (cyan). Solid curves refer to a shear rate of $\dot{\gamma}^* = 39$ and dashed curves to $\dot{\gamma}^* = 84$. At low H_{t} values elongated shapes marginate better. At high H_{t} the disc marginates similar as the sphere, whereas the margination probability of the ellipsoid decreases. At $H_{\mathrm{t}} = 0.5$ and $\dot{\gamma}^* = 84$ also the margination of the disc is reduced.

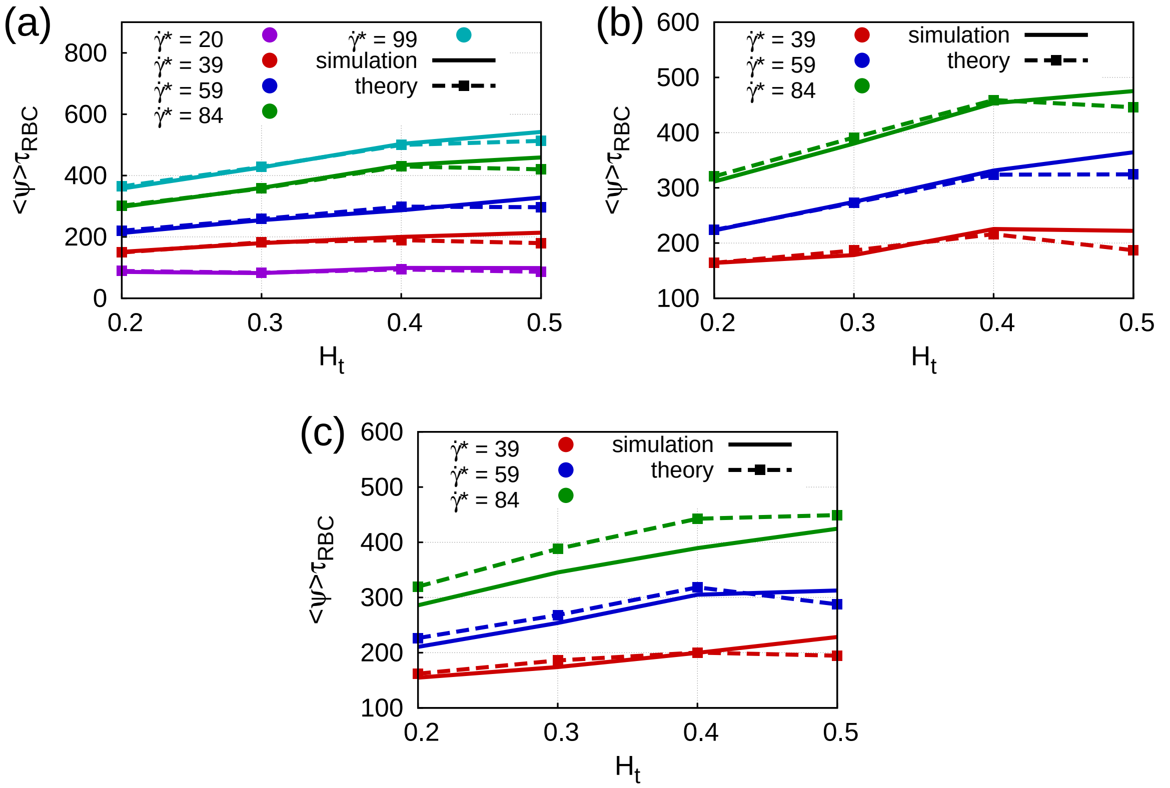

Figure C.7.: Average angular velocities $\langle\psi\rangle$ as given in Eq. (4.3) normalized by the RBC relaxation time τ_{RBC} for the spheres with the diameters (a) $D_{\mathrm{c}} = 0.28 D_{\mathrm{r}}$, (b) $D_{\mathrm{c}} = 0.25 D_{\mathrm{r}}$, and (c) $D_{\mathrm{c}} = 0.15$. Solid curves: simulation results and dashed curves: theoretical predictions by Jeffery [168] for the near-wall shear rate that has been estimated from the simulation velocity profiles.
For all spheres the theoretically predicted and the measured average angular velocities agree.

C.2. Simulations of carriers in two-dimensional model systems

Table C.3 presents the number of particles (vertices) per carrier and the number of carriers per simulation for the 2D simulations for different sizes of carriers and different channel sizes presented in Sections 4.2 and 4.3.

cell size	$D_\mathrm{c} = 0.6D_r$	$D_\mathrm{c} = 0.3D_r$	$D_\mathrm{c} = 0.22D_r$	$D_\mathrm{c} = 0.15D_r$	$D_\mathrm{c} = 0.04D_r$
N_v^c	40	20	15	10	1
$N_{W=20\,\mu\mathrm{m}}$	4	6	20	20	100
$N_{W=10\,\mu\mathrm{m}}$	/	6	/	14	/
$N_{W=15\,\mu\mathrm{m}}$	/	6	/	/	/
$N_{W=40\,\mu\mathrm{m}}$	/	12	/	30	/
$N_{W=60\,\mu\mathrm{m}}$	/	27	/	/	/

Table C.3.: Carrier characteristics. N_v^c is the number of particles (vertices) per carrier for 2D simulations and N is the number of carriers in the system depending on the channel width W and particle size. For the ellipse N_v^c and $N_{W=20\,\mu\mathrm{m}}$ is similar as for the circle with $D_\mathrm{c} = 0.3D_r$.

Figure C.8 is complementary to Fig. 4.17. Here, the distance Δ_{MAX} of the peak maximum to the wall and the distance $\Delta_{<r>}$ of the average COM position in the whole channel is compared for 2D and 3D for different shear rates and for round and elongated shapes.

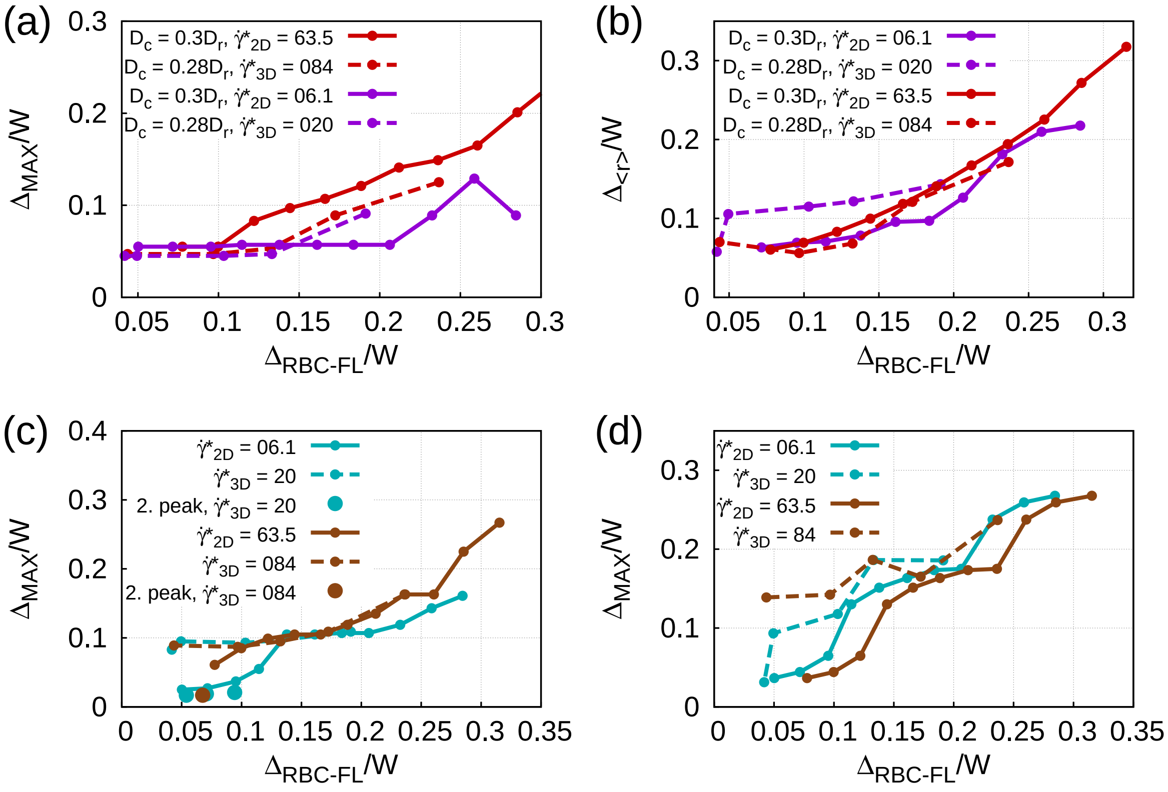

Figure C.8.: Comparison of carrier distribution characteristics in 2D and 3D. (a) Distance Δ_{MAX} of the peak position to the wall and (b) distance $\Delta_{<r>}$ of the mean position in the whole channel to the wall normalized by the channel width/diameter W for round carriers. In 2D, the examined carrier size is $D_{\mathrm{c}}^{\mathrm{2D}} = 0.3 D_{\mathrm{r}}^{\mathrm{2D}}$, while in 3D, $D_{\mathrm{c}}^{\mathrm{3D}} = 0.28 D_{\mathrm{r}}^{\mathrm{3D}}$. The considered shear rates are $\dot{\gamma}^*_{\mathrm{2D}} = 6.1$ (purple) and $\dot{\gamma}^* = 63.5$ (red) for 2D and $\dot{\gamma}^*_{\mathrm{3D}} = 20$ (purple) and $\dot{\gamma}^* = 84$ (red) for 3D. (c) Distance Δ_{MAX} of the peak position to the wall and (d) distance $\Delta_{<r>}$ of mean position in the whole channel to the wall for ellipse (purple) and disc (cyan). The considered shear rates are $\dot{\gamma}^*_{\mathrm{2D}} = 6.1$ (cyan) and $\dot{\gamma}^* = 63.5$ (brown) for 2D and $\dot{\gamma}^*_{\mathrm{3D}} = 20$ (cyan) and $\dot{\gamma}^* = 84$ (brown) for 3D. The different curves correspond to 2D (solid) and 3D (dashed) simulations.
The distribution characteristics agree well in 2D and 3D. Just the disc distribution does not possess a second peak as already shown in Fig. 4.17 and some deviations are observed for high shear rates.

C.3. Channel-size dependence

Figure C.9 presents the probability of margination into the RBC-FL and the PAL for carriers with $D_\mathrm{c} = 0.15D_\mathrm{r}$ complementary to Fig. 4.28, which shows the margination probabilities for carriers with $D_\mathrm{c} = 0.3D_\mathrm{r}$. Figure C.9 shows similar results as Fig. 4.28. However, compared to Fig. 4.28 (a), the probability of margination into the RBC-FL of the smallest channel differs less from the probabilities of the wider channels for the smaller carriers as presented in Fig. C.9 (a).

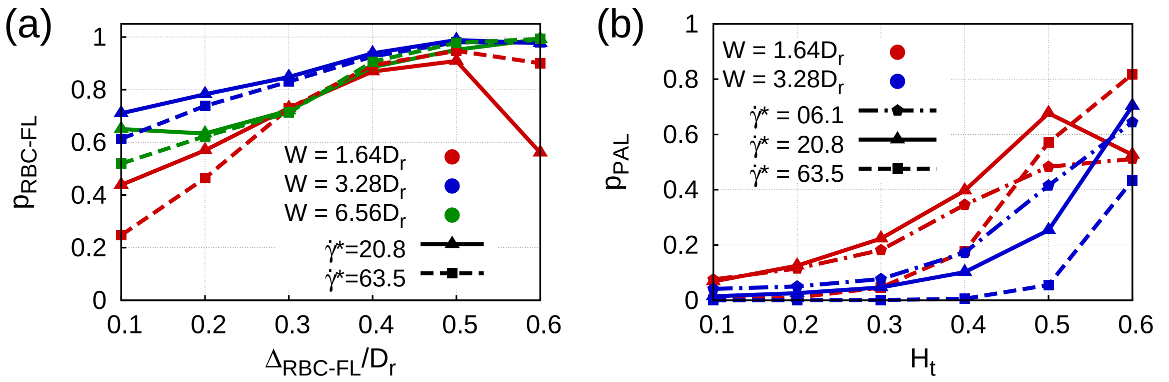

Figure C.9.: (a) Margination probability $p_{\mathrm{RBC-FL}}$ into the RBC-FL and (b) margination probability into the PAL p_{PAL} depending on hematocrit H_t for a carrier of size $D_\mathrm{c} = 0.15D_\mathrm{r}$. Different curve colours correspond to different channel sizes: $W = 1.64D_\mathrm{r}$ (red), $W = 3.28D_\mathrm{r}$ (blue), and $W = 6.56D_\mathrm{r}$ (green). Different shear rates correspond to different curve types: $\dot\gamma^* = 6.1$ (dot-dashed), $\dot\gamma^* = 20.8$ (solid), and $\dot\gamma^* = 63.5$ (dashed).
The results agree with the observations for carriers with $D_\mathrm{c} = 0.3D_\mathrm{r}$ in Fig. 4.28.

Figure C.10 shows the distance of the peak of the COM distribution for the carriers with $D_\mathrm{c} = 0.3D_\mathrm{r}$ and $D_\mathrm{c} = 0.15D_\mathrm{r}$ for different shear rates for a large channel width $W = 6.56D_\mathrm{r}$. As stated in the main text of Section 4.3.1 the peak reaches the minimal distance of $D_\mathrm{c}/2$ from the wall only for the highest hematocrit besides for the lowest shear rate.

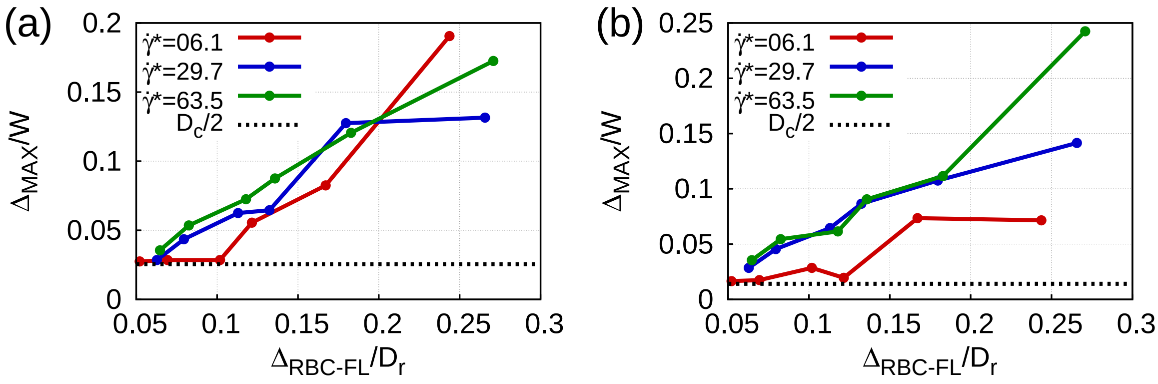

Figure C.10.: Carrier peak position Δ_{MAX} for a large channel width $W = 6.56D_{\mathrm{r}}$ for the carriers with size $D_{\mathrm{c}} = 0.3D_{\mathrm{r}}$ (a) and $D_{\mathrm{c}} = 0.15D_{\mathrm{r}}$ (b) for different shear rates: $\dot{\gamma}^* = 6.1$ (red), $\dot{\gamma}^* = 29.7$ (blue), and $\dot{\gamma}^* = 63.5$ (green). The minimal distance $D_{\mathrm{c}}/2$ is marked by the black dotted line.

Except the lowest shear rate, the peak reaches the minimum position only for the smallest RBC-FL thickness.

C.4. Margination mechanism

Regarding the test, if the alteration of hydrodynamic and excluded-volume interactions between RBCs and platelets influence the RBC COM distributions, Fig. C.11 shows the comparison of the RBC COM distribution for the cases of the original simulation, the simulation where excluded-volume interactions are turned off, where excluded volume interactions are turned off and the carriers are constrained to a near-wall region and for the simulation where the hydrodynamic simulations are turned off. For all these cases the RBC COM distribution agree well for the same shear rate and hematocrit values as mentioned in Section 4.4.

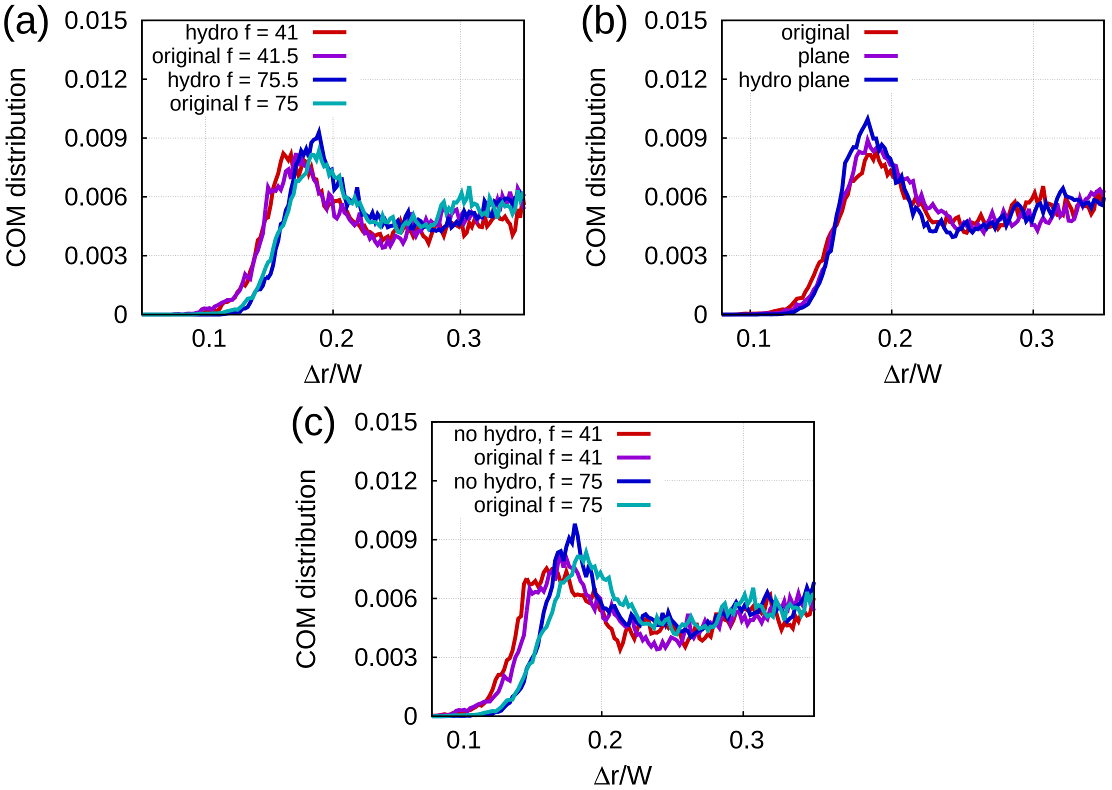

Figure C.11.: Comparison of RBC COM distributions depending on the distance Δr of the COM to the wall normalized by the channel width W, for (a) simulations with only hydrodynamic interactions, (b) simulations with platelets constrained to a near-wall region with and without hydrodynamic interactions, and (c) simulations without hydrodynamic interactions. These examples are for a sphere with $D_\mathrm{c} = 0.28D_\mathrm{r}$ at $H_\mathrm{t} = 0.3$. The force on the fluid particles is $f' = fk_\mathrm{B}T/W$
For all cases the RBC COM distributions agree well.

Appendix D.

VWF stretching in simple shear and blood flow

Figure D.1 shows the radius of gyration depending on the length of the polymers defined by the number N_m of beads and the attraction between the monomers. Similar to the 2D results shown in Fig. 5.2 changing the LJ interaction is the same as changing the quality of the solvent, see Fig. D.1 (c). For the investigated system, the $\epsilon = \tilde{\epsilon}/k_\mathrm{B}T$ that corresponds to the theta solvent is close to $\epsilon = 0.5$, because this is when the lines for different numbers N_m of monomers in Fig. D.1 (a) cross each other. Furthermore, Fig. D.1 (b) shows that an increase of temperature and simultaneously increase of $\tilde{\epsilon}$ leads to the same radius of gyration.

Figure D.2 presents the probability distribution of the bond length Δb between neighbouring monomers of a polymer chain that is tethered to the wall with one end (top) and a chain that is additional decorated with a platelet (bottom) for all three polymer types (a-c) scaled by the expected length of $2a_\mathrm{m}$. In all cases the distributions are narrow, thus almost no stretching of the bonds is observed and the measured extension is indeed due to unravelling of the polymer coil.

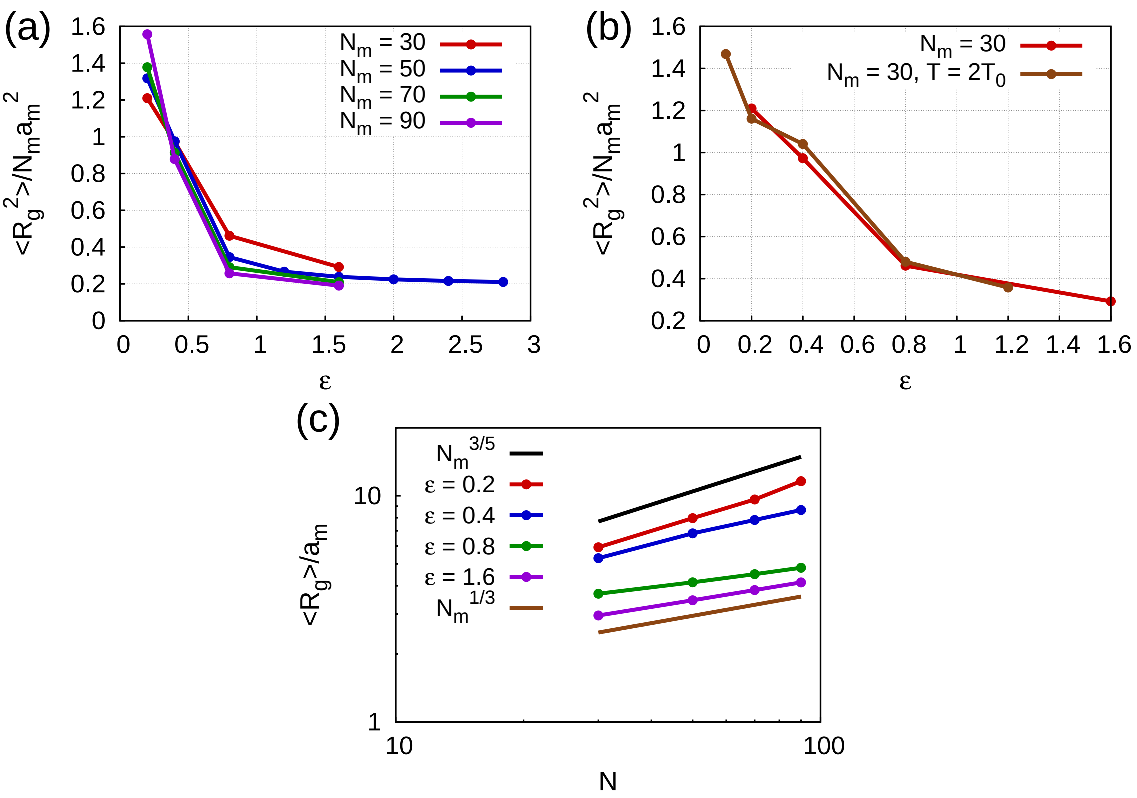

Figure D.1.: Measurements of the 3D average radius of gyration squared $\langle R_g^2 \rangle$ of a polymer chain. (a) $\langle R_g^2 \rangle$ is normalized by $N_\mathrm{m} a_\mathrm{m}^2$, with N_m the number of beads and a_m the bead radius. It depends on the attraction strength $\tilde{\epsilon} = \epsilon k_\mathrm{B} T$. Different curves correspond to different chain length: $N_\mathrm{m} = 30$ (red), $N_\mathrm{m} = 50$ (blue), $N_\mathrm{m} = 70$ (green), and $N_\mathrm{m} = 90$ (purple). (b) $\langle R_g^2 \rangle$ for $N_\mathrm{m} = 30$ and different temperatures T. (c) Logarithm of $\langle R_g^2 \rangle$ depending on the number of beads compared to the expected scaling from theory. Different curves correspond to different monomer interactions.

The radius of gyration for a repulsive polymer behaves as in a good solvent and for increasing attraction strength the polymer coil is almost closed packed.

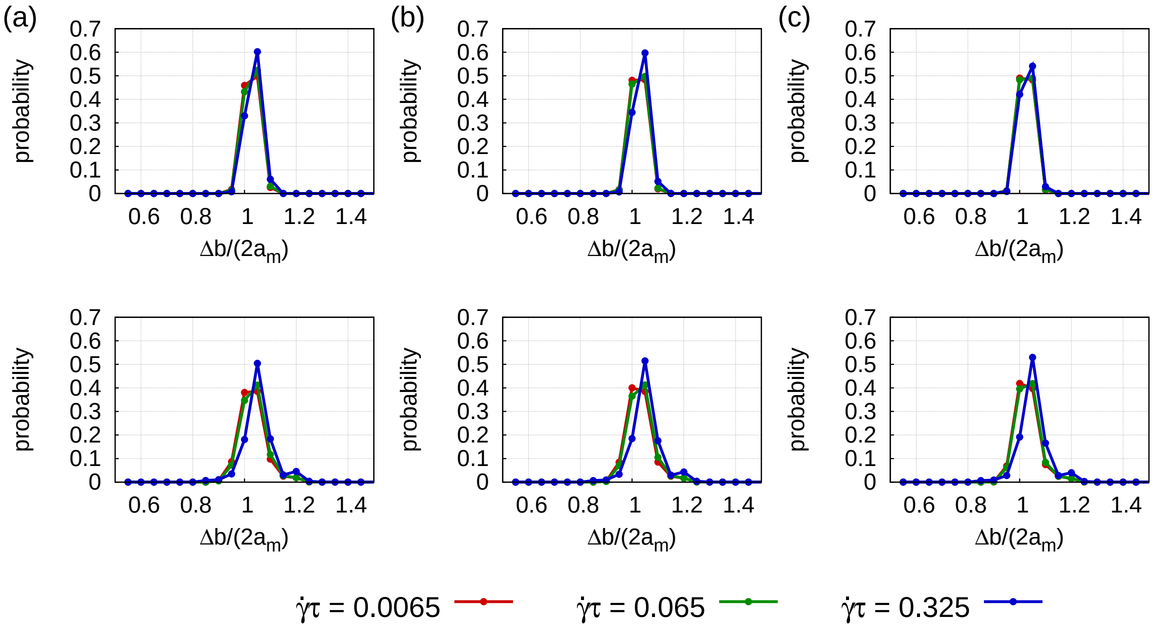

Figure D.2.: Probability distribution of bond length Δb normalized by the desired value the polymer diameter $2a_{\mathrm{m}}$ for (a) the repulsive polymer, (b) the attractive polymer with $\epsilon = 2$, and (c) $\epsilon = 4$. (top) The polymers are tethered with one end to the wall and (bottom) additionally a platelet is attached to the free end of the chain. Different curves correspond to different normalized shear rates: $\dot{\gamma}\tau = 0.0065$ (red), $\dot{\gamma}\tau = 0.065$ (green), and $\dot{\gamma}\tau = 0.325$ (cyan).

Almost no stretching of the bonds is observed and the measured extension is indeed due to unraveling of the polymer coil.

Bibliography

[1] G. Pocock, C. D. Richards, and D. A. Richards. *Human Physiology.* Oxford University Press (2006).

[2] *Global atlas on cardiovascular disease prevention and control.* World Health Organisation (WHO) http://www.who.int/ (2011).

[3] M. Furlan. Von Willebrand factor: molecular size and functional activity. *Annals of Hematology* **72**(6), 341–348 (1996).

[4] R. Schneppenheim and U. Budde. *von Willebrand Disease and von Willebrand Factor.* UNI-MED Verlag AG (2008).

[5] *Cancer fact sheet.* WHO http://www.who.int/mediacentre/factsheets/fs297/en/.

[6] E. Blanco, A. Hsiao, A. P. Mann, M. G. Landry, F. Meric-Bernstam, and M. Ferrari. Nanomedicine in cancer therapy: Innovative trends and prospects. *Cancer Science* **102**(7), 1247–1252 (2011).

[7] J. W. von Goethe. *Faust: Der Tragödie erster Teil.* (1808).

[8] A. D. Michelson. *Platelets, Second Edition.* Academic Press (2007).

[9] S. I. Hajdu. *A Note from History:* The Discovery of Blood Cells. *Annals of Clinical & Laboratory Science* **33**(2), 237–238 (2003).

[10] D. A. Jones. The important of surface area/volume ratio to the rate of oxygen uptake by red cells. *The Journal of General Physiology* **74**(5), 643–646 (1979).

[11] K. D. Vandegriff and J. S. Olson. Morphological and Physiological Factors Affecting Oxygen Uptake and Release by Red Blood Cells. *Journal of Biological Chemistry* **259**(20), 12619–12627 (1984).

[12] Y. C. Fung. *Biomechanics: Mechanical Properties of Living Tissues.* Springer-Verlag New York second edition (1993).

[13] J. D. Moyer, R. B. Nowak, N. E. Kim, S. K. Larkin, L. L. Peters, J. Hartwig, F. A. Kuypers, and V. M. Fowler. Tropomodulin 1-null mice have a mild spherocytic elliptocytosis with appearance of Tropomodulin 3 in red blood cells and disruption of the membrane skeleton. *Blood* **116**(14), 2590–2599 (2010).

[14] H. Zhao and E. S. G. Shaqfeh. Shear-induced platelet margination in a microchannel. *Phys. Rev. E* **83**, 061924 (2011).

[15] A. J. Reininger. Function of von Willebrand factor in haemostasis and thrombosis. *Haemophilia* **14**(Suppl. 5), 11–26 (2008).

[16] B. P. Nuyttens, T. Thijs, H. Deckmyn, and K. Broos. Platelet adhesion to collagen. *Thrombosis Research* **127**(Suppl. 2), S26–S29 (2011).

[17] K. Broos, H. B. Feys, S. F. De Meyer, K. Vanhoorelbeke, and H. Deckmyn. Platelets at work in primary hemostasis. *Blood Reviews* **25**, 155–167 (2011).

[18] T. A. Springer. Traffic signals on endothelium for lymphocyte recirculation and leukocyte emigration. *Annu. Rev. Physiol.* **57**, 827–872 (1995).

[19] S. W. Schneider, S. Nuschele, A. Wixforth, C. Gorzelanny, A. Alexander-Katz, R. R. Netz, and M. F. Schneider. Shear-induced unfolding triggers adhesion of von Willebrand factor fibers. *Proc. Natl. Acad. Sci. USA* **104**(19), 7899–7903 (2007).

[20] J.-f. Dong. Cleavage of ultra-large von Willebrand factor by ADAMTS-13 under flow conditions. *Journal of Thrombosis and Haemostasis* **3**, 1710–1716 (2005).

[21] D. J. Bowen. Sugar targets VWF for the chop. *Blood* **115**(13), 2565–2565 (2010).

[22] T. Goerge, F. Kleinerüschkamp, A. Barg, E.-M. Schnaeker, V. Huck, M. F. Schneider, M. Steinhoff, and S. W. Schneider. Microfluidic reveals generation of platelet-strings on tumor-activated endothelium. *Thrombosis and Haemostasis* **98**, 283–286 (2007).

[23] M. F. Schneider and S. W. Schneider. Der von Willlebrand-Faktor: ein intelligenter gefässkleber. *Biospektrum* **2**, 134–139 (2008).

[24] T. A. Springer. von Willebrand factor, Jedi knight of the bloodstream. *Blood* **124**(9), 1412–1425 (2014).

[25] Y.-F. Zhou, E. T. Eng, J. Zhu, C. Lu, T. Walz, and T. A. Springer. Sequence and structure relationships within von Willebrand factor. *Blood* **120**(2), 449–458 (2012).

[26] A. J. Reininger, H. F. G. Heijnen, H. Schumann, H. M. Specht, W. Schramm, and Z. M. Ruggeri. Mechanism of platelet adhesion to von Willebrand factor and microparticle formation under high shear stress. *Blood* **107**(9), 3537–3545 (2006).

[27] B. Savage, E. Saldivar, and Z. M. Ruggeri. Initiation of Platelet Adhesion by Arrest onto Fibrinogen or Translocation on von Willebrand Factor. *Cell* **84**, 289–297 (1996).

[28] M. J. Maxwell, E. Westein, W. S. Nesbitt, S. Giuliano, S. M. Dopheide, and S. P. Jackson. Identification of a 2-stage platelet aggregation process mediating shear-dependent thrombus formation. *Blood* **109**(2), 566–576 (2007).

[29] J. L. Moake, N. A. Turner, N. A. Stathopoulos, L. H. Nolasco, and J. D. Hellums. Involvement of Large Plasma von Willebrand Factor (vWF) Multimers and Unusually Large vWF Forms Derived from Endothelial Cells in Shear Stress-induced Platelet Aggregation. *J. Clin. Invest.* **78**(6), 1456–1461 (1986).

[30] Z. M. Ruggeri. von Willebrand Factor. *J. Clin. Invest.* **99**(4), 559–564 (1997).

[31] Z. M. Ruggeri. Von Willebrand factor, platelets and endothelial cell interactions. *Journal of Thrombosis and Haemostasis* **1**, 1335–1342 (2003).

[32] A. Barg, R. Ossig, T. Goerge, M. F. Schneider, H. Schillers, H. Oberleithner, and S. W. Schneider. Soluble plasma-derived von Willebrand factor assembles to a haemostatically active filamentous network. *Thrombosis and Haemostasis* **97**, 514–526 (2007).

[33] H. Chen, M. A. Fallah, V. Huck, J. I. Angerer, A. J. Reininger, S. W. Schneider, M. F. Schneider, and A. Alexander-Katz. Blood-clotting-inspired reversible polymer-colloid composite assembly in flow. *Nat. Commun.* **4**, 1333 (2013).

[34] R. Schneppenheim, U. Budde, F. Oyen, D. Angerhaus, V. Aumann, E. Drewke, W. Hassenpflug, J. Häberle, K. Kentouche, E. Kohne, K. Kurnik, D. Mueller-Wiefel, T. Obser, R. Santer, and K.-W. Sykora. von Willebrand factor cleaving protease and *ADAMTS13* mutations in childhood TTP. *Blood* **101**(5), 1845–1850 (2003).

[35] B. Petri, A. Broermann, H. Li, A. G. Khandoga, A. Zarbock, F. Krombach, T. Goerge, S. W. Schneider, C. Jones, B. Nieswandt, M. K. Wild, and D. Vestweber. von Willebrand factor promotes leukocyte extravasation. *Blood* **116**(22), 4712–4719 (2010).

[36] M. Ferrari. Cancer nanotechnology: opportunities and challenges. *Nat. Rev. Cancer* **5**, 161–171 (2005).

[37] R. K. Jain and T. Stylianopoulos. Delivering nanomedicine to solid tumors. *Nat. Rev. Clin. Oncol.* **7**, 653–664 (2010).

[38] W. R. Sanhai, J. H. Sakamoto, R. Canady, and M. Ferrari. Seven challenges for nanomedicine. *Nat. Nanotechnol.* **3**, 242–244 (2008).

[39] R. K. Jain. Delivery of Novel Therapeutic Agents in Tumors: Physiological Barriers and Strategies. *Journal of the National Cancer Institute* **81**(8), 570–576 (1989).

[40] S. Muro, C. Garnacho, J. A. Champion, J. Leferovich, C. Gajewski, E. H. Schuchman, S. Mitragotri, and V. R. Muzykantov. Control of Endothelial Targeting and Intracellular Delivery of Therapeutic Enzymes by Modulating the Size and Shape of ICAM-1-targeted Carriers. *Mol. Ther.* **16**(8), 1450–1458 (2008).

[41] R. Duncan. Polymer conjugates as anticancer nanomedicines. *Nat. Rev. Cancer* **6**, 688–701 (2006).

[42] B.-S. Ding, T. Dziubla, V. V. Shuvaev, S. Muro, and V. R. Muzykantov. Advanced drug delivery systems that target the vascular endothelium. *Mol. Interv.* **6**(2), 98–112 (2006).

[43] J. P. Rolland, B. W. Maynor, L. E. Euliss, A. E. Exner, G. M. Denison, and J. M. DeSimone. Direct Fabrication and Harvesting of Monodisperse, Shape-Specific Nanobiomaterials. *J. Am. Chem. Soc.* **127**, 10096–10100 (2005).

[44] J. D. Slack, M. Kanke, G. H. Simmons, and P. P. DeLuca. Acute Hemodynamic Effects and Blood Pool Kinetics of Polystyrene Microspheres following Intravenous Administration. *Journal of Pharmaceutical Sciences* **70**(6), 660–664 (1981).

[45] P. Decuzzi, B. Godin, T. Tanaka, S.-Y. Lee, C. Chiappini, X. Liu, and M. Ferrari. Size and shape effects in the biodistribution of intravascularly injected particles. *Journal of Controlled Release* **141**, 320–327 (2010).

[46] M. Herant, V. Heinrich, and M. Dembo. Mechanics of neutrophil phagocytosis: experiments and quantitative models. *Journal of Cell Science* **119**(9), 1903–1913 (2006).

[47] D. C. Litzinger, A. M. J. Buiting, N. van Rooijen, and L. Huang. Effect of liposome size on the circulation time and intraorgan distribution of amphipathic poly(ethylene glycol)-containing liposomes. *Biochim. Biophys. Acta* **1190**, 99–107 (1994).

[48] W. H. De Jong, W. I. Hagens, P. Krystek, M. C. Burger, A. J. A. M. Sips, and R. E. Geertsma. Particle size-dependent organ distribution of gold nanoparticles after intravenous administration. *Biomaterials* **29**, 1912–1919 (2008).

[49] K. Namdee, A. J. Thompson, P. Charoenphol, and O. Eniola-Adefeso. Margination Propensity of Vascular-Targeted Spheres from Blood Flow in a Microfluidic Model of Human Microvessels. *Langmuir* **29**, 2530–2535 (2013).

[50] J. A. Champion and S. Mitragotri. Role of target geometry in phagocytosis. *Proc. Natl. Acad. Sci. USA* **103**(13), 4930–4934 (2006).

[51] F. Gentile, C. Chiappini, D. Fine, R. C. Bhavane, M. S. Peluccio, M. M.-C. Cheng, X. Liu, M. Ferrari, and P. Decuzzi. The effect of shape on the margination dynamics of non-neutrally buoyant particles in two-dimensional shear flows. *Journal of Biomechanics* **41**, 2312–2318 (2008).

[52] A. J. Thompson, E. M. Mastria, and O. Eniola-Adefeso. The margination propensity of ellipsoidal micro/nanoparticles to the endothelium in human blood flow. *Biomaterials* **34**, 5863–5871 (2013).

[53] P. Decuzzi and M. Ferrari. The adhesive strength of non-spherical particles mediated by specific interactions. *Biomaterials* **27**, 5307–5314 (2006).

[54] S. Dasgupta, T. Auth, and G. Gompper. Wrapping of ellipsoidal nano-particles by fluid membranes. *Soft Matter* **9**, 5473–5482 (2013).

[55] I. Cantat and C. Misbah. Lift Force and Dynamical Unbinding of Adhering Vesicles under Shear Flow. *Phys. Rev. Lett.* **83**(4), 880–883 (1999).

[56] M. Abkarian, C. Lartigue, and A. Viallat. Tank Treading and Unbinding of Deformable Vesicles in Shear Flow: Determination of the Lift Force. *Phys. Rev. Lett.* **88**(6), 068103 (2002).

[57] G. Gompper and M. Schick, editors. *Soft Matter: Volume 1 - Polymer Melts and Mixtures*. Wiley-VCH Verlag (2005).

[58] E. Guyon, J.-P. Hulin, and L. Petit. *Physical Hydrodynamics*. Oxford University Press (2001).

[59] J. K. G. Dhont. *An Introduction to Dynamics of Colloids*. Elsevier (1996).

[60] D. Frenkel and B. Smit. *Understanding Molecular Simulation*. Academic Press (2001).

[61] P.-G. De Gennes and J. Prost. *The Physics of Liquid Crystals*. Clarendon Press Oxford (1993).

[62] K. Binder and W. Paul. Monte Carlo Simulations of Polymer Dynamics: Recent Advances. *Journal of Polymer Science Part B: Polymer Physics* **35**, 1–31 (1997).

[63] K. Müller, N. Osterman, D. Babic, C. N. Likos, J. Dobnikar, and A. Nikoubashman. Pattern Formation and Coarse-Graining in Two-Dimensional Colloids Driven by Multiaxial Magnetic Fields. *Langmuir* **30**, 5088–5096 (2014).

[64] M. P. Allen and D. J. Tildesley. *Computer Simulation of Liquids*. Clarendon Press Oxford (1991).

[65] B. J. Alder and T. E. Wainwright. Phase Transition for a Hard Sphere System. *J. Chem. Phys.* **27**(5), 1208–1209 (1957).

[66] A. Einstein. *Investigations on the Theory of the Brownian Movement*. Courier Dover Publications (1956).

[67] M. Karplus and J. A. McCammon. Molecular dynamics simulations of biomolecules. *Nat. Struct. Biol.* **9**(9), 646–652 (2002).

[68] T. E. Cheatham III and P. A. Kollman. Observation of the *A*-DNA to *B*-DNA Transition During Unrestrained Molecular Dynamics in Aqueous Solution. *Journal of Molecular Biology* **259**, 434–444 (1996).

[69] D. S. Lemons and A. Gythiel. Paul Langevin's 1908 paper "On the Theory of Brownian Motion" ["Sur la théorie du mouvement brownien," C. R. Acad. Sci. (Paris) 146, 530-533 (1908)]. *American Journal of Physics* **65**(11), 1079–1081 (1997).

[70] A. Satoh. *Introduction to Practice of Molecular Simulation.* Elsevier (2011).

[71] J. F. Brady and G. Bossis. Stokesian Dynamics. *Annual Review of Fluid Mechanics* **20**, 111–157 (1988).

[72] G. Gompper, T. Ihle, D. M. Kroll, and R. G. Winkler. Multi-Particle Collision Dynamics – a Particle-Based Mesoscale Simulation Approach to the Hydrodynamics of Complex Fluids. In C. Holm and K. Kremer, editors, *Advanced Computer Simulation Approaches for Soft Matter Sciences III* volume 221 of *Advances in Polymer Science* pages 1–87. Springer Berlin Heidelberg (2009).

[73] U. Frisch, B. Hasslacher, and Y. Pomeau. Lattice-Gas Automata for the Navier-Stokes Equation. *Phys. Rev. Lett* **56**(14), 1505–1508 (1986).

[74] A. J. C. Ladd, M. E. Colvin, and D. Frenkel. Application of Lattice-Gas Cellular Automata to the Brownian Motion of Solids in Suspension. *Phys. Rev. Lett.* **60**(11), 975–978 (1988).

[75] A. Vianney and J. M. Koelman. Cellular-Automaton-Based Simulation of 2D Polymer Dynamics. *Phys. Rev. Lett.* **64**(16), 1915 (1990).

[76] P. Ahlrichs and B. Dünweg. Lattice-Boltzmann Simulation of Polymer-Solvent Systems. *International Journal of Modern Physics C* **09**(08), 1429–1438 (1998).

[77] M. E. Cates, O. Henrich, D. Marenduzzo, and K. Stratford. Lattice Boltzmann simulations of liquid crystalline fluids: active gels and blue phases. *Soft Matter* **5**, 3791–3800 (2009).

[78] J. Zhang, P. C. Johnson, and A. S. Popel. Red blood cell aggregation and dissociation in shear flows simulated by lattice Boltzmann method. *Journal of Biomechanics* **41**, 47–55 (2008).

[79] A. Malevanets and R. Kapral. Mesoscopic model for solvent dynamics. *J. Chem. Phys.* **110**(17), 8605–8613 (1999).

[80] R. Kapral. *Multiparticle Collision Dynamics: Simulation of Complex Systems on Mesoscales* pages 89–146. John Wiley & Sons, Inc. (2008).

[81] M. Peltomäki and G. Gompper. Sedimentation of single red blood cells. *Soft Matter* **9**, 8346–8358 (2013).

[82] P. J. Hoogerbrugge and J. M. V. A. Koelman. Simulating microscopic hydrodynamic phenomena with dissipative particle dynamics. *EPL (Europhysics Letters)* **19**(3), 155–160 (1992).

[83] P. Español and P. Warren. Statistical mechanics of dissipative particle dynamics. *EPL (Europhysics Letters)* **30**(4), 191–196 (1995).

[84] P. Español and M. Revenga. Smoothed dissipative particle dynamics. *Phys. Rev. E* **67**, 026705 (2003).

[85] J. J. Monaghan. Smoothed particle hydrodynamics. *Annu. Rev. Astron. Astrophys.* **30**, 543–574 (1992).

[86] J. J. Monaghan. Smoothed particle hydrodynamics. *Reports on Progress in Physics* **68**, 1703–1759 (2005).

[87] X. Y. Hu and N. A. Adams. Angular-momentum conservative smoothed particle dynamics for incompressible viscous flows. *Phys. Fluids* **18**, 101702 (2006).

[88] K. Müller, D. A. Fedosov, and G. Gompper. Smoothed dissipative particle dynamics with angular momentum conservation. *Journal of Computational Physics* **281**, 301–315 (2015).

[89] B. M. Johnston, P. R. Johnston, S. Corney, and D. Kilpatrick. Non-Newtonian blood flow in human right coronary arteries: steady state simulations. *Journal of Biomechanics* **37**, 709–720 (2004).

[90] P. Bagchi. Mesoscale Simulation of Blood Flow in Small Vessels. *Biophysical Journal* **92**, 1858–1877 (2007).

[91] D. A. Fedosov. *Multiscale Modeling of Blood Flow and Soft Matter.* PhD thesis Brown University, USA (2010).

[92] V. Kantsler and V. Steinberg. Transition to Tumbling and Two Regimes of Tumbling Motion of a Vesicle in Shear Flow. *Phys. Rev. Lett.* **96**, 036001 (2006).

[93] M.-A. Mader, V. Vitkova, M. Abkarian, A. Viallat, and T. Podgorski. Dynamics of viscous vesicles in shear flow. *Eur. Phys. J. E* **19**, 389–397 (2006).

[94] M. Abkarian, M. Faivre, and A. Viallat. Swinging of Red Blood Cells under Shear Flow. *Phys. Rev. Lett.* **98**, 188302 (2007).

[95] S. R. Keller and R. Skalak. Motion of a tank-treading ellipsoidal particle in a shear flow. *Journal of Fluid Mechanics* **120**, 27–47 (1982).

[96] R. Tran-Son-Tay, S. P. Sutera, and P. R. Rao. Determination of Red Blood Cell Membrane Viscosity from Rheoscopic Observations of Tank-Treading Motion. *Biophysical Journal* **46**, 65–72 (1984).

[97] H. Noguchi and G. Gompper. Dynamics of fluid vesicles in shear flow: Effect of the membrane viscosity and thermal fluctuations. *Phys. Rev. E* **72**, 011901 (2005).

[98] C. Misbah. Vacillating Breathing and Tumbling of Vesicles under Shear Flow. *Phys. Rev. Lett.* **96**, 028104 (2006).

[99] H. Noguchi and G. Gompper. Fluid Vesicles with Viscous Membranes in Shear Flow. *Phys. Rev. Lett.* **93**, 258102 (2004).

[100] A. Yazdani and P. Bagchi. Three-dimensional numerical simulation of vesicle dynamics using a front-tracking method. *Phys. Rev. E* **85**, 056308 (2012).

[101] H. Noguchi. Swinging and synchronized rotations of red blood cells in simple shear flow. *Phys. Rev. E* **80**, 021902 (2009).

[102] H. Noguchi and G. Gompper. Swinging and Tumbling of Fluid Vesicles in Shear Flow. *Phys. Rev. Lett.* **98**, 128103 (2007).

[103] H. Zhao and E. S. G. Shaqfeh. The dynamics of a vesicle in simple shear flow. *Journal of Fluid Mechanics* **674**, 578–604 (2011).

[104] S. Meßlinger, B. Schmidt, H. Noguchi, and G. Gompper. Dynamical regimes and hydrodynamic lift of viscous vesicles under shear. *Phys. Rev. E* **80**, 011901 (2009).

[105] P. Olla. The role of tank-treading motions in the transverse migration of a spheroidal vesicle in a shear flow. *Journal of Physics A: Mathematical and General* **30**, 317–329 (1997).

[106] B. Lorz, R. Simson, J. Nardi, and E. Sackmann. Weakly adhering vesicles in shear flow: Tanktreading and anomalous lift force. *EPL (Europhysics Letters)* **51**(4), 468–474 (2000).

[107] N. Callens, C. Minetti, G. Coupier, M.-A. Mader, F. Dubois, C. Misbah, and T. Podgorski. Hydrodynamic lift of vesicles under shear flow in microgravity. *EPL (Europhysics Letters)* **83**, 24002 (2008).

[108] U. Seifert. Hydrodynamic Lift on Bound Vesicles. *Phys. Rev. Lett.* **83**(4), 876–879 (1999).

[109] S. Sukumaran and U. Seifert. Influence of shear flow on vesicles near a wall: A numerical study. *Phys. Rev. E* **64**, 011916 (2001).

[110] J. Beaucourt, T. Biben, and C. Misbah. Optimal lift force on vesicles near a compressible substrate. *EPL (Europhysics Letters)* **67**(4), 676–682 (2004).

[111] D. A. Fedosov, B. Caswell, A. S. Popel, and G. E. Karniadakis. Blood Flow and Cell-Free Layer in Microvessels. *Microcirculation* **17**, 615–628 (2010).

[112] B. Kaoui, G. H. Ristow, I. Cantat, C. Misbah, and W. Zimmermann. Lateral migration of a two-dimensional vesicle in unbounded Poiseuille flow. *Phys. Rev. E* **77**, 021903 (2008).

[113] J. L. McWhirter, H. Noguchi, and G. Gompper. Flow-induced clustering and alignment of vesicles and red blood cells in microcapillaries. *Proc. Natl. Acad. Sci. USA* **106**(15), 6039–6043 (2009).

[114] D. A. Fedosov, B. Caswell, and G. E. Karniadakis. A Multiscale Red Blood Cell Model with Accurate Mechanics, Rheology, and Dynamics. *Biophysical Journal* **98**, 2215–2225 (2010).

[115] D. A. Reasor Jr, J. R. Clausen, and C. K. Aidun. Coupling the lattice-Boltzmann and spectrin-link methods for the direct numerical simulation of cellular blood flow. *Int. J. Num. Meth. Fluids* **68**, 767–781 (2012).

[116] G. Tomaiuolo, M. Simeone, V. Martinelli, B. Rotoli, and S. Guido. Red blood cell deformation in microconfined flow. *Soft Matter* **5**, 3736–3740 (2009).

[117] E. W. Merrill, E. R. Gilliland, G. Cokelet, H. Shin, A. Britten, and R. E. Wells Jr. Rheology of Human Blood near and at Zero Flow. Effects of Temperature and Hematocrit Level. *Biophysical Journal* **3**, 199–213 (1963).

[118] D. A. Fedosov, W. Pan, B. Caswell, G. Gompper, and G. E. Karniadakis. Predicting human blood viscosity in silico. *Proc. Natl. Acad. Sci. USA* **108**(29), 11772–11777 (2011).

[119] A. Kumar and M. D. Graham. Margination and segregation in confined flows of blood and other multicomponent suspensions. *Soft Matter* **8**, 10536–10548 (2012).

[120] D. A. Fedosov, J. Fornleitner, and G. Gompper. Margination of White Blood Cells in Microcapillary Flow. *Phys. Rev. Lett.* **108**, 028104 (2012).

[121] U. Bagge and R. Karlsson. Maintenance of White Blood Cell Margination at the Passage through Small Venular Junctions. *Microvascular Research* **20**, 92–95 (1980).

[122] H. L. Goldsmith and S. Spain. Margination of Leukocytes in Blood Flow through Small Tubes. *Microvascular Research* **27**, 204–222 (1984).

[123] J. C. Firrell and H. H. Lipowsky. Leukocyte margination and deformation in mesenteric venules of rat. *Am. J. Physiol.* **256**, H1667–H1674 (1989).

[124] M. J. Pearson and H. H. Lipowsky. Influence of erythrocyte aggregation on leukocyte margination in postcapillary venules of rat mesentery. *Am. J. Physiol.* **279**, H1460–H1471 (2000).

[125] D. A. Fedosov and G. Gompper. White blood cell margination in microcirculation. *Soft Matter* **10**, 2961–2970 (2014).

[126] G. J. Tangelder, H. C. Teirlinck, D. W. Slaaf, and R. S. Reneman. Distribution of blood platelets flowing in arterioles. *Am. J. Physiol.* **248**, H318–H323 (1985).

[127] B. Woldhuis, G. J. Tangelder, D. W. Slaaf, and R. S. Reneman. Concentration profile of blood platelets differs in arterioles and venules. *Am. J. Physiol.* **262**, H1217–H1223 (1992).

[128] A. W. Tilles and E. C. Eckstein. The Near-Wall Excess of Platelet-Sized Particles inBlood Flow: Its Dependence on Hematocrit and Wall Shear Rate. *Microvascular Research* **33**, 211–223 (1987).

[129] C. Yeh and E. Eckstein. Transient Lateral Transport of Platelet-Sized Particles in Flowing Blood Suspensions. *Biophysical Journal* **66**, 1706–1716 (1994).

[130] L. Crowl and A. L. Fogelson. Analysis of mechanisms for platelet near-wall excess under arterial blood flow conditions. *Journal of Fluid Mechanics* **676**, 348–375 (2011).

[131] H. Zhao, E. S. G. Shaqfeh, and V. Narsimhan. Shear-induced particle migration and margination in a cellular suspension. *Phys. Fluids* **24**, 011902 (2012).

[132] D. A. Reasor Jr, M. Mehrabadi, D. N. Ku, and C. K. Aidun. Determination of Critical Parameters in Platelet Margination. *Ann. Biomed. Eng.* **41**(2), 238–249 (2013).

[133] A. A. Tokarev, A. A. Butylin, E. A. Ermakova, E. E. Shnol, G. P. Panasenko, and F. I. Ataullakhanov. Finite Platelet Size Could Be Responsible for Platelet Margination Effect. *Biophysical Journal* **101**, 1835–1843 (2011).

[134] R. D. Groot and P. B. Warren. Dissipative particle dynamics: Bridging the gap between atomistic and mesoscopic simulation. *J. Chem. Phys.* **107**(11), 4423–4435 (1997).

[135] I. V. Pivkin and G. E. Karniadakis. Coarse-graining limits in open and wall-bounded dissipative particle dynamics systems. *J. Chem. Phys.* **124**(18), 184101 (2006).

[136] X. Fan, N. Phan-Thien, S. Chen, X. Wu, and T. Y. Ng. Simulating flow of DNA suspension using dissipative particle dynamics. *Phys. Fluids* **18**, 063102 (2006).

[137] D. A. Fedosov, I. V. Pivkin, and G. E. Karniadakis. Velocity limit in DPD simulations of wall-bounded flows. *Journal of Computational Physics* **227**, 2540–2559 (2008).

[138] D. W. Condiff and J. S. Dahler. Fluid mechanical aspects of antisymmetric stress. *Phys. Fluids* **7**(6), 842–854 (1964).

[139] P. Español. Fluid particle model. *Phys. Rev. E* **57**(3), 2930–2948 (1998).

[140] R. Couillet and M. Debbah. *Random Matrix Methods for Wireless Communications.* Cambridge University Press (2011).

[141] L. B. Lucy. A numerical approach to the testing the fission hypothesis. *Astronom. J.* **82**(12), 1013–1024 (1977).

[142] S. Litvinov, M. Ellero, X. Hu, and N. A. Adams. Self-diffusion coefficient in smoothed dissipative particle dynamics. *J. Chem. Phys.* **130**(2), 021101 (2009).

[143] G. K. Batchelor. *An Introduction to Fluid Dynamics.* Cambridge University Press (2000).

[144] D. A. Fedosov and G. E. Karniadakis. Triple-decker: Interfacing atomistic-mesoscopic-continuum flow regimes. *Journal of Computational Physics* **228**, 1157–1171 (2009).

[145] M. Revenga, I. Zuniga, and P. Español. Boundary conditions in dissipative particle dynamics. *Computer Phys. Comm.* **122**, 309–311 (1999).

[146] A. Vázquez-Quesada, M. Ellero, and P. Español. Consistent scaling of thermal fluctuations in smoothed dissipative particle dynamics. *J. Chem. Phys.* **130**(3), 034901 (2009).

[147] I. O. Götze, H. Noguchi, and G. Gompper. Relevance of angular momentum conservation in mesoscale hydrodynamics simulations. *Phys. Rev. E* **76**, 046705 (2007).

[148] D. A. Fedosov, G. E. Karniadakis, and B. Caswell. Steady shear rheometry of dissipative particle dynamics models of polymer fluids in reverse Poiseuille flow. *J. Chem. Phys.* **132**, 144103 (2010).

[149] M. Serrano. Comparison between smoothed dissipative particle dynamics and Voronoi fluid particle model in a shear stationary flow. *Physica A* **362**, 204–209 (2006).

[150] C. Pozrikidis. Numerical Simulation of Cell Motion in Tube Flow. *Ann. Biomed. Eng.* **33**(2), 165–178 (2005).

[151] Y. Liu and W. K. Liu. Rheology of red blood cell aggregation by computer simulation. *Journal of Computational Physics* **220**, 139–154 (2006).

[152] S. K. Doddi and P. Bagchi. Three-dimensional computational modeling of multiple deformable cells flowing in microvessels. *Phys. Rev. E* **79**, 046318 (2009).

[153] D. A. Fedosov, H. Noguchi, and G. Gompper. Multiscale modeling of blood flow: from single cells to blood rheology. *Biomech. Model. Mechanobiol.* **13**, 239–258 (2014).

[154] W. Helfrich. Elastic properties of lipid bilayers: theory and possible experiments. *Z. Naturforschung* **28 C**(11), 693–703 (1973).

[155] E. A. Evans and R. Skalak. *Mechanics and Thermodynamics of Biomembranes*. CRC Press, Inc. (1980).

[156] D. A. Fedosov, B. Caswell, and G. E. Karniadakis. Systematic coarse-graining of spectrin-level red blood cell models. *Comput. Meth. Appl. Mech. Eng.* **199**, 1937–1948 (2010).

[157] S. Suresh, J. Spatz, J. P. Mills, A. Micoulet, M. Dao, C. T. Lim, M. Beil, and T. Seufferlein. Connections between single-cell biomechanics and human disease states: gastrointestinal cancer and malaria. *Acta Biomaterialia* **1**, 15–30 (2005).

[158] K. Müller, D. A. Fedosov, and G. Gompper. Margination of micro- and nano-particles in blood flow and its effect on drug delivery. *Sci. Rep.* **4**, 4871 (2014).

[159] A. S. Popel and P. C. Johnson. Microcirculation and Hemorheology. *Annu. Rev. Fluid Mech.* **37**, 43–69 (2005).

[160] A. R. Pries, T. W. Secomb, and P. Gaehtgens. Structure and hemodynamics of microvascular networks: heterogeneity and correlations. *Am. J. Physiol.* **269**, H1713–H1722 (1995).

[161] R. K. Jain. Determinants of Tumor Blood Flow: A Review. *Cancer Res.* **48**, 2641–2658 (1988).

[162] F. Yuan, H. A. Salehi, Y. Boucher, U. S. Vasthare, R. F. Tuma, and R. K. Jain. Vascular Permeability and Microcirculation of Gliomas and Mammary Carcinomas Transplanted in Rat and Mouse Cranial Windows. *Cancer Res.* **54**, 4564–4568 (1994).

[163] H. Lei, D. A. Fedosov, B. Caswell, and G. E. Karniadakis. Blood flow in small tubes: quantifying the transition to the non-continuum regime. *Journal of Fluid Mechanics* **722**, 214–239 (2013).

[164] N. Maeda, Y. Suzuki, J. Tanaka, and N. Tateishi. Erythrocyte flow and elasticity of microvessels evaluated by marginal cell-free layer and flow resistance. *Am. J. Physiol.* **271**, H2454–H2461 (1996).

[165] S. Kim, R. L. Kong, A. S. Popel, M. Intaglietta, and P. C. Johnson. Temporal and spatial variations of cell-free layer width in arterioles. *Am. J. Physiol* **293**, H1526–H1535 (2007).

[166] N. W. Moore and T. L. Kuhl. The Role of Flexible Tethers in Multiple Ligand-Receptor Bond Formation between Curved Surfaces. *Biophysical Journal* **91**, 1675–1687 (2006).

[167] J.-f. Dong, J. L. Moake, L. Nolasco, A. Bernardo, W. Arceneaux, C. N. Shrimpton, A. J. Schade, L. V. McIntire, K. Fujikawa, and J. A. López. ADAMTS-13 rapidly cleaves newly secreted ultralarge von Willebrand factor multimers on the endothelial surface under flowing conditions. *Blood* **100**(12), 4033–4039 (2002).

[168] G. B. Jeffery. The Motion of Ellipsoidal Particles Immersed in a Viscous Fluid. *Proc. R. Soc. Lond. A.* **102**, 161–179 (1922).

[169] J. Feng and D. D. Joseph. The unsteady motion of solid bodies in creeping flows. *Journal of Fluid Mechanics* **303**, 83–102 (1995).

[170] T.-R. Lee, M. Choi, A. M. Kopacz, S.-H. Yun, W. K. Liu, and P. Decuzzi. On the near-wall accumulation of injectable particles in the microcirculation: smaller is not better. *Sci. Rep.* **3**, 2079 (2013).

[171] *LAMMPS Molecular Dynamics Simulator.* Sandia National Laboratories http://lammps.sandia.gov.

[172] J.-P. Hansen and I. R. McDonald. *Theory of Simple Liquids.* Elsevier (2006).

[173] J. A. Barker and D. Henderson. Perturbation Theory and Equation of State for Fluids. II. A Successful Theory of Liquids. *J. Chem. Phys.* **47**(11), 4714–4721 (1967).

[174] H. C. Andersen, J. D. Weeks, and D. Chandler. Relationship between the Hard-Sphere Fluid and Fluids with Realistic Repulsive Forces. *Phys. Rev. A* **4**(4), 1597–1607 (1971).

[175] R. Fåhraeus. The suspension stability of the blood. *Physiol. Rev.* **9**(2), 241–274 (1929).

[176] R. Skalak and P.-I. Branemark. Deformation of Red Blood Cells in Capillaries. *Science* **164**, 717–719 (1969).

[177] H. Noguchi and G. Gompper. Shape transitions of fluid vesicles and red blood cells in capillary flows. *Proc. Natl. Acad. Sci. USA* **102**(40), 14159–14164 (2005).

[178] J. H. Barbee and G. R. Cokelet. The Fahraeus Effect. *Microvascular Research* **3**, 6–16 (1971).

[179] A. R. Pries, D. Neuhaus, and P. Gaehtgens. Blood viscosity in tube flow: dependence on diameter and hematocrit. *Am. J. Physiol.* **263**, H1770–H1778 (1992).

[180] A. R. Pries, T. W. Secomb, P. Gaehtgens, and J. F. Gross. Blood Flow in Microvascular Networks. Experiments and Simulation. *Circulation Research* **67**, 826–834 (1990).

[181] A. A. Tokarev, A. A. Butylin, and F. I. Ataullakhanov. Platelet Adhesion from Shear Blood Flow is Controlled by Near-Wall Rebounding Collisions with Erythrocytes. *Biophysical Journal* **100**, 799–808 (2011).

[182] V. T. Turitto, A. M. Benis, and E. F. Leonard. Platelet Diffusion in Flowing Blood. *Industrial & Engineering Chemistry Fundamentals* **11**(2), 216–223 (1972).

[183] H. L. Goldsmith and S. G. Mason. The flow of suspensions through tubes. I. Single spheres, rods, and discs. *Journal of Colloid Science* **17**(5), 448–476 (1962).

[184] F. P. Bretherton. The motion of rigid particles in a shear flow at low Reynolds number. *Journal of Fluid Mechanics* **14**, 284–304 (1962).

[185] P. G. Saffman. The lift on a small sphere in a slow shear flow. *Journal of Fluid Mechanics* **22**, 385–400 (1965).

[186] G. Segré and A. Silberberg. Radial Particle Displacements in Poiseuille Flow of Suspensions. *Nature* **189**, 209–210 (1961).

[187] G. Segré and A. Silberberg. Behaviour of macroscopic rigid spheres in Poiseuille flow. Part 1. Determination of local concentration by statistical analysis of particle passages through crossed light beams. *Journal of Fluid Mechanics* **14**, 115–135 (1962).

[188] G. Segré and A. Silberberg. Behaviour of macroscopic rigid spheres in Poiseuille flow. Part 2. Experimental results and interpretation. *Journal of Fluid Mechanics* **14**, 136–157 (1962).

[189] E. C. Eckstein, D. G. Bailey, and A. H. Shapiro. Self-diffusion of particles in shear flow of a suspension. *Journal of Fluid Mechanics* **79**, 191–208 (1977).

[190] M. Frank, D. Anderson, E. R. Weeks, and J. F. Morris. Particle migration in pressure-driven flow of a Brownian suspension. *Journal of Fluid Mechanics* **493**, 363–378 (2003).

[191] D. Semwogerere, J. F. Morris, and E. R. Weeks. Development of particle migration in pressure-driven flow of a Brownian suspension. *Journal of Fluid Mechanics* **581**, 437–451 (2007).

[192] H. M. Vollebregt, R. G. M. van der Sman, and R. M. Boom. Model for particle migration in bidisperse suspensions by use of effective temperature. *Faraday Discussions* **158**, 89–103 (2012).

[193] C. Sendner and R. R. Netz. Shear-induced repulsion of a semiflexible polymer from a wall. *EPL (Europhysics Letters)* **81**, 54006 (2008).

[194] C. E. Sing and A. Alexander-Katz. Non-monotonic hydrodynamic lift force on highly extended polymers near surfaces. *EPL (Europhysics Letters)* **95**, 48001 (2011).

[195] A. Alexander-Katz, M. F. Schneider, S. W. Schneider, A. Wixforth, and R. R. Netz. Shear-Flow-Induced Unfolding of Polymeric Globules. *Phys. Rev. Lett.* **97**, 138101 (2006).

[196] J. R. C. van der Maarel. *INTRODUCTION TO BIOPOLYMER PHYSICS*. World Scientific (2008).

[197] P. J. Flory. *Principles of Polymer Chemistry*. Cornell University Press, (1953).

[198] P. G. de Gennes. *Scaling Concepts in Polymer Physics*. Cornell University Press (1979).

[199] Y. Kong, C. W. Manke, W. G. Madden, and A. G. Schlijper. Simulation of a Confined Polymer in Solution Using the Dissipative Particle Dynamics Method. *International Journal of Thermophysics* **15**(6), 1093–1101 (1994).

[200] D. E. Smith, H. P. Babcock, and S. Chu. Single-Polymer Dynamics in Steady Shear Flow. *Science* **283**, 1724–1727 (1999).

[201] A. Alexander-Katz and R. R. Netz. Surface-enhanced unfolding of collapsed polymers in shear flow. *EPL (Europhysics Letters)* **80**, 18001 (2007).

[202] A. Padilla, J. L. Moake, A. Bernardo, C. Ball, Y. Wang, M. Arya, L. Nolasco, N. Turner, M. C. Berndt, B. Anvari, et al. P-selectin anchors newly released ultralarge von Willebrand factor multimers to the endothelial cell surface. *Blood* **103**(6), 2150–2156 (2004).

[203] T. A. Springer. Biology and physics of von Willebrand factor concatamers. *Journal of Thrombosis and Haemostasis* **9**(Suppl. 1), 130–143 (2011).

[204] C. Baldauf, R. Schneppenheim, W. Stacklies, T. Obser, A. Pieconka, S. Schneppenheim, U. Budde, J. Zhou, and F. Gräter. Shear-induced unfolding activates von Willebrand factor A2 domain for proteolysis. *Journal of Thrombosis and Haemostasis* **7**, 2096–2105 (2009).

[205] B. Savage, J. J. Sixma, and Z. M. Ruggeri. Functional self-association of von Willebrand factor during platelet adhesion under flow. *Proc. Natl. Acad. Sci. USA* **99**(1), 425–430 (2002).

[206] C. E. Sing and A. Alexander-Katz. Elongational Flow Induces the Unfolding of von Willebrand Factor at Physiological Flow Rates. *Biophysical Journal* **98**, L35–L37 (2010).

[207] C. E. Sing, J. G. Selvidge, and A. Alexander-Katz. Von Willlebrand Adhesion to Surfaces at High Shear Rates is Controlled by Long-Lived Bonds. *Biophysical Journal* **105**, 1475–1481 (2013).

[208] G. Interlandi and W. Thomas. The catch bond mechanism between von Willebrand factor and platelet surface receptors investigated by molecular dynamics simulations. *Proteins: Structure, Function, and Bioinformatics* **78**(11), 2506–2522 (2010).

[209] U. S. Agarwal, A. Dutta, and R. A. Mashelkar. Migration of macromolecules under flow: the physical origin and engineering implications. *Chemical Engineering Science* **49**(11), 1693–1717 (1994).

[210] D. Stein, F. H. J. van der Heyden, W. J. A. Koopmans, and C. Dekker. Pressure-driven transport of confined DNA polymers in fluidic channels. *Proc. Natl. Acad. Sci. USA* **103**(43), 15853–15858 (2006).

[211] R. Khare, M. D. Graham, and J. J. de Pablo. Cross-Stream Migration of Flexible Molecules in a Nanochannel. *Phys. Rev. Lett.* **96**, 224505 (2006).

[212] O. B. Usta, J. E. Butler, and A. J. C. Ladd. Flow-induced migration of polymers in dilute solution. *Phys. Fluids* **18**, 031703 (2006).

[213] O. B. Usta, J. E. Butler, and A. J. C. Ladd. Transverse Migration of a Confined Polymer Driven by an External Force. *Phys. Rev. Lett.* **98**, 098301 (2007).

[214] L. Cannavacciuolo, R. G. Winkler, and G. Gompper. Mesoscale simulations of polymer dynamics in microchannel flows. *EPL (Europhysics Letters)* **83**, 34007 (2008).

[215] R. Chelakkot, R. G. Winkler, and G. Gompper. Migration of semiflexible polymers in microcapillary flow. *EPL (Europhysics Letters)* **91**, 14001 (2010).

[216] S. Lippok, T. Obser, J. P. Müller, V. K. Stierle, M. Benoit, U. Budde, R. Schneppenheim, and J. O. Rädler. Exponential Size Distribution of von Willebrand Factor. *Biophysical Journal* **105**, 1208–2016 (2013).

[217] A. R. Pries, T. W. Secomb, and P. Gaehtgens. The endothelial surface layer. *Pflügers Archiv – Eur. J. Physiol.* **440**, 653–666 (2000).

[218] A. R. Pries and T. W. Secomb. Rheology of the microcirculation. *Clin. Hemorheol. Microcirc.* **29**, 143–148 (2003).

[219] A. R. Pries, K. Ley, M. Claassen, and P. Gaehtgens. Red Cell Distribution at Microvascular Bifurcations. *Microvascular Research* **38**, 81–101 (1989).

[220] H. H. Lipowsky. Microvascular Rheology and Hemodynamics. *Microcirculation* **12**, 5–15 (2005).

[221] B. Ji and A. Ündar. Comparison of perfusion modes on microcirculation during acute and chronic cardiac support: is there a difference? *Perfusion* **22**, 115–119 (2007).

[222] K. H. Fraser, M. E. Taskin, B. P. Griffith, and Z. J. Wu. The use of computational fluid dynamics in the development of ventricular assist devices. *Medical Engineering & Physics* **33**, 263–280 (2011).

[223] W. Wang, T. G. Diacovo, J. Chen, J. B. Freund, and M. R. King. Simulation of Platelet, Thrombus and Erythrocyte Hydrodynamic Interactions in a 3D Arteriole with *In Vivo* Comparison. *PLOS ONE* **8**(10), e76949 (2013).

[224] C. E. Sing and A. Alexander-Katz. Globule-Stretch Transitions of Collapsed Polymers in Elongational Flow Fields. *Macromolecules* **43**, 3532–3541 (2010).

[225] A. Colagrossi and M. Landrini. Numerical simulation of interfacial flows by smoothed particle hydrodynamics. *Journal of Computational Physics* **191**, 448–475 (2003).

Danksagung

An dieser Stelle danke ich allen Menschen, die mich in der Vergangenheit unterstützt und zum Gelingen dieser Arbeit beigetragen haben.

Besonders danke ich Gerhard Gompper dafür, dass er mir die Möglichkeit gegeben hat in seiner Gruppe und vor allem an dem faszinierenden DFG Projekt „SHENC“ mitzuarbeiten. Außerdem danke ich ihm für die Betreuung dieser Doktorarbeit. In zahlreichen und langen Diskussionen hat er sich allen meinen Problemen und Fragen angenommen und selber die richtigen Fragen gestellt, wodurch fast alle Probleme spätestens nach einem Gespräch mit ihm gelöst werden konnten. Diese Gespräche habe mir nicht nur weiter geholfen sondern haben mich auch einiges gelehrt. Ich danke ihm auch dafür, dass er mir die Chance gegeben hat an einer Vielzahl von Konferenzen teilzunehmen, bei denen ich viele wertvolle Erfahrungen sammeln und Kontakte knüpfen konnte und zusätzlich viel Spaß hatte.

Ich danke Joachim Krug, dass er die Zweitbegutachtung dieser Doktorarbeit übernommen hat.

Ein großer Dank gebührt auch meinem Betreuer Dimtry Fedosov! Er hat immer eine offene Bürotür und ein offenes Ohr für mich und hat ganz gelassen und manchmal gleich mehrfach meine vielen Fragen beantwortet, die nicht immer so einfach zu beantworten waren wie ich dachte, was nicht selten zu längeren Diskussionen geführt hat. Ich danke Dmitry auch sehr dafür, dass er mir genügend Freiräume gegeben hat, die es mir ermöglicht haben eigene Ideen zu entwickeln und mich zu entfalten.

Ich danke unserer Sekretärin Helga Paffen dafür, dass sie auch uns Doktoranden die ganze bürokratische Arbeit abnimmt und auch noch ein offenes Ohr für sämtliche Probleme hat und alles daran setzt diese zu lösen und ich danke ihr für die netten Gespräche zwischendurch.

Ich danke allen Mitgliedern des ICS-2 in Jülich dafür so herzlich aufgenommen worden zu sein. Vielen Dank, für die hilfreichen Diskussionen, Ratschläge, Antworten, die

interessanten Gespräche und den Spaß beim täglichen Mittagessen, Eis essen, Kaffee trinken, dem jährlichen Grillabend und Wanderausflug. Besonders möchte ich mich bei Nils und Guglielmo bedanken, für die vielen Gespräche zwischendurch, im Büro und auf dem Weg zum Essen und ich danke ihnen dafür, dass sie es drei Jahre lang mit mir in einem Büro ausgehalten haben.

Ich danke der DFG für die Finanzierung meiner Doktorandenstelle innerhalb des Projekts: SHENC–Shear Flow Regulation in Hemostasis. Ich danke allen Mitgliedern von SHENC: es war lehrreich, faszinierend und auch lustig mit euch zusammen zu arbeiten.

Ich danke der Helmholtz research school BioSoft für die guten Weiterbildungsmöglichkeiten und ich danke den Mitgliedern von BioSoft für viele tolle Erfahrungen und Bekanntschaften.

Zu guter Letzt danke ich allen meinen Freunden und natürlich meiner Familie für ihren Beistand.

Dabei danke ich ganz besonders meiner Mutter, die mich mein Leben lang immer unterstützt hat und ohne die ich nicht der Mensch wäre der ich bin. Wenn es auch nicht immer so scheint, bin ich sehr dankbar dafür, dass sie sich immer noch um mich sorgt und kümmer und auch hoffentlich nie damit aufhören wird. Ich danke Wolfgang dafür, dass er Teil meiner Familie geworden ist und immer für meine Mutter und auch für mich da ist.

Ich danke meinem Freund, der mir in den vergangen Jahren immer zur Seite gestanden ist, sämtliche meiner Launen erträgt und mich immer wieder zum lachen bringt, wenn es mal nicht so gut läuft. Ich danke ihm auch dafür, dass er sich immer wieder Zeit gefunden hat mir bei allen möglichen Fragen und Probleme zu helfen und sich meine Vorträge angehört hat, obwohl er nur von sehr heißem Plasma etwas versteht und.

Ich danke meiner Freundin Ronja die als einzige wenigstens etwas von meiner Arbeit versteht, wie ich glaube, und auf die ich immer zählen kann. Außerdem hat sie ganz besonders dazu beigetragen hat, dass mein Leben in Jülich nicht nur von Arbeit geprägt war sondern auch weitere spannende Inhalte dazugekommen sind.

Erklärung

Ich versichere, dass ich die von mir vorgelegte Dissertation selbstständig angefertigt, die benutzten Quellen und Hilfsmittel vollständig angegeben und die Stellen der Arbeit – einschließlich Tabellen, Karten und Abbildungen –, die anderen Werken im Wortlaut oder dem Sinn nach entnommen sind, in jedem Einzelfall als Entlehnung kenntlich gemacht habe; dass diese Dissertation noch keiner anderen Fakultät oder Universität zur Prüfung vorgelegen hat; dass sie abgesehen von unten angegebenen Teilpublikationen noch nicht veröffentlicht worden ist, sowie, dass ich eine solche Veröffentlichung vor Abschluss des Promotionsverfahrens nicht vornehmen werde.

Die Bestimmungen der Promotionsordnung sind mir bekannt. Die von mir vorgelegte Dissertation ist von Prof. Dr. Gerhard Gompper betreut worden.

Jülich, den

Ort, Datum

Unterschrift

Articles in peer-reviewed journals:

K. Müller, D. A. Fedosov, and G. Gompper. Margination of micro- and nano-particles in blood flow and its effect on drug delivery. *Sci. Rep.* **4**, 4871 (2014).

K. Müller, D. A. Fedosov, and G. Gompper. Smoothed dissipative particle dynamics with angular momentum conservation. *J. Comp. Phys.* **281**, 301-315 (2015).

Articles in conference proceedings:

K. Müller, D. A. Fedosov, and G. Gompper. Margination of Micro- and Nano-Particles in Blood Flow and its Effect on the Efficiency of Drug Delivery. *Proceedings of 4th Micro and Nano Flows Conference* (2014)

K. Müller, D. A. Fedosov, and G. Gompper. Behaviour of the von Willebrand Factor in Blood Flow. *Proceedings of 4th Micro and Nano Flows Conference* (2014)

D. A. Fedosov, J. Fornleitner, J. L. McWhirter, K. Müller, H. Noguchi, M. Peltomäki, and G. Gompper. Blood Flow *in silico*: From Single Cells to Blood Rheology. *Proceedings of 4th Micro and Nano Flows Conference* (2014)